UNIVERSITÀ
DEGLI STUDI
DI UDINE
hic sunt futura

Analysis of top-quark production processes for the search of new physics and correlated tracking studies in the ATLAS experiment at the LHC

Dottorando

Mohammed I. H. Faraj

Corso di dottorato di ricerca in

Informatica e Scienze Matematiche e Fisiche

Ciclo 32° XXXll

Supervisors

Prof. Andrea Vacchi **Prof. Marina Cobal**

2020

Abstract

Dipartimento di Scienze Matematiche, Informatiche e Fisiche (DMIF)

Doctor of Philosophy

by Mohammed I. H. Faraj

Since the top-quark is the heaviest elementary particle in the Standard Model (SM), with a mass close to the scale of electroweak symmetry breaking[1, 2], it plays an essential role in many models (SM and beyond SM (BSM)), and it might answer several questions still unanswered in the SM. For this reason, I tackled this topic in different ways. This thesis presents a study of the tracking-efficiency performance of the Inner Detector of the ATLAS experiment to reconstruct pion tracks in data and simulated events. Also, it presents analyses of different processes involving top quarks. The first one is the study of four-top-quark production in the single-lepton and opposite-sign dilepton final states, where a new method has been developed to reject backgrounds in the signal region for both channels. The second search looks for the existence of new particles as predicted by several theoretical BSM models, which are the Topcolor Assisted Technicolor model (TC2) [3–5], and the Randall-Sundrum model [6–9]. No evidence for resonant productions of top-quark pairs is found. As a result, expected limits are set on the production cross-section times branching ratio of these models at 95% confidence level. Both these analyses are based on data from proton-proton collisions at a centre-of-mass energy $\sqrt{s} = 13$ TeV collected by the ATLAS experiment at the Large Hadron Collider (LHC) at CERN and simulated Monte Carlo (MC) events as predicted from the SM and BSM models.


سُورَةُ العَلَقِ
بِسْمِ اللَّهِ الرَّحْمَٰنِ الرَّحِيمِ
اقْرَأْ بِاسْمِ رَبِّكَ الَّذِي خَلَقَ ١ خَلَقَ الْإِنسَانَ مِنْ عَلَقٍ ٢ اقْرَأْ
وَرَبُّكَ الْأَكْرَمُ ٣ الَّذِي عَلَّمَ بِالْقَلَمِ ٤ عَلَّمَ الْإِنسَانَ
مَا لَمْ يَعْلَمْ ٥ كَلَّا إِنَّ الْإِنسَانَ لَيَطْغَىٰ ٦ أَن رَّآهُ اسْتَغْنَىٰ
٧ إِنَّ إِلَىٰ رَبِّكَ الرُّجْعَىٰ ٨

Contents

Acknowledgements

I would like to express my special appreciation and thanks to Prof. Marina Cobal and Prof. Bobby Acharya for their continuous support during my PhD study and related research, for the motivation and the immense knowledge which they transmitted to me. They have been an excellent mentor for me. Their guidance helped me in all the research period and the writing of this thesis. Besides them, I would like to thank all Udine University and ICTP professors, staff, and Postdoctoral and PhD students. All of them have been there to support and help me in several ways. A special thanks to Prof. Andrea Vacchi.

My sincere thanks also go to Dr Michele Pinamonti, Dr Leonid Serkin, and Dr Giancarlo Panizzo, who supported me during my PhD study and helped me with their great knowledge and experience. Without their precious support, this thesis would have been not possible. A special thanks to Dr Vivek Jain for his assistance in the qualification task and Dr Kate Shaw for her great work in the developing countries.

I gratefully acknowledge the funding received for my PhD from the Kuwait Foundation for the Advancement of Science (KFAS). I am also grateful to the support received through the Istituto Nazionale di Fisica Nucleare (INFN) during my PhD. I greatly appreciate the funding received through the International Centre for Theoretical Physics (ICTP) for the last period of my PhD.

A special thanks to my family. Words cannot express how grateful I am to my mother, father, and to my brothers and sister for all of the sacrifices and supports that they have made for me. I would also like to thank all of my friends who supported me during my study and life in general. In the end, I would like to express appreciation to my beloved wife, who always supports me in all moments.

Finally, I would like to thank from all my heart all the medical staff around the whole world for their tremendous work, help and care in this hard period of 2020.

List of Figures

List of Tables

Chapter 1

Introduction

Since the break of dawn humankind has been wondering about Nature. Among other things, human beings have been trying to understand which elementary components Nature is made up of. There have been then many theories and experiments conducted to arrive at a comprehensive answer to the fundamental question: What is the world made of?

Starting from the twentieth century, we changed our knowledge about particles and their properties after the great discoveries of different sub-atomic objects such as electrons, protons, neutrons, and photons. We found that classical mechanics cannot describe objects at very small length scales and which move at speed (close to the speed of light). Special Relativity and Quantum Mechanics were needed to describe these particles, and by combining these two theories, we got the Quantum Field Theory, which describes all the elementary particles and their interactions. Furthermore, with the study of the cosmic rays and the huge advancements in experimental equipment, such as the particle colliders, several elementary particles were identified, which interact with each other via four fundamental forces: strong, weak, electromagnetic, and gravitational.

In the world of elementary particles, at small length scales and high speeds, the most powerful model that describes properties and interactions of these particles is the Standard Model (SM) [10, 42]. This model was developed and built as a result of lengthy experimental and theoretical researches. The SM combines the Quantum Electrodynamics theory known as Glashow–Weinberg–Salam electroweak theory [43–45] (GWS model)

which describes the electroweak interaction processes (such as beta decay, leptons interaction, heavy leptons decay, etc.) and the Quantum Chromodynamics QCD, that describes the interaction of strongly interacting particles (hadrons) [46, 47]. This model classifies all the building blocks of matter and their properties, such as parity, charges, colour, etc. together with their interactions. Also, we can predict and calculate different physics quantities to describe particle interactions, like cross-section, decay width, lifetime, etc. However, the SM is incomplete, since the gravitational force is not included in this model, and the idea of unification between all forces cannot be accomplished within the SM. Also, Dark Matter, and neutrino masses and oscillation are not predicted. Many theories try to find and describe new areas in physics that are not covered by the SM.

The SM was developed on the base of the results of many experiments performed to complete our knowledge and understanding of fundamental particles. Many experiments also searched for particles predicted from other theories beyond the Standard Model, such as Supersymmetry (SUSY). However, up to now, none of these theories have been confirmed.

From the 1970s up to nowadays, there has been an impressive development in high energy accelerators and detectors which help us to provide us with an in-depth look into the world of fundamental particles, understand their interactions with different materials, how they create and annihilate in various processes, and how our universe has been created. The Large Hadron Collider (LHC) is the most powerful machine that provides us with a huge amount of data at different collision centre of mass energies. The LHC is hosted in the CERN laboratory, close to the Geneva town. It is a circular collider whose circumference is 27 km, located 100 meters underground. It is designed to provide the scientists with different data by colliding proton-proton (pp), heavy ions and proton heavy-ion. The centre of mass-energy for the collisions $\sqrt{s}$ was increased from 7 TeV in 2008 to 13 TeV in 2015.

LHC hosts four main detectors (CMS, LHCb, ALICE and ATLAS detectors), each one built for different purposes. They intend to cover many scientific fields such as SM or beyond SM physics, plasma physics, dark matter, etc. For this thesis, I analysed data collected by the ATLAS detector. ATLAS is the largest detector in the world, composed of three main layers to detect all fundamental and composite particles.

The top quark is the heaviest in between the known elementary particle predicted by the SM, which plays a crucial role in particle physics. Its mass is $\sim$ 170 times larger than the proton mass and $\sim$ 40 times larger than the second heaviest elementary particle in the SM, the bottom quark. Due to its large mass close to the electroweak symmetry breaking, as well as to the value of its Yukawa coupling to the Higgs boson close to unity, it might play a crucial role in searches for new physics beyond the SM. In the LHC, the dominant process for top-quarks production is in pairs via strong interaction, referred to as top-antitop ($t\bar{t}$) process.

In the ATLAS experiment at the LHC, a large number of top-antitop pairs is produced which allows a precise measurement of the process cross-section essential for searches predicted by the SM, e.g. four-top-quark production and by several BSM theories where new particles decaying into top-antitop pairs, e.g. Z', graviton, may appear.

In this thesis, three works are presented which use data collected in proton-proton collisions at the centre of mass-energy $\sqrt{s}$ = 13 TeV with the ATLAS experiment at the LHC. The first one is a performance study which evaluates the efficiency of reconstructing pion track in data and simulated events. The second one develops the χ^2–method to reconstruct two top quarks decaying hadronically in the single-lepton and opposite-sign dilepton final states using simulated data generated at $\sqrt{s}$ = 13 TeV. The last one is which is the core of the thesis, is the search for top-antitop quark resonances production where upper limits are set on the cross-sections for new physics particles in dilepton channel.

In the following, chapters are organised as follows: Chapter 2 gives an introduction to the Standard Model, to the top-quark physics and the new physics predicted by several BSM theories. Chapter 3 describes the LHC and one of the general-purpose detectors, ATLAS detector. In Chapter 4, particles reconstruction and identification are presented, and the observables used in the analyses are shown. An introduction to tracks and vertices reconstructions, and to the efficiency measurement of reconstructing pion track, is presented in Chapter 5. In Chapter 6, a new method based on χ^2 is presented to reconstruct top-quarks in the SM production of four-top-quark. Finally, search on new physics particles decaying to top-antitop quark pairs is presented in Chapter 7.

Chapter 2

Theoretical Framework

The SM of particle physics is the theoretical framework of this thesis. Up to now, the SM proved to be in excellent agreement with all the collected results in the present and past experiments, including by the LHC and Tevatron. However, it is not considered to be a complete theory since it does not cover many-particle physics aspects, such as gravity, neutrino oscillations and the existence of dark matter in the universe.

In this chapter, an overview of the SM is given in Section 2.1 The electroweak theory and the theory of strong interactions are covered in more detail in Section 2.1.1 and Section 2.1.3, respectively. Top quark production and decay mechanisms, in particular, are discussed in details in Section 2.2 since the top quark plays an essential role within the SM as well as in theories beyond the Standard Model (BSM). Finally, a short overview of some BSM, which can be interesting for the work presented here is given in Section 2.3.

2.1 The Standard Model of Particle Physics

The SM is a theoretical framework which describes elementary particles (Matter) and their interactions (Forces) [43–48]. As of today, it is the most accurate theoretical model describing the submolecular world, capable of providing correct predictions and confirmed by several experiments. The SM is based on the idea of local gauge symmetries, which are combined and lead to conservation laws according to the Noether Theorem.

The SM of particle physics classifies the visible matter, which forms ∼5% of the Universe, and their interactions. Besides, it includes a mass-generating mechanism, referred to as the Higgs mechanism, which is responsible for particle masses. Within the SM, the gauge group of quantum electrodynamics (QED) is combined with the weak interaction, leading to a unified theory known as the theory of electroweak interactions. It combines as well the gauge group of the electroweak theory with one of the theory of the strong interaction (Quantum Chromodynamics or QCD). Gravity, which is the fourth force in nature, can not be included in the SM due to the mathematical limitations at high energy scales, where it has a negligible effect compared to other forces.

In the SM, elementary particles (matter) are fermions with spin $\frac{1}{2}$ divided into six leptons and six quarks. These fermions are then classified into three families (generations), as shown in table 2.1. Each family contains pairs of leptons and quarks. Additionally, each fermion has its anti-particle with opposite quantum numbers, like charges and parity, but with the same mass.

	Leptons			Quark		
	Particle	Charge[e]	$\frac{Mass}{GeV}$	Particle	Charge[e]	$\frac{Mass}{GeV}$
First generation	e^-	-1	0.00051	d	$-1/3$	0.0047
	ν_e	0	10^{-9}	u	$+2/3$	0.0022
Second generation	μ^-	-1	0.1056	s	$-1/3$	0.95
	ν_μ	0	10^{-9}	c	$+2/3$	1.275
Third generation	τ^-	-1	1.776	b	$-1/3$	4.18
	ν_τ	0	10^{-9}	t	$+2/3$	173

TABLE 2.1: Leptons and Quarks in the SM with their properties [37].

In the quantum-relativistic framework units ($c = 1, \hbar = 1, e = 1$) of the SM, forces are transported by gauge bosons, which are quanta of gauge fields. The gauge vector bosons in the SM with spin-one are listed with their properties in table 2.2. Each boson associated with one of the interactions included in the SM. Additionally, there is a scalar boson with spin-zero called the Higgs boson presented in table 2.2, and it will be introduced in the following section (2.1.2).

Gauge Boson	Interaction	Charge[e]	$\frac{Mass}{GeV}$	Spin
γ	Electromagnetic	0	$< 1 \times 10^{-27}$	1
$W^{\pm}$	Weak	± 1	80.379 ± 0.015	1
Z^0	Weak	0	91.1876 ± 0.0021	1
gluon	Strong	0	0	1

TABLE 2.2: SM gauge vector bosons properties and their associated interactions [37].

2.1.1 Electroweak Interactions

In the 1960s, Glashow, Salam and Weinberg proposed the first theoretical attempt to unify QED (Quantum Electrodynamics) [43, 45] with the theory of weak interactions [44], introducing the theory of electroweak interactions. It combines the symmetries of the gauge groups $SU(2)$ (weak interactions) and $U(1)$ (QED), to produce the electroweak $SU(2)_L \times U(1)_Y$ where $U(1)_{QED} \subset SU(2) \times U(1)$. Therefore, this theory describes both the electromagnetic and weak charged current processes.

The first part of the symmetry group, $SU(2)_L$, introduces the so-called the weak isospin, T, which can be written in the form of $T_i = \tau_i/2$, $i = 1, 2, 3$ (τ_i are the Pauli-matrices) and they correspond to three massless gauge fields W_{μ^i}. Since in group theory, the number of $SU(N)$ generators, which corresponds to the number of gauges, is equal to $N^2 - 1$, where N is the group dimension. On the other hand, the $U(1)_Y$ symmetry group introduces the hypercharge (Y), and it corresponds to one massless gauge field, B_μ. The hypercharge, Y, is associated with the electric charge and T_3 is the third component of the weak isospin via the Gell-Mann Nishijima formula:

$$Y = 2(Q - T_3) \tag{2.1}$$

Left-handed fermions (ψ_L) and right-handed anti-fermions are represented as doublets with isospin $T_3 \neq 0$ under the $SU(2)$ transformation, and they interact via the exchange of the gauge bosons $W^{\pm}$ and Z^0. While the right-handed fermions (ψ_R) and left-handed anti-fermions are singlets with $T_3 = 0$ and they interact via the exchange of a Z^0 boson and γ only.

The full Lagrangian of the electroweak interactions can be written as

$$\mathcal{L}_{EW} = \ \psi_L^\dagger \ i\gamma^\mu \ D_\mu \ \psi_L + \psi_R^\dagger \ i\gamma^\mu D_\mu \psi_R - \tfrac{1}{4} W^i_{\mu\nu} W_i^{\mu\nu} - \tfrac{1}{4} B_{\mu\nu} B^{\mu\nu} \tag{2.2}$$

where the first two terms describe particles interactions while the last two terms are related to the gauge fields interactions. The gauge bosons (A_μ, Z_μ and $W_\mu^\pm$) in this model are massless particles because they are described as linear combinations of massless gauge files.

The covariant derivative in the electroweak interactions for ψ_L fermions is given as,

$$D^\mu = \ \partial^\mu + ig \ \tfrac{\tau_i}{2} \ W_\mu^i + i \ \tfrac{g'}{2} \ Y B^\mu \tag{2.3}$$

while for ψ_R fermions, the covariant derivative is

$$D^\mu = \ \partial^\mu + i \ \tfrac{g'}{2} \ Y B^\mu \tag{2.4}$$

where g and g' are the coupling constants for $SU(2)$ and $U(1)$, respectively.

The physics fields (gauge bosons) can be derived, using the previous covariant derivatives and from the linear combinations of the gauge fields W_μ and B_μ,

$$A_\mu = \ W_\mu^3 \ \sin(\theta_W) + B_\mu \ \cos(\theta_W) \tag{2.5}$$

$$Z_\mu = \ W_\mu^3 \ \cos(\theta_W) - B_\mu \ \sin(\theta_W) \tag{2.6}$$

$$W_\mu^\pm = \ \tfrac{1}{\sqrt{2}} \ (W_\mu^1 \mp W_\mu^2 \ ) \tag{2.7}$$

where A_μ, Z_μ and $W_\mu^\pm$ correspond to the gauge bosons, photon, Z-boson and charged W-boson fields, respectively. θ_W is the Weinberg-angle, which describes the mixing between $SU(2)$ and $U(1)$. It is defined in terms of the weak and electromagnetic coupling constants, as:

$$\sin(\theta_W) = \tfrac{g'}{\sqrt{(g^2+g'2)}} \ or \ \tan(\theta_W) = \tfrac{g'}{g} \tag{2.8}$$

Furthermore, $\sin^2(_W)$ measured experimentally from the Z decay in different channels to be [37]:

$$\sin^2(_W) = 0.23122 \pm 0.00012 \tag{2.9}$$

The electroweak theory also describes the weak interactions between quarks from different generations through the exchange of a charged W-boson. The down-type (q') eigenstates are connected to their mass eigenstates by the unitary Cabibbo-Kobayashi-Maskawa (CKM) mixing matrix (V_{CKM}) [37, 49],

$$\begin{pmatrix} d' \\ s' \\ b' \end{pmatrix} = V_{CKM} \begin{pmatrix} d \\ s \\ b \end{pmatrix} \tag{2.10}$$

$$V_{CKM} = \begin{pmatrix} V_{ud} & V_{us} & V_{ub} \\ V_{cd} & V_{cs} & V_{cb} \\ V_{td} & V_{ts} & V_{tb} \end{pmatrix} = \begin{pmatrix} 0.97420 \pm 0.00021 & 0.2243 \pm 0.0005 & (3.94 \pm 0.36) \times 10^{-3} \\ 0.218 \pm 0.004 & 0.997 \pm 0.017 & (42.2 \pm 0.8) \times 10^{-3} \\ (8.1 \pm 0.5) \times 10^{-3} & (39.4 \pm 2.3) \times 10^{-3} & 1.019 \pm 0.025 \end{pmatrix} \tag{2.11}$$

where $|V_{ij}|$ is the probability of transition between q_i and q_j via the exchange of a charged W-boson. V_{CKM} is a diagonal matrix with $|V_{ij}| \approx 1$, which means the probability of transition between quarks of the same generation is dominating [50, 51].

2.1.2 The Higgs Mechanism

Experimentally the gauge bosons, $W^{\pm}$ and Z^0, are found to be massive particles with mass 80.379 ± 0.012 GeV and 91.1876 ± 0.0021 GeV [37], respectively. On the other hand, including the gauge boson mass terms in the electroweak theory violate the gauge invariance. In order to solve this problem, an extension has been added to the electroweak Lagrangian introducing a new field (ϕ):

$$\mathcal{L}_{Higgs} = (D_\mu \phi)^\dagger (D_\mu \phi) + \mu^2 \phi^\dagger \phi - \lambda (\phi^\dagger \phi)^2 \tag{2.12}$$

where the first term is the kinetic energy of the Higgs field, and the last two terms are the gauge field interaction and the Higgs potential, respectively. ϕ is a new scalar field,

referred to as the Higgs field, and it is given by a doublet of two complex scalar fields in $SU(2) \times U(1)$ representation:

$$\phi = \frac{1}{\sqrt{2}} \begin{pmatrix} \phi_1 + i\phi_2 \\ \phi_3 + i\phi_4 \end{pmatrix} \tag{2.13}$$

The shape for the potential term in the $\mathcal{L}_{Higgs}$ is shown in Figure 2.1. As one can see,

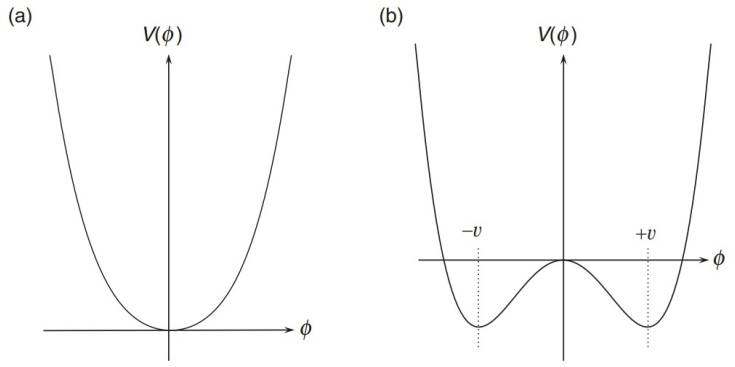

FIGURE 2.1: The shape of potential $V(\phi) = \frac{1}{2}\mu^2\phi^2 + \frac{1}{4}\lambda\phi^4$ for $\lambda > 0$ and for the cases (a) $\mu^2 > 0$ and (b) $\mu^2 < 0$ [10].

the expectation value for the vacuum (v) is given by:

$$v = \pm\sqrt{\frac{-\mu^2}{\lambda}} \tag{2.14}$$

If the free parameters λ and μ in the last two terms of $\mathcal{L}_{Higgs}$ are chosen to be $\lambda > 0$ and $\mu^2 < 0$, the vacuum state, which corresponds to the lowest energy state of Higgs field, does not occur at $\phi = 0$. Therefore, the expectation value for the vacuum will be non-zero; they will be at $\phi = +v$ and $\phi = -v$. The choice of the vacuum state will break the symmetry, and it is referred to as spontaneous symmetry breaking. As a result of the spontaneous symmetry breaking, the mass term problem is solved without violating the gauge invariance. The gauge bosons masses are then given in terms of the expectation value for the vacuum state as:

$$M_W = g\frac{v}{2}, \;\; M_Z = \frac{v}{2}\sqrt{g^2 + g'^2}, \;\; M_\gamma = 0 \tag{2.15}$$

From this mechanism, known as the Brout-Englert-Higgs mechanism [52–55], turns out the existence of a new scalar particle with spin = 0 and mass equal to $\sqrt{2\mu}$, which is known

as Higgs boson. In 2012, The ATLAS and CMS experiments at the LHC announced for the first time the discovery of this new particle [56–58]. The Higgs boson has a mass $m_H = 125.09 \pm 0.21(stat) \pm 0.11\ (sys)$ GeV, and it has no electric charge or colour charge [37].

The Higgs mechanism for the spontaneous symmetry breaking in the electroweak theory also can be used to generate the masses for the fermions by adding another term to the SM Lagrangian. It is describing the coupling between fermions and the Higgs field. The mass for fermions is given as:

$$\mathcal{L}_{yukawa} = y_f \phi \bar{\psi_L}^f \psi_R{}^f + h.c \tag{2.16}$$

$$m_f = \frac{v}{\sqrt{2}} y_f \tag{2.17}$$

where y_f is another coupling constant referred to as Yukawa coupling (proposed by Weinberg), and proportional to the fermion mass [42]. From this relation turns out that, massive particles are those which have the most significant coupling to the Higgs field. Therefore, the top quark, which is the most massive elementary particle with a mass $173. \pm 0.4$ GeV, has the largest coupling to the Higgs field with $y_f \approx 1$ [37].

2.1.3 Quantum Chromodynamics

The Quantum Chromodynamics referred to as QCD, is the theory which describes the strong interactions, and is based on the non-Abelian symmetry group, $SU(3)$. In strong interaction, a new quantum number is defined, carried by the quarks and by the $SU(3)$ force carriers, the gluons. This quantum number is the colour charge since for each quark can occur in one of three states red(r), green(g) and blue(b). Anti-quarks can have three different anti-colours. Colour has been proposed as a solution for the violation of Pauli's principle for quarks in a bound state, for example, baryon with the state uuu. The gauge bosons, which are eight gluons, carry $(r + b + g) \otimes (\bar{r} + \bar{b} + \bar{g}) - (r\bar{r} + b\bar{b} + g\bar{g})$ colour charges. Hence, they can have self-interactions. The only bound states invariant under the $SU(3)$ transformations and that can be observed experimentally are the colourless

bound states. These states are grouped into two configurations, baryons ($\bar{q}\bar{q}\bar{q}$ or qqq) and mesons ($q\bar{q}$), which are referred to as hadrons [10].

The QCD Lagrangian, which describes the strong interactions, is:

$$\mathcal{L}_{QCD} = \sum_q i\bar{q}\gamma^\mu D_\mu \; q - \tfrac{1}{4} G^a_{\mu\nu} G^{\mu\nu}_a \tag{2.18}$$

where $q(\bar{q})$ is the quark (anti-quark) field, respectively, while $G^\mu_a\nu$ is the gluon fields. The covariant derivative for the $SU(3)$ symmetry group is given by:

$$D_\mu = \partial_\mu + i g_s T_a G^a_\mu \tag{2.19}$$

where T_a, the generators, are three-dimensional matrices with $a = 1, , 8$ which can be expressed in terms of the Gell-Mann matrices. The g_s is a coupling constant, related to the coupling strength α_s by:

$$\alpha_s = \frac{g_s^2}{4\pi} \tag{2.20}$$

Indeed, the coupling constant, α_s, is not a real constant, but it depends on the energy scale:

$$\alpha_s(Q^2) = \frac{12\pi}{(33-2n_f)\log(\frac{Q^2}{\Lambda_{QCD}^2})} \tag{2.21}$$

The parameter n_f is the number of quark flavours, ($n_f = 6$), while Q^2 is the momentum transfer and Λ_{QCD} is a scale defined to be ≈ 200 MeV. $\alpha_s(Q^2)$ decreases at high energies (small distances), which means the quarks can be considered as free particles and referred to as asymptomatic freedom. On the other hand, quarks and gluons (Partons), cannot appear as free particles at large distances (small Q^2). When trying to separate quarks, as shown in Figure 2.2, a pair of quarks with the opposite colour charge will be created from the vacuum, and new bound states will appear. This phenomenon is one of the main features of QCD, and it is called colour confinement [59–61].

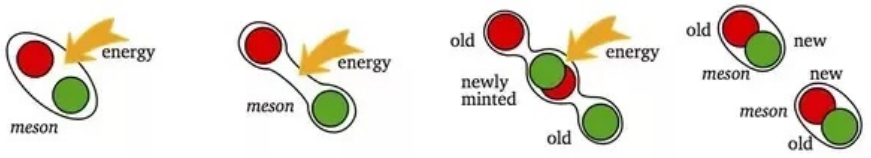

FIGURE 2.2: Schematic plot of the confinement principle, which a new bound state is created in the attempt to separate two quarks.

2.2 Top Quark Physics

In 1995, the last fermion predicted by the SM, the top quark, was discovered at the Tevatron collider by the CDF and DØ experiments [1, 2]. It is the most massive elementary particle in the SM with a mass close to the scale of electroweak symmetry breaking, $m_{Top} = 173.0 \pm 0.4$ GeV [37]. Besides, it is predicted to have the largest coupling constant to the Higgs field, $y_{Top} \approx 1$. Furthermore, from the SM prediction, the top quark has a very short lifetime $\tau_{Top} \approx 5 \times 10^{-25}$ sec, which means it has a lifetime shorter than the hadronisation scale. As a consequence, the spin information of the top quark is passing to its decay products, and it provides a unique opportunity to study the bare quark.

The top quark plays an essential role in the SM and many BSM models, and it is predicted to have a large coupling besides the SM Higgs boson to many new particles. Therefore, studying and measuring the top-quark properties with high precision is crucial for several BSM analyses, which predict the production of new massive particles in association with the top quark. In the LHC, top quarks are produced in pairs via strong interaction or single top via weak interaction in association with a b-quark, light-quarks or a W-boson (see Ref[62–66]). In this thesis, the study of SM four-top-quark production, as well as the search for top-pair resonances, are presented. In the following, the top quark productions and decays are discussed.

2.2.1 Top quark strong production

Top quarks at the hadron colliders, p-p or p-$\bar{p}$ collisions are mainly produced in pairs via the strong interaction. At the leading-order (LO) in perturbation theory, top pairs are produced either by gluon-gluon (gg) fusion or quark-antiquark annihilation ($q\bar{q}$), as

shown in Figure 2.3. There are also, higher-order diagrams for $t\bar{t}$ production such as the next-leading-order (NLO) ones where $t\bar{t}$ pairs are produced from quark-gluon (qg) scattering, as shown in Figure 2.4a, and from gluon bremsstrahlung or virtual corrections to the LO (see Figure 2.4).

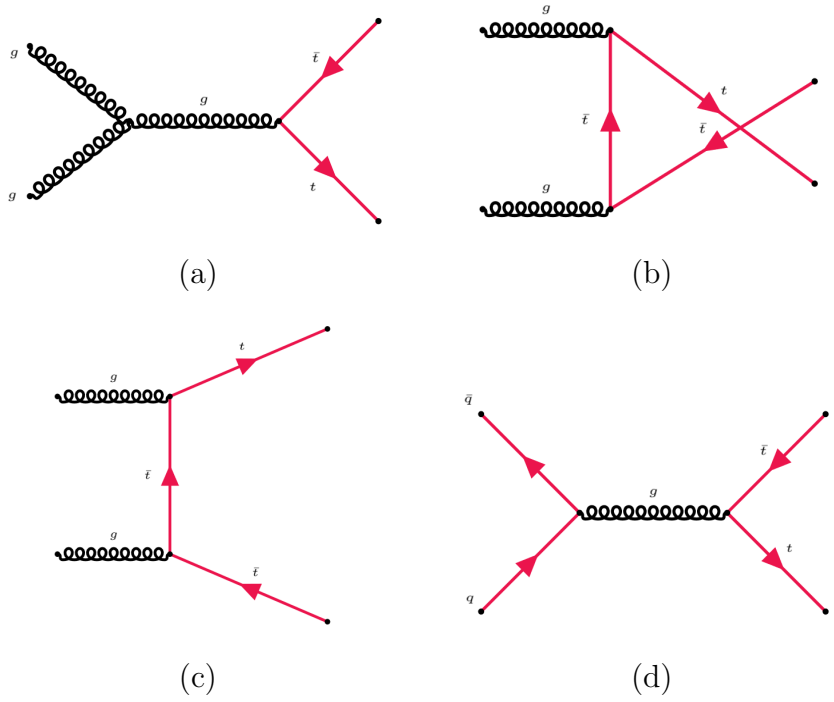

FIGURE 2.3: Feynman diagrams for $t\bar{t}$ production via (a-c) gg fusion and (d) $q\bar{q}$ annihilation.

The centre-of-mass energy of the colliding partons, $\sqrt{\hat{s}}$, needs to be larger than twice of the top-quark mass (m_{top}) for $t\bar{t}$ production since $\sqrt{\hat{s}}$ is given as:

$$\sqrt{\hat{s}} = \sqrt{x_i x_j s} \geq 2m_{Top} \tag{2.22}$$

where x_i (x_j) is momentum fractions of the partons participating in the p-p collision (LHC) or proton-antiproton collision (Tevatron). In the case of two partons carrying the same fraction $x_i = x_j = x$, $\sqrt{\hat{s}}$ becomes

$$x \geq \frac{2m_{Top}}{\sqrt{s}} \tag{2.23}$$

At the LHC, the centre-of-mass energy $\sqrt{s}$ is equal to 13 TeV, which gives $x \approx 0.03$. At this x, one finds mostly gluons, and this is why the main $t\bar{t}$ production is gg fusion. On the other hand, at the Tevatron where $\sqrt{s} \approx 2$ TeV, the parton momentum fraction

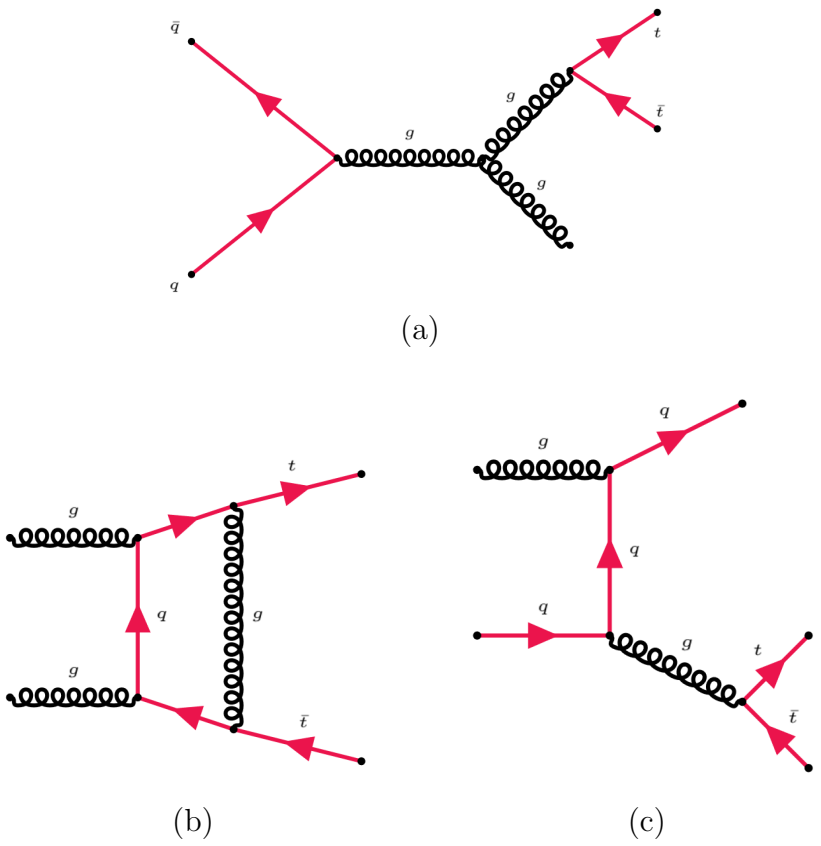

FIGURE 2.4: Feynman diagrams for $t\bar{t}$ production via (a) g bremsstrahlung, (b) the gg fusion with virtual correction, and (c) the qg scattering.

needed is $x \approx 0.18$. In this region, the dominant mechanism for $t\bar{t}$ production is the $q\bar{q}$ annihilation [67].

The contribution of the various processes to $t\bar{t}$ production depends on the centre-of-mass energy $\sqrt{s}$ and whether the collisions occur between partons in p-p (LHC) or p-$\bar{p}$ (Tevatron). At the Tevatron collider, where p-$\bar{p}$ are colliding particles at $\sqrt{s} = 1.93$ TeV, the dominant process for $t\bar{t}$ production was $q\bar{q}$ annihilation. On the other hand, at the LHC where p-p collisions occur at $\sqrt{s} = 13$ TeV, gg fusion is the dominant process, $\approx 95\%$. This difference is because at Tevatron, the anti-quark is a valance quark, and it is more likely to occur at any $\sqrt{s}$. In contrast, at the LHC, the anti-quark has to be a sea quark. On top of that, at Tevatron, partons carry a high fraction of the proton (anti-proton) momentum ($p_i = x_i p_{proton}$) while at the LHC small fractions x_i are enough to produce top quarks pairs.

The probability for any physics process to occur at particle collisions is referred to as the cross-section, σ, measured in barns which is an area unit equal to 10^{-24} cm^2,

$$\sigma = \frac{N}{\mathcal{L}} \tag{2.24}$$

where N is the number of events, and $\mathcal{L}$ is the total integrated luminosity. The cross-section for any process depends on the centre-of-mass energy for the colliding particles. For example, the cross-section for $t\bar{t}$ production, $\sigma_{t\bar{t}}$, at $\sqrt{s} = 13$ TeV in the LHC is $\sigma_{t\bar{t}} = 830^{+13}_{-14}$ pb where the calculation has been done for a top quark of mass equal to 173.3 GeV [68–70]. Figure 2.5 shows the measurement of top-quark mass from different experiments and the world combination results. On the other hand, Figure 2.6 shows the $t\bar{t}$ production cross-section as a function of $\sqrt{s}$ from different experiments compared to theoretical prediction [11, 71, 72].

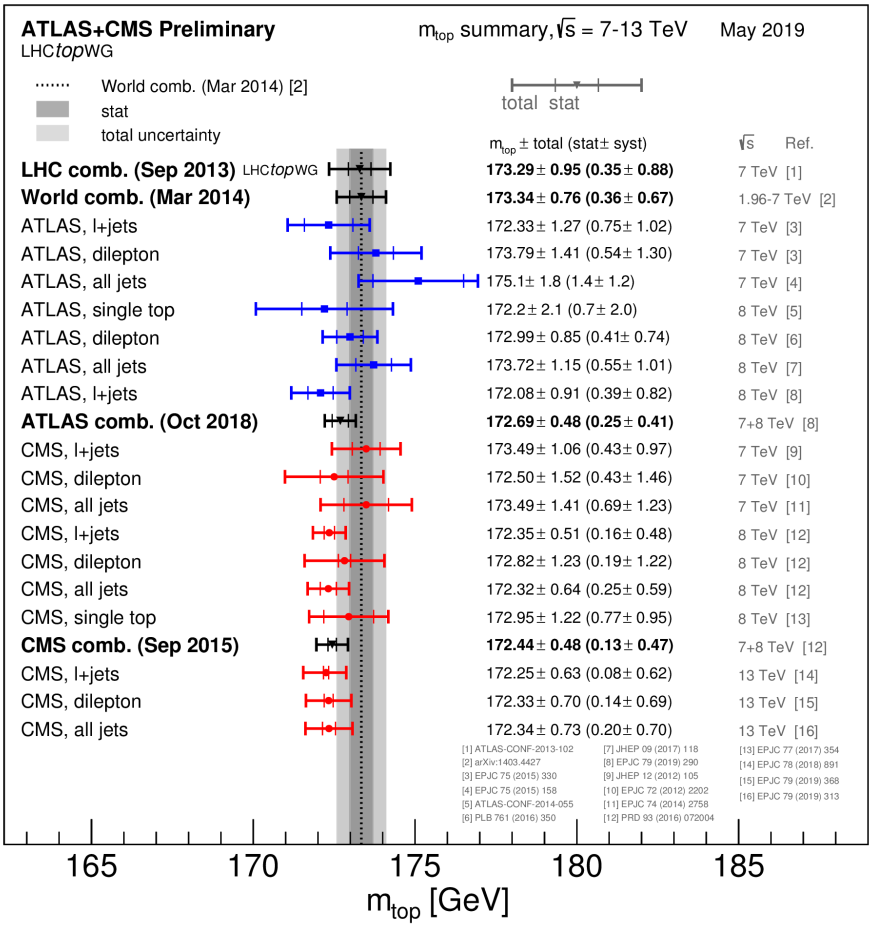

FIGURE 2.5: Summary of direct measurement for the top-quark mass (m_{top}) from the ATLAS and CMS in the LHC compared with world combinations [11].

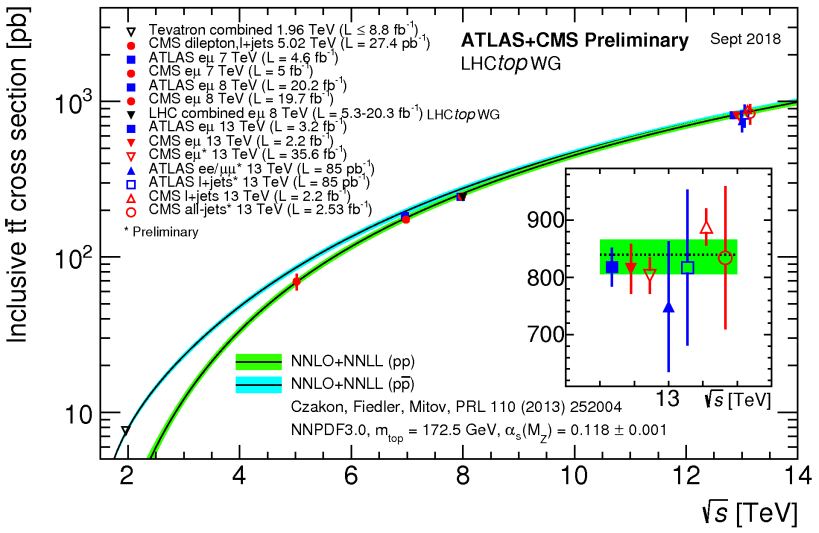

FIGURE 2.6: Summary of measurements for $t\bar{t}$ production cross-section as a function of $\sqrt{s}$ at the LHC and Tevatron compared with the theoretical calculation at NNLO+NNLL [11].

For the analyses presented in this thesis, top pairs play a primary role as background for the four-top-quark signal reconstruction (Chapter 6) as well as in the search for new massive particles (Chapter 7) predicted by BSMs. Therefore, it is crucial to study the pair of top-antitop quarks kinematics to discriminate them from other processes, e.g. four-top-quark reconstruction and new massive particles decaying to $t\bar{t}$ pairs.

2.2.2 Top quark decay

Within the SM, the top quark decays with probability close to one through electroweak force in the channels, $t \to Wb$, $t \to Ws$ and $t \to Wc$. The branching ratio (BR) for the various top quark decay is proportional to the $|V_{tj}|$ elements squared in the CKM matrix, with $j = b, s$ and c. $|V_{tb}|$ is larger than $|V_{ts}|$ and $|V_{tc}|$, therefore, the top quark almost 100% of the time decays to a W-boson and a b-quark. The W-boson is an unstable particle and can decay in two channels, the leptonic and the hadronic one. In the leptonic channel, the W-boson decay with equal probability to a charged lepton and the corresponding neutrino ($e\bar{\nu}_e$, $\mu\bar{\nu}_\mu$ or $\tau\bar{\nu}_\tau$), and the total branching ratio in the leptonic channel is BR $\approx 1/3$. On the other hand, in the hadronic channel, the W-bosons can decay to two $q\bar{q}$ pairs ($u\bar{d}$ or $c\bar{s}$) with a total BR $\approx 2/3$. Therefore, the decay of the two W-bosons from $t\bar{t}$ pairs characterises the $t\bar{t}$ decay channels, as shown in Figure 2.7.

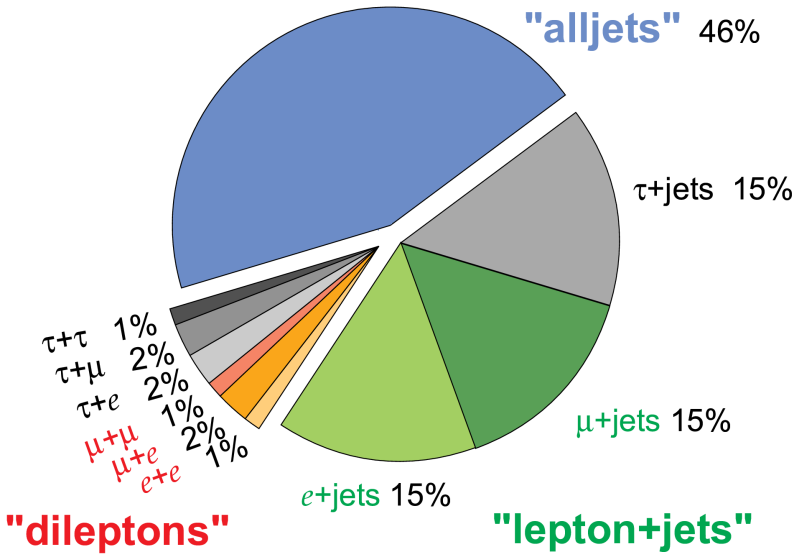

FIGURE 2.7: BRs for the different $t\bar{t}$ decay channels.

From Figure 2.7, one can see that the $t\bar{t}$ final states can be classified into three categories:

- **All jets (Hadronic channel)**: It is the most probable channel with BR $\approx 46\%$, and its reconstruction is very challenging due to the high contribution from the QCD multijet background. The $t\bar{t}$ final states in this channel consist of four light quarks and two b-quarks.

- **Dilepton channel**: The final states in this channel consist of two b quarks and two pairs of lepton-neutrino. The expected BR for this channel is $\approx 9\%$ and the background compared to other channels is the lowest. Despite that, it is quite challenging to reconstruct the full $t\bar{t}$ pair event due to the presence of two neutrinos, which cannot be identified.

- **Single-lepton channel**:The branching ratio for this channel where one of the W-boson decays leptonically while the other one decays hadronically is BR $\approx 45\%$. The $t\bar{t}$ final states consist of one pair of lepton-neutrino, two light-quarks and two b-quarks. Contributions from other physics processes give a background which is high compared to the dilepton channel case.

2.3 Beyond The Standard Model

As explained in Section 2.1, despite all the success of the SM, it is not considered as a complete theory of particle physics. It does not include gravity and does not explain why the Higgs boson has its particular mass. For these and other reasons, experimental searches for new phenomena predicted by theories which try to go beyond the Standard Model can help to establish new theoretical frameworks in particle physics able to cover the SM weaknesses.

Several massive particles are predicted to decay to pairs of top-antitop quarks by BSM theories, such as the Topcolor [4, 5, 73], supersymmetric extensions to the SM (SSM, MSSM, etc.) [74–76] and Randall-Sundrum Models [8, 9]. Two of these models will be briefly outlined in the following subsections (2.3.1 and 2.3.2).

The invariant mass of the reconstructed $t\bar{t}$ is given by

$$M_{t\bar{t}} = \sqrt{(P^{\bar{t}} + P^{t})_{\mu}(P^{\bar{t}} + P^{t})^{\mu}} \tag{2.25}$$

where $P^{t}(P^{\bar{t}})$ is the four-momentum of the (anti)top-quark with $\mu = 0, .., 3$. (The expected $M_{t\bar{t}}$ distribution is exponentially decreasing under the SM prediction, whereas in other models a resonance bump at a given mass can appear on top of the SM prediction.)

2.3.1 Sequential Standard and Topcolor Models

Many BSM models predict the existence of new neutral or charged gauge bosons which can be produced at the LHC. These gauge bosons are massive, spin-1 particles and predicted to have the same coupling strength to the SM fermions as the SM gauge boson. These new extra bosons, if not too heavy, should be identified at the LHC. In particular, the Z' and W', which are predicted within the Sequential Standard Model (SSM) [77] and have the same properties as the ordinary SM gauge bosons (W-boson and Z-boson). Besides, the Z' that predicted by the Topcolour Assisted Technicolor model (TC2) [4, 5, 73], which is introduced to explain the large top-quark mass and to provide a mechanism for the

electroweak symmetry breaking. Furthermore, these models are needed and presented in several analyses, see Ref[74, 75, 78, 79].

In the analysis presented in Chapter 7, the possible production of a new massive neutral Z' boson (with width set to 1.2%), which couples significantly to quarks and leptons and can be easily observed in the Drell-Yan processes, is studied. The Z' bosons expected to have a mass at the TeV scale can decay to a pair of top-antitop quark, as shown in Figure 2.8, and resonances can be observed as bumps on the top of $M_{t\bar{t}}$ spectrum. The cross-section for the produced Z' boson is predicted to decrease as the Z' mass increases [4, 73].

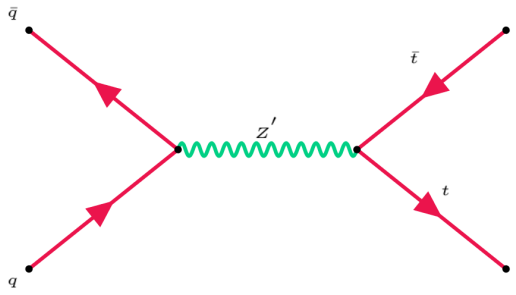

FIGURE 2.8: Feynman diagram for the production of Z' bosons decaying to $t\bar{t}$ pair.

2.3.2 Randall-Sundrum Model

Some theoretical models propose extra dimensions to solve the so-called hierarchy problem, which is related to the high discrepancy between the strength of the electroweak force and gravity. One of these models is the Randall-Sundrum model, which is proposed a so-called warped-geometry, wherein an extra dimension is added to the usual four-dimensional space-time, and it becomes 5-dimensional warped geometry (see Ref[8, 9]). The practical consequences of this model are that the SM fields, which are correspondent to the SM particles, can freely propagate in the warped spatial dimension and result in massively excited states referred to as Kaluza-Klein (KK) excitations. Also, there are spin-2 excitations produced with the mass of weak scale order (GeV and TeV), and they are correspondent to KK excitations of the graviton.

In this thesis, the Kaluza-Klein excitations studied are those of the gluon (KK_g) and graviton, referred to as G for simplicity. The primary production modes of the KK_g and

G are the $q\bar{q}$ annihilation and gluon-gluon fusion, respectively, as shown in Figure 2.9. These excitations are with widths set to 30% of the KK_g mass and from 3% to 6% of the G mass in the range 0.4 to 3 TeV, respectively [41].

In the Randall-Sundrum model, both KK_g and G (in some references G is corresponding to G_{RS}), respectively, are expected to acquire enough mass such as to decay to $t\bar{t}$. Broad resonances are expected and predicted to have a bump on top of the $M_{t\bar{t}}$ spectrum at different masses [6, 80]. The cross-section for the produced excitations is predicted to decrease as the mass increases. For example, the predicted cross-section for $m_{KKg} = 1$ TeV is $\sigma_{KKg,1TeV} = 20.176$ pb while for $m_{KKg} = 3$ TeV is $\sigma_{KKg,3TeV} = 0.156$ pb [40**?** , 41].

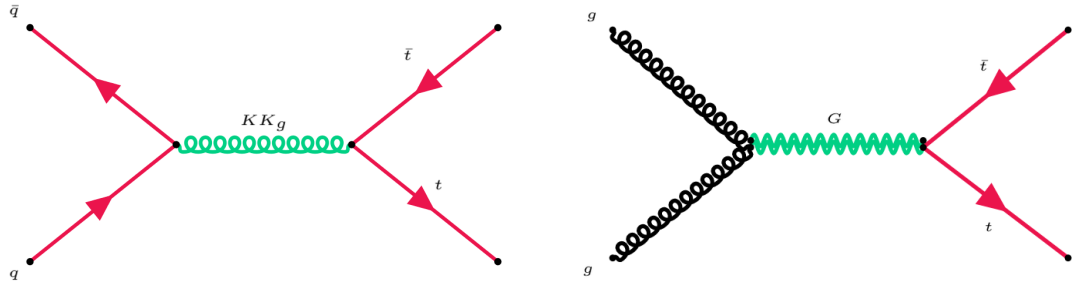

(a) (b)

FIGURE 2.9: Feynman diagram for the production of spin-1 KK_g and spin-2 G excitations decaying to $t\bar{t}$ pair.

Chapter 3

The Experiment

Several theoretical models beyond the Standard Model (BSM), predict new physics processes as well as rare processes which are predicted by the SM. These processes can be identified and studied only by producing and collecting enough events. This can be done at a hadron collider machine, which has to provide enough energy in the centre of mass of the collisions as well as a considerable number of collisions. The LHC is a proton-proton collider, which has been built to address the answers for several questions in the field of particle physics. Starting in 2010, the LHC has provided centre-of-mass energies up to 13 TeV and instantaneous luminosities up to few 10^{34} cm^2 s^{-1}. The analyses presented in this thesis used a data set collected by the ATLAS experiment from 2015 to 2018 at the LHC working with centre-of-mass of energy $\sqrt{s} = 13$ TeV and corresponding to an integrated luminosity 140 fb^{-1}.

In this Chapter, the LHC is presented in Section 3.1, while a brief description of the ATLAS detector that was used to record the p-p collision data and of its sub-detectors in Section 3.2. The last section (Section 3.2.6) is about the trigger systems used in the ATLAS experiment.

3.1 CERN and The Large Hadron Collider

The LHC [81] is the largest, and most powerful proton-proton accelerator in the world hosted in the CERN laboratory near the Swiss-France border. The collider tunnel has a circumstance of 27 Km and is 100 m underground. The tunnel was previously hosting a collider machine used to accelerate electrons-positrons (e^+-e^-) (from 1989 to 2000), and known as the Large Electron-Positron collider (LEP). The LHC consists of two circular rings designed to accelerate protons (*p*-*p*) and heavy ions (*Pb*-*Pb*) in opposite directions at a centre-of-mass energy up to 14 TeV (2.5 TeV) for protons (heavy ions) and with an instantaneous luminosity up to few of 10^{34} cm^2 s^{-1}. The proton beams (heavy ion beams) are made to collide at four interaction points along the ring. In correspondence to these points, there are four experiments: A Toroidal LHC **A**pparatu**S** (ATLAS) [14], **C**ompact **M**uon **S**olenoid (CMS) [82], **L**arge **H**adron **C**ollider **b**eauty (LHCb) [83], and **A** **L**arge **I**on **C**ollider **E**xperiment (ALICE) [84], as shown in Figure 3.1.

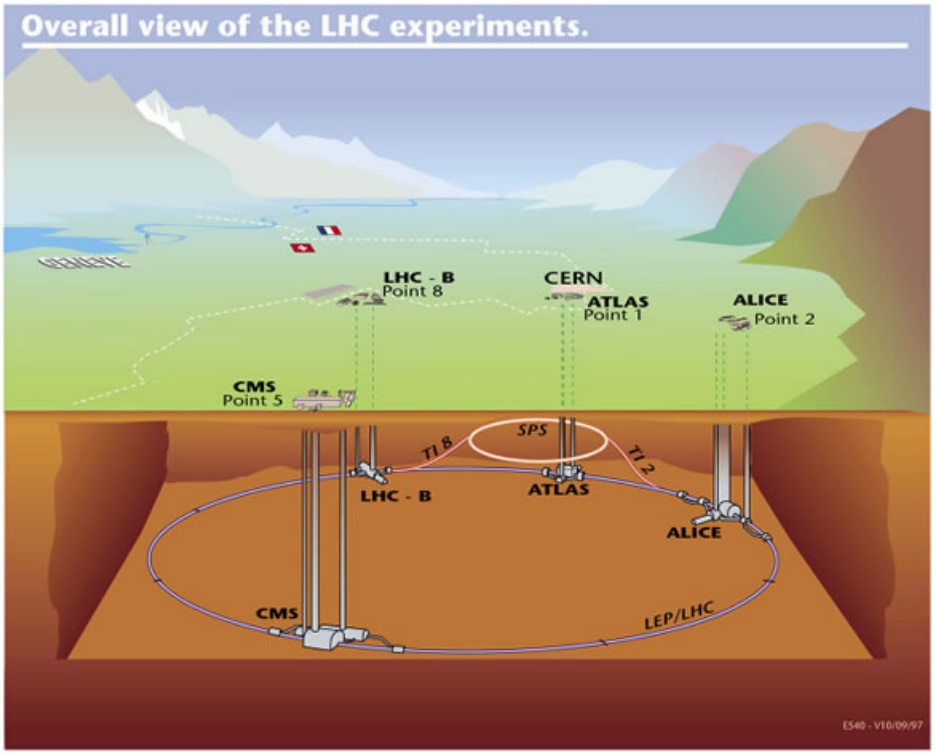

FIGURE 3.1: The LHC tunnel with the four experiments, ATLAS, CMS, LHCb, and ALICE.

ATLAS and CMS are general-purpose detectors capable of providing high precision measurements of a wide range of particle properties and physics processes within the SM predictions as well as BSM. The LHCb experiment focuses on b-physics and Charge-Parity (CP) violation studies, while the ALICE experiment is studying the quark-gluon plasma state with heavy-ion collisions at high energy. Additionally, there are other three small experiments installed at the LHC for specific purposes. The first one is the **Mo**nopole and **E**xotics **D**etector **a**t the **L**HC (MoEDAL) [85]; used for the search of magnetic monopoles and exotic Stable Massive Particles (SMPs).

The second is **L**arge **H**adron **C**ollider **f**orward (LHCf) [86], which uses particles thrown forward by the LHC collisions to simulate the cosmic rays. Finally, The **Tot**al, **E**lastic, and diffractive cross-section **M**easurement (TOTEM) [87]; studies the protons which emerge from collisions at small angles and explores the elastic and diffractive cross-section from proton-proton collisions in the forward region.

Before being accelerated in the LHC ring, protons and heavy ions pass through a chain of smaller accelerators (see Figure 3.2), which were already built for previous experiments before LHC. Protons are extracted using an electric field, ionising hydrogen gas. Protons are then accelerated to 50 MeV in the only linear collider (LINAC2) in the chain. As a next step, the Proton Synchrotron BOOSTER is used to accelerate the protons to 1.4 GeV. Then, protons are accelerated in the Proton Synchrotron (PS) to an energy of 25 GeV. After that, they are transferred to the last accelerator in the chain, the Super Proton Synchrotron (SPS) before being injected into the LHC, where they reach the energy of 450 GeV. Finally, the protons are injected into the two LHC pipelines to reach the centre-of-mass energy of 13 TeV (6.5 TeV/beam) and to collide at different interaction points [12, 81].

3.1.1 Run 2

The data used for the analyses presented in this thesis have been collected during the LHC data taken at $\sqrt{s} = 13$ TeV, the so-called Run 2. In the period between 2015-2018, the LHC delivered proton-proton collisions to the ATLAS detector equivalent to an integrated luminosity of 156 fb^{-1}, as shown in Figure 3.3. ATLAS recorded good quality

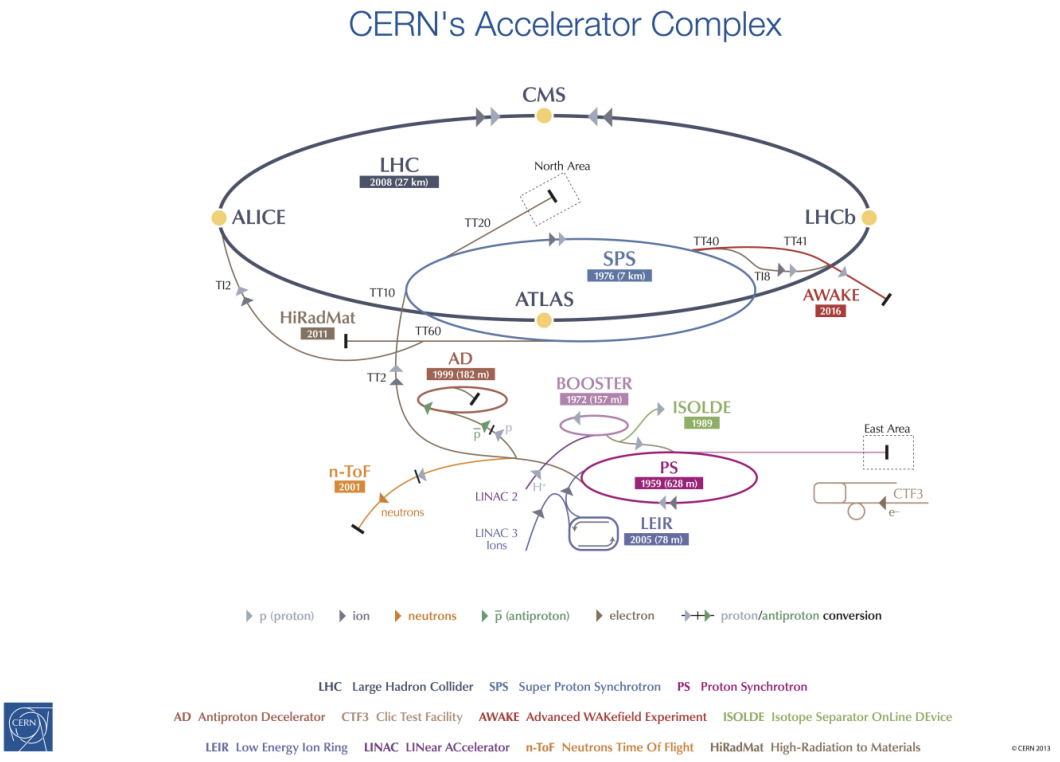

FIGURE 3.2: The LHC accelerators chain with the four main experiments [12].

data in the years between 2016-2018 for a total of 140 fb^{-1}. In the year 2015, due to the several challenges needed to upgrade the LHC after the shutdown, the recorded good quality data has been equal to 3.2 fb^{-1}) [13].

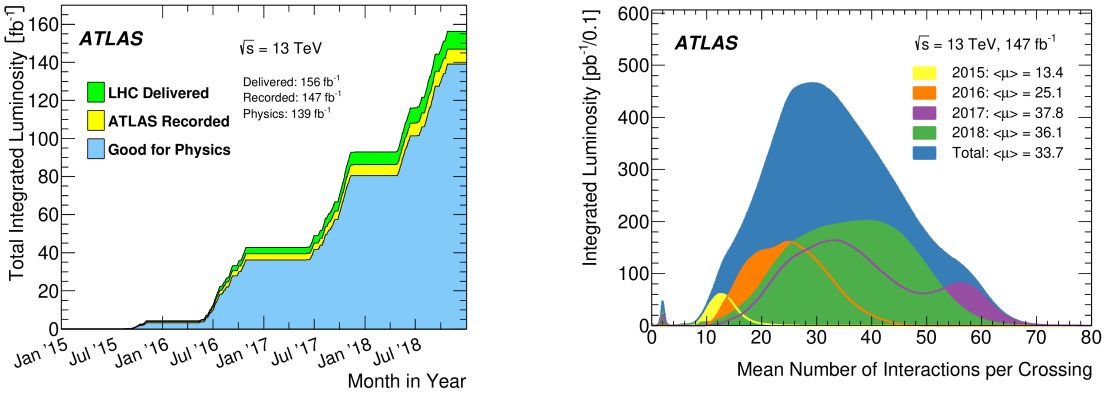

FIGURE 3.3: Total integrated luminosity collected (left) and the mean number of interaction for each year in the period 2015-2018 [13].

In table 3.1, some parameters related to Run2 are shown. One can observe how the LHC performance has been improving in several aspects, for example, the instantaneous

luminosity (introduced in Section 3.1.2) has doubled. Besides, the number of protons per bunch and the number of bunches per beam increased [38, 39].

Parameter	Design	2015	2016	2017	2018
Energy	7.0	6.5	6.5	6.5	6.5
Energy per beam [MJ]	362	280	280	315	312
Number of bunches	2808	2244	2220	1868-2556	2556
Proton per bunch [$10^1$1]	1.15	1.2	1.25	1.25	1.11
Bunches per train	288	144	96	144-128	144
$\beta*$[cm]	55	80	40	30-40	25-30
Emittance[μm]	3.75	2.6-3.5	1.8-2	1.8-2.2	1.8-2.2
Half Crossing Angle[μrad]	142.5	185	140-185	120-150	130-150
Peak luminosity[$10^{-34}cm^2sec^{-1}$]	1.0	<0.6	1.5	2	2.1

TABLE 3.1: LHC parameters during Run 2 [38, 39].

3.1.2 Luminosity measurements

The instantaneous luminosity ($\mathcal{L}$) is a parameter, which is defined as the number of particles passing through the transverse unit area at the interaction point per unit time. $\mathcal{L}$ depends only on the beam parameters, as shown in table 3.1, and for a collider, it is defined as:

$$\mathcal{L} = (N_{proton} n_{bunch} f_{rev}) S_T^{-1} \gamma F \tag{3.1}$$

where, N_{proton} is the number of protons ber bunch, and n_{bunch} is the number of bunches per beam with crossing frequency f_{rev}. The γ factor is the relativistic factor, and F is the geometric luminosity reduction factor. The factor S_T is the transverse area (XY-plane) of the beam at the interaction point and is equal to $4\pi\sigma_x\sigma_y$ [81].

3.2 The ATLAS Detector

ATLAS [14] is one of the general-purpose detectors at the LHC, designed to cover a wide range of physics processes and to investigate several theoretical models Beyond the Standard Model (BSM) as well as the physics processes predicted by the SM. It is 44 m

long, has a 25 m diameter and a mass of 7000 tons. It consists of multiple subdetectors layers surrounding the interaction point, Figure 3.4.

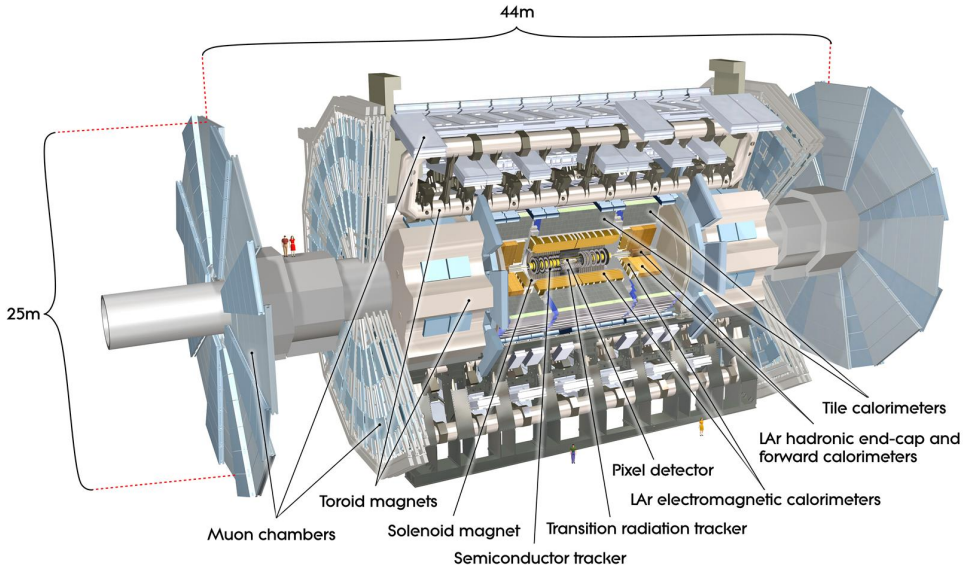

FIGURE 3.4: Graphical scheme of the ATLAS detector, with its various subdetectors indicated [14].

Each layer has the task to identify individual particles when they interact with the sub-detector materials, Figure 3.5. These layers have a cylindrical shape, with the axis along the beamline, and are arranged in a concentric configuration. They can intercept almost all the particles produced in the collisions. For those emitted in the forward region, two endcap detectors, perpendicular to the beam pipe are used. The closest detector to the beamline is the Inner Detector, which is made up of three sub-detectors and a solenoidal magnet surrounds them. The calorimeters are next and consist of an Electromagnetic, and a Hadronic one (ECAL and HCAL). Finally, one can find the muon spectrometer, located at the outermost position of the ATLAS detector, embedded in a toroidal magnet. In the following, the ATLAS sub-detectors will be described in more details, illustrating the role of each subdetector.

3.2.1 The ATLAS coordinate system

The ATLAS detector coordinate system is based on a right-handed Cartesian system with axes (X, Y, Z), as shown in Figure 3.6. The origin is located at the proton interaction

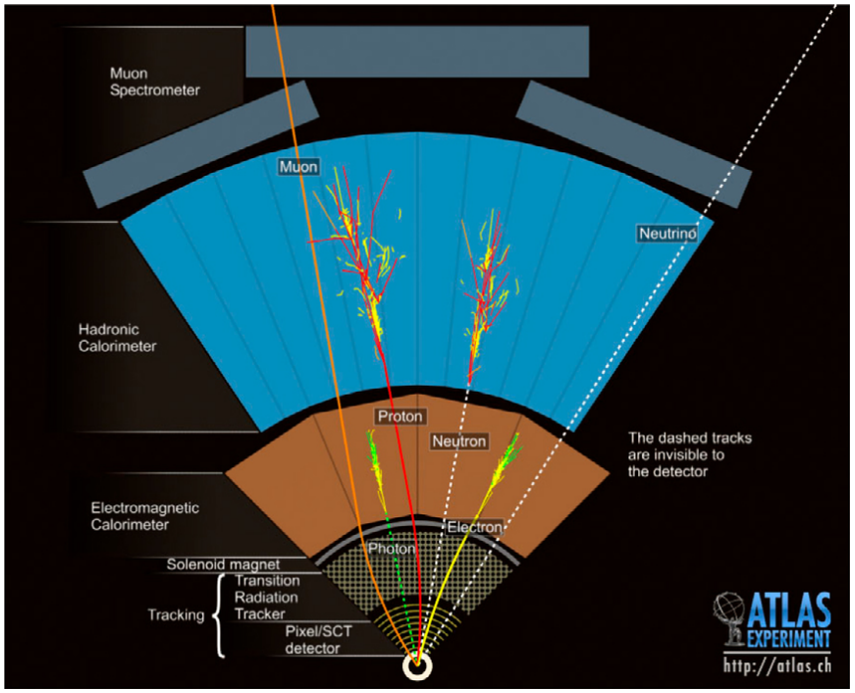

FIGURE 3.5: Schematic view of a transverse slice of the ATLAS experiment showing how different particles interact with the layers of the detector [14].

point. The positive X and the Y axes are perpendicular to the beam-pipe. The X-axis points to the LHC centre, while the Y-axis increases in the direction of the ATLAS height. The Z-axis is along the beamline direction with a small angle of deviation from the beamline.

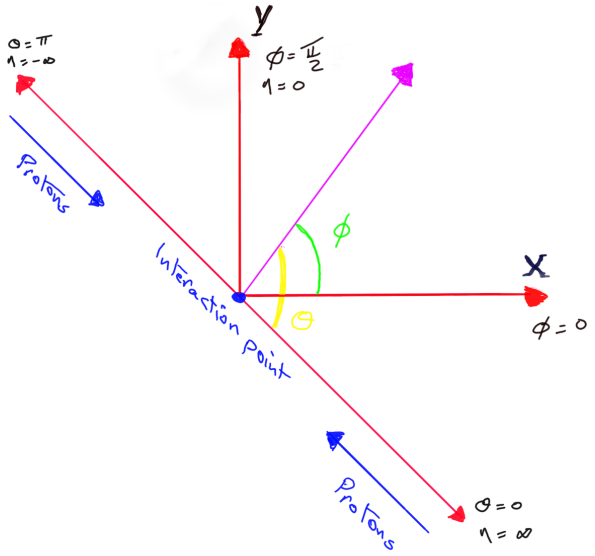

FIGURE 3.6: The ATLAS coordinate system.

It is useful to define the position of a particle in the Cartesian system using: the rapidity (ξ) and the azimuth angle (ϕ). The rapidity is defined as:

$$\xi = \frac{1}{2}\ln(\frac{E+p_z}{E-p_z}) = \frac{1}{2}\ln(\frac{1+\beta\cos(\theta)}{1-\beta\cos(\theta)}) \tag{3.2}$$

where E is the particle energy, and p_z its longitudinal momentum component, θ being the polar angle between the particle and the Z-axis. At high energy ($m \ll E \approx p$), the rapidity becomes equal to the so-called pseudorapidity (η), defined as:

$$\eta = -\ln(\tan\frac{\theta}{2}) \tag{3.3}$$

The angular distance between two particles produced in the ATLAS detector is given by ΔR:

$$\Delta R = \sqrt{(\Delta\eta)^2 + (\Delta\phi)^2} \tag{3.4}$$

with $\Delta\eta = \eta_2 - \eta_1$ and $\Delta\phi = \phi_2 - \phi_1$ where η and ϕ are the particle position coordinates.

The longitudinal momentum component of colliding quarks is unknown after the collision, but it is known that total transverse momentum is equal to zero before the collision. Therefore, the total transverse momentum has to be conserved in the final state, and it is defined as:

$$p_T = psin(\theta) = \sqrt{(p_x)^2 + (p_y)^2}, \quad p_z = cos(\theta) \tag{3.5}$$

and their transverse energy as:

$$E_T = Esin(\theta) \tag{3.6}$$

The ATLAS detector is not able to detect and measure neutrino particles. However, an unbalance between the initial and final transverse momentum can be an indirect indication of the presence of an escaped neutrino. Its energy is referred to as the missing energy in the transverse plane, E_T^{miss}.

3.2.2 The magnetic systems

The charged-particle momentum is determined from the curvature of the particle trajectory since their trajectories are bent when they move in a magnetic field. In the ATLAS

detector, there are two magnetic systems: the first one provides a solenoid field in the Inner Detector (barrel and endcap). This magnet is inserted in the central region, between the inner tracker and the ECAL, in the region covering the space: $1.22 < r < 1.32$ meter with a distance 5.8 m along the z-direction. The average magnetic field provided by the solenoid is 2 T. The second one provides a Toroidal field in the muon system, which is the outermost detector, as shown in Figure 3.7. The toroidal magnet consists of eight coils in both the barrel and endcap regions and provides an average magnetic field of 0.5 T in the barrel region and 1 T in the endcap regions [14].

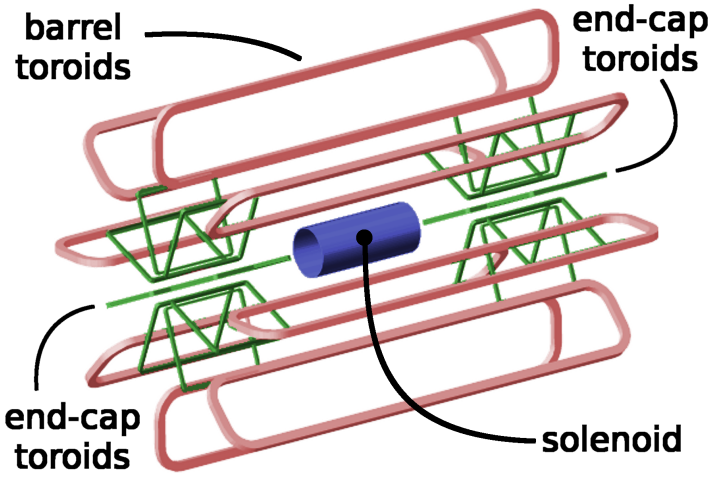

FIGURE 3.7: Schematic view of Barrel and End-cap toroids [14].

3.2.3 Inner Detector

The Inner tracking Detector (ID) [14] is the innermost detector, closest to the interaction point. The primary purposes of the ID are the track reconstruction of the charged particle, as well as the determination of the transverse momentum of the particles, using the relation:

$$p_T = 0.3B.R, \quad R = \frac{L^2}{8s} \tag{3.7}$$

where p_T is the particle transverse momentum in GeV/c, B is the magnetic field strength in Tesla (T), and R is the radius of the particle trajectory in meter, Figure 3.8.

The ID is a cylinder of 6.2 m long, and a radius of 1.15 m. It covers the tracks in the region $|\eta| < 2.5$. Three subsystems compose it: The Pixel detector, the Semiconductor Tracker (SCT), and the Transition Radiation Tracker (TRT), as shown in Figure 3.9.

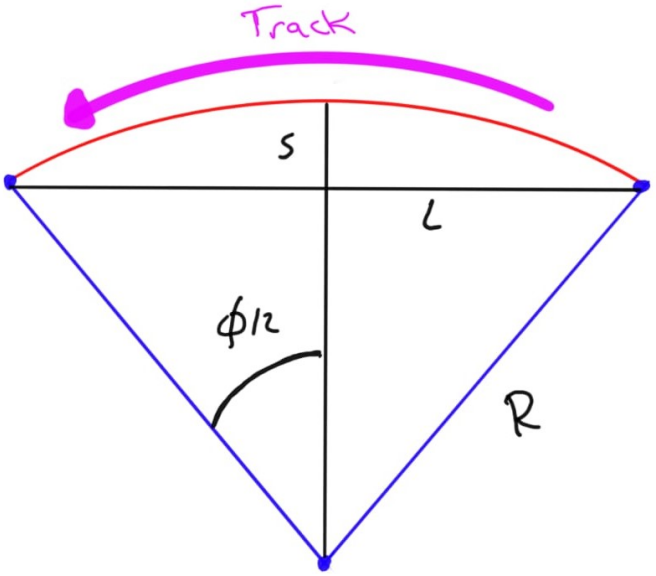

FIGURE 3.8: The track particle parameters.

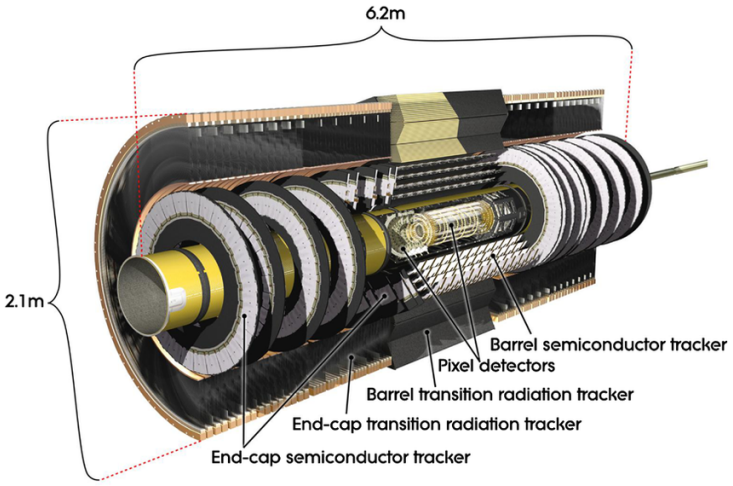

FIGURE 3.9: Sketch of the ATLAS Inner Detector and its components [15].

Also, the ID helps to distinguish electrons from pions and to determine the position of the primary vertex (where the quarks collision took place) as well as the secondary vertices, for particles travelling to longer distances before decaying or fragmenting.

3.2.3.1 The Pixel Detector

The Pixel Detector is the closest sub-detector to the interaction point in the ATLAS experiment. It is installed directly around the beamline to measure with high resolution the charged-particle impact parameters and to reconstruct the primary and secondary

vertices. A schematic view of the Pixel Detector with its components is shown in Figure 3.10.

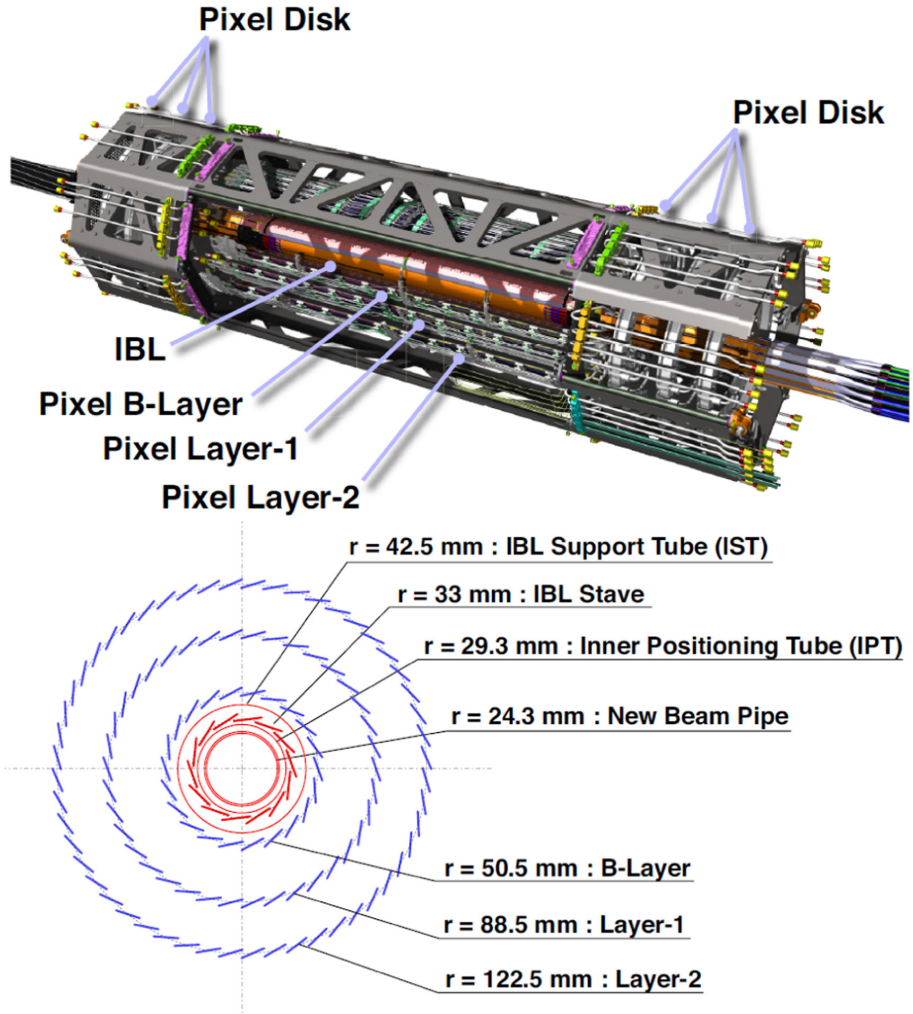

FIGURE 3.10: Schematic view of the Pixel Detector (top) and a transverse slice (bottom) [16].

The Pixel Detector is made up of four cylindrical layers in the barrel and six disks in the End-cap region. The building unit in the B-layer, Layer-1, and Layer-2 (known as the Original Pixel Detector OPD), is a rectangular module with dimensions $50 \times 400\ \mu m^2$ in the $R - \phi$ plane. In these layers, there are 1744-pixel modules with 80.4 million readout channels. Each module is made up of 16 sensors with an electronic readout channel, and each sensor consists of 47232 pixels. The OPD layers are located at 50.5 mm, 88.5 mm, and 122.5 mm, respectively, from the beamline, as shown in Figure 3.11.

To restore the original Pixel Detector performances after years of data taken, and radiation damage which affects mostly the innermost pixel layers, a new layer has been added

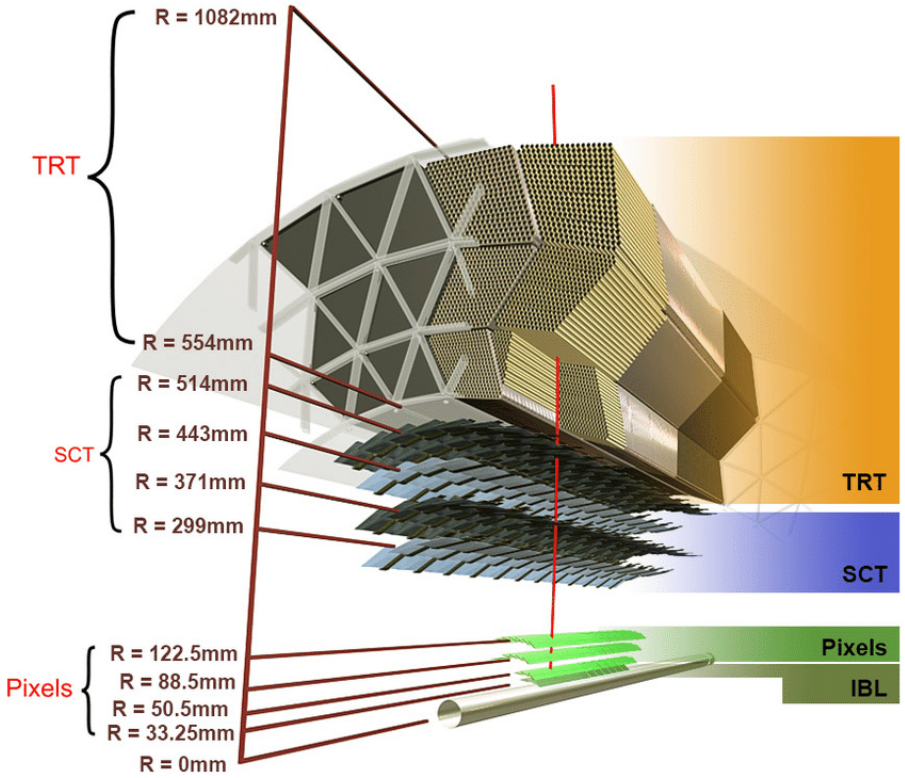

FIGURE 3.11: Schematic view of the various ID layers and their distances from the beamline [15].

to the pixel detector. This layer is the Insertable B-layer (IBL). It has been installed before the start of Run2, during the extended shutdown in 2015, and it is now the closest layer to the beam pipe located at a radius of 33 mm. The IBL is made up of 14 building units, known as staves, and each stave consists of 12 silicon planar sensors. Each sensor is composed of 71429 pixels. The pixel size in the IBL is 50×200 μm^2 in $R-\phi$, smaller than the OPD pixel. This allows an accuracy resolution for tracks and vertex reconstructions to be 10 μm in the $R-\phi$ plane and 60 μm in the z-direction. In the OPD instead, the resolution is 20 μm in $R-\phi$ plane and 115 μm in the z-direction.

The addition of the IBL has allowed improving the track impact parameter measurements and increased the efficiency to find the position of secondary vertices from long-lived particles or jets originated from b-hadrons.

3.2.3.2 The Semiconductor Tracker (SCT)

The middle section of the ID is the SCT detector is, as the pixel detector, for detecting charged particles. It is made of silicon microstrip sensors distributed over 4088 modules, 6.3 million read-out channels, and with size larger than the ones in pixel detector. These modules form 18 disks in the forward regions ($|\eta| > 2.5$), and four layers in the barrel region ($|\eta| < 2.5$) at 299 mm, 371 mm, 443 mm and 512 mm, respectively, from the beamline. The modules in the SCT are arranged in pairs at a distance of 80 μm and connected back-to-back with an angle of 40 mrad to each other, to provide 3D information on the particle hit position.

3.2.3.3 The Transition Radiation Tracker (TRT)

The TRT is the outermost section of the ID. Its main task, besides helping in the particle trajectories reconstruction, is to separate the electron from charged hadrons, like pions, using the transition radiation pieces. The TRT building blocks are straw drift tubes with a diameter of 4mm filled with a mixture of gases: 70% of Xe, 27% of CO_2, and 3% of O_2. The barrel region in the TRT consists of 73 layers of straws with length 144 cm. In the End-cap region, there are instead 160 layers of 37 cm straws. Inside the End-cap straws, there is a gold-plated Tungsten wire with a radius of 0.015 mm.

When a relativistic particle crosses many TRT straws, it emits photons since there is a change in the material dielectric constant. At each interface between materials, the probability of transition radiation increases with the relativistic γ factor. Thus for a given energy, particles with large γ (like electrons) will give off many photons, while particle with small γ (like pions) will give off few photons. This means that the light particles, like electrons, emit a higher number of photons compared to more massive particles, like the pions. The radiated photons give energy (based on photoelectric effect) which ionised the gas in the straw and produced currents in the Tungsten wire. The TRT is designed to detect particles with $p_T > 500$ MeV, and in the region $|\eta| < 2$. It provides 30 hit/track which can give a resolution of 130 μm, lower than the one of the Pixel and SCT detectors.

3.2.4 Calorimetry

The ATLAS calorimetric system [14] is used to measure the energy deposits from charged and neutral particles, such as electrons, taus, and photons, as well as from jets of particles produced by quarks and gluons, for energies in the range between a few GeV up to several TeV. It is also used to measure the imbalance between the initial total transverse momenta of the colliding quarks ($\vec{P}_T^{intial}$) and the final ones, which are obtained by summing up all the final particles vector transverse momenta ($\sum \vec{P}_T^{final}$). The imbalance is then attributed to escaping neutrinos which cannot be directly detected in ATLAS and so-called missing transverse energy (MET or E_T^{miss}).

$$E_T^{miss} = -\sum \vec{P}_T^{final} \tag{3.8}$$

The calorimetry is made of two parts, as shown in Figure 3.12, which cover the full range in ϕ and extend up to $|\eta| = 4.9$. The first one is the electromagnetic calorimeter (ECAL), used to measure electrons, positrons and photons. The hadronic calorimeter (HCAL) measures the energy from hadronic particles and jets instead.

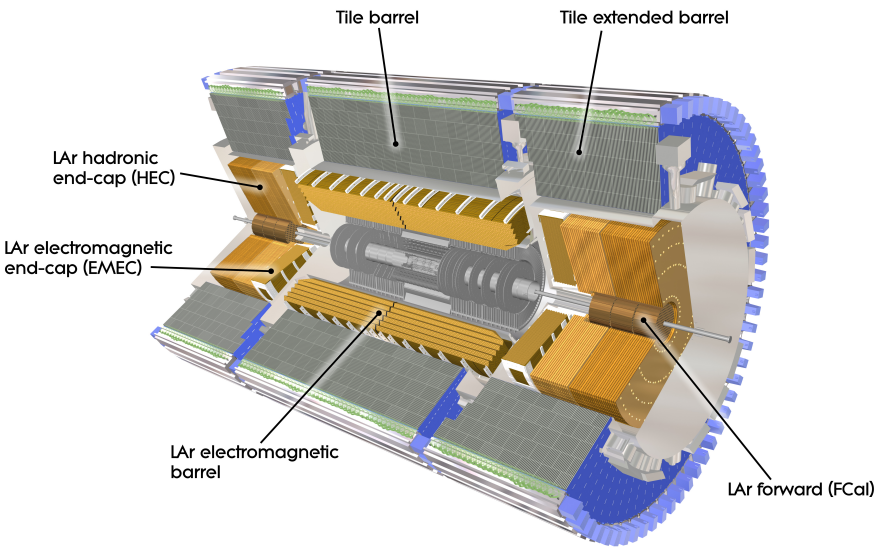

FIGURE 3.12: Schematic view of the calorimetric system of the ATLAS experiment [14].

3.2.4.1 The Electromagnetic Calorimeter (ECAL)

ECAL is the first calorimeter [14, 17], which uses the electromagnetic interaction of the particle with its material to collect the particle energy. It is a sampling calorimeter, which uses liquid Argon (LAr) as an active material, and Lead plates as an absorber in the endcaps and barrel regions and copper plates in the forward part. The central region (barrel) is divided into three longitudinal layers with radiation thicknesses 4.3 X_0, 16 X_0 and 2 X_0 (X_0 is the average distance for electrons or photons to travel until their energies decrease by $1/e$) characterised by various $\eta - \phi$ granularity, as illustrated in Figure 3.13.

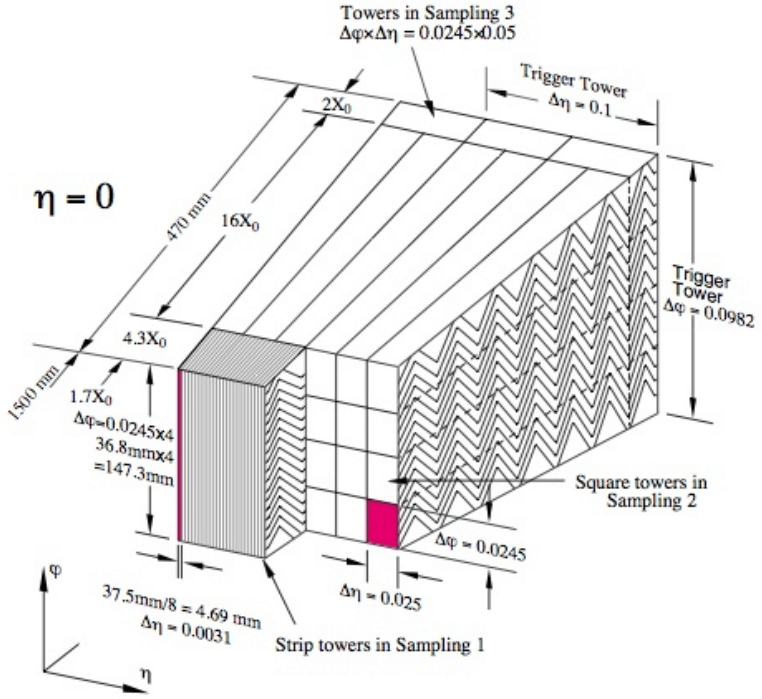

FIGURE 3.13: Scheme of barrel module and segmentation of the electromagnetic calorimeter [17].

When highly relativistic electrons, positrons and photons pass through the ECAL detector, they interact with its material via Bremsstrahlung and pair production. Electrons then decelerate and radiate photons, while photons with energy at least twice the electron mass will produce electron-positron pairs. These processes cause the formation of a so-called electromagnetic shower. Since the produced electrons and photons will be slower and lower in energies; as a result, they will be absorbed by the ECAL material.

ECAL consists of a) two half barrels separated by a gap of 4 mm wide and covers the region $|\eta| < 1.475$, b) two End-caps, divided into two wheels each: the inner wheel covers

the region $1.375 < |\eta| < 2.5$ while the outer one covers $2.5 < |\eta| < 3.2$, c) two forward regions at $3.1 < |\eta| < 4.9$.

The first layer, which has a granularity $\Delta\eta \times \Delta\phi = 0.0031 \times 0.1$, measures a fraction of the total energy deposit and allow to reconstruct the photon position. The second layer, with $\Delta\eta \times \Delta\phi = 0.025 \times 0.0245$, is designed to contain most of the electron and photon energies, while the last one, with $\Delta\eta \times \Delta\phi = 0.05 \times 0.0245$, collect the tails of the electromagnetic showers.

The energy resolution for the ECAL is:

$$\frac{\sigma(E)}{E} = \frac{0.1}{\sqrt{E(GeV)}} \oplus 0.7\% \tag{3.9}$$

where E is the particle energy, $\sigma(E)$ is the energy resolution and $\oplus$ represents a quadratic sum.

3.2.4.2 The Hadronic Calorimeter (HCAL)

The HCAL [14, 17] is designed to measure energies deposits from hadrons and jets originated from quarks and gluons. It consists of two parts; the hadronic Tile calorimeter which covers the region $|\eta| < 1.7$ and the hadronic LAr calorimeter, which is in the region $|\eta| < 4.9$.

The Tile calorimeter is made up of two parts; the barrel Tile calorimeter for $|\eta| < 1$ and two extended Tile calorimeters covering the region $0.8 < |\eta| < 1.7$. It uses scintillating plastic tiles as an active material, while steel is used as an absorber. For the endcap, at $1.5 < |\eta| < 3.1$ and the forward calorimeters, which cover the region $3.1 < |\eta| < 4.9$, the same active material for the ECAL, (LAr), is used. The absorber is Copper in the endcaps and tungsten in the forward region, to properly cope with the higher radiation level.

The HCAL detector is segmented into three longitudinal layers. All the various parts, with their granularity and the number of interaction lengths, are listed in table 3.2 [14].

Detector	granularity $\Delta\eta \times \Delta\phi$	Interactions lengths [λ]
Tile Calorimeter ($\|\eta\| < 1$)		
Layer-1	$0.1 \times 2\pi/64$	1.5
Layer-2	$0.1 \times 2\pi/64$	4.1
Layer-3	$0.2 \times 2\pi/64$	1.8
($0.8 < \|\eta\| < 1.7$)		
Layer-1	$0.1 \times 2\pi/64$	1.5
Layer-2	$0.1 \times 2\pi/64$	2.6
Layer-3	$0.2 \times 2\pi/64$	3.3
LAr Endcap	$(0.1 \times 0.1\text{-}0.2 \times 0.2)$	≈ 10
Forward Cal		
Layer-1	0.1×0.1	2.66
Layer-2	$\sim 0.2 \times 0.2$	3.68
Layer-3	$\sim 0.2 \times 0.2$	3.60

TABLE 3.2: Hadronic calorimeter layers with their granularity and segmentation [14].

The energy resolution for the HCAL in the central region is:

$$\frac{\sigma(E)}{E} = \frac{0.55}{\sqrt{E(GeV)}} \oplus \frac{3.2GeV}{E} \oplus 2.3\% \tag{3.10}$$

while in the endcap region, the energy resolution is:

$$\frac{\sigma(E)}{E} = \frac{1}{\sqrt{E(GeV)}} \oplus \frac{3.2GeV}{E} \oplus 10\% \tag{3.11}$$

3.2.5 Muon Spectrometer

The muon spectrometer [14], MS, is the outermost part of the ATLAS detector. It is used to provide a precise measurement of the muon trajectories and momenta after they have travelled through the whole ATLAS detector without stopping. The MS is made up of two regions: the barrel region, with three cylindrical layers covering $|\eta| < 1$, and two endcap chambers to cover the region $1 < |\eta| < 2.7$. The muon path is bent by a toroidal magnetic field, which allows measuring the muon momenta. The strength of the magnetic field in the central region (barrel) is 0.5 T, while in the endcap region the magnetic field is 1 T.

The MS consists of four operating systems, as illustrated in Figure 3.14.

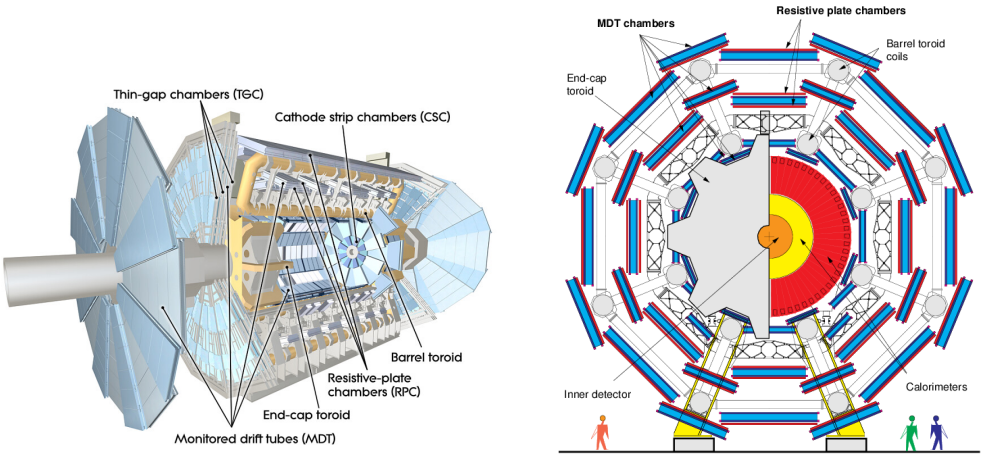

FIGURE 3.14: A schematic longitudinal (left) and transverse (right) view of the muon spectrometer components.

3.2.5.1 Monitored Drift Tubes (MDT)

The MDTs are rectangular chambers consisting of drift tubes with radius 15 mm, filled by a mixture of 90% of Argon and 10% of CO_2. The MDTs are placed at radii 5 m, 7.5 m and 10 m from the interaction point in the central region. The endcap region four wheels are placed at 7 m, 13 m, and 21 m away from the interaction point in the beamline direction while the fourth one is installed at 11 m distance from the interaction point. When the muons interact with the gas mixture in the tube, free electrons are produced via ionisation and collected using a Tungsten-Rhenium wire inserted in the centre of the tubes, thus producing a current signal. The single-tube position resolution is about 60-80 μm, allowing momentum resolution of 10% for muons with p_T =1 TeV and up to p_T = 3 TeV for charge identification, while entire chambers have a position resolution of approximately 30-60 μm.

3.2.5.2 Cathode Strip Chambers (CSC)

The CSCs are installed close to the beamline on the innermost wheel in the region $2.0 < |\eta| < 2.7$. They are multiwire proportional chambers, which are sandwiched between two cathode plates and filled with a gas mixture made of 80% Argon, and 20% CO_2. The position resolution provided by the CSCs in the R-direction is 60 μm, and 5 mm in the transverse plane.

3.2.5.3 Resistive Plate Chambers (RPC)

The RPC chambers consist of two parallel plates with 2 mm of separation and filled with $C_2H_2F_4$. In each chamber, there are two orthogonal readout strips: one in the z-direction and the other in the ϕ-direction. The applied voltage between the two plates is 9.8 kV. The RPC chambers are used to trigger the muons in the central region with a time resolution comprises between 15-25 ns, and they are located either on the bottom or the top of the MDTs.

3.2.5.4 Thin Gap Chambers (TGC)

As the RPCs, the TGCs are multiwire proportional chambers able to cope with the high particle flux present in the η region where they are installed. They are filled with a mixture of gases: 55% of CO_2 and 45% of C_5 H_{12}. The TGCs provide triggering information for the muons in the endcap regions ($1.0 < |\eta| < 2.4$), and their timely response and resolution, are comparable to the RPCs in the barrel region.

3.2.6 Trigger and Data Acquisition

The LHC is designed to produce $\sim$ 2 billion of proton-proton collisions per second in the ATLAS experiment, which corresponds to a data size of more than 60 terabytes per second. However, this huge amount of data cannot be stored for later analysis. Therefore, a triggering system is needed to filter all these data and to keep only events which might be of interest. To reduce the flow of data to feasible levels in the ATLAS experiment, the trigger system [88–90] is split into a hardware trigger, the Level-1 (L1), and software based trigger, which is referred to High Level Trigger (HLT).

The L1, which is constructed with custom-made electronics, works to reduce the data rate from 30 MHz to 100 KHz by using a subset of information from the calorimeters or the muon RPC and TGC. The L1 is identifying the events with high transverse momentum (p_T) of leptons, jets, and photons, as well as high missing transverse energy and the time required for the single-event processing is of 2.5 μsec [90]. The regions where the objects

of interest passed the L1 trigger threshold are defined as Regions of Interest (RoIs). The RoIs then are sent to the second level of triggers, which is the HLT, where advanced algorithms are run using the full detector granularity information in either the RoIs or the whole event. The decision to keep the event data is made in times of 2.5 μsec. The event then is stored in pipelined storage buffers for further use [13, 89].

The HLT trigger is a software-based trigger with a large farm of CPUs used to refine the L1 trigger analysis. The HLT trigger performs a detailed analysis either on the whole event using full granularity information from the full detector (e.g. Trackers, Calorimeters and Muon detectors) or by utilising the data in smaller-isolated regions of the ATLAS detector. Fewer events per second ($\sim$ 1000 events) are analysed using the HLT trigger. Therefore, it has a longer time, on average 200 msec, to decide to store the events for offline analysis [90].

In the ATLAS experiment, there are a variety of L1 and HLT algorithms designed to record and identify events based on the physical object of interest. For example, there are sets of triggers referring to the physics objects in the analysed events such as electrons, muons, photons, jets, b-tagged jets, or E_T^{miss} [89, 90].

Chapter 4

Particle Reconstruction and Identification

When new physics objects are produced in proton-proton collisions, they interact with the detector material, leaving different signals in different detector sections. These signals are converted using dedicated software algorithms into tracks, energy clusters, and momenta. After that, physics objects are reconstructed and compared between data and MC samples, to derive the scale factors parameterised corrections, which are then used to calibrate and match the results from MC and data.

In this thesis, several physics objects are presented: charged leptons (in particular electrons and muons), jets originated from quarks or gluons hadronisation and the missing transverse energy: all essential for the search for $t\bar{t}$-resonances (Chapter 7) and four-top-quark reconstruction based on χ^2–method(Chapter 6).

4.1 Electrons

In the ATLAS experiment, the signature of an electron produced from a pp collision is a track in the Inner Detector and an energy deposit in the electromagnetic calorimeter. When an electron passes through the EM material, it will interact with its material producing electromagnetic shower in the cells. These cells, which are square elements in

the η-ϕ plane will form a cluster and the energy deposit by the electron will be obtained by summing the energies in all the cluster cells.

In the central region of the Inner Detector $|\eta| < 2.5$, the reconstructed track with at least three hits in the ID layers is extrapolated to the second layer of the EM calorimeter cluster, which contains the largest fraction of the energy deposited by the electron.

Then, the electron candidate is reconstructed when at least one track is matching one EM cluster [19, 91]. In the case of multiple tracks matching the same cluster, the decision is made by selecting track with Silicon hits ($N_{\text{Si}}^{\text{hits}}$) in the Pixel Detector and with the closest distance $\Delta R = \sqrt{(\eta)^2 + (\phi)^2}$ to the cluster. The four-momentum vector for the electron is obtained by including the information from the EM, where the energy resolution scale for the reconstructed electrons is approximately 1% [92]. The efficiencies, which depend on several factors to reconstruct electrons with transverse momentum more significant than 15 GeV, are in the range of 97% to 99% in the barrel and endcap regions. The electron candidate has a sharp energy tower in the EM cluster with a small leakage in the HCAL. The energy deposit is required to be compatible with the momentum measured in the ID [91].

Identification

Additional requirements are applied to distinguish electrons from other particles, such as pions or converted photons. Several identification criteria are defined to reduce the misidentification of electrons, which are essential for several analyses. These identification criteria are grouped into three different categories by imposing either independent selections on the discriminating variables (like the shape of the energy shower (tower), the number of track hits and the matching quality between the EM cluster and the track in the ID), referred to as cut-based identification, or a single selection on the ratio of the likelihood functions for the signal and background (see Ref[18]).

In this thesis, the so-called likelihood-based (LH) method [18], which is a multivariate technique used to evaluate several properties of the electron candidates and to discriminate them from other particles, is used. In this method, the probability density functions (PDFs) of the discriminating variables for both the signal and background candidates

are used to calculate the probability of the object to be either signal or background candidate. The advantages of using this method over the cut-based identification that the LH method gives a better background rejection, and the discriminating variables, with similar distributions, can be added easily [18].

The primary identification groups are: Loose, Medium and Tight, which implies increasingly strict selections applied to reject more background. For example, in the Tight criteria, more requirements are used than in the Medium and Loose criteria, therefore the background rejection increases, as well as the efficiency of charge misidentification for electron, as shown in Figure 4.1. From Figure 4.1a, it can be seen that the identification

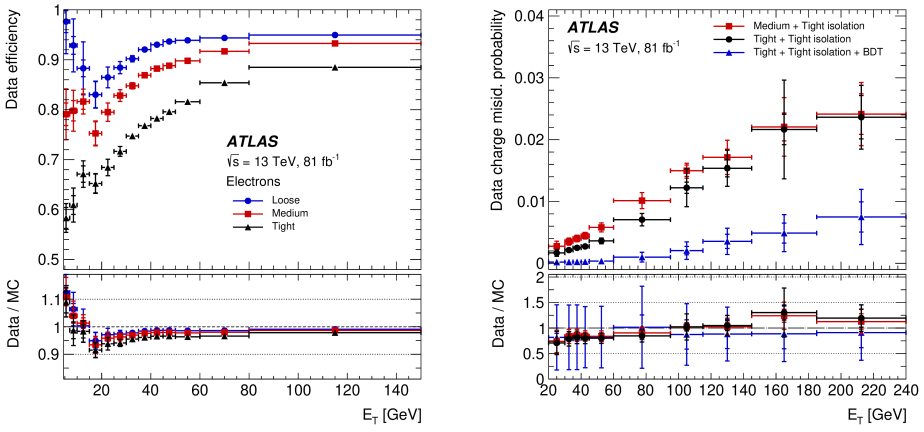

(a) (b)

FIGURE 4.1: The efficiency of electron identification (a) and charge misidentification for electrons (b) as a function of E_T and using different working points [18].

efficiency increases with transverse energy. This is due to the reduction in the detector systematic uncertainties at high energies, as well as to a better background rejection from other processes, like QCD, which increases with energy. In the Loose criteria, the efficiency to reject the backgrounds is lower with respect to the other identification criteria, while the efficiency for reconstructing electrons is higher due to the less restrictive selections applied. However, in this thesis, electrons are required to pass the Tight (TightLH) identification criteria.

Isolation

The electron isolation is related to the energy deposit in the EM layers by other physics objects close to the electron energy cluster [18]. Electrons produced from the decay of resonant particles, Z or W bosons, muon and tau lepton, are known as prompt electrons.

Non-prompt electrons can result from a hadronic decay, photon conversions, as part of jet products, and misidentification of light hadrons, mostly coming from up and down quarks. Two additional variables are used to distinguish prompt electrons from non-prompt ones. The first one is the sum of the energy $\sum_{\text{cluster}} E_T$ deposits in the EM within a cone of $\Delta R = 0.2$ around the associated cluster to the electron, $E_T^{\text{cone0.2}}$. In contrast, the second one is track isolation, which is denoted as $p_T^{\text{cone0.2}}$. It is defined as the scalar sum of the track transverse momenta $\sum_{\text{tracks}} p_T$ within a cone size of $\Delta R = 0.2$, except the track associated with the electron.

Several isolation efficiencies are used in the ATLAS experiment. These working points are defined either as fixed cuts on the isolation variables or as a function of the transverse energy E_T targeting a fixed value of the efficiency. An example of a fixed value of efficiency as a function of the E_T, is the Gradient working point, which is designed to give an efficiency of 90% and 99% for electrons with $E_T = 25$ GeV and $E_T = 60$ GeV, respectively, estimated from the simulated $Z \to ee$ events [18, 91]. In this thesis, electrons considered in chapter 6 must satisfy the so-called FixedCutTight (FCTight) isolation working point, which is corresponded to the fixed requirements on the calorimeter ($E_T^{\text{cone0.2}}$) and track ($p_T^{\text{cone0.2}}$) isolation variables (see Ref[19, 92] for more details about different isolation working points). In contrast, there are no isolation requirements for those in chapter 7 for reasons will describe in details in Section 7.2.

Electron efficiency The total efficiency of identifying and selecting electrons is defined as:

$$\epsilon_{\text{electron}} = \epsilon_{\text{reconsrtuction}} \times \epsilon_{\text{identification}} \times \epsilon_{\text{isolation}} \times \epsilon_{\text{trigger}} \tag{4.1}$$

Each efficiency is evaluated in both data and MC samples to correct and match the MC samples to the measured efficiencies in data. This correction is done by selecting electrons coming from resonant particles, $Z \to ee$ and $J/\psi \to ee$, and factors are derived for electrons in bins of E_T and η [91, 93]. Figure 4.2 shows the reconstructed efficiency of electrons using $Z \to ee$ events as a function of the transverse energy and η.

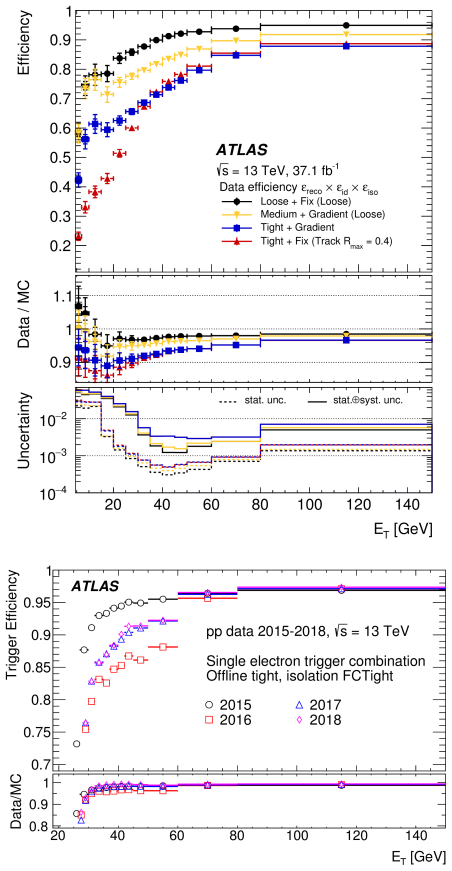

FIGURE 4.2: Product of reconstruction, identification and isolation efficiencies from a $Z \rightarrow ee$ data sample as a function of E_T (top), the trigger efficiency of identifying electrons passing the Medium criteria (bottom) [18, 19].

4.2 Muons

Muons are charged particles which interact inside the ID sub-detectors, and deposit a small fraction of energy in the calorimeters, as well as leave hits in the muon spectrometer MS [21, 94]. The crucial part for muon identification and reconstruction is the information coming from the MS, as well as the hits left by muons in the ID. Based on information coming from the ID, the MS and the calorimeters, there are several algorithms to identify and reconstruct muons which lead to different types of reconstructed muons. These methods are shown in Figure 4.3 and classified as [20, 21]:

- **Combined Muons (CB)**: Muons are leaving several hits in the ID subdetectors, which are used to reconstruct tracks in the ID, in addition to the hits in the MS. A global fit is performed using an algorithm to find the best trajectory between the reconstructed tracks in both the ID and MS. The produced track is referred to as

the combined track, from which the muon momentum is evaluated using the track curvature. Muon momenta are corrected using the small energy fraction, which is deposited in the calorimeters.

- **Standalone muons (SA)**: The reconstruction of muons tracks is performed using only hits produced in the MS. In this method, muon trajectories are extrapolated back to the ID to the origin point of the ATLAS detector. The fraction of energy deposited in the calorimeters is also taken into account.

- **Segment-Tagged muons (ST)**: In this method, the ID tracks are extrapolated to the MS sub-detectors. Therefore, tracks in the ID are classified as muons if they match the segmented tracks, which are produced by the muons in the CSC and MDT chambers.

- **Calorimeter-Tagged Muons (CaloTag)**: Muon identification is performed by extrapolating ID tracks to the energy deposit in calorimeters without using information from the MS.

Identification

Based on the applied selection and on discriminating variables, such as the muon p_T, charge, the energy deposit and the fitting-method for track reconstruction, muons are grouped into four different identification categories, depending on the signal efficiency and background rejection: Loose, Medium, Tight and High p_T. The identification efficiencies for the first three categories are between $92\% - 98\%$ in the range $20 < p_T < 100$ GeV and $|\eta| < 2.5$, while the last method is a particular case used in specific analyses [21]. In this thesis, muons are required to pass the Medium identification criteria, which is the standard criteria in the ATLAS experiment, and it minimises the associated calibration and reconstruction uncertainties of muons. In this criteria, muons are retained if they leave, in at least two MDT layers, ≥ 3 hits, except in the region $|\eta| < 0.1$, those with at least one MDT layer and not more than one MDT hole layer are allowed. Additionally, muons are required a q/p significance, which is defined as the absolute value of the difference between the ratio of the muon charge and momentum that measured in the ID and MS divided by the sum in quadrature of the corresponding uncertainties, to be less than seven.

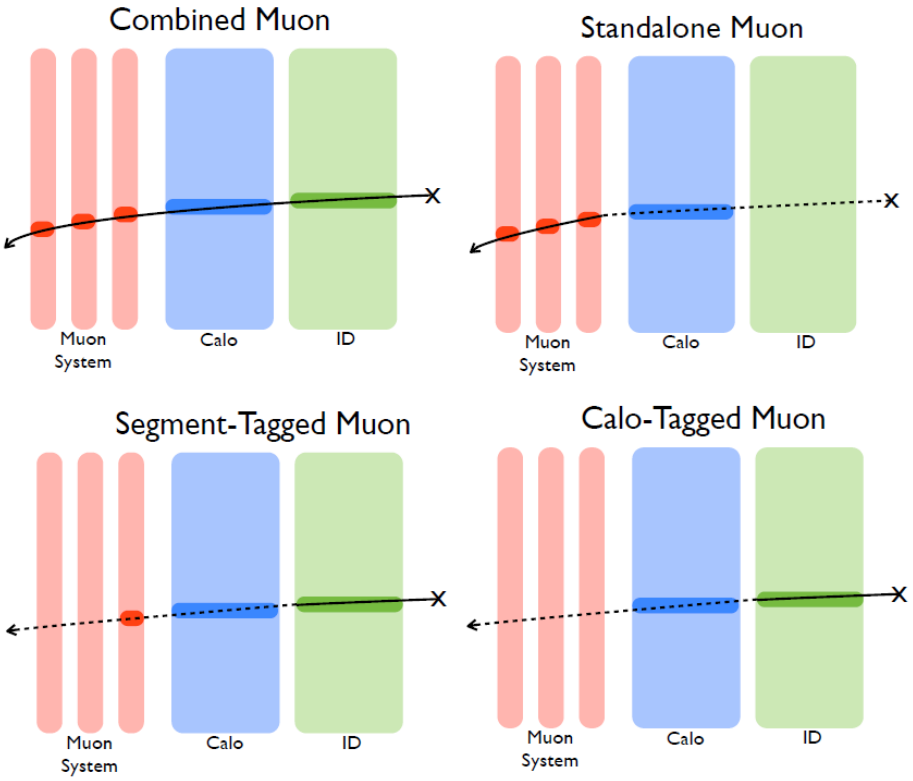

FIGURE 4.3: Muon reconstruction methods depending on the signals provided from different part of the ATLAS detector [20].

Isolation

With a very similar procedure to the one used to isolate the prompt electrons, two additional variables, $E_T^{\text{cone0.2}}$ and $p_T^{\text{cone0.2}}$, are defined to assess the muon isolation [21]. Muons considered in this thesis are required to pass an isolation requirement based only on the track information, which is found to be very efficient at high p_T, and it is referred to as FixedCutTightTrackOnly.

Muon efficiency

As for the case of the electrons, the overall muon efficiency is defined as:

$$\epsilon_\mu = \epsilon_{\text{reconstruction}} \times \epsilon_{\text{isolation}} \times \epsilon_{\text{trigger}} \times \epsilon_{\text{identification}} \tag{4.2}$$

The correction factors are derived using events from resonant particles, $Z \to \mu\mu$ and $J/\psi \to \mu\mu$, to match the efficiencies evaluated from data. The efficiency of reconstructing muons, which pass Medium criteria, is shown in Figure 4.4 as a function of p_T and for $|\eta| > 0.1$ [21].

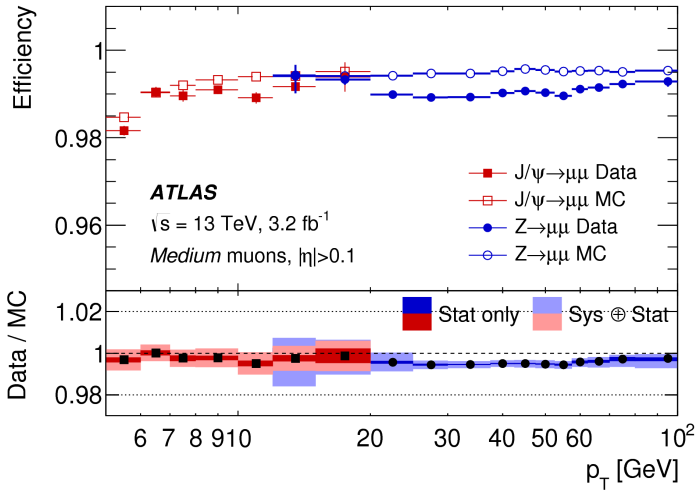

FIGURE 4.4: The efficiency of muon reconstruction as a function of p_T for those who pass the Medium identification requirements [21].

4.3 Jets

Due to the confinement principle, gluons and quarks (partons), are not detected in nature as isolated particles. Still, they rather hadronise to form a cascade of hadrons (baryons and mesons) and create so-called jets [95, 96]. Jets are collimated sprays of hadrons which can be reconstructed by several algorithms using the fractions of energies deposited in the calorimeters. In the ATLAS experiment, the anti-kt algorithm [97] is used to reconstruct jets, and the input for this algorithm are: groups of energy clusters from the calorimeters [98], the distances d_{ij} between the jet candidates i and j as well as the distance between a jet candidate i with respect to the beam d_{iB} [22]. These distances, d_{ij} and d_{iB}, are defined as:

$$d_{ij} = \min\left(p_{T,i}^{-2}, p_{T,j}^{-2}\right)\frac{(\Delta R_{ij})^2}{R^2}, \;\; d_{iB} = p_{T,i}^{-2} \tag{4.3}$$

where $p_{T,i}$ and $p_{T,j}$ are the transverse momentums of the jet candidates i, and j, respectively. Also, $\Delta R_{ij} = \sqrt{(\Delta\eta_{ij})^2 + (\Delta\phi_{ij})^2}$ is the angular distance between the jet candidates (i and j) for a jet with cone radius R set to 0.4 in this thesis.

Algorithm proceeds by finding the smallest distance between jet candidates d_{ij}^{min} and between the jet with respect to the beam d_{iB}. In the case of $d_{ij}^{min} < d_{iB}^{min}$, the two jets are combined to form a pseudo-jet by summing the four-momenta of jet i and j. Then, the new jet candidate is added back to the jet candidates list. Finally, the previous steps

are repeated until d_{ij}^{min} becomes larger than d_{iB}^{min}, then the jet candidate i is considered as a final jet and removed from the input list.

The anti-kt algorithm is infrared, collinear safe and straightforward, which means the reconstructed jets, as well as their shape, are stable. The infrared safety means that presence of the soft radiation (soft jets) does not alter the reconstructed jet. On the other hand, the collinear safety means that the splitting of hard jets does not change the final state jets. The infrared and collinear safeties are illustrated in Figure 4.5.

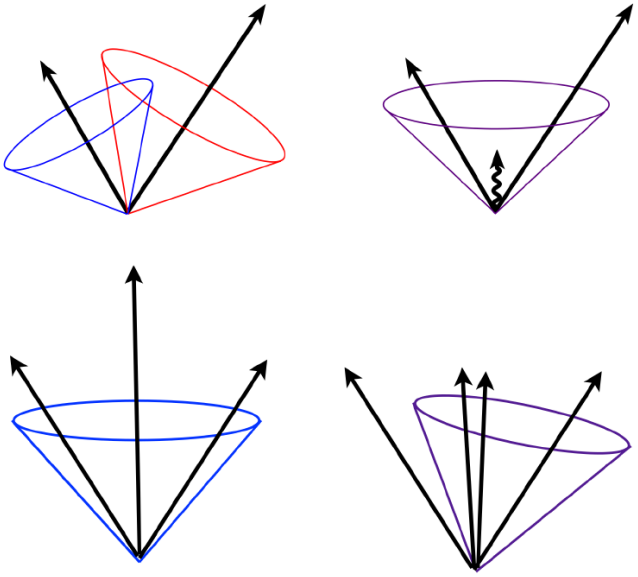

FIGURE 4.5: Schematic plot of the infrared unsafe (top) where the soft radiation changed the shape of the reconstructed jet. In contrast, the collinear unsafe (bottom) shows the hard jets splitting that produced different jet clustering [22].

Jet calibration

Several calibration steps are then applied to the topological clusters (topo-cluster), to produce jets with correct energies and consistent with those predicted from the simulation. The first step is to calibrate the jet energies at the electromagnetic (EM) scale by measuring the energy deposits in the calorimeters. The local cluster weighting method (LCW) uses shower shapes and depths in the ECAL and HCAL to distinguish between them [99]. Also, it applies a set of corrections to the hadronic showers based on simulated pions showers. Additional calibrations, known as jet energy scale JES, are used to match the energy scale of reconstructed jets to the simulated ones [100, 101]. These calibrations are applied in sequence, as shown in Figure 4.6, and illustrated below.

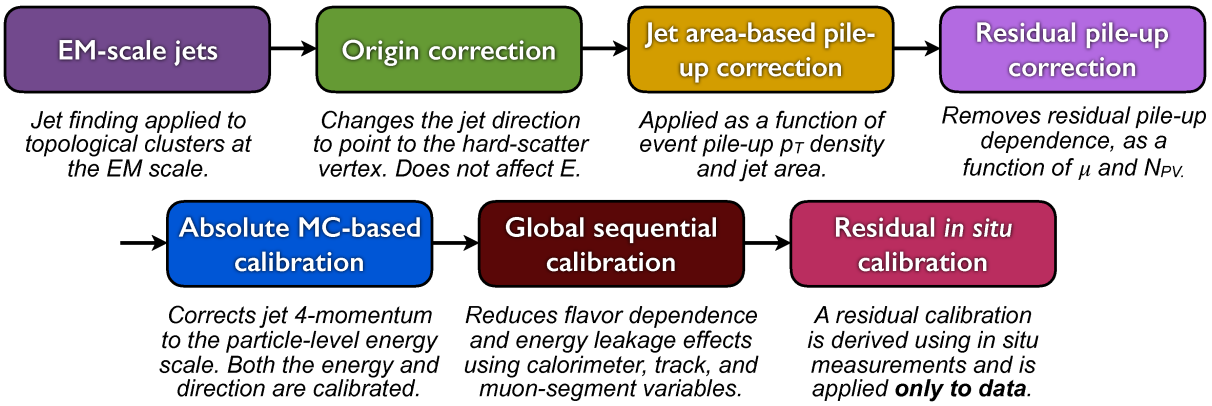

FIGURE 4.6: The jet energy scale JES calibration procedure [23].

- **Origin correction**: The jet direction is shifted from the centre of the ATLAS detector to the hard-scattering vertex (primary vertex). It means the four-momentum of the jet is defined considering the primary vertex position.

- **Pile-up corrections**: Two subtraction methods are applied to reduce the effect of pile-up on the jet momentum. The first one is subtracting the pile-up contribution to the jet area, while the second one depends on the number of primary vertices and the total number of interactions per bunch crossing μ [101, 102].

- **MC-based jet corrections**: A jet energy scale is derived from the energy of simulated jets and applied to reconstructed jet energy. Also, a small correction is applied to the reconstructed jet pseudorapidity (η).

- **Global sequential corrections**: these corrections are taking into account the different response of the calorimeter to jets originated either from quarks or gluons. They depend on track and muon spectrometer information, as well as from the various energy deposits from quark and gluon jets. Also, special corrections are applied to jets with high p_T [103].

- **In situ energy correction**: This correction is applied only to data by considering the different response of jets between data and simulations. To derive the JES, several well-defined samples are used such as Z jets, γ jets and multijet [104].

Jet Pile-up rejection

An additional variable is defined using the tracks and calorimeters information associated

with the jet to discriminate between jets originating from the hard-scattering and those from the pile-up. This variable is the Jet Vertex Tagger (JVT), which is constructed based on a multivariate analysis using the corrJVF and R_{p_T} variables, see Ref[24].

The corrJVF variable is the ratio of the sum of all the track p_T's associated to jet originating from the primary vertex (PV) to the sum of all track p_T's matching to jet (tracks from PV and pile-up). This variable is expected to be close to one for the jets originated from the hard-scattering, and zero for those originated from the pile-up. On the other hand, the R_{p_T} is defined as the ratio of the scalar sum of tracks p_T associated with the jet originating from the PV to the fully calibrated jet p_T after the pile-up subtraction.

Figure 4.7 shows the JVT distributions for jets originated from the hard-scattering interaction (PV) and those from soft interaction (pile-up). From this figure, one can see that the JVT for jets originated from the PV are closed to one and zero for those from the pile-up. Jets with a p_T less than 60 GeV and with $|\eta| < 2.4$ (the pile-up contribution negligible at hight p_T) are required to have a JVT value larger than the threshold values which correspond to three working points: Loose, Medium and Tight. The default working point in this analysis is the Medium one, which corresponds to the threshold value equal to 0.59 (JVT > 0.59), and has a selection efficiency up to 92% for the hard scattering jets.

The efficiency of the JVT selection for hard-scattering jets and the corresponding scale factors (SF) are determined in data and MC from $Z \to \mu^+\mu^-$ events. On the other hand, the JVT systematic uncertainty is derived using $Z \to \mu^+\mu^-$ events simulated by different MC generators.

Jet flavour tagging

The reconstructed jets in the ATLAS experiment originate from the hadronisation of quarks or gluons as well as from the hadronic decays of the most massive lepton, which is the tau. These jets have different peculiar properties that can be used to discriminate between them. Jet tagging is used in several analyses: in the ones presented in this thesis, jets initiated from b-quarks are essential in the search for the $t\bar{t}$ resonances (Chapter 7) and the SM four-top-quark reconstruction based on χ^2–method (Chapter 6).

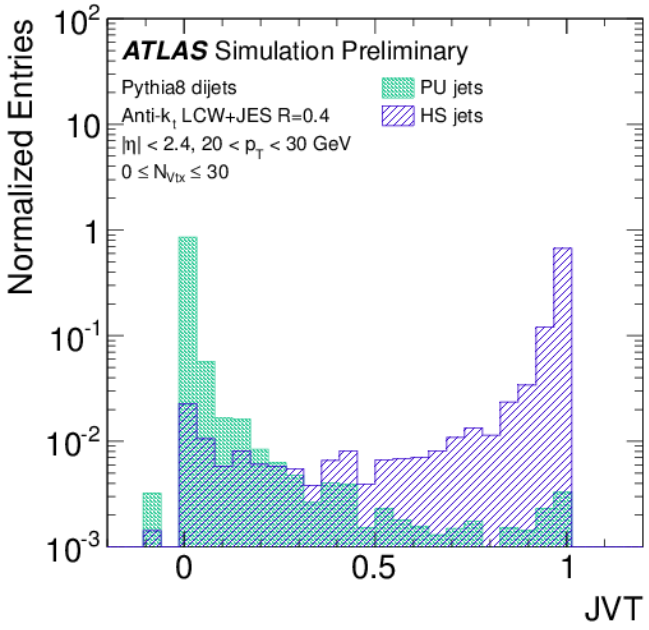

FIGURE 4.7: JVT distribution for the jets originated from the hard-scattering (blue), and pile-up (green) with $20 < p_T < 30$ GeV and $|\eta| < 2.4$ in the simulated dijets events. JVT value equal to -0.1 is assigned to the jets with no associated tracks [24].

The b-jets initiated from b-quarks have specific properties, which can be used to tag them from other jets (light jets) originated from the fragmentation of up, down and strange quarks. These properties are that b-hadrons have a long lifetime, of order 1.5 ps, and they can travel to ~ 1 mm before decaying [95, 96]. This long travelling in the ID can be detected as a reconstructed vertex, which is displaced from the position of the primary vertex and known as the secondary vertex, as shown in Figure 4.8. Another feature of b-quarks is that the masses of the b-hadrons are more significant than those of the light-hadrons.

To improve the b-tagging efficiency and to discriminate them from other light-jets and c-jets that originated from the charm quarks which have similar properties as the b-jets, several algorithms have been combined and used in the ATLAS experiments. They are briefly discussed below, and more details can be found in [25, 105, 106]. The tagging algorithm considered in Run2 as well as in these analyses is based on a multivariate technique, MV2, using boosted tree decision which utilises information from the following b-taggers algorithms as input to the MV2 algorithm, see Ref[25, 105].

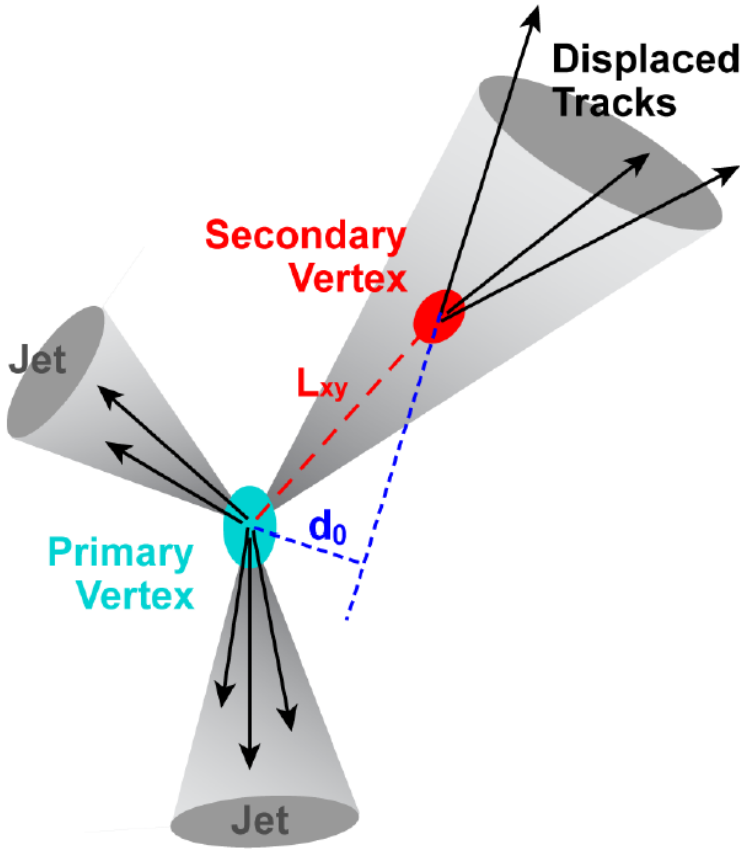

FIGURE 4.8: A schematic plot which shows the formation of secondary vertex from the decay of long-lived particle compared to other jets initiated from the primary vertex.

- **Impact parameter algorithm**: Tracks produced in a b-hadron decay will be displaced from the hard-scattering vertex because the lifetime for the b-hadrons is longer than other light-hadrons. Therefore, the transverse distance between the track and the primary vertex, d_0, as well as the longitudinal one, $z_0 \sin(\theta)$, in the $R - \phi$ plane, will be larger than for the tracks coming from b-hadrons decays. In practice, the significances of these variables $z_0 \sin(\theta)/\sigma_{z_0 \sin(\theta)}$ and d_0/σ_{d_0} are used and combined into a log-likelihood to produce the probability density functions for each jet flavours and to discriminate between them.

- **Secondary vertex (SV)**: An algorithm is used to reconstruct the additional vertex displaced from the primary vertex by checking all track pairs inside the b-jets. The properties of SV are combined using other variables such as the vertex invariant mass. The number of reconstructed vertices in the b-jets and energy fraction for

each vertex is used to discriminate b-jets vertices from other criteria that might be passing the same selections.

- **JetFitter**: It is a multi-vertex algorithm used to reconstruct the decay chain of b-hadrons inside the jet. It finds a common line where the decay vertex (SV) of b- or c-hadrons and the primary vertex lies. This gives information about the flight path and the SV position, which are used as inputs to a neural network and multivariate analyses.

Results from previous techniques are used as input to the boosted decision tree (BDT) to discriminate b-jets from light and c-jets. In the analyses presented in this thesis, the MV2c10 version of the multivariate technique is used as based tagger of the b-jets [107, 108]. The MV2c10 provides higher rejection for c- or light-jets by using 7% of c-jets in the background sample while in the previous algorithm MV2c20 the fraction of c-jets in the background sample is 20%.

Different variables are defined in the tagging algorithm to quantify its performance. One of these variables is the tagging efficiency ϵ_b, which is defined as the efficiency to tag jets originating from b-quarks. The other variables are the mistagging rates $\epsilon_{c;light}$, which are the efficiencies to reject c-jets and light-jets, respectively [108, 109].

Several working points are defined based on the BDT cuts and selected efficiencies. In this thesis, the working point used was MV2c10_77, which corresponds to an efficiency of tagging b-jets (ϵ_b) of 77%. The tagging efficiency of b-jets, as well as the rejection efficiency of c- and light-jets at that working point ($\epsilon_b = 77\%$) are shown in Figure 4.9 as a function of the transverse jet momentum p_T and for different tagging algorithms.

4.4 Missing Transverse Energy (E_T^{miss})

From the conservation of momentum, all 4-momenta is conserved before and after the collision. In the ATLAS experiment particles produced in the region at 4π in ϕ and $|\eta| < 2.5$ are fully reconstructed, while particles which escape along the beamline direction or do not interact with subdetector materials are not detected, such as neutrinos. The

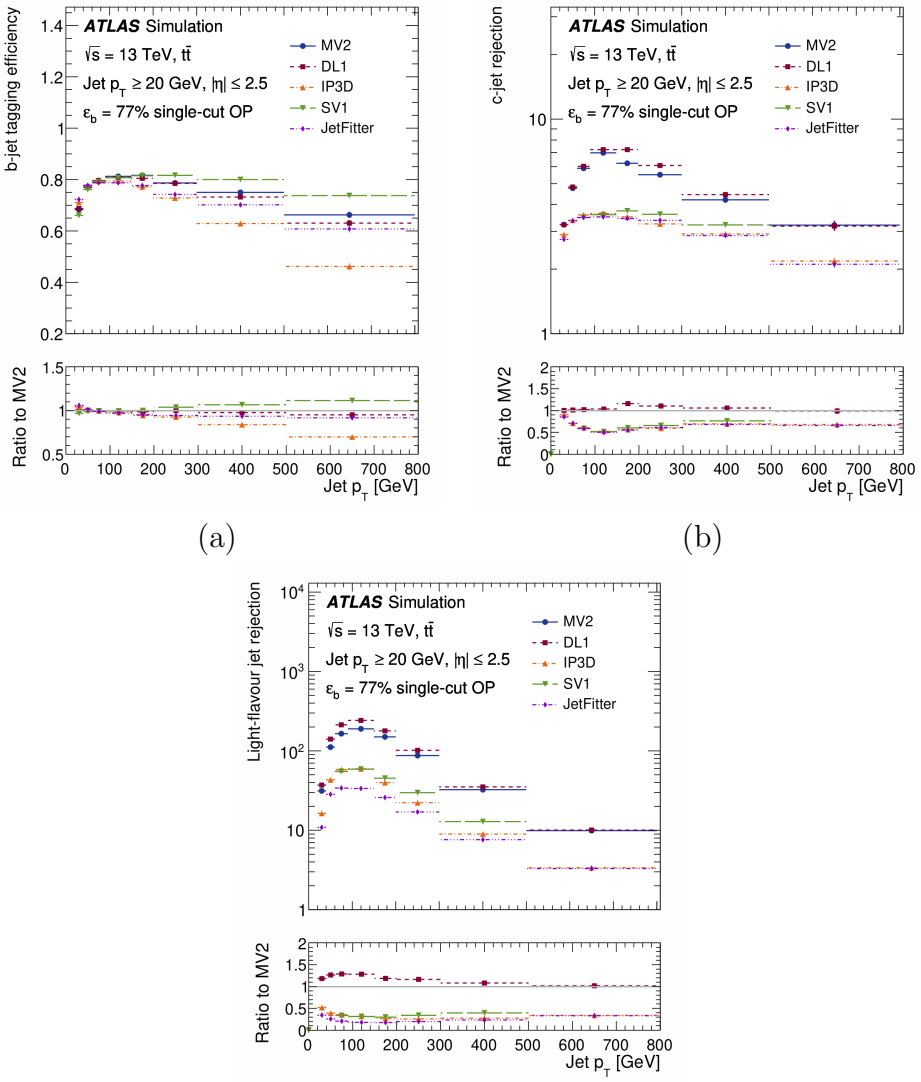

FIGURE 4.9: The efficiency of tagging b-jets (a) and rejection efficiencies of tagging the c-jets (b) as well as the light jets (c) as a function of jet p_T at $\epsilon_b = 77\%$ using simulated $t\bar{t}$ events [25].

imbalance in the transverse momentum after collisions is an indirect indication for the neutrino escaping and is referred to as the missing transverse momentum E_T^{miss} [95, 110].

$$(E_T^{miss})^2 = (E_x^{miss})^2 + (E_y^{miss})^2 \tag{4.4}$$

where the direction of E_T^{miss} is obtained from the azimuthal angle, ϕ^{miss}:

$$\phi^{miss} = tan^{-1}(\frac{E_y^{miss}}{E_x^{miss}}) \tag{4.5}$$

The E_T^{miss} is reconstructed from the imbalance in the vector sum of the transverse energies (transverse momenta) from the calibrated physics objects, which are electrons, photons, jets and muons, referred to as Hard terms. The energy deposits in the cells, not corresponding to other Hard terms, referred to as softer terms are also used. The E_x^{miss} and E_y^{miss} are given as:

$$E_{x(y)}^{miss} = E_{x(y)}^{miss,jet} + E_{x(y)}^{miss,e} + E_{x(y)}^{miss,\mu} + E_{x(y)}^{miss,photon} + E_{x(y)}^{miss,soft} \tag{4.6}$$

To find the E_T^{miss} resolution and response, samples with and without real E_T^{miss} in both data and MC samples are used. The E_T^{miss} resolution is defined as the width of the $E_{x(y)}^{miss}$ distribution and the difference between the reconstructed E_T^{miss} and the true E_T^{miss}. The E_T^{miss} response is defined as the difference between the reconstructed E_T^{miss} and the expected value. In several analyses, we need to obtain the P_z component of the neutrino from the missing energy to build the four-momentum component of the neutrino vector and to reconstruct the top quark, the W-boson or new massive particles masses. There are many analytical methods to obtain the 4-momenta using the information from E_T^{miss} [110, 111]. One of these methods is to solve the quadratic equation to obtain the momentum component in the z-axis, P_z (see Appendix A).

Chapter 5

Track and Vertex Reconstruction

A precise determination of charged-particle momentum is essential for all the analyses of the ATLAS experiment. It plays a significant role in the particle identification, especially for the b-hadrons, the charged leptons and the jets. This means that a high-efficiency reconstruction of the vertices and the charged particles tracks from proton-proton collisions is essential. In this analysis, a new method is developed to measure the efficiency in reconstructing pion tracks, in the low transverse momentum region. The pion tracks reconstruction plays a central role in the identification of the b- and c-hadrons and the discrimination of pions from other particles, such as electrons.

In this chapter, the reconstruction of tracks and both primary and secondary vertices are presented in general in Section 5.1 and Section 5.2. In Section 5.3, a new method for measuring the relative efficiency for pion tracks in data (minimum-bias 2018 data) and MC at low transverse momentum in the ATLAS inner detector is presented. The production rate measurement for $D^0 \to K^- 2\pi^+\pi^-$ relative to $D^0 \to K^-\pi^+$ in both data and MC, is also presented as part of the study; more details are given in Section 5.3.1.

5.1 Track Reconstruction

A track in the ATLAS detector is a collection of hits produced along the path in the tracker of a charged particle. In the ATLAS detector, a charged particle can leave several

hits in the various components of the Inner Detectors [112]. Tracks are defined using a set of standard parameters: charge, momentum and position. Track momentum and position are measured relative to the beam-spot in general or from other defined points, e.g. the primary vertex, for any particular analysis [113]. Track position is represented using two observables named: impact parameters d_0 and z_0, which are, respectively, the radial and longitudinal distances of the tracks to the beam-spot, as shown in Figure 5.1. All selected tracks are required to have a transverse momentum larger than 400 MeV. Otherwise, the curvature radius for a track with a transverse momentum lower than 400 MeV will be small, and the low number of hits produced in the Inner Detector will make the tracks fitting very hard.

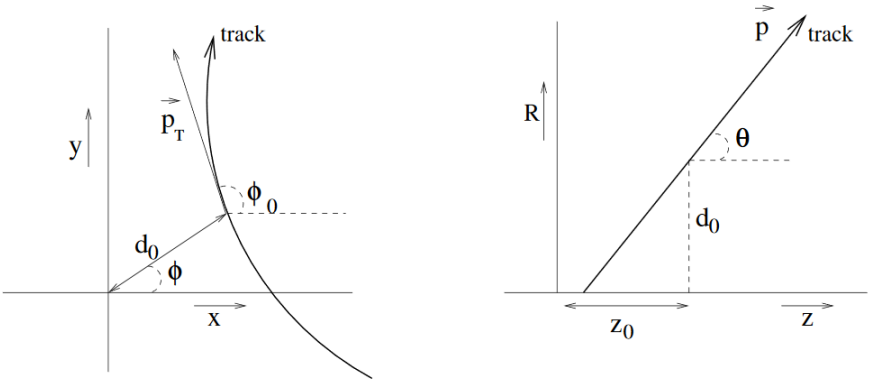

FIGURE 5.1: The track perigee parameters in the xy-plane (left) and $R-Z$plane (right) [26].

A track is reconstructed in the ATLAS experiment using two algorithms: the inside-out algorithm and the outside-in one. In the inside-out algorithm [114], which is the most general one, the tracks are seeded at first in the Pixel Detector and then extrapolated to the outer layer of the SCT and TRT. In contrast, the outside-in algorithm track seeds start from the TRT and are then extrapolated to the Pixel and SCT detectors. The outside-in method is used to recover tracks which are not reconstructed due to the low efficiency of the detector, or because they have originated from particles decayed in the Pixel or SCT detectors.

The first input for the inside-out algorithm is three-dimensional points (space-points). These points are created from the hits registered in the Pixel and SCT detectors as a charged particle crosses them. The track seeds in this algorithm, are built from the combination of at least three space-points since these seeds are the measured momentum

and transverse impact parameter. Figure 5.2 shows the various steps involved in the reconstruction. On Figure 5.2(a) the track seed formed by matching three space-points is sketched. Wherein, Figure 5.2(b) shows how the track seed is used to build a road to other layers of the Inner Detector. Roads are built by adding hits from the other ID sub-detectors to the track seed and extending it to the SCT. The Kalman Filter algorithm [114] is used to extend the track length to all the ID sub-detectors in order to produce the track candidate, as shown in Figure 5.2(c,d). From this algorithm, track's parameters and their uncertainties are estimated from the track seeds and used to determine the position of the next hit. If the next hit is consistent with the original track, the length of the track is extended. Then, the track parameters are updated to predict the next hit position, and so on. The process ends when the end of the track is achieved, and no more hits can be added from the silicon detectors [113–115].

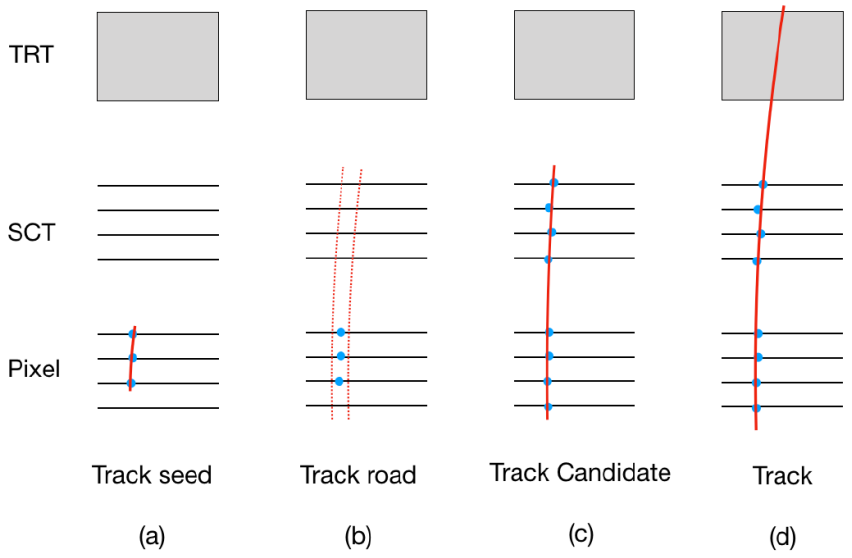

FIGURE 5.2: Schematic plot for the track reconstruction procedure where the layers of the pixel, SCT and TRT detectors are shown. (a) Space-points in the pixel detector are used to form the track seeds. (b) Rodes reconstructed from the track seeds and extended to other layers. (c,d) The track candidates are found using the Kalman Filter and extended to the TRT to form the full track [27].

Track candidates are ranked depending on the number of hits or missing hits (holes) involved in their reconstruction as well as on the result of their quality fit ($\chi^2/n.d.f$). Tracks with a high number of hits are given top ranking while tracks with a large number of holes have a lower ranking. The final track candidates will be selected based on the

ranking score; some of them will be chosen for further analyses, while others will be rejected or combined to produce new tracks [115].

In the ATLAS experiment, tracks are grouped into two categories: Loose and Tight. The Loose category selects tracks reconstructed with an efficiency not optimised to reject the so-called fakes coming from the wrong or accidental combination of hits. On the opposite, the Tight category is applied a more restrict selection to reduce fake reconstruction. Therefore, the track reconstruction efficiency under the Tight selection is lower than the one reconstructed under the Loose selections. In table 5.1, the Loose and Tight selection requirements are defined [27, 115].

Loose Track
$p_T > 500$ MeV
$\|\eta\| < 2.5$
$N_{Si} \geq 7$ (Number of Pixel+SCT hits, including dead sensors)
$N^S_{mod} \leq 1$ (Number of shared silicon hits)
$N^{hole}_{Si} \leq 2$ (Number of missing hits in Pixel+SCT (holes))
$N^{hole}_{pixel} \leq 1$ (Number of Pixel holes)
Tight Track
In addition to the Loose requirements
$N_{Si} \geq 9$ if $\|\eta\| < 1.65$
$N_{Si} \geq 11$ if $\|\eta\| > 1.65$
At least one hit in one of the two innermost Pixel layers
$N^{hole}_{pixel} = 0$

TABLE 5.1: Summary of the Loose and Tight track quality requirements [27].

Figure 5.3(a,b) shows the track reconstruction efficiency in the ID as a function of the track transverse momentum p_T and pseudo-rapidity η, within the ID geometrical acceptance ($p_T > 500$ MeV and $|\eta| < 2.5$). From Figure 5.3(a) it can be seen that the efficiency increases with p_T. In contrast, at low p_T, the efficiency of reconstituting a track decreases, due to the probability to reconstruct tracks coming from multiple scattering are high. On the other hand, the efficiency decreases at high values of η, as shown in Figure 5.3(b), since in this case, tracks are passing through a high density of material compared to the central region. Also, multiple scattering is higher at large η.

The reconstruction efficiency for tracks passing the Loose selection is in the range between 73% and 91%. For tracks reconstructed with the Tight criteria, the efficiency is instead

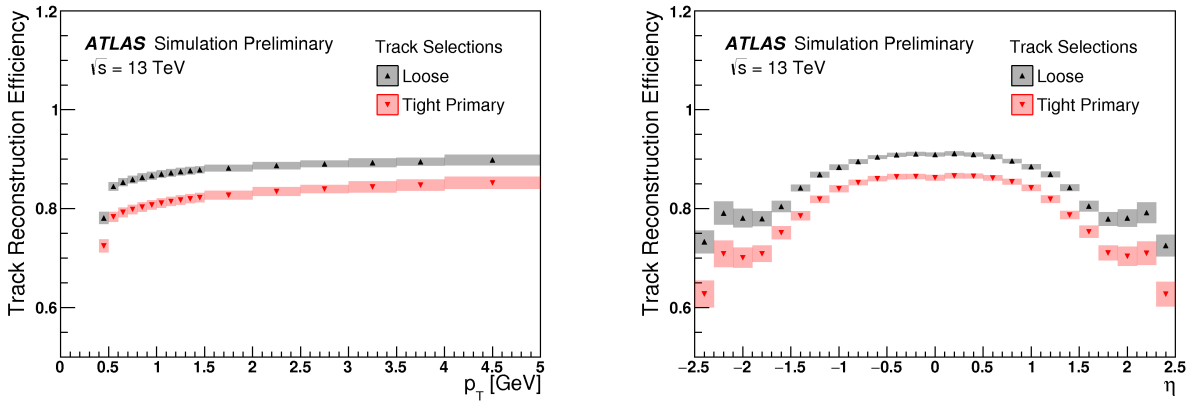

(a) (b)

FIGURE 5.3: The efficiency of reconstructing tracks using Loose and Tight quality requirements in the ID as a function of p_T (a) and η (b) [28].

in the range between 63% and 86%. The number of reconstructed tracks as a function of the average number of scattering per bunch ($< \mu >_{bunch}$), is shown in Figure 5.4. One can see that tracks reconstructed under Loose criteria have a non-linear distribution in the region $< \mu >_{bunch} > 30$, while tracks were passing the Tight selection, have a linear behaviour in all regions. The non-linearity in the first case is due to the higher probability to reconstruct a fake track where the $< \mu >_{bunch}$ value is high [28, 29].

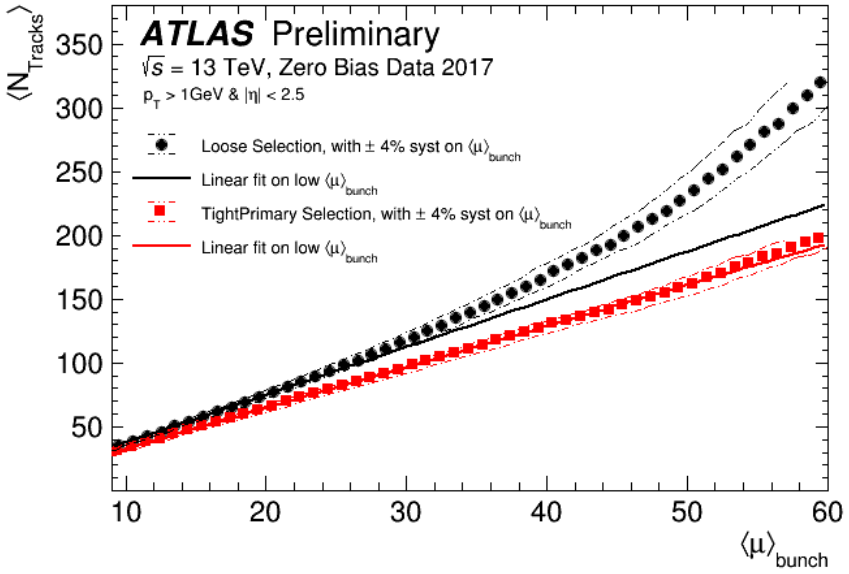

FIGURE 5.4: The average number of reconstructed tracks per event in the ID passing the Loose and Tight and preselection requirements $|\eta| < 2.5$ and $p_T > 1$ GeV. The solid lines are the linear fit to data in the region $9 < < \mu >_{bunch} < 16$ and extrapolated to higher $< \mu >_{bunch}$ [28, 29].

5.2 Vertex Reconstruction

The primary vertex (PV) is a space-point resulting from the hard-inelastic scattering of p-p collision. The reconstruction of the PV is crucial for the identification of physics objects coming from the hard scattering of the colliding protons. These collisions can also be of different nature, e.g. soft collisions or scattering from other bunches. These, together with a delayed response of the detector, can produce another type of vertices overlapping to the primary one, referred to as pileup. The procedure of isolating the PV uses two separate algorithms: the vertex finding algorithm and the vertex fitting algorithm (for more details see Ref[26, 114, 116, 117]). In general, a vertex is reconstructed from at least two tracks that pass either the Loose or Tight selections. The position of the reconstructed vertices, PV or pileup, is determined by minimising the χ^2 for the beam-spot.

Vertices are classified depending on the number of tracks belonging to them, their size and position with respect to the beam-spot as well as from the value of the scalar sum of tracks transverse momentum ($\sum {p_{T,\text{Trk}}}^2$). The vertex with the higher value of $\sum {p_{T,\text{Trk}}}^2$ is assigned to be the PV, while the others are treated as pileup vertices.

The Inner Detector can also reconstruct and detect vertices resulting from the decay of long-lived particles. These particles can travel before they decay to other particles, such as heavy hadrons produced from b- or c-quarks hadronisation. The resulting vertex from the decay of a long-lived particle is referred to as the secondary vertex (SV). The main characteristic of the SV is to be displaced away from the PV, as shown in Figure 5.5. Besides, the tracks belonging to it are characterised by more significant impact parameters than those belonging to the PV. The reconstruction of the SV is vital to distinguish the b- from other jets.

5.3 Pion Track

The efficient and precise reconstruction of the charged-particle tracks is crucial to understand collisions in the dense environment, which is presented at the LHC. Several methods have been developed to measure the track reconstruction efficiency for different

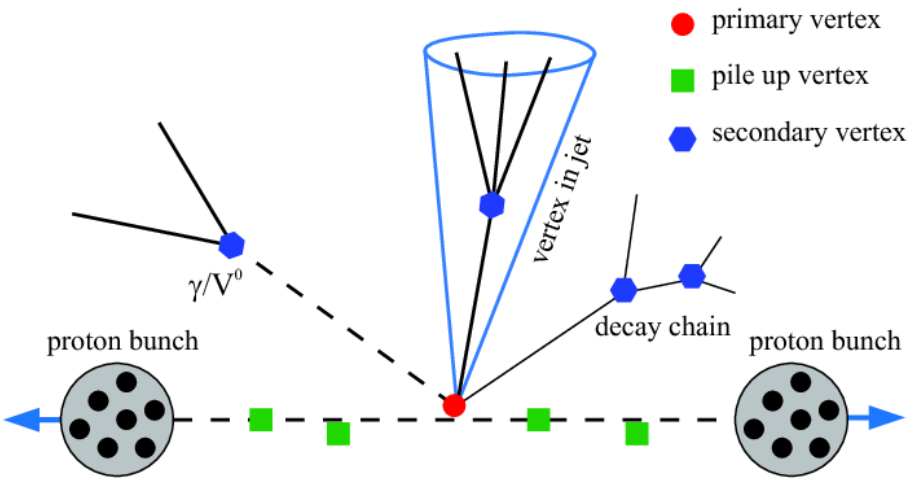

FIGURE 5.5: Sketch showing the different type of reconstructed vertices in the ATLAS experiment.

types of charged-particles covering all their kinematic range with the correct systematics. In this thesis, a new method is developed to measure the tracking efficiency for a particular hadronic particle, the pion. The goal of this study is to extract the detector efficiency to reconstruct the charged pion at low transverse momentum and to have a cross-check on the MC estimations and performance. Besides, it is crucial to tag long-lived particles and to reconstruct their SV inside jets. An example is the reconstruction of the SV of charmed mesons in jets initiated by a b- and c-quarks, which are essential for several analyses, e.g. those involving top-quark decays.

5.3.1 Pion Track Reconstruction Efficiency

The efficiency to reconstruct pion tracks can be measured in data and MC by finding the ratio of the number of neutral charmed-meson decays to four or two charged particles final states. In particular, in this thesis, the relative rate for D^0 decays in the $K3\pi$ ($D^0 \rightarrow K^-2\pi^+\pi^-$) channel to the $K\pi$ ($D^0 \rightarrow K^-\pi^+$) decay channel has been measured. To increase the purity of the signal, a unique source for D^0 is used in this analysis (see Ref[118]). This is the chain of D^{*+} that decays with probability $\sim 67 \pm 0.5\%$ to D^0 and π_s^+, which is referred to as the slow pion because it has low energy in this channel, see Section 5.3.2. Additionally, from SM prediction, a non-resonant peak appears around the mass value of 145.4257 ± 0.0017 MeV when we take the mass difference between $D^{*+}(2010.26 \pm 0.05$ MeV) and $D^0(1864.83 \pm 0.05$ MeV) [37, 119].

The relative efficiency for the reconstruction of pions tracks in data and MC can be found using the formula:

$$\frac{\epsilon(Data)}{\epsilon(MC)} = \sqrt{\frac{R}{R(PDG)}} \tag{5.1}$$

where R is the ratio between the branching ratios in the four-body and two-body decay,

$$R = \frac{N_{K3\pi}}{N_{K\pi}} \frac{\epsilon_{K3\pi}}{\epsilon_{K\pi}} \tag{5.2}$$

with $N_{K3\pi}$ ($N_{K\pi}$) being the number of reconstructed events in the four-body (two-body) decay channel for data collected at $\sqrt{s}$ = 13 TeV. $\epsilon_{K3\pi}$ ($\epsilon_{K\pi}$) is the efficiency of the reconstructed four-body (two-body) decay channel using MC samples generated at $\sqrt{s}$ = 13 TeV. The expected value for R should be equal to $R(PDG) = 2.08 \pm 0.04$ as predicted by the SM.

5.3.2 Particle Level

In the following, the analysis performed on particle level is referred to as the truth-level in this analysis. Shortly, the particle level in this analysis looks at the charged particles produced from proton-proton collisions at $\sqrt{s}$ = 13 TeV before the propagation in the detector. In particular, the studied charged particles are charmed mesons, D^{*+} and D^0.

The selected tracks in both simulated samples (two-body and four-body decay channels) are in the active region of the Inner Detector $|\eta| < 2.5$ and at 4π in ϕ. Tracks are required to pass the Tight selections as defined in table 5.1 and to have transverse momentum p_T larger than 500 MeV. Figure 5.6(a-c) shows the transverse momentum distributions for the reconstructed D^0, D^{*+} and π_s^+ at truth-level in the two-body decay channel ($D^0 \rightarrow K^-\pi^+$) for tracks with $p_T > 500$ MeV generated at $\sqrt{s}$ = 13 TeV. While, Figure 5.6(d) shows the transverse momentum distribution for the slow pion, π_s^+, at truth-level in the two-body decay channel ($D^0 \rightarrow K^-\pi^+$) without any cuts on the tracks p_T.

From Figure 5.6(d), one can see that the transverse momentum distribution for the π_s^+ is in the MeV range with a maximum p_T around 300 MeV. The pion is then a soft particle, and the default selection on the track p_T will affect the reconstruction efficiency of the

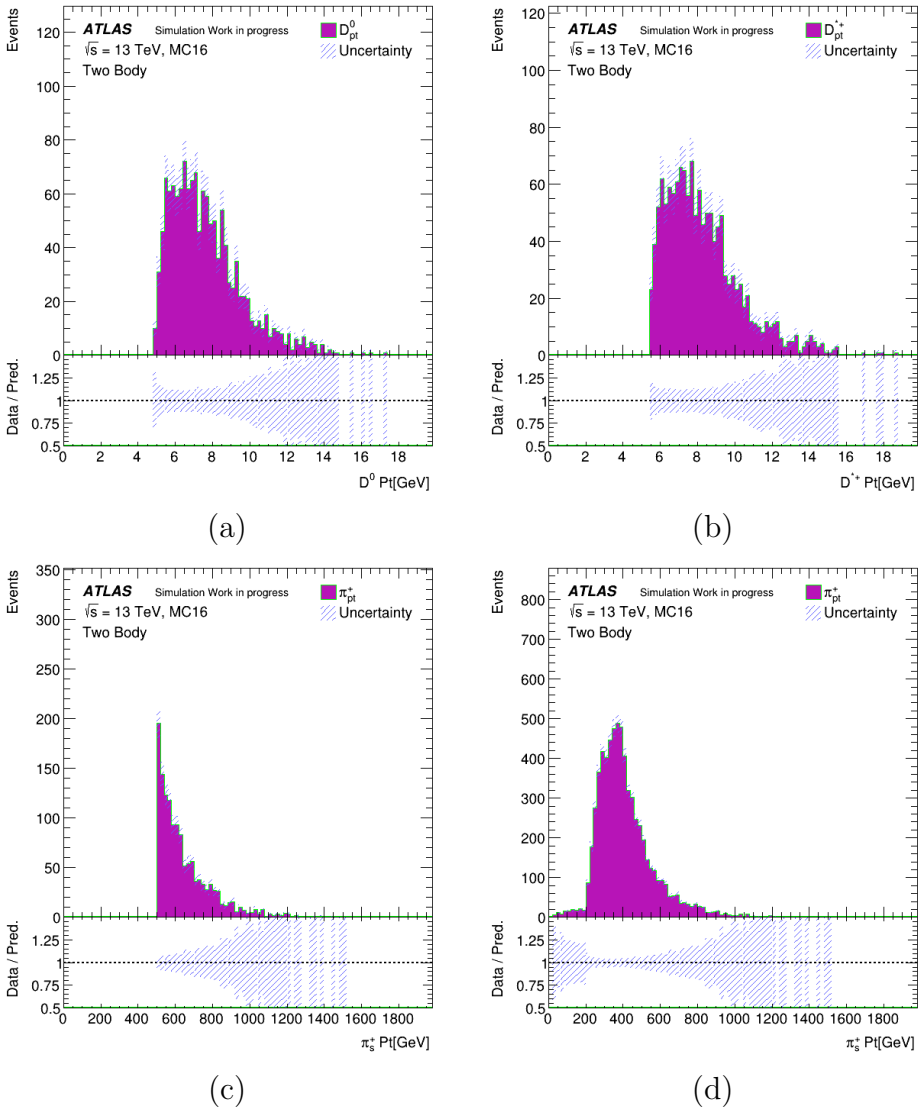

FIGURE 5.6: p_T distributions for the reconstructed (a) D^0 and (b) D^{*+} and for the slow pion π_s^+ produced from the D^{*+} decay for MC events at truth-Level with (c) $p_T > 500$ MeV and (d) $p_T > 0$ MeV, respectively (Uncertainty here is stat only).

D^0. The reconstructed D^0 and D^{*+} (as seen in Figure 5.6(a,b)) have p_T in the range GeV with $p_T > 4$ GeV since D^0 and D^{*+} have close masses ($D^0 \sim 1864$ MeV and $D^{*+} \sim 2020$ MeV).

Other parameters have been defined and used to discriminate the signal candidates (correct tracks combination) from other candidates (wrong charge combination). These parameters are: 1- position (x, y, z) of the D^0 decay vertex, which is an SV, with respect to the beam spot position. 2- $\cos(\theta^*)$ between the kaon candidate and the reconstructed D^0 in the reference frame of the D^0. 3- transverse decay length L_{xy} defined as the distance

between the SV and the primary vertex (PV) projected along the D^0 transverse momentum direction. Figure 5.7 shows the expected position of the SV from the D^0 decay, as well as the expected position of D^{*+} decay vertex in Cartesian coordinates (x, y, z) at truth-level.

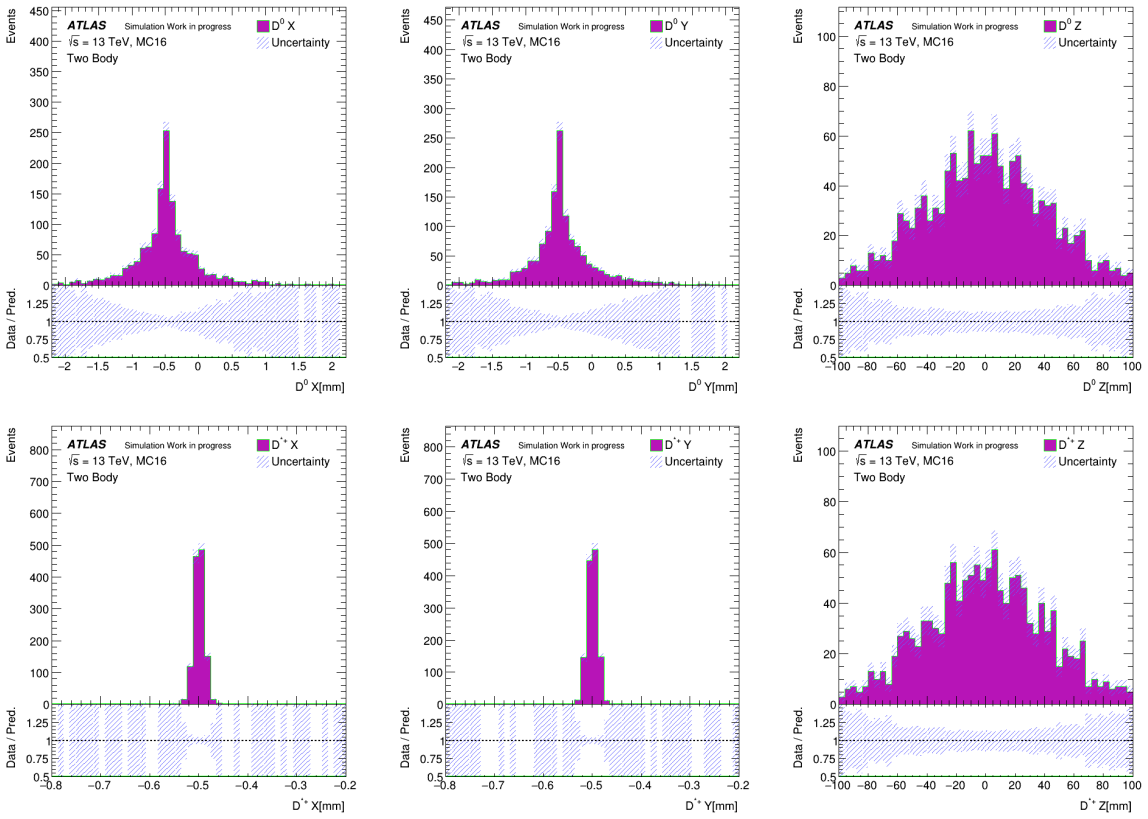

FIGURE 5.7: Decay vertex position (SV) for the D^0 in $K\pi$ (top), and for D^{*+} (bottom) at truth-level for simulated events (Uncertainty here is stat only).

In the ATLAS experiment, the PV's position in the MC simulation is set by default to be at (-0.5, -0.5) in XY-plane. On the other hand, in data, the position of the PV is at point (-0.4, -0.9) in the XY-plane. From Figure 5.7, one can see that the position of the simulated D^0 decay vertex is distributed according to a Gaussian around the point $(-0.5, -0.5)$ mm in (x, y) coordinate. This means that the D^0 meson flies the PV and forms an SV that can be reconstructed in the inner detector. In contrast, the decay vertex for the D^{*+} meson at truth-level is located inside the PV resolution, which means, in this analysis, that it cannot be reconstructed or detected by the inner detector.

In Figure 5.8(a,b), the $\cos(\theta^*)$ and L_{xy} distributions at truth-level (see Appendix B for four-body decay channel) are shown. It can be seen that the $\cos(\theta^*)$ distribution is uniform

over the full range $(-1, 1)$. This is because D^0 is a spin-zero particle. Therefore, from the conservation of angular momentum, the produced K^- meson in the reference frame of the D^0 does not have a specific orientation. On the other hand, the L_{xy} distribution shows that the D^0 meson flies away from the PV before it decays.

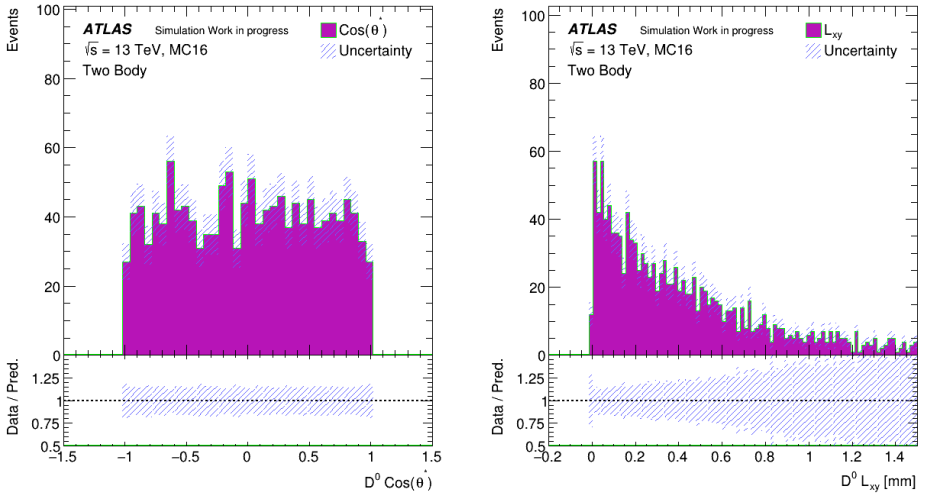

(a) (b)

FIGURE 5.8: (a) $\cos(\theta^*)$ distribution between the Kaon meson the in $K\pi$ channel and the D^0 meson in the reference frame of the D^0. (b) the D^0 meson transverse decay length, L_{xy} (Uncertainty here is stat only).

Other channels have been studied to evaluate the effects on the efficiency measurement of reconstructing pion tracks in the four-body decay channel, $D^0 \rightarrow K^-2\pi^+\pi^-$. Also, to see if a significant contribution is coming from other processes, which have similar final states (Inclusive processes) to the studied one (Exclusive four-body decay channel) and might affect the calculated MC efficiency. The first channel is $D^0 \rightarrow K^-\pi^+\rho^0 (BR = 6.77 \pm 0.31)\%$ where ρ^0 has a mass of 775.26 ± 0.25 MeV and decays to $\pi^-\pi^+$. In addition, the channel where D^0 decays to $\bar{K}^{*0}\rho^0 (BR = 5.8 \pm 0.8) \times 10^{-3})$ and $\bar{K}^{*0}$ decays to $K^-\pi^+$ has been investigated. The ρ^0 and $\bar{K}^{*0}$ decay via strong interaction, which means the decay width for these particles is of the order of $\sim fm$. However, the decay width for the D^0 is $\sim 122\ \mu m$ since its decay goes via the weak interaction. Figure 5.9(a, b) shows the transverse momentum (see Appendix B for other distributions) for the K^- and π^- mesons produced in the three studied channels.

From Figure 5.9(a,b), one can see that the transverse momentum of the K^- and π^- mesons produced in the channels $D^0 \rightarrow K^-\pi^+\rho^0$ and the $D^0 \rightarrow \bar{K}^{*0}\rho^0$, respectively,

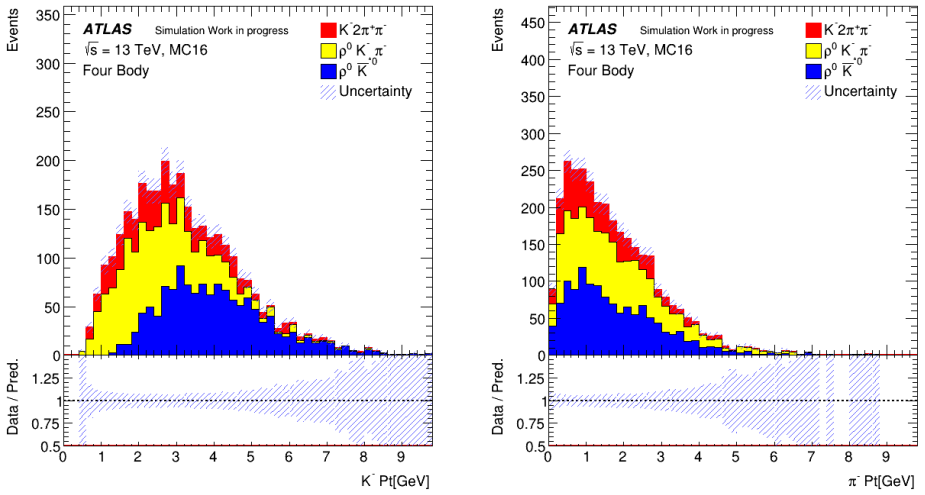

(a) (b)

FIGURE 5.9: Transverse momentum distribution for the K^-(a) and π^- (b) produced from different decay channels, where (red) is for $D^0 \rightarrow K^-2\pi^+\pi^-$ (yellow) for $D^0 \rightarrow K^-\pi^+\rho^0$; $\rho^0 \rightarrow \pi^-\pi^+$ and (blue) for $D^0 \rightarrow \bar{K}^{*0}\rho^0$;$\bar{K}^{*0} \rightarrow K^-\pi^+$ and $\rho^0 \rightarrow \pi^-\pi^+$ (Uncertainty here is stat only).

have similar distributions to the ones produced in $D^0 \rightarrow K^-2\pi^+\pi^-$ channel. However, the K^- (blue) produced from $\bar{K}^{*0} \rightarrow K^-\pi^+$, has higher transverse momentum compared to the other channels. Nevertheless, the effect from this channel on the efficiency of reconstructing pion track in the $D^0 \rightarrow K^-2\pi^+\pi^-$ is negligible because of the small branching ratio of this channel compared to the other ones.

5.3.3 Event Selection

The track collections from simulated MC and real data events used in this analysis contains tracks, which are required to pass the Tight requirements already discussed in table 5.1, and also the trigger selections listed in table 5.2. These triggers are related to the dataset collected by the ATLAS experiment in the period 2018 for pp collisions at $\sqrt{s} = 13$ TeV. The number of generated MC events for the two-body and four-body decays channels is 1215000 and 250500, respectively.

Additionally, other selection criteria have been applied to discriminate signal combinatorial from another combinatorial background. These selection criteria, listed in the following, are extracted from the truth-level study:

Trigger	Data(%)	MC $K\pi$ (%)	MC $K3\pi$ (%)
HLT-j20-L1J12	1.4	16.4	0.014
HLT-j15	0.42	98.2	4.4
HLT-j10-L1RD0-FILLED	0.9	98.3	4.33
HLT-j20-L1JRD0-FILLED	3.35	94.6	3.11

TABLE 5.2: Summary of the applied trigger selections with the event percentages for those passing these triggers for each decay channels.

- Tracks should form a secondary vertex (SV) with a total charge equal to zero. The number of tracks which belongs to the SV is two (four) in the two-body (four-body) decay channel.
- The χ^2 for the resulting SV has to be less than 25.
- $140 < \Delta M < 170$ MeV, where ΔM is the mass difference between the D^{*-} and D^0 (in data, the charge conjugate is also included).
- $L_{xy} > 0.1$ mm.
- To retain the D^* candidates, the invariant mass of D^0 is required to be in the range $1830 < D^0_M < 1900$ MeV.
- $|\cos(\theta^*)| < 0.5$.
- Combine all the D^0 candidates with and additional track, which is the π^+_s from the D^{*-} decay, and require the p_T of D^{*-} to be larger than 5.5 GeV.

5.4 Analysis Strategy

After the truth study using the simulated MC samples for four-body and two-body decay channels, the reconstruction of D^0 begins by using a tool (so-called JpsiUpsilon tool) to form an SV from four and two sets of tracks, respectively, with total zero charged. The reconstruction starts using only the simulated tracks (data blinded) that are passed the event selection without the trigger requirements since all events in MC samples are passing the same trigger selections. To examine the vertexing performance using the

JpsiUpsilon tool, and to check the validity of this tool, R (defined in Section 5.3.1) is evaluated and expected to equal to 1.0 using the MC samples only. This is done by splitting the MC sample for each decay channel into two parts. The first one is used to evaluate the reconstruction efficiency, $\epsilon_{K3\pi}$ and $\epsilon_{K\pi}$, respectively. The second part is referred to as pseudo-data, used to extract the number of reconstructed events, $N_{K3\pi}$ and $N_{K\pi}$, respectively.

After the tool is checked and it returns the expected value for R (see the following Section 5.5), data are now unblinded, and the relative efficiency of reconstructing pion tracks in data and MC is evaluated as follows:

- $\epsilon_{K3\pi}$ and $\epsilon_{K\pi}$: The efficiencies of reconstructing the correct combinations (signal) in both decay channels are determined from the simulated events, which pass both event and trigger selections, and using a fitting function (see the following section).
- $N_{K3\pi}$ and $N_{K\pi}$: The number of reconstructed events in data for both decay channels are found from using the fitting function for the signal.
- ratio R: It is measured from the fitted signal yields in data and the efficiencies obtained from the simulated events.

The expected value of R, after determining the $\epsilon_{K3\pi}$ and $\epsilon_{K\pi}$ using MC and the number of reconstructed events $N_{K3\pi}$ and $N_{K\pi}$ in data, is equal to R(PDG). Figure 5.10 shows a schematic plot summarising the flow steps presented in this analysis.

5.5 Results and Conclusion

A new method has been presented to determine the efficiency of reconstructing the pion track in the ATLAS inner detector. It is also used to measure the ratio of BR($D^0 \to K^-2\pi^+\pi^-$) relative to BR($D^0 \to K^-\pi^+$) as well as to estimate the ΔM value in both decay channels ($K3\pi$ and $K\pi$) using data provided by the Inner Detector only. The predicted ratio, R, from the SM is 2.08 ± 0.04 where BR($D^0 \to K^-2\pi^+\pi^-$) and BR($D^0 \to$

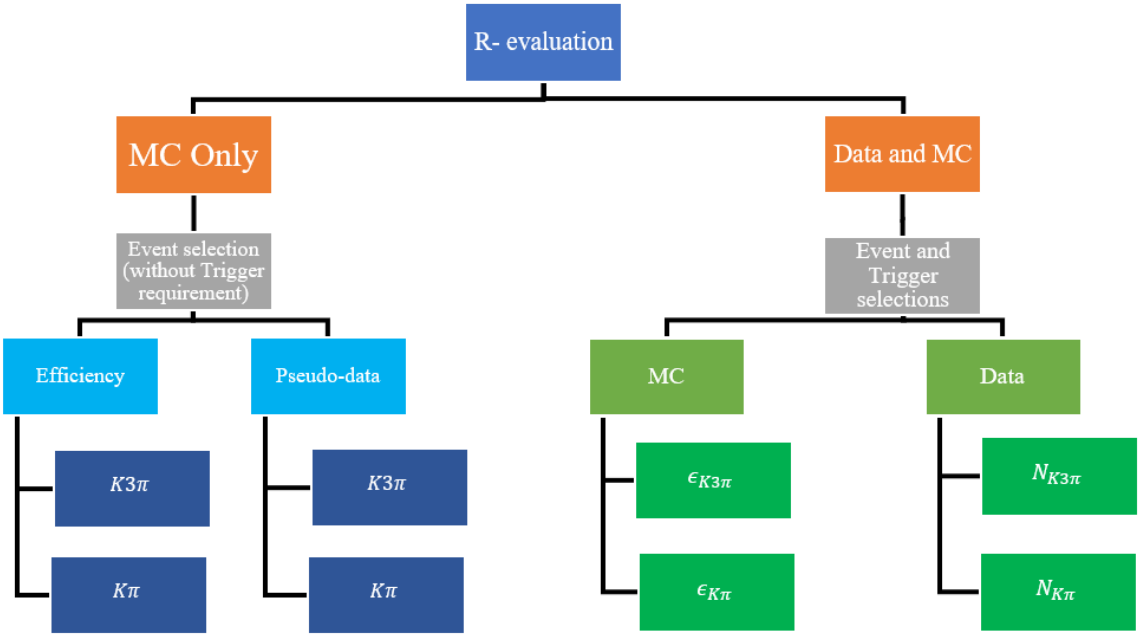

FIGURE 5.10: Schematic plot summarises the analysis steps.

$K^-\pi^+$) are $(8.11 \pm 0.15)\%$ and $(3.89 \pm 0.04)\%$, respectively. A non-resonant peak is predicted to appear around 145.4257 ± 0.0017 MeV.

The number of reconstructed events in both MC and data is determined by fitting the $\Delta M = D^{*-}_{Mass} - D^{0}_{Mass}$ distributions. The non-resonant peak appears around the world average value (PDG). The ΔM distributions are fitted using the sum of the modified Gaussian function, which is describing the signal, and a threshold function to fit the combinatorial background. In the following, the modified Gaussian ($Gauss^{Mode}$) and the threshold function (f^T) are defined:

$$Gauss^{Mode} = P \times \exp\left(-0.5x^n\right) \tag{5.3}$$

$$f^T = A \times (\Delta M - m_{\pi^+})^B \times \exp\left[C \times (\Delta M - m_{\pi^+}) + D \times (\Delta M - m_{\pi^+})^2\right] \tag{5.4}$$

where $n = 1 + \frac{1}{1+0.5x}$, $x = \frac{\Delta M - m_0}{\sigma}$ and $m_{\pi^+} = 139.57$ MeV while P, m_0 and σ are free parameters as well as A, B, C and D.

Initially, R is evaluated using MC samples to test the JpsiUpsilon tool and to check the validity of the defined selections (see Section 5.4). MC samples are split into two parts: the first one is used to measure the efficiency of the reconstructing pion tracks in both

channels, $\epsilon_{K\pi}$ and $\epsilon_{K3\pi}$. The second one is used to determine the number of reconstructed events (Pseudo-data), $N_{K\pi}$ and $N_{K3\pi}$. Using the MC sample only, R is defined as:

$$R = \frac{Numberofgenerated K3\pi}{Numberofgenerated K\pi} = \frac{N^{gen}_{K3\pi}}{N^{gen}_{K\pi}} \tag{5.5}$$

The number of generated events in the $K3\pi$ ($K\pi$) channel is 250500 (1215000). In the case of an equal number of generated events in both channels, R should be equal to one. Therefore, the number of generated $K3\pi$ events is scaled to the number of generated $K\pi$ events to evaluate R using MC samples only. This scale is equal to $N^{gen}_{K\pi}/N^{gen}_{K3\pi}$, which turns out to be 4.58.

The number of events used to measured the $\epsilon_{K3\pi}$ ($\epsilon_{K\pi}$) is 93500 (496000), while the number of events used as pseudo-data in $K3\pi(K\pi)$ is 157000 (719000). From the fit, the measured $\epsilon_{K3\pi}(\epsilon_{K\pi})$, for events passing the requirements in Section 5.3.3 ignoring the trigger selections, is equal to $(0.214\pm0.017)\%$ ($(0.414\pm0.006)\%$). Also, the fit returns the number of reconstructed events using the second part of the MC sample, $N_{K3\pi}$ ($N_{K\pi}$), to be 303 ± 19.5 (2535 ± 43) (see table 5.3).

Four Body Decay ($K3\pi$)	
Efficiency ($\epsilon_{K3\pi}$)	$N^{\epsilon_{K3\pi}}_{Event}$
$(0.214 \pm 0.017)\%$	93500
Pseudo-data	$N^{K3\pi}_{Event}$
313 ± 19.5	157000
Two Body Decay ($K\pi$)	
Efficiency ($\epsilon_{K\pi}$)	$N^{\epsilon_{K\pi}}_{Event}$
$(0.414 \pm 0.006)\%$	496000
Pseudo-data	$N^{K\pi}_{Event}$
2535 ± 43	719000

TABLE 5.3: Summary of the expected efficiencies and the number of reconstructed events obtained from the simulated MC events.

The R factor using MC only is calculated to be:

$$R = \frac{303\times4.58}{2535}\frac{0.414}{0.214} \tag{5.6}$$

$$R = 1.059^{-0.017}_{+0.023} \cong 1.06 \pm 0.03 \tag{5.7}$$

where the included uncertainty is only statistical. Figure 5.11 shows the ΔM distributions for $K\pi$ and $K3\pi$ channels using data collected by the ATLAS experiment at $\sqrt{s} = 13$ TeV in 2018. The fitting function for signal returns the number of reconstructed events in both channels for combinations passing all requirements described in Section 5.3.3. The number of reconstructed events, $N_{K\pi}$ and $N_{K3\pi}$, obtained from the fit of the data are 130±12($stat$) and 26±10($stat$), respectively. The efficiencies, $\epsilon_{K3\pi}$ and $\epsilon_{K\pi}$, obtained from MC are $(0.0347 \pm 0.004(stat))\%$ and $(0.353 \pm 0.005(stat))\%$, respectively (see table 5.4).

Four Body Decay ($K3\pi$)	
Efficiency ($\epsilon_{K3\pi}$)	$N_{Event}^{\epsilon_{K3\pi}}$
$(0.0347 \pm 0.004)\%$	250500
Data	N_{Event}
26 ± 10	$\sim 57M$
Two Body Decay ($K\pi$)	
Efficiency ($\epsilon_{K\pi}$)	$N_{Event}^{\epsilon_{K\pi}}$
$(0.353 \pm 0.005)\%$	1215000
Data	N_{Event}
130 ± 12	$\sim 57M$

TABLE 5.4: Summary of the expected efficiencies from MC samples and the number of reconstructed events in Data sample for both channels (charge conjugate is included in Data).

The R ratio (equation 5.2) is calculated data and MC as following:

$$R = \frac{26}{130}\frac{0.353}{0.0346} \tag{5.8}$$

$$R = 2.04^{+0.31}_{-0.44} \cong 2.04 \pm 0.54 \tag{5.9}$$

Then, the relative efficiency of pion track in data and MC, defined in equation 5.1, is measured to be:

$$\frac{\epsilon(data)}{\epsilon(MC)} = \sqrt{\frac{2.04}{2.08}} \tag{5.10}$$

$$\frac{\epsilon(data)}{\epsilon(MC)} = 0.99 \pm 0.13(stat) \tag{5.11}$$

The relative efficiency for reconstructing pion track at transverse momentum $p_T > 500$ MeV in data and MC is measured to be $0.99 \pm 0.13(stat)$. That means the ID efficiency

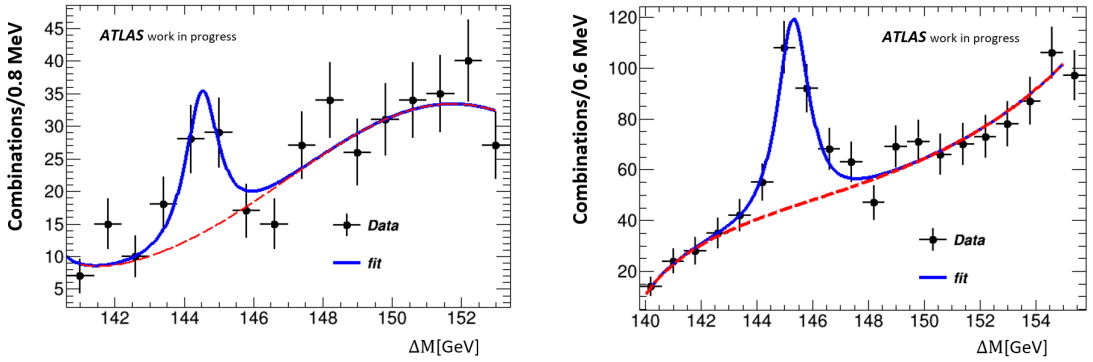

(a) (b)

FIGURE 5.11: Mass difference distributions, $\Delta M = D^{*+}_{Mass} - D^{0}_{Mass}$, for the reconstructed data events in the decay channels $K3\pi$ (a) and $K\pi$ (b). The data is represented by points with error bars (stat). The sold blue line is the resulting fit from the sum of $Gauss^{Mode}$ and f^{T}. The dashed red line is representing the expected wrong charge combination.

of reconstructing the pion track is equal to the predicted one from MC simulation, which is equal to 1.06±0.03 (see equation5.7). The main uncertainty affecting the value of $\epsilon(data)/\epsilon(MC)$ is statistical, in particular, in the case of the $K3\pi$. This is because the number of generated events in $K3\pi$ is small compared to the $K\pi$, and the number of reconstructed events, $N_{K3\pi}$, in data is five times less the amount of $N_{K\pi}$. From the fitting of the data, Figure 5.11, the estimated ΔM in $K\pi$ and $K3\pi$ are 145.57 ± 0.17 MeV and 144.62 ± 0.17 MeV, respectively. From the fitted signal in $K3\pi$, the uncertainty in ΔM is higher than the ones for $K\pi$ because of the number of events which pass the trigger selection is very low (only $\sim 5\%$ of events in the $K3\pi$ MC sample), see table 5.2. Also, the number of MC events in the $K3\pi$ sample is small compared to the $K\pi$ (see table 5.4).

Chapter 6

$t\bar{t}t\bar{t}$ reconstruction based on χ^2–method in 1L and OS dilepton channels

The top quark plays an essential role in the SM and many BSM models, as it is predicted to have a large coupling, besides to the SM Higgs boson, to other BSM particles. As a consequence, through the production of new massive particles in association with top-quark pairs, production cross-sections for specific processes may be significantly enhanced with respect to the SM predictions, in particular for events containing four top quarks (Figure 6.1). Hence, search for the four-top-quark production via the SM processes, allowing the possibility to recast relevant limits within several BSM models such as $t\bar{t}t\bar{t}$ production via the four-top-quark effective field theory model [32], universal extra dimensions scenarios [120] and through the two Higgs-double Model [30].

In the SM, four-top-quark events are produced either by gluon-gluon fusion or quark-antiquark annihilation (see Figure 6.2) with a cross-section, $\sigma^{t\bar{t}t\bar{t}}_{SM}$, of Next-Leading-Order (NLO) accuracy in QCD at a centre-of-mass energy $\sqrt{s} = 13$ TeV as predicted at $\sigma^{t\bar{t}t\bar{t}}_{SM} \approx 12^{+18\%}_{-21\%}$ fb [121].

The four-top-quark process is characterised by several final states depending on the W-boson decays, as shown in Figure 6.3. From Figure 6.3(a), one can see the BRs for all the

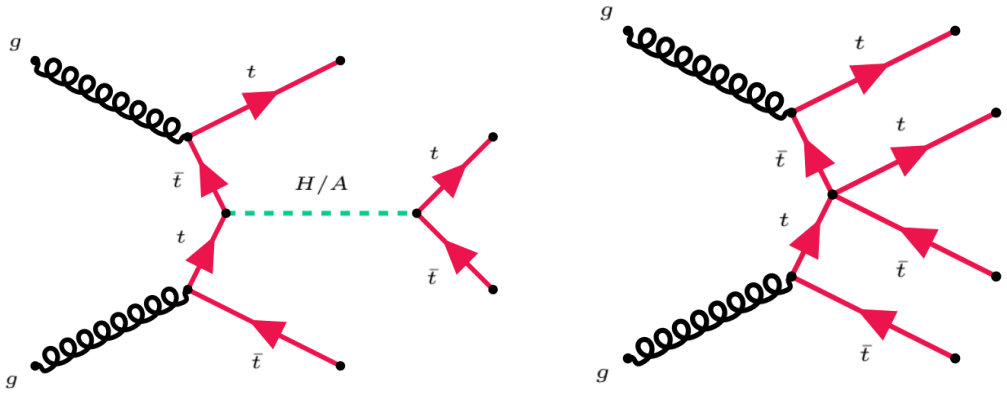

FIGURE 6.1: Representative Feynman diagrams for four-top-quark production through (left) heavy-Higgs-boson production in the two Higgs doublet model (2HDM) [30, 31] and (right) four-fermion contact interaction (CI) [32, 33].

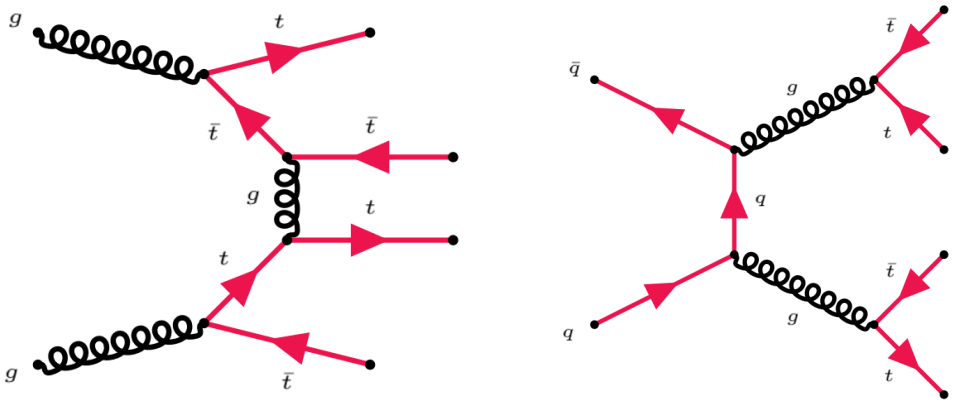

FIGURE 6.2: The SM production of four top quarks through gluon-gluon fusion (left) and quark-antiquark annhilation (right).

final states, where the dominant final state is the single-lepton (lep is either electorn or muon while electrons and muons from tau decay are included in the totals) channel with a branching ratio, BR, of $\sim 42\%$. The other final states are the fully-hadronic channel (fully-had), the opposite- and same-sign dilepton one (OS and SS) and the multilepton one (multi-lep), with BRs of 31%, 21.5% and 5.3%, respectively.

In this chapter, a new method is developed (based on a χ^2 test) to improve the background rejection in the single-lepton (1L) and opposite-sign (OS) dilepton channels using the simulated data generated at $\sqrt{s} = 13$ TeV. This χ^2–method is used to reconstruct hadronically-decaying top-quark from the final-state physics objects such as calorimeter jets. Section 6.3 studies the performance of the method when selecting events where all

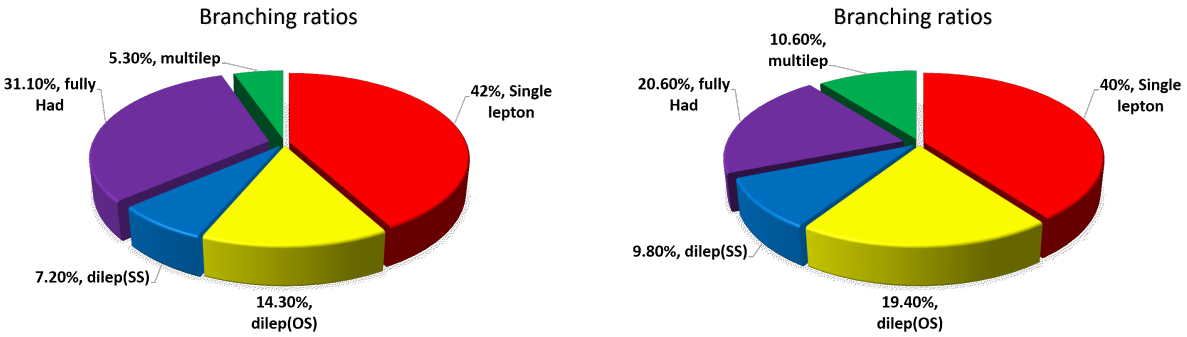

(a) (b)

FIGURE 6.3: The branching ratios of the four-top-quark final state where electrons and muons from tau decay are included in the totals (a) and considering the tau τ as a stable particle (b), respectively.

the physics objects are matched to partons generated by the MC simulation (parton-level), in the 1L channel. In Section 6.4, the algorithm is applied to the 1L and OS channel as well, but no parton-level information is used. A multivariate analysis technique using the boosted decision tree (BDT) algorithm is presented to show the gain of using the output of the χ^2 algorithm as input to the BDT on the discrimination between $t\bar{t}t\bar{t}$ events and those from several backgrounds in the 1L and OS dilepton signal regions, in Section 6.5.

6.1 Analysis Strategy

Previous searches for four-top-quark production using Run 2 data at $\sqrt{s} = 13$ TeV were performed both by the ATLAS [31, 33] and CMS [122, 123] experiments. No significant excess of data above the background expectation was observed. In particular, the observed (expected) upper limit obtained by the ATLAS collaboration on the SM $t\bar{t}t\bar{t}$ production cross-section in the combined single-lepton and opposite-sign dilepton channels, is 5.1 (3.6) times the SM predictions at the 95% confidence level, assuming SM-like event kinematics, see Ref[33].

The search for $t\bar{t}t\bar{t}$ SM production in all decay channels rely on the distinctive high jet and b-tagged jet multiplicity of the signal events with respect to the main backgrounds, as well as on high scalar sum of the jet transverse momenta, referred to as H_{had}^{T}. Additionally, in the 1L and OS channels, collimated hadronically-decaying top-quark candidates can be identified by combining small radius parameter R jets into larger-R jets, referred

to as RCLR jets, which increases the sensitivity to $t\bar{t}t\bar{t}$ signal, see Ref[33]. The signal sensitivity in the 1L and the OS channels is expected to be highly affected by the presence of large backgrounds, in particular from $t\bar{t}$+jet production events. Therefore, particular attention has to be devoted to studying the possibility of designing or improving existing techniques in order to discriminate these backgrounds, such as the χ^2–method described in Section 6.1.1. In particular, in high jets and b-tagged jets multiplicity regions with higher sensitivity to $t\bar{t}t\bar{t}$ signal.

The χ^2–method can be used to reconstruct the hadronically-decaying top-quark in events containing four top quarks to produce a set of variables which might increase the sensitivity to $t\bar{t}t\bar{t}$ signal. This method is applied to $t\bar{t}t\bar{t}$ events in the 1L channel where the physics objects are matched to parton-level objects (see Section 6.3) to study the kinematic distributions of the reconstructed top-quark originated from $t\bar{t}t\bar{t}$. Additionally, it is applied to both $t\bar{t}t\bar{t}$ and $t\bar{t}$+jets events in the 1L and OS dilepton channels without requiring any matching to parton-level objects to produce a set of variables as inputs for a multivariate technique, e.g. BDT (see Section 6.4 and 6.5) in order to increase the discrimination between the background and single events.

6.1.1 χ^2–method

The Chi-Square (χ^2) method is a statistical method used to test a hypothesis. For example, if there are two uncorrelated measurements, $O_1 \pm \sigma_1$ and $O_2 \pm \sigma_2$, e.g. particles masses, cross-sections, etc., and we want to test a hypothesis (model), which predicts these measurements. The χ^2–method can be defined as follows [124]:

$$\chi^2 = \sum_i \frac{(O_i - E_i)^2}{(\sigma_i)^2} \tag{6.1}$$

where, for each measurement i, O_i is the measured (observed) quantity from experimental data, and E_i corresponds to the prediction (hypothesis), e.g. from theory calculations. At the same time, σ_i is the standard deviation of the distribution of the observed quantity. When the observed quantity $O_i \pm \sigma_i$ is closed to the predicted one, the χ^2 value becomes close to zero, and then the observed quantities are well described by the hypothesis.

In this analysis, the observed hypotheses correspond to each jet combination since for each, there are two observed quantities, the invariant masses of the three jets (hadronic top-quark) and the two jets (hadronic W-boson). In contrast, the theoretical hypotheses are the predicted central mass values from the SM (top-quark and W-boson). Still, σ_i^2 are the standard deviations of the invariant mass distributions for the top-quark and W-boson, which can be extracted either from experimental measurements or theoretical prediction. The χ^2–method is then applied to selected events containing jets, leptons and missing transverse energy, to identify combinations of physics objects most likely originating from top-quark decays. Additionally, it is used to test the compatibility of such events with the hypothesis of the presence of more than two top quarks.

$$\chi^2_{Top-leptonic} = \frac{(M_{W\to l\nu}-m_W)^2}{\sigma^2_{W\to l\nu}} + \frac{(M_{t\to lb\nu}-m_{top})^2}{\sigma^2_{t\to lb\nu}} \tag{6.2}$$

$$\chi^2_{Top-hadronic} = \frac{(M_{W\to q\bar{q}}-m_W)^2}{\sigma^2_{W\to q\bar{q}}} + \frac{(M_{t\to q\bar{q}b}-m_{top})^2}{\sigma^2_{t\to q\bar{q}b}} \tag{6.3}$$

where $M_{W\to l\nu}$, $M_{W\to q\bar{q}}$, $M_{t\to l\nu b}$, $M_{W\to q\bar{q}b}$ are the invariant masses of the jet and lepton combinations aimed to reconstruct the leptonically and hadronically decaying W bosons and top quarks, respectively. At the same time, m_{top} and m_W are the masses of top-quark and W-boson predicted by the SM, while $\sigma^2_{top}(\sigma^2_W)$ is the experimental width of the top-quark (W-boson) invariant mass distribution.

Depending on the top-quark decay channel, the full χ^2 can be built by summing the individual χ^2 described in relations 6.2 and 6.3. For example, in the case of the four-top-quark in the 1L channel, there are three hadronically and one leptonically decaying top-quarks, respectively. Therefore, the full χ^2 for the four-top-quark system in the 1L and OS dilepton decay channels can be defined as:

$$\begin{aligned}\chi^2_{full-1L} = (\sum_{i=1}^{3} &\frac{(M_{i,W\to q\bar{q}} - m_W)^2}{\sigma^2_{W\to q\bar{q}}} + \frac{(M_{i,top\to q\bar{q}b} - m_{top})^2}{\sigma^2_{top\to q\bar{q}b}}) \\ &+\frac{(M_{W\to l\nu} - m_W)^2}{\sigma^2_{W\to l\nu}} + \frac{(M_{top\to l\nu b} - m_{top})^2}{\sigma^2_{top\to l\nu b}}\end{aligned} \tag{6.4}$$

$$\chi^2_{full-OS\ dilepton} = (\sum_{i=1}^{2} \frac{(M_{i,W\to q\bar{q}} - m_W)^2}{\sigma^2_{W\to q\bar{q}}} + \frac{(M_{i,top\to q\bar{q}b} - m_{top})^2}{\sigma^2_{top\to q\bar{q}b}}) + (\sum_{j=1}^{2} \frac{(M_{j,\ W\to l\nu} - m_W)^2}{\sigma^2_{W\to l\nu}} + \frac{(M_{j,top\to l\nu b} - m_{top})^2}{\sigma^2_{top\to l\nu b}}) \quad (6.5)$$

In this analysis, the χ^2–method is applied to reconstruct two top quarks decaying hadronically (for reasons described later) in the 1L and OS dilepton channels. However, the χ^2–method is built only relying on fully reconstructed physics objects, in particular jets, without the need to infer on the information from missing energy. The performance of such a partial χ^2 reconstruction is tested in the 1L channel for the SM four-top-quark ($t\bar{t}t\bar{t}$) events with physics objects are fully-matched to those at parton-level (see Section 6.3.2). Then, the χ^2–method is applied using the $t\bar{t}t\bar{t}$ and total background (mainly $t\bar{t}$+jets) events in the 1L and OS dilepton channels to estimate the separation between the background and signal using different kinematic distributions (Section 6.4). The kinematic parameters produced by χ^2–method is used as input for multivariate analysis (Section 6.5) to discriminate the signal $t\bar{t}t\bar{t}$ events from total background ones in 1L and OS dilepton channels, respectively.

6.2 Physics Objects and Event Selection

6.2.1 Physics Objects

The physics objects used in the χ^2–method and considered in the event selection are jets originated from b-quarks, c-quarks as well as light-quarks. Furthermore, the presence of one or two leptons (electrons and muons) to identify the studied channel, as well as the missing transverse energy (E_T^{miss}), are considered here. In contrast, the leptonically-decaying channel $\tau(\tau \to e\upsilon_e\upsilon_\tau\ or\ \tau \to \mu\upsilon_\mu\upsilon_\tau\ )$ contribute similarly to the other charged leptons, while no attempt to explicitly reconstruct hadronic τ decays is made.

In this analysis, the considered jet candidates are reconstructed and calibrated based on the methods, which are presented in Section 4.3. The anti-kT algorithm is used to reconstruct the jet candidates with $\Delta R = 0.4$, and they must have passed the JetVertexTagger (JVT) selection (Section 4.3). After the energy calibration, jets with transverse momenta

$p_T > 25$ GeV and $|\eta| < 2.5$ are considered. Additionally, a multivariate technique based on the MV2c10 algorithm with the working point referred to as MV2c10_77, which corresponds to an efficiency of tagging b-jets (ϵ_b) of 77%, is used to identify jets initiated from b-quarks (Section 4.3).

Electron and muon candidates are reconstructed and isolated based on methods presented in Section 4.1 and Section 4.2, respectively. The identification criteria applied to electron candidates is the Tight (TightLH) identification criteria with the so-called FixedCutTight (FCTight) isolation working point. Furthermore, electrons are required to have $p_T > 28$ GeV ($p_T > 10$ GeV) in the 1L (OS dilepton) channel and to be in the active region with $|\eta| < 2.5$ while those in the so-called LAr crack region with $1.37 < |\eta| < 1.52$ are rejected to reduce the non-prompt and fake contributions. On the other hand, muon candidates are reconstructed based on the combined method (Section 4.2), and to pass the Medium identification criteria selection. At the same time they are required to have $p_T > 28$ and $p_T > 10$ GeV in the 1L and OS dilepton, respectively, and to be in the region $|\eta| < 2.5$. Also, muons are required to pass the so-called FixedCutTightTrackOnly isolation working point, which is based only on the track information and very efficient at high p_T. In table 6.1, a summary of the object requirements is presented.

6.2.2 Event Selection

The simulated MC events used in this study, are required to pass a set of selection requirements based on the physics objects (discussed in Section 6.2.1) and trigger selections, see table 6.2. Here, the trigger selection corresponds to the dataset collected by the ATLAS experiment in the period 2015-2018 at $\sqrt{s} = 13$ TeV where events should fire single electron or muon triggers with thresholds defined for the period of the collected dataset.

Events in the 1L channel are retained if they have one lepton (electron or muon) with at least ten jets, of which at least four are b-tagged jets. On the other hand, events containing two leptons with an opposite electrical charge and have at least eight jets, of which at least four are b-tagged, are considered in the OS dilepton channel. To reduce the background contributions, e.g. multijet production, in the single lepton channel, additional selections are applied. These are: 1- the E_T^{miss} to be larger than 20 GeV and

	Electrons	Muons	Jets	b-jets
p_T(GeV)	> 10 (OS dilepton) or > 28 (1L)	> 10 (OS dilepton) or > 28 (1L)	> 25	> 25
$\|\eta\|$	< 1.37 or $1.52 - 2.47$	< 2.5	< 2.5	< 2.5
ID quality	TightLH	Medium	Cleaning+JVT	MV2c10 77%
Isolation	FCTight	FixedCutTightTrackOnly		
Track Vertex:				
$-\|d_0/\sigma_{d_0}\|$	< 5	< 3		
$-\|z_0 sin(\theta)\|$mm	< 0.5	< 0.5		

TABLE 6.1: Summary of the requirements applied to various physics objects

Year of Data taking	Electron Triggers	Muon Triggers
2015	e24_lhmedium_L1EM20VH e60_lhmedium e120_lhloose	mu20_iloose_L1MU15 mu50
2016,2017 and 2018	e26_lhtight_nod0_ivarloose e60_lhmedium_nod0 e140_lhloose_nod0	mu26_ivarmedium mu50

TABLE 6.2: List of a single electron and muon triggers used per data period.

2- the transverse mass (m_T^W) for the combined lepton with the E_T^{miss} to be larger than 60 GeV. In the case of OS dilepton, another cut is required on the invariant mass of the same flavour leptons (m_{ll}) to be outside the mass range for the Z-boson, to suppress the background coming from the Drell-Yan processes. Table 6.3 summarises all selection requirements applied to both channels. In this analysis, two signal regions are built upon on the described selections and used to reconstruct the χ^2 output variables. The first one referred to as SR1L, is in the 1L channel and requiring ≥ 10 jet and ≥ 4 b-tag. On the other hand, events in the OS dilepton channel and with ≥ 8 jet and ≥ 4 b-tag, are considered in the signal region, SROS.

Requirement	Single-lepton	Dilepton
Trigger	Single-lepton triggers	
Leptons	one	two OS
Jets	≥ 10	≥ 8
b-jets	≥ 4	
Other	$E_T^{miss} > 20$ GeV	$m_{ll} > 50$ GeV
	$E_T^{miss} + m_T^W > 60$ GeV	$\lvert m_{ll} - 90GeV \rvert > 10$ GeV

TABLE 6.3: Summary of the event selection requirements.

6.3 The χ^2–method for matched events in 1L Channel

Richard Feynman has proposed the parton model to analyse and describe particle interactions at high energies before the discovery of quarks and gluons. In High Energy Particle

physics, the term parton-level refers to the theoretical predictions for gluons and quarks that are produced from collisions at high centre-of-mass energy and can be modelled using several Monte Carlo generators (e.g. PYTHIA8, SHERPA, aMC@NLO), as shown in Figure 6.4. In this section, χ^2–method is used to reconstruct the hadronically-decaying top-quark in events contain $t\bar{t}t\bar{t}$ where the physics objects (particles at detector-level and also known as Reco-level) are fully-matched to those at parton-level. This is important to compare the kinematic distributions for jet combinations corresponding to top-quark products with other combinations. Furthermore, the χ^2 output variables can be used as input for more advanced methods.

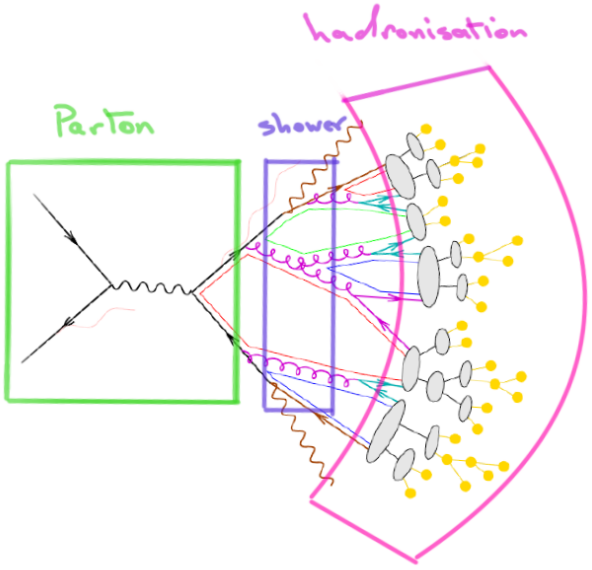

FIGURE 6.4: Signal event generated using an MC generator. The green box is the parton-level (quark or gluon). The violet box is parton-level after showering using different approaches, e.g. PYTHIA8. The purple box is the final state particles produced after the hadronization process for partons.

A Leading-Order (LO) $t\bar{t}t\bar{t}$ samples were generated using MADGRAPH5_aMC@NLO [125] v2.2.2 generator with the PDF set NNPDF2.3LO. The events were interfaced with PYTHIA8.186 [126] using the A14 tune and the NNPDF2.3LO PDF set. The total number of generated $t\bar{t}t\bar{t}$ events used to match the physics objects (jets and leptons) to the parton-level, is 600000. At the beginning, the branching ratio for each decay channel of the four-top-quark production using the LO sample is computed to check the validity of the simulation by comparing it to the SM prediction, as shown on Figure 6.5, to be compared to the expected shown on Figure 6.3(b). The computation is done by counting

the number of events for each decay channel and divided by the total number of events generated in the LO $t\bar{t}t\bar{t}$ sample.

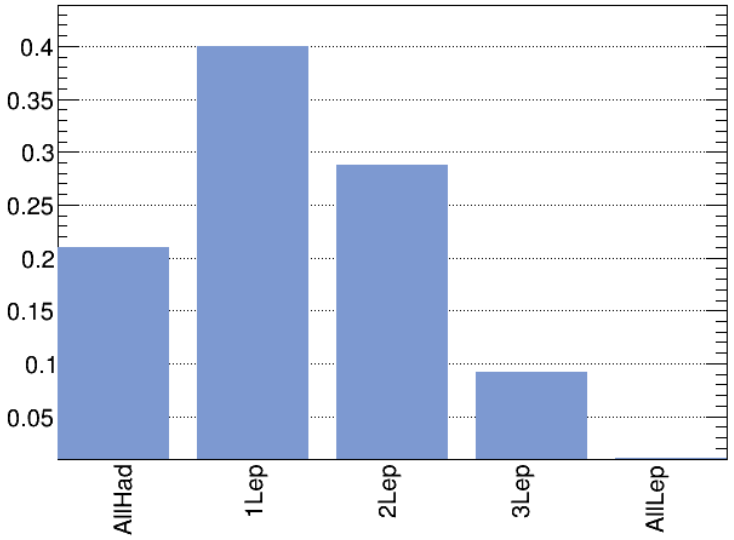

FIGURE 6.5: The branching ratios for several decay channels measured using LO $t\bar{t}t\bar{t}$ sample produced for the period between 2015-2018 (lep is either electron (e) or muon (μ) or tau (τ), which means the τ is considered as a stable particle).

6.3.1 Matching Criteria

Matching criteria are methods used to match the physics objects after detector simulation, which are jets, electrons and muons, to the objects at parton-level. In order to match the physics objects after detector simulation and to find the fraction of the physics objects that are indeed coming from the process of interest ($t\bar{t}t\bar{t}$) in the 1L channel, the χ^2–method is used.

Due to the radiation that is coming from partons and leptons, other physical objects (in particular for jets) may be removed or added, to the final state of $t\bar{t}t\bar{t}$ events and effecting the matching process. Therefore, a selection is applied on the angular distance ($\Delta R = \sqrt{(\Delta\eta)^2 + (\Delta\phi)^2}$, see equation 3.4) between jets and the final state partons to be less than 0.3. On the other hand, for the isolated leptons (electron and muon), the ΔR between lepton and the truth one is required to be less than 0.01.

Figure 6.6 shows the fraction of events for several matching categories in 1L decay channel in the region SR1L. From this figure, one can see that all events have 100% matched lepton

(electron or muon) while $\sim$ 54% of events have all b-tagged jets matched to the finial state b-quark. On the other hand, only $\sim$ 6% of events have ten jets matched to the parton-level jets (all matching categories are illustrated in table 6.4).

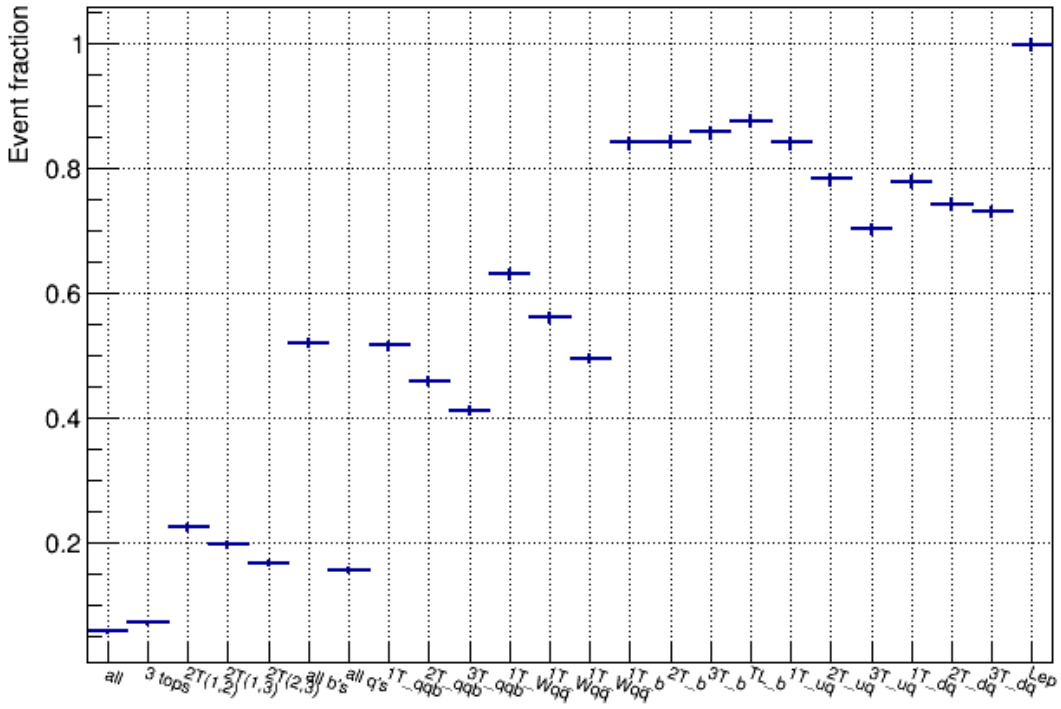

FIGURE 6.6: The Event fraction for each matching criteria. The first bin (right) is the fraction of event that have matched lepton (electron or muon) while the last bin (left) is the event fraction for events having all 10 jets matched to 10 partons.

6.3.2 χ^2–method applied using Fully–matched physics objects

The fully-matched (see Figure 6.7 and table 6.4) $t\bar{t}t\bar{t}$ events, $\sim$ 700, in the 1L signal SR1L region are used as input to the χ^2–method to reconstruct two top quarks decaying hadronically. The jet combinations referred to as the correct jet permutations, which give the minimum χ^2 value (χ^2_{min}), will be the most probable to come from the top-quark decay. In each fully-matched event, specific jets are assigned to specific top quarks: for example, jet_1, jet_8, b_3 could be assigned to Top_1 while jet_9, jet_3, b_1 to Top_3. Furthermore, they can be used as input for more advanced methods, e.g. NeuroBayes method [127] (not presented in this analysis).

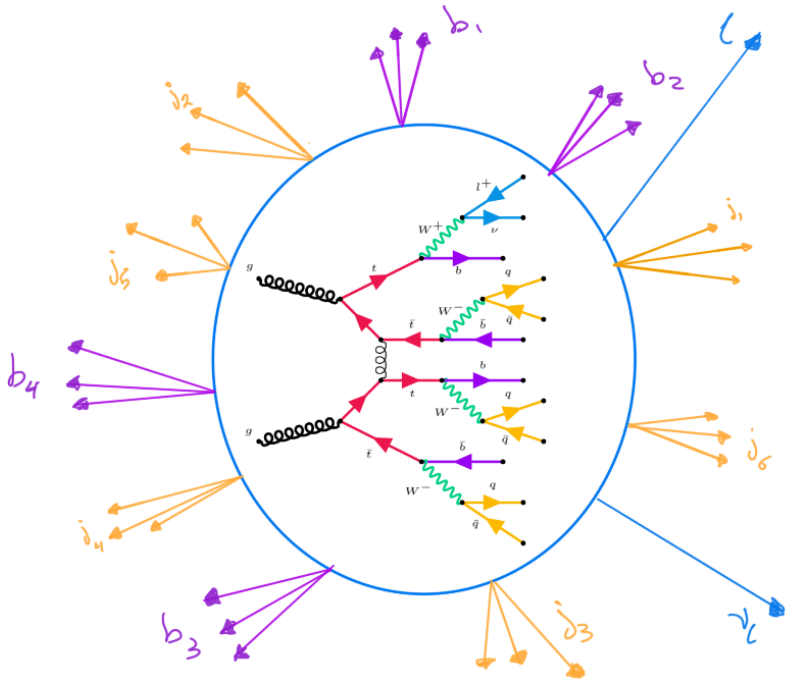

FIGURE 6.7: Schematic plot for matching physics objects to those at parton-level.

The idea behind reconstructing only two hadronic top quarks is that the number of hadronically-decaying top-quark in the $t\bar{t}t\bar{t}$ events in the 1L and OS dilepton channels is three and two, respectively. In contrast, the expected number of hadronically-decaying top-quarks in the $t\bar{t}$+jets events in the two channels is one and zero, respectively, as shown in Figure 6.8 and Figure 6.9 (See Appendix C for other reasons).

Bin Name	Bin Number	Definition
all	1	10 selected jets are uniquely matched to 10 paratons.
3tops	2	9 selected jets are uniquely matched to 9 partons, which came from 3 tops decay hadronicllly.
2T(1,2) & 2T(1,3) & 2T(2,3)	3,4,5	6 selected jets from two tops (2T(1,2) means the fist and second tops) decaying hadronically are uniquely matched to 6 partons.
all b's	6	4 selected b-jets are uniquely matched to 4 b-quarks.
all q's	7	6 selected light-jets (W-boson decay) are uniquely matched to 6 quarks.
(1,2,3)T_qqb	8,9,10	3 jets (two light-jets and one b-tagged) are uniquely matched to the first or the second or the third (top_1 or top_2 or top_3) hadronically-decaying top-quark.
(1,2,3)T_Wqq	11,12,13	2 jets are uniquely matched to the W-boson produced in the decay chain of the first or the second or the third hadronic (top_1 or top_2 or top_3) top-quark.
T_b	14,15,16,17	b-tagged jet is uniquely matched to the one hadronic top-quark(top_1 or top_2 or top_3), and to the leptonic top-quark (top_L).
T_uq	18, 19, 20	one light-jet is matched to u-quark from one of W-boson produced in decay chain of one hadronic Top-quark(top_1 or top_2 or top_3).
T_uq	21, 22, 23	one light-jet is matched to d-quark from one of W-boson produced in decay chain of one hadronic Top-quark(top_1 or top_2 or top_3).
Lep	24	Lepton (e or μ) is matched to the truth-lepton which came from the leptonic decay of W-boson.

TABLE 6.4: Summary of all possible matching criteria.

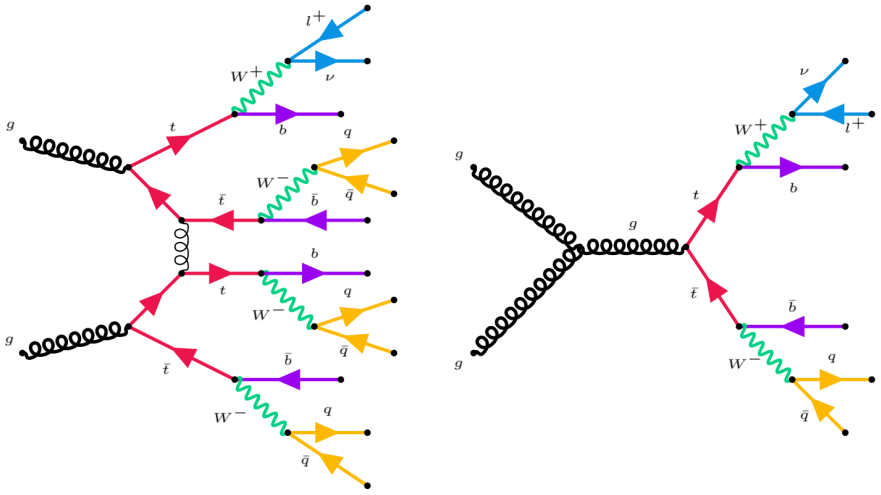

FIGURE 6.8: Feynman diagram for the SM four-top-quark (left) and top-antitop (right) productions, respectively, and decaying in the 1L channel.

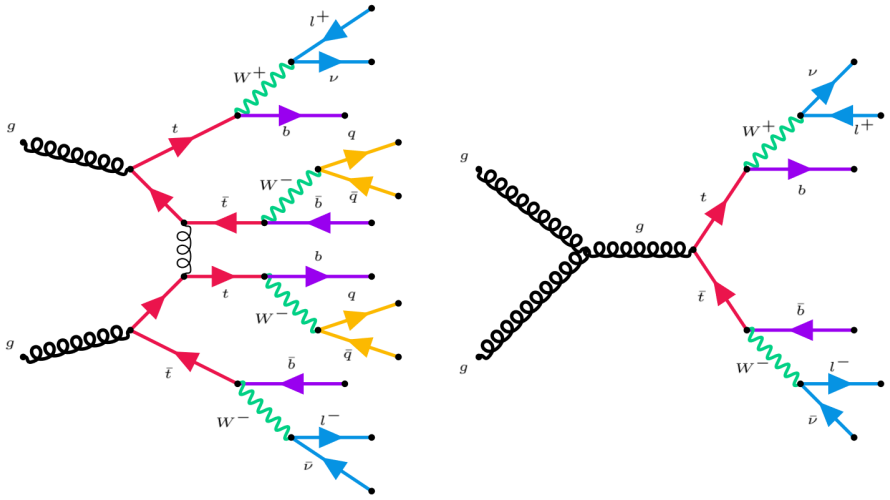

FIGURE 6.9: Feynman diagram for the SM four-top-quark (left) and top-antitop (right) productions, respectively, and decaying in OS dilepton channel.

The χ^2 for two hadronic top quarks in the 1L channel can be derived from relation 6.4 where the leptonic part is set to zero. Then, the $\chi^2_{top-had}$ becomes:

$$\chi^2_{top-had} = \sum_{i=1}^{2} \frac{(M_{i,W\to q\bar{q}} - m_w)^2}{\sigma^2_{W\to q\bar{q}}} + \frac{(M_{i,top\to q\bar{q}b} - m_{top})^2}{\sigma^2_{top\to q\bar{q}b}} \tag{6.6}$$

where $M_{1,2top\to q\bar{q}b}(M_{1,2W\to q\bar{q}})$ is the reconstructed top-quark (W-boson) obtained from the correct jet permutations with minimum $\chi^2_{top-had}$ value. In the same time, $m_{top}(m_W)$ is the theoretical prediction for the top (W-boson) mass, equal to 172.5 GeV (80.1 GeV), while $\sigma_{top}(\sigma_W)$ is the experimental decay width for the hadronically-decaying top-quark (W-boson), equal to 13.4 GeV (7.40 GeV) [128]. The efficiency of such χ^2–method (ϵ_{χ^2})

is defined as:

$$\epsilon_{\chi^2} = \frac{N^{\text{Correct permutation}}_{at\chi^2_{min}}}{N_{\text{Fully-matched}}} \tag{6.7}$$

This efficiency corresponds then to the fraction of fully matched events where the method was able to correctly assign reconstructed jets to two of the hadronically decaying top quarks. On the available simulated $t\bar{t}t\bar{t}$ sample ($\sim$ 700 fully matched events) it is evaluated to be 32%. From this result, one can conclude that the χ^2 is not necessarily the most powerful method to assign the correct jets permutation to one of the top quarks in $t\bar{t}t\bar{t}$ production, see Ref[129] for other techniques. However, kinematic variables of the reconstructed top quarks and W bosons, as well as the χ^2 output value itself can provide useful input information for further steps of the analysis, such as a multi-variate discriminant, as shown in Section 6.5.

Figure 6.10 shows the reconstructed mass and transverse momentum distributions for the two top quarks (Top_1^{Had}, Top_2^{Had}) using the correct jet permutations, which gave minimum χ^2 value, compared with other permutations (incorrect permutations). Additionally, Figure 6.11 shows the expected distributions for the reconstructed W-bosons produced in the decay chain of top-quark with correct jet permutations versus other permutations (see Section 6.5 for the Separation definition that used and implemented in this analysis). The $\chi^2_{min}(\exp^{-\chi^2_{min}})$ distribution for the correct jet permutations, which are assigned to two hadronically-decaying top-quark, compared with different permutations, is shown in Figure 6.12.

Figure 6.10 and Figure 6.11 show that the reconstructed mass is in agreement with the SM predictions as well as the experimentally measured. Furthermore, a new variable is defined $\exp[^{-\chi^2_{min}}]$. The jet permutation is considered as a correct permutation and likely to be initiated from the four-top-quark production if $\exp[^{-\chi^2_{min}}]$ ($\chi^2 \to 0$) minimum value is close to unity.

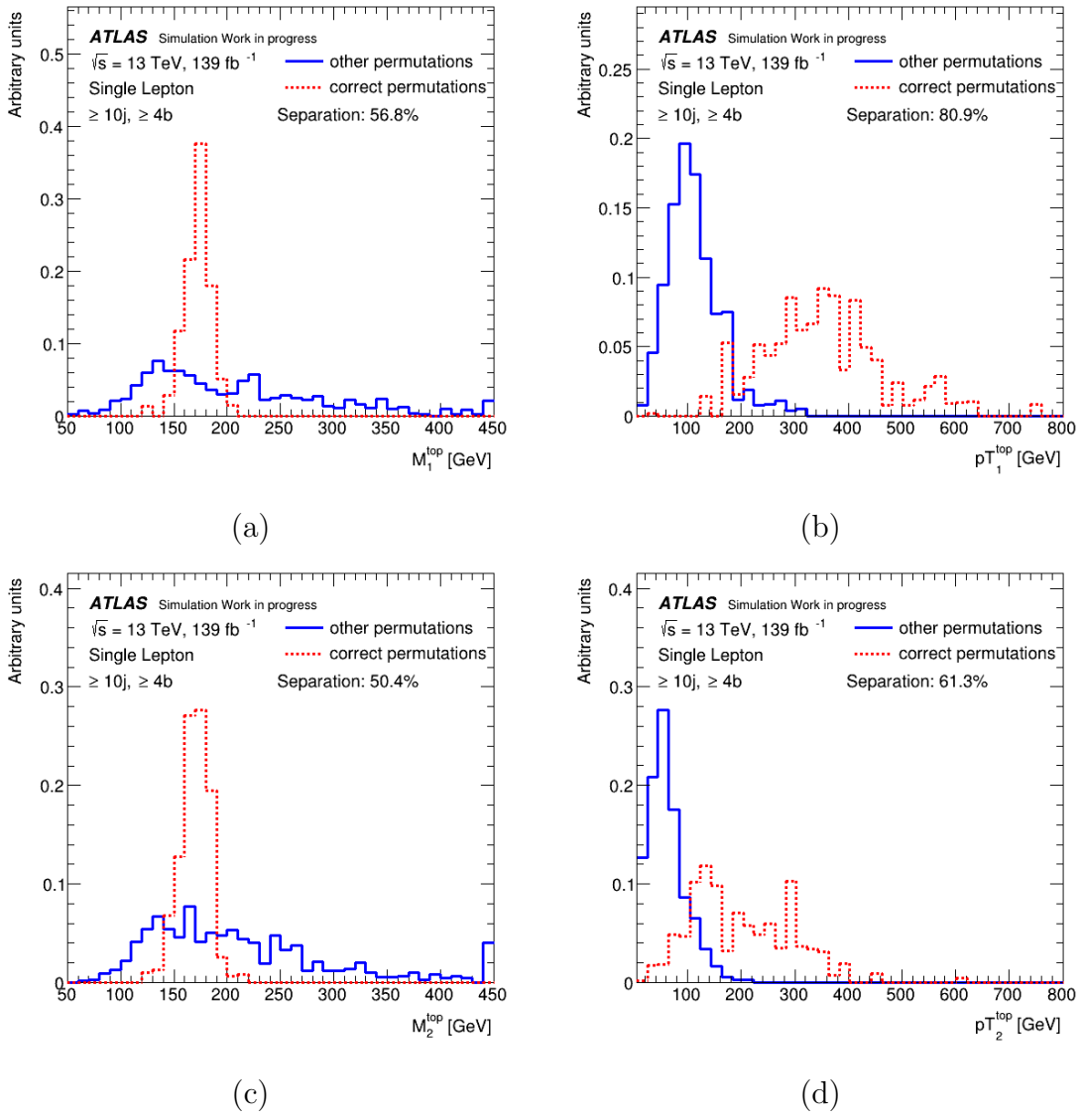

FIGURE 6.10: The invariant mass and p_T distributions for the reconstructed two hadronically-decaying top-quark, M_1^{top} and pT_1^{top} (a,b) and M_2^{top} and pT_2^{top} (c,d) using the correct (red) and other jet permutations (blue), respectively, for fully-matched events.

6.4 χ^2–method study in 1L and OS dilepton channels

Events in the defined signal regions, SR1L and SROS, are used to reconstruct two hadronically-decaying top-quark regardless the patron-level information (it means that all events in the signal regions are used regardless if they are matched or not to those at parton-level). Figure 6.13 shows the reconstructed mass and transverse momentum distributions for two top quarks (Top_1^{Had}, Top_2^{Had}) in the signal regions for 1L and OS dilepton, respectively. The distributions of the invariant mass and the p_T of each of the

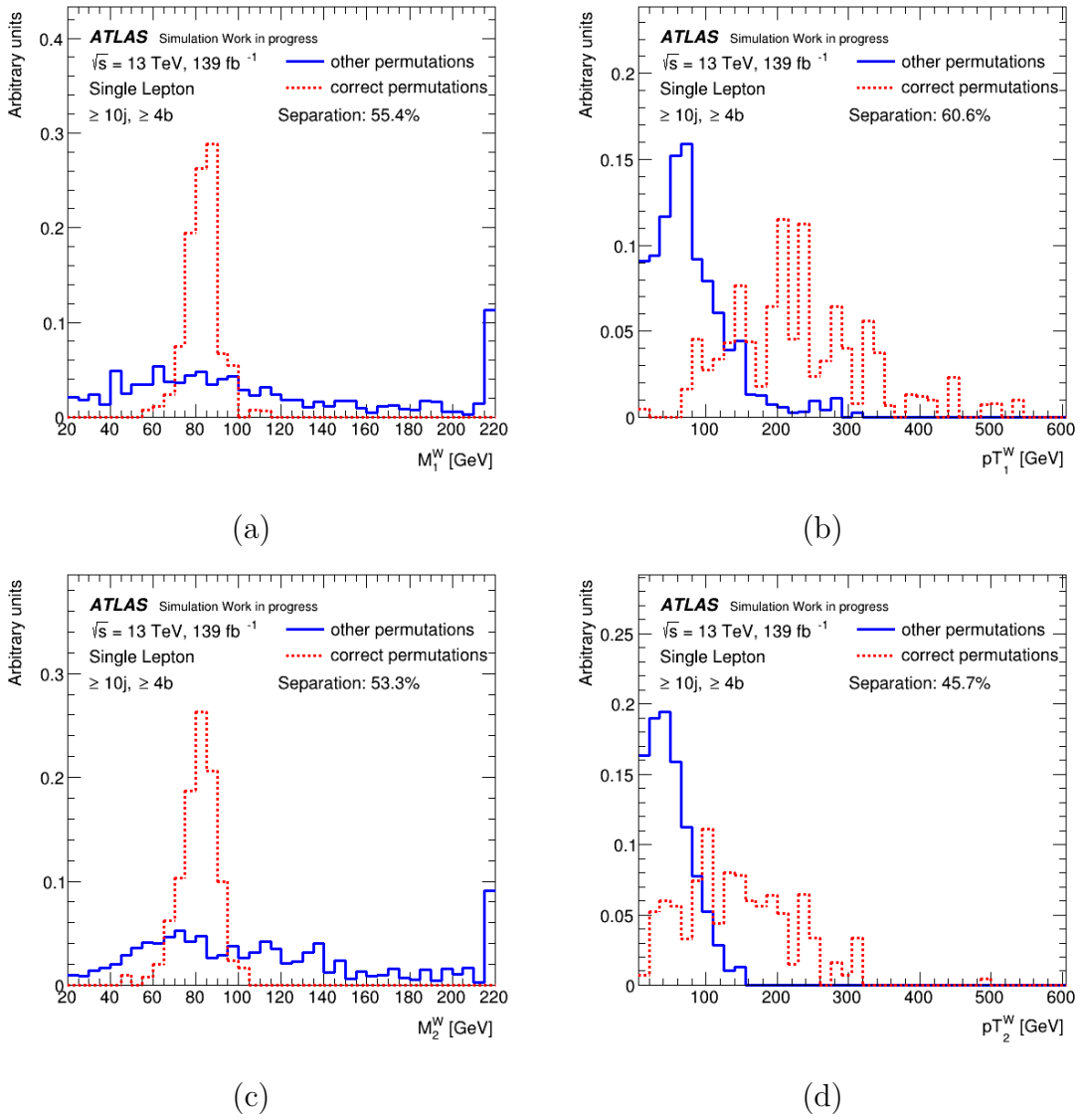

FIGURE 6.11: The invariant mass and p_T distributions for the reconstructed two hadronically-decaying W-boson in the chain of top-quark decay, M_1^W and pT_1^W (a,b) and M_2^W and pT_2^W (c,d) using the correct (red) and other jet permutations (blue), respectively, for fully-matched events.

two reconstructed hadronically-decaying top-quark, built with the jet permutation giving the minimum χ^2 value in $t\bar{t}t\bar{t}$ events, are compared with the same distributions obtained in the same way, but on simulated background events from $t\bar{t}$+jets production plus the other, smaller backgrounds. The kinematic distributions for the reconstructed W-bosons using the jet permutations with minimum χ^2 value in 1L and OS channels as well as the χ^2_{min} and $e^{-\chi^2_{min}}$ distribution for these permutations, are shown in Figure 6.14 and Figure 6.15, respectively.

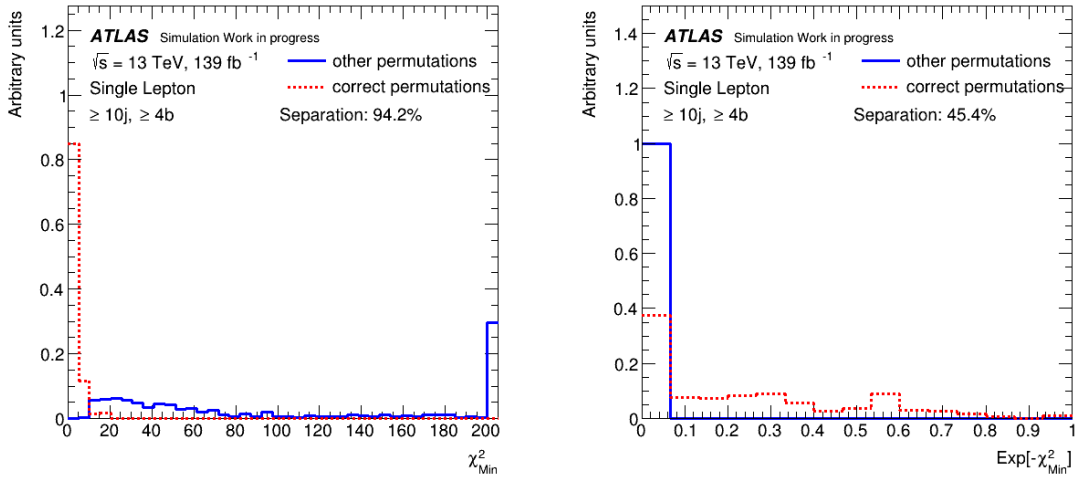

(a) (b)

FIGURE 6.12: χ^2_{min} (a) and exp[$-\chi^2_{min}$] (b) distributions for the correct jet permutations (red) compared to incorrect jet permutations (blue).

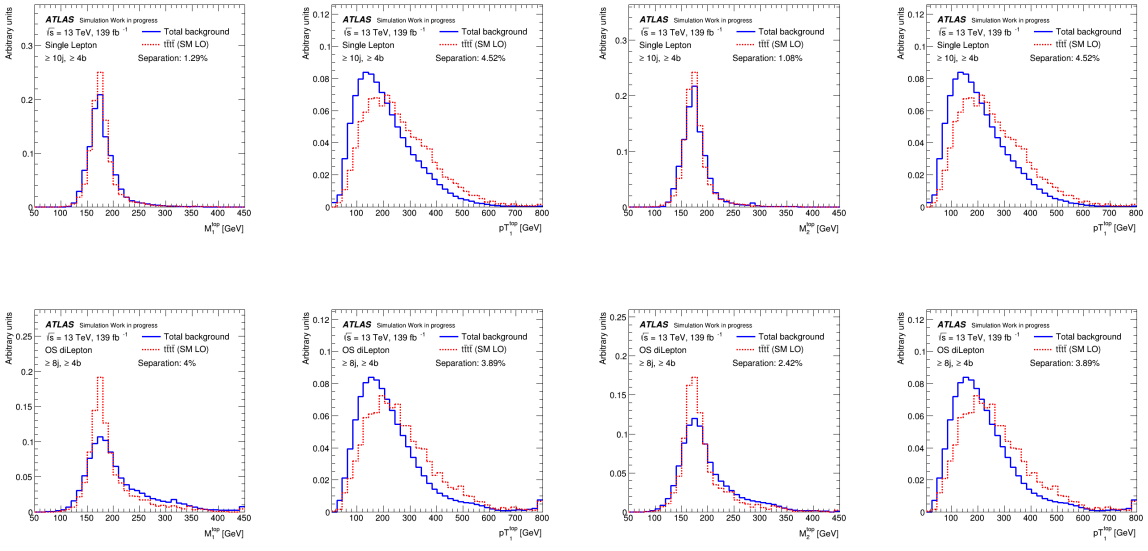

FIGURE 6.13: The invariant mass and p_T distributions for the reconstructed two hadronically-decaying top-quark for jet permutations with χ^2_{min} in the defined signal region for 1L (top) and OS dilepton (bottom) channels, respectively, using $t\bar{t}t\bar{t}$ (red) and $t\bar{t}$+jets (blue) events.

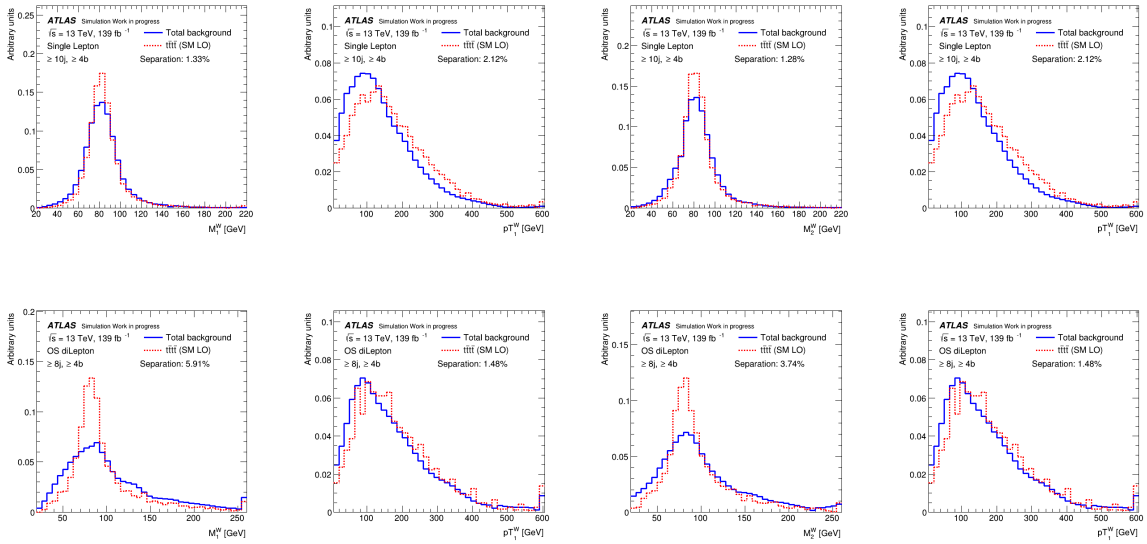

FIGURE 6.14: The invariant mass and p_T distributions for the reconstructed two hadronically-decaying W-boson using the jet permutations with χ^2_{min} in the defined signal region of 1L (top) and OS dilepton channels (bottom), respectively, using $t\bar{t}t\bar{t}$ (red) and $t\bar{t}$+jets (blue) events.

The p_T for each jet (in total six jets) used to reconstruct the hadronically-decaying top-quark and W-boson in the 1L and OS dilepton channels are shown in Figure 6.16 and Figure 6.17, respectively. Finally, the expected distributions of the number of jets, b-tagged jets and the H_T^{Had} for events in the defined signal regions for 1L and OS dilepton are shown in Figure 6.18.

As seen in Figure 6.13 (Figure 6.14), the invariant mass obtained from the jet permutations with minimum χ^2, are centred around the input mass value for top quark (W-boson) decaying hadronically. It can be noticed that the reconstructed top-quark candidates are produced with energy slightly higher than those from the background. Moreover, jets that entering the minimum-χ^2 permutations are in general only slightly harder for signal than for background.

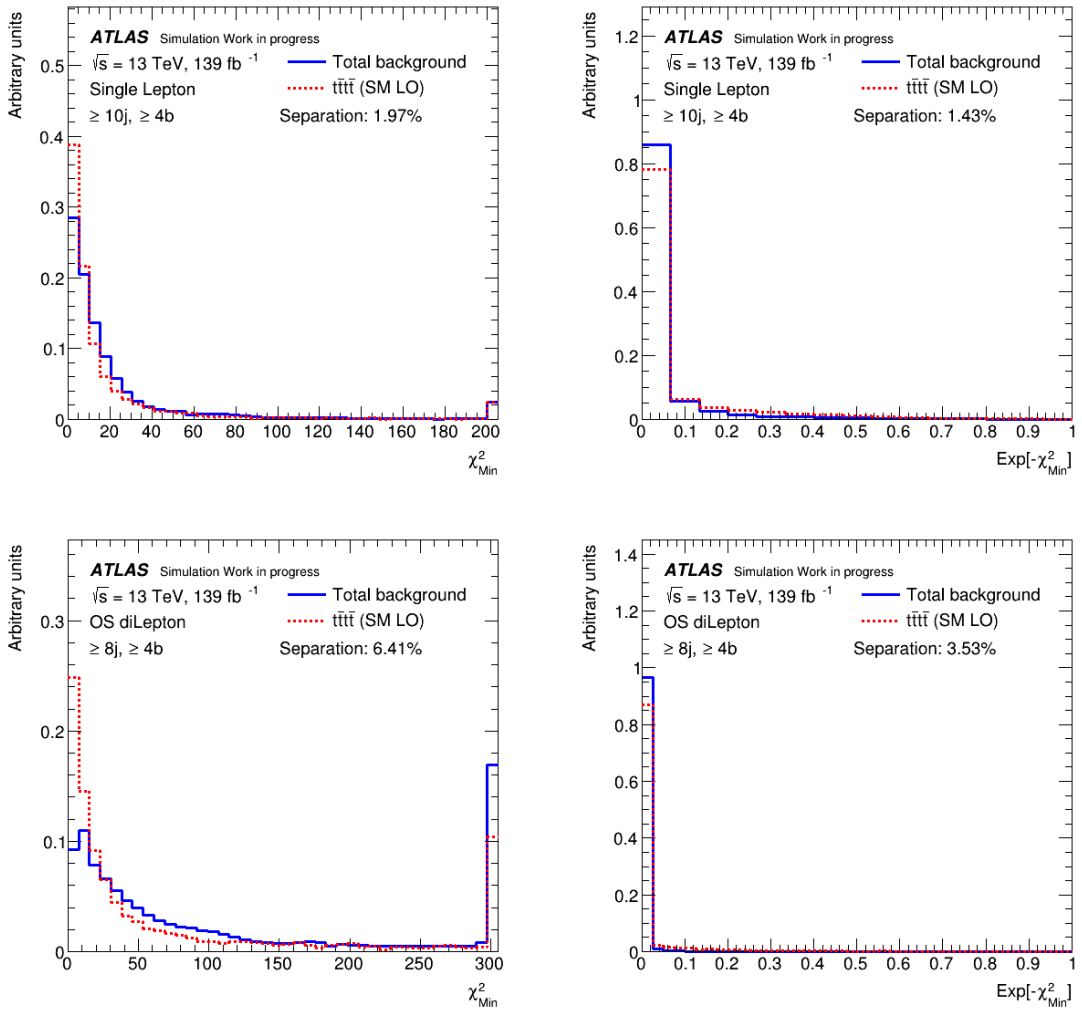

FIGURE 6.15: The χ^2_{min} (exp[$-\chi^2_{min}$]) distributions for the jet permutations minimized the χ^2 value in the defined signal region of 1L (top) and OS dilepton channels (bottom), respectively, using $t\bar{t}t\bar{t}$ (red) and $t\bar{t}$+jets (blue) events.

6.5 MVA Training using Boosted Tree Decision (BDT)

Multivariate analysis (MVA) techniques, based on different algorithms, are often used in particle physics to combine several input variables into a single output variable, retaining as much as possible the input variable signal-versus-background discrimination power [130, 131]. In this analysis for events regardless if they are matched or not to those at parton-level, the kinematics variables obtained from the jet permutations with a minimum value of χ^2, e.g., the reconstructed top-quarks and W-bosons kinematics, are used as input variables, and they are referred to as χ^2 output variables (see table 6.5). Here a boosted decision tree (BDT) [130, 131] algorithm is used to discriminate the signal ($t\bar{t}t\bar{t}$)

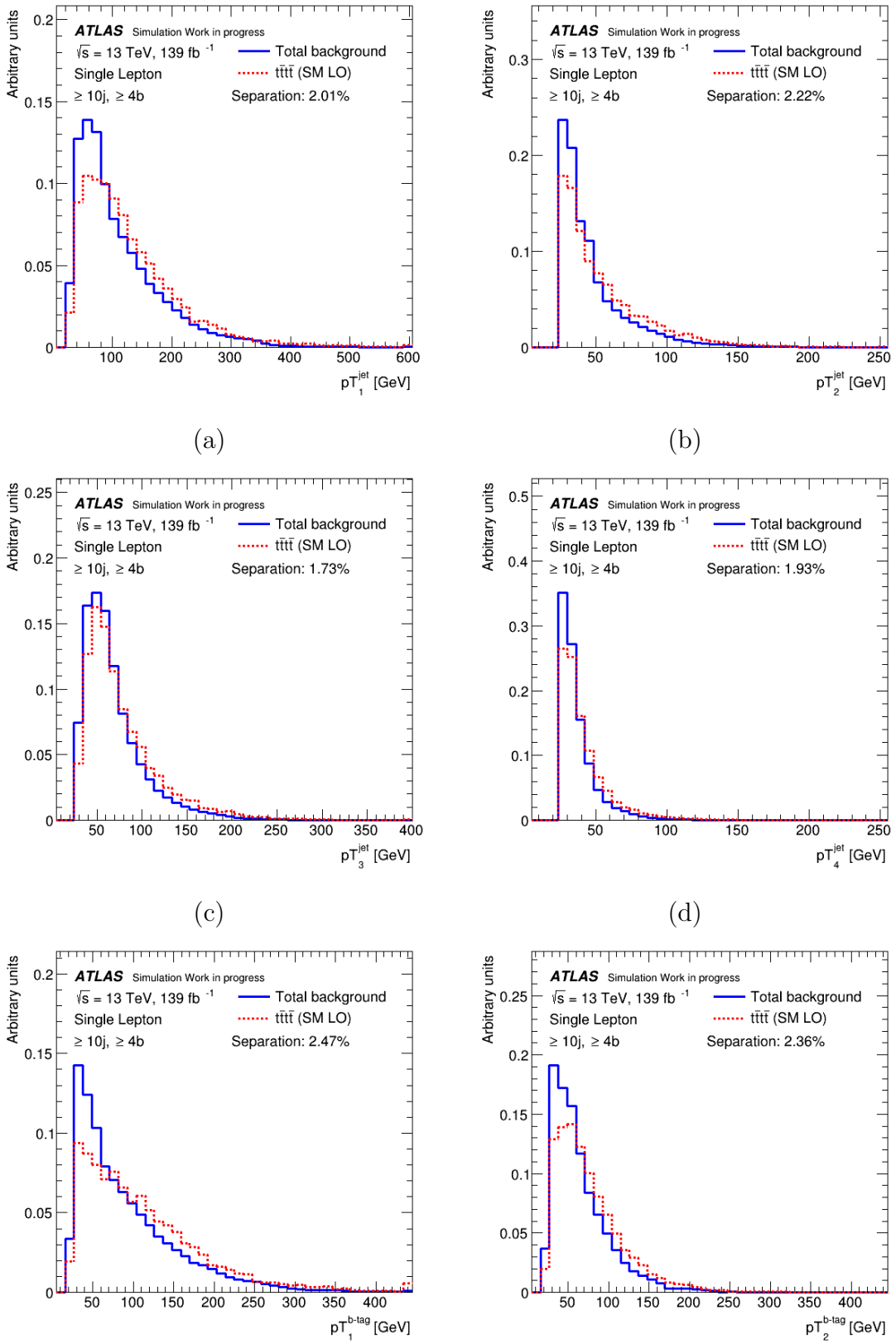

FIGURE 6.16: Expected p_T distributions for each jet (a-d) and b-tagged jet (e,f) considered in the jet permutations with χ^2_{min} value in the signal region of the 1L channel using $t\bar{t}t\bar{t}$ (red) and $t\bar{t}$+jets (blue) events.

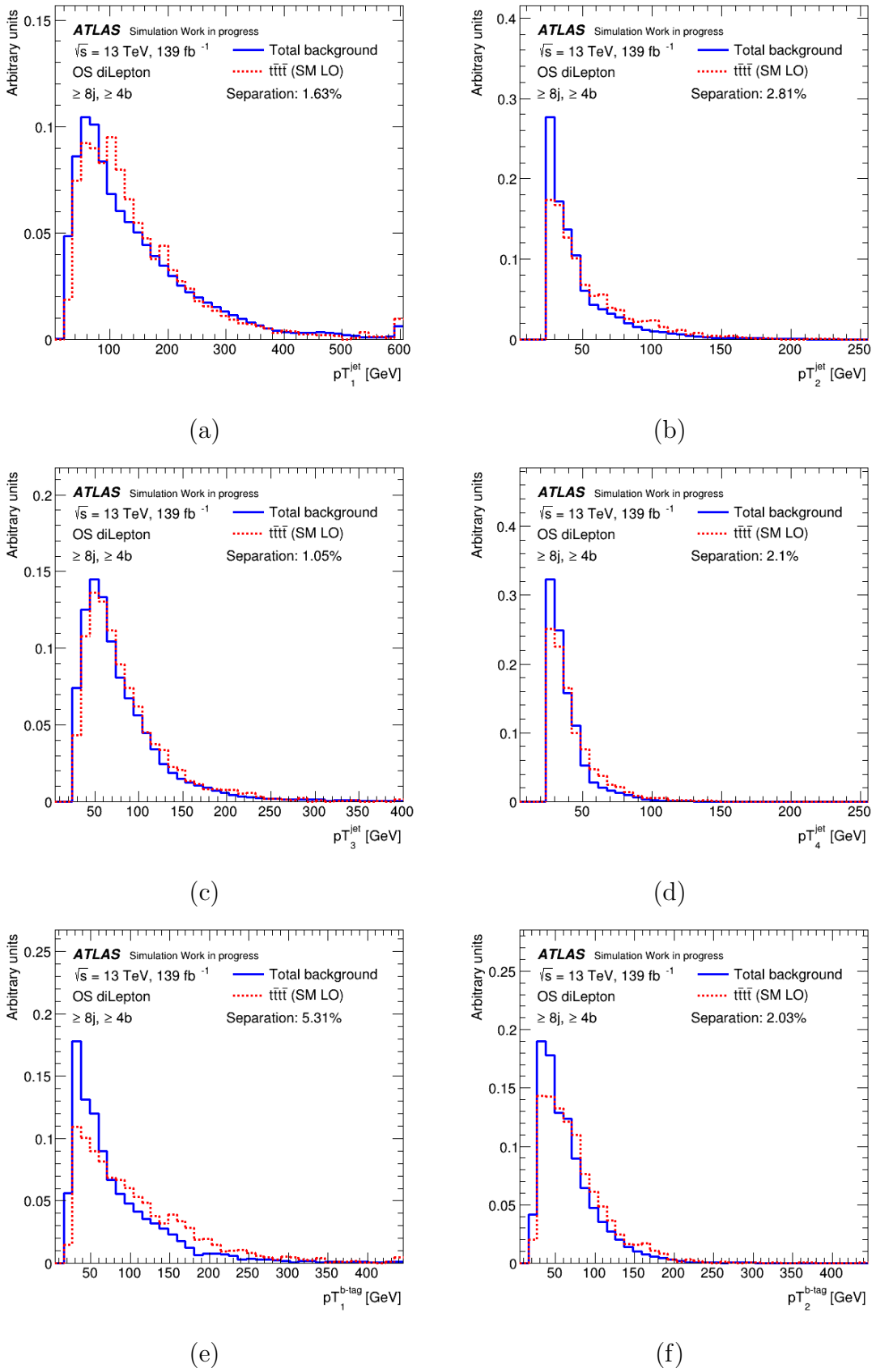

FIGURE 6.17: Expected p_T distributions for each jet (a-d) and b-tagged jet (e,f) considered in the jet permutations with χ^2_{min} value in the signal region of the OS dilepton channel using $t\bar{t}t\bar{t}$ (red) and $t\bar{t}$+jets (blue) events.

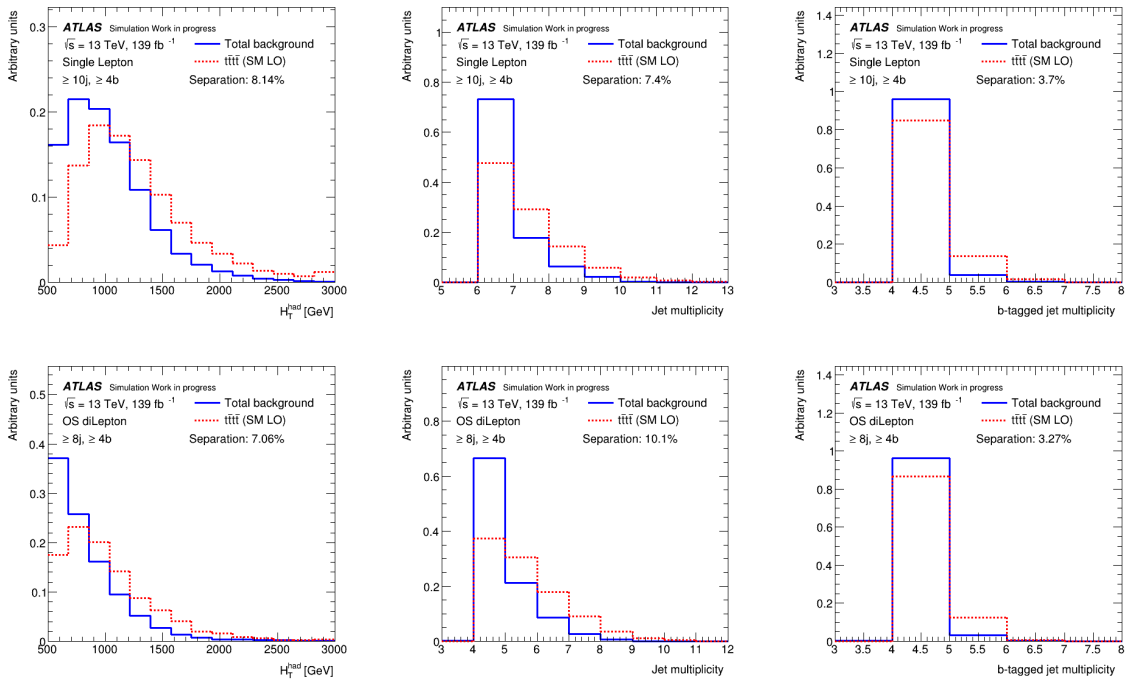

FIGURE 6.18: Event variable distributions in the signal regions of 1L (top) and OS (bottom) dilepton decay channels, respectively, using $t\bar{t}t\bar{t}$ (red) and $t\bar{t}$+jets (blue) events.

events from the total expected background estimated via MC simulation in the defined signal regions of 1L and OS dilepton decay channels, respectively. The BDT algorithm is trained using two sets of variables; the first set (s1) includes only χ^2 output variables and the second set (s2) includes both χ^2 output variables and event variables (i.e. the number of jets, the number of b-tagged jets and H_T^{Had}).

The parameters $t^{1,2}_{p_T,Mass}$ and $W^{1,2}_{p_T,Mass}$ in table 6.5 are the reconstructed masses and p_T using the six jets with permutation gives the minimum χ^2 value. On the other hand, $jet^{1,2,3,4}_{p_T}$ and $b^{1,2}_{p_T}$ are the jet p_T used to reconstruct the hadronically-decaying top-quark with minimum χ^2. Other variables are considered as χ^2 parameters and used as input for BDT algorithm. These parameters are the angular distance between two top quarks $\Delta R_{top_1,top_2}$ as well as the invariant mass ($M_{top_{1,2}}$) and the ($p_{T_{top_{1,2}}}$) of two top quarks, respectively.

The BDT [130, 131] is trained, ignoring the negative weights of events, on half of the events in LO $t\bar{t}t\bar{t}$ sample (total number of training+testing events for the 1L and OS dilepton decay channels are $\sim$ 10000 and $\sim$ 3000 events, respectively) and in the total background while the second half of events is used as an overtraining-test sample. The

applied algorithm for boosting is the AdaBoost [130] with 600 decision trees; the maximum depth of a tree is set to be three, and the number of cuts is 20 (See Ref[129] for other techniques).

top^1_{pT}	top^2_{pT}	top^1_{Mass}	top^2_{Mass}	W^1_{pT}	W^2_{pT}
W^1_{pT}	W^2_{pT}	$\Delta R_{top_{1,2}}$	$p_{T\,top_{1,2}}$	$M_{top_{1,2}}$	$\exp[-\chi^2]$
jet^1_{pT}	jet^2_{pT}	jet^3_{pT}	jet^4_{pT}	b^1_{pT}	b^2_{pT}

TABLE 6.5: List of all variables used as input for the BDT

.

In this analysis, separation (S^2) between the signal and background distributions is obtained using the TMVA definition, and it is defined as follows (see Ref[37, 132] for more details):

$$S^2 = \frac{1}{2}\int \frac{(\hat{y_s}-\hat{y_b})^2}{(\hat{y_s}+\hat{y_b})}dy \tag{6.8}$$

where $\hat{y_s}$ and $\hat{y_b}$ are the signal and background distributions, respectively. S^2 is equal to one when there is no overlap between the signal and background distributions, while it is equal to zero for identical distributions. The expected distributions of the BDT output, trained on the $t\bar{t}t\bar{t}$ signal and the total estimated background in the 1L (OS dilepton) channel using the first (s1) and second sets (s2) of variables, respectively, are shown in Figure 6.19.

The estimated separation of the BDT output between $t\bar{t}t\bar{t}$ signal and the predicted background in the 1L (OS dilepton) channel when using the first set of input variables is 9.4% (16.6%) and when using the second set is 18.4% (21.6%), respectively. The disagreement between the training distributions and testing ones, which is referred to as overtraining, in both channels (1L and OS dilepton) is due to the low number of available simulated events in the signal regions.

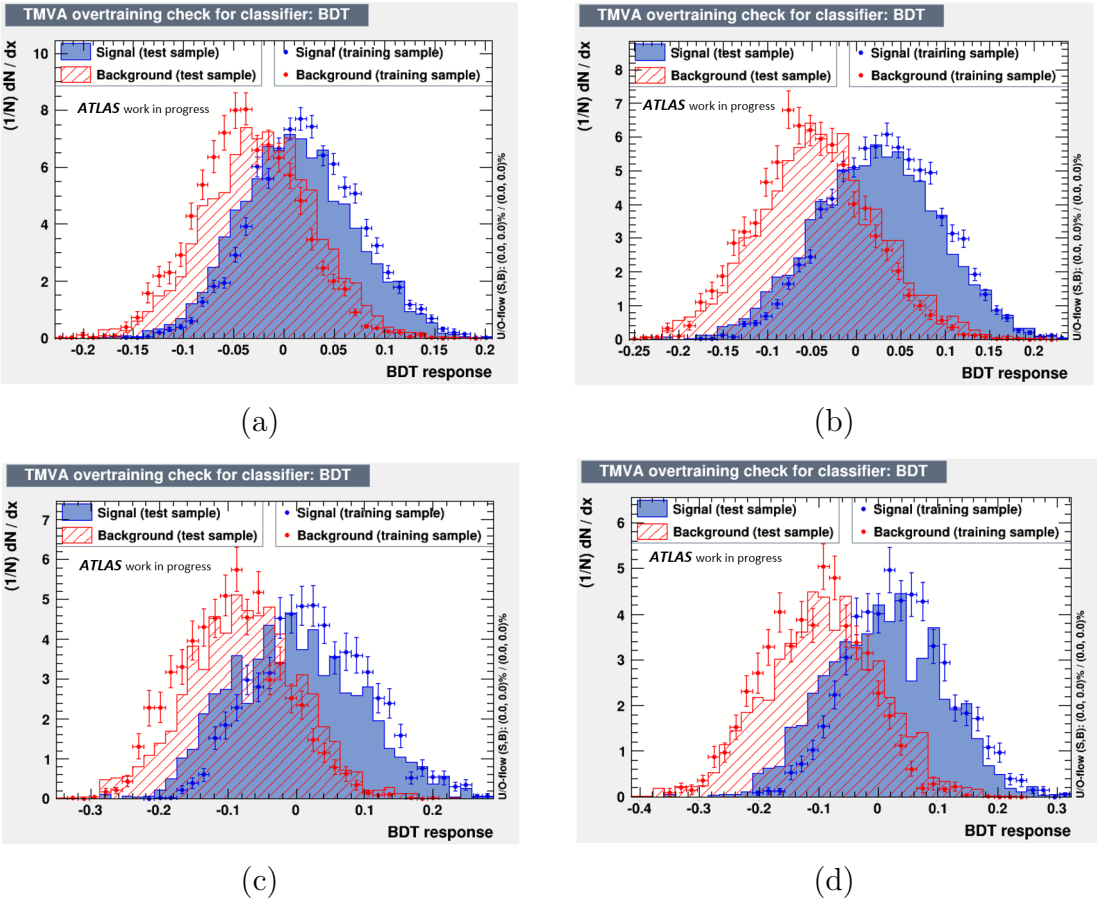

FIGURE 6.19: The BDT response for the training on the four-top-quark signal and total background events in the 1L channel using set1(a), set2(b) and OS dilepton set1(c), set2(d) channels.

6.6 Results and Conclusion

A χ^2–based method is introduced to solve the final-state combinatorics in four-top-quark events partially using MC events only and to help to discriminate this process from background processes. In both the single-lepton (1L) and the opposite-sign dilepton (OS) channels, the method relies on reconstructing two hadronically decaying top quarks as combinations of jets that minimise a χ^2 function.

Such a χ^2 method is first applied and studied in the 1L channel, in the signal region characterised by $\geq$ 10 jet and $\geq$ 4 b-tagged jets, by selecting only events where all the reconstructed physics objects (jets and charged leptons) are matchable to individual parton-level objects (partons and truth-level leptons). On this "fully matched" 1L simulated sample (counting $\sim$ 700 events), the efficiency of the reconstruction of the two

hadronic top quarks through the χ^2 method is estimated to be 32%.

As a second step, the χ^2 method is applied and studied in both the 1L and OS highest sensitive signal regions, SR1L (containing $\geq$ 10 jet and $\geq$ 4 b-tagged jets) and SROS ($\geq$ 10 jet and $\geq$ 4 b-tagged jets), respectively, without requiring the events to be "fully matched", but comparing the χ^2 output variable distributions (i.e. the kinematics of the reconstructed top quarks and W-bosons, of the jets forming the minimum-χ^2 combinations and the minimum χ^2 values themself) for $t\bar{t}t\bar{t}$ signal and predicted background events (mainly from $t\bar{t}$+jets). Finally, these χ^2 output variables are used as inputs for a BDT discriminant, reaching a separation of 18.4% and 21.4% in the two channels, respectively, when combining with other simple event variables. Even if other, more elaborated methods could give better performance, this χ^2–method is found to be simple, fast and useful in order to provide inputs for further analysis steps, such as an MVA signal-versus-background discrimination.

Chapter 7

Search for $t\bar{t}$ resonances in the dilepton channel

Despite its success, the SM is not considered as a complete theory since several aspects are not included within its prediction, e.g. gravity. For this reason, experimental searches on new BSM phenomena are essential to establish new theoretical frameworks for particle physics to cover the SM weakness. Since the top-quark is the most massive elementary particle in the SM with a mass close to the electroweak symmetry breaking scale (≈ 173 GeV), it plays a crucial role in several BSM models.

In this chapter, search for $t\bar{t}$ resonances in the dilepton channel is presented based on proton-proton collision data with a centre-of-mass energy $\sqrt{s} = 13$ TeV collected by the ATLAS experiment at the LHC. The integrated luminosity corresponds to the full Run 2 dataset with $\mathcal{L} = 139$ fb^{-1}. In Section 7.1, the analysis strategy and the considered BSM models are introduced. In Section 7.2 and Section 7.3, the event selections applied, and the MC samples used in this analysis are described. Finally, the expected limits on the cross-section times the branching ratio for the studied signals are presented in Section 7.7.

7.1 Analysis Strategy

Several BSM models predict the existence of new particles that decay in a large proportion to $t\bar{t}$ pairs. An example is the so-called Z', a heavier partner of the ordinary Z boson, which can decay to a $t\bar{t}$ pair if massive enough. Additionally, many BSM models predict the existence of massive excitations for the SM and BSM fields when they propagate to extra dimension (see Chapter 2), in particular, for gluon (KK_g) and graviton (G) fields (in some references G corresponding to G_{RS}). In this analysis, three BSM physics particles with different mass hypotheses predicted by the Topcolor Model (TC2) [4, 5, 73] (For TC2 model, samples were generated based on the Sequential Standard Model (SSM) [3] while the cross-sections are corresponding to the TC2) and Randall-Sundrum Model [8, 9] (see Chapter 2) are studied.

The invariant mass of a pair of top-antitop quarks is given by:

$$m_{t\bar{t}} = \sqrt{(P^{\bar{t}} + P^{t})_{\mu}(P^{\bar{t}} + P^{t})^{\mu}} \tag{7.1}$$

where P^{t} and $P^{\bar{t}}$ are the top and antitop quarks four-momentum vector, respectively. The expected $m_{t\bar{t}}$ distribution under the SM prediction is expected to be smooth and exponentially decaying. At the same time, a resonant bump is predicted by the BSM models to appear on top of the SM $m_{t\bar{t}}$ distribution. For example, a new gauge boson, Z', with mass 3 TeV, 4 TeV or 5 TeV, decaying in the dielectron channel is expected to bumps on top of the SM prediction, as shown in Figure 7.1.

In general, the $m_{t\bar{t}}$ in the dilepton decay channel cannot be fully reconstructed experimentally due to the presence of two neutrinos that are not detected by the ATLAS detector and are only considered by the E_T^{miss} (see Appendix D for another reason). Therefore, two variables are introduced in this analysis, m_{llbb} and $\Delta\phi_{l^+l^-}$ as defined below. The m_{llbb} variable is defined as the partial invariant mass of the top-antitop quark, and it is given as:

$$m_{llbb} = \sqrt{(P^{l^+} + P^{l^-} + P^{b_1} + P^{b_2})_{\mu}(P^{l^+} + P^{l^-} + P^{b_1} + P^{b_2})^{\mu}} \tag{7.2}$$

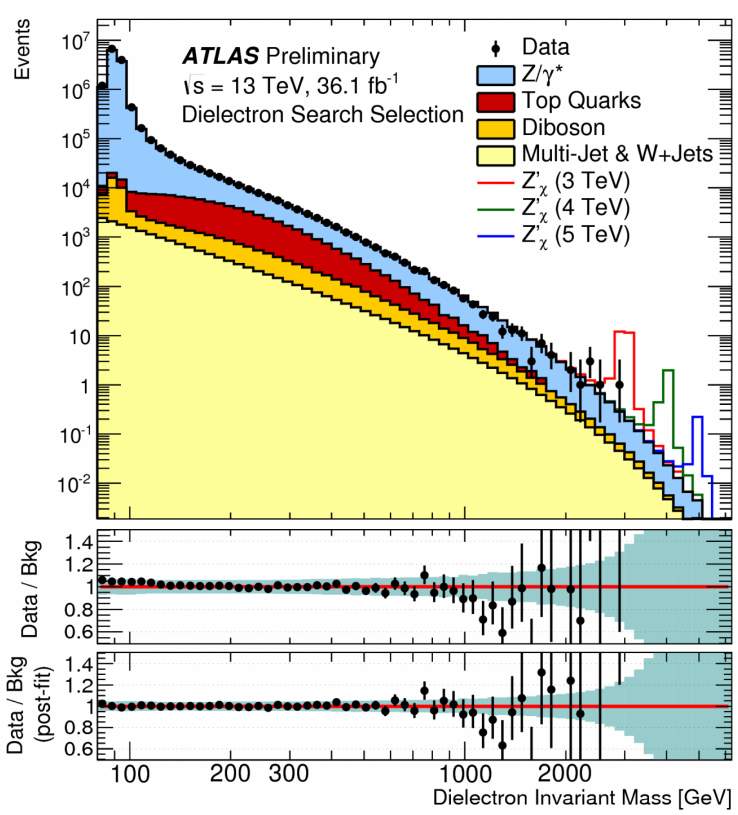

FIGURE 7.1: Expected invariant masses of Z' decaying to dielectron final state, 3 TeV, 4 TeV and 5 TeV, respectively, [3].

where $P^{l^{\pm}}$ and $P^{b}_{1,2}$ are the four-momentum vectors for electron or muon and b-tagged jets, respectively. Besides the difficulty of reconstructing the $m_{t\bar{t}}$, which could be evaluated experimentally with techniques such as the neutrino weighting (NW) method (see Ref[133, 134]), but m_{llbb} is chosen because of its simplicity and because of the arguments presented in Appendix D.

Due to the short lifetime of the top-quark, which is shorter than the hadronisation timescale ($\sim 10^{-23}$sec), and of the spin decorrelation time ($\sim 10^{-21}$sec) [37], the spin information of the top-quark is transferred to its decay products. However, not all top-quark decay products carry the same degree of spin information. Still, the charged leptons arising from the W-boson decay are predicted to take almost the full top-quark spin information. Therefore, the spin correlation of the top and antitop quarks, which is predicted in the SM (see Figure 7.2), can be measured directly from the angular distributions of the charged leptons produced from the leptonic decay of W-boson in $t\bar{t}$ events. The spin correlation has been observed experimentally by the ATLAS and CMS experiments at the

LHC in proton-proton collisions at $\sqrt{s} = 7$ TeV [135–138] and $\sqrt{s} = 8$ TeV [139–142] as well as at $\sqrt{s} = 13$ TeV [134, 143]. Also, it is observed in proton-antiproton collisions at the Tevatron collider [144–148]. On the other hand, the appearance of new physics in association with top-antitop quark pairs is likely to modify the spin correlation information of the top-antitop quark pairs.

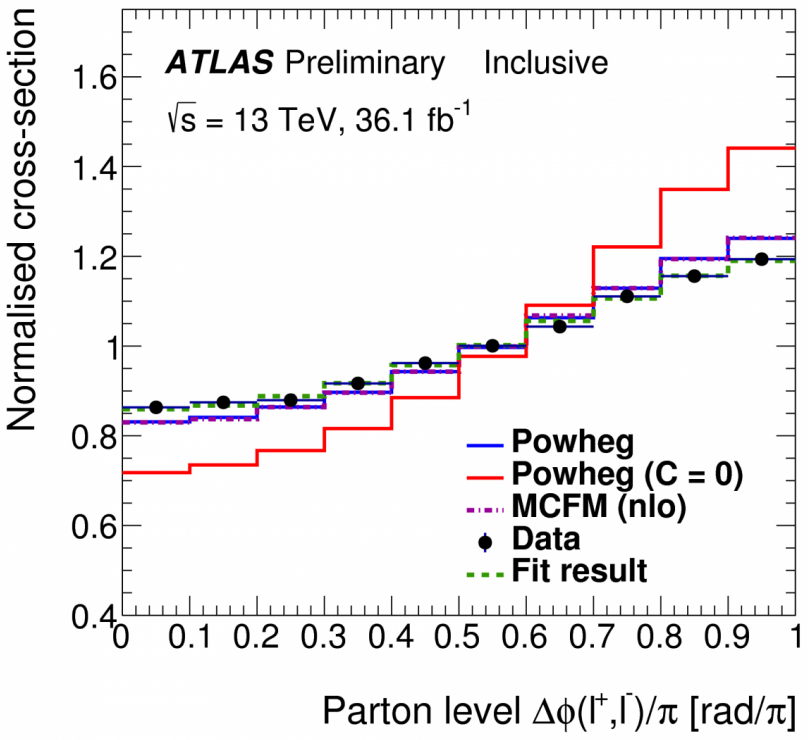

FIGURE 7.2: Azimuthal angle distribution between two leptons produced from the decay of a top-antitop quark pair as predicted by the SM (blue). The expected distribution for the azimuthal angle with no correlation assumption, as shown in red [34].

As a result, the second studied variable is the azimuthal opening angle between the two charged leptons (electron or muon), $\Delta\phi_{l^+l^-}$, which is measured in the transverse plane with respect to the beamline in the laboratory frame. Figure 7.3 shows the expected $\Delta\phi_{l^+l^-}$ at truth-level in the dilepton decay channel of $t\bar{t}$ events produced by different BSM signal processes, see table 7.1, versus the expected one from the SM (produced either from gluon-gluon fusion or quark-antiquark annihilation). The expected $m_{t\bar{t}}$ and m_{llbb} mass distributions for the studied signals versus the SM $t\bar{t}$ ones are shown in Figure 7.4 for events at truth-level and Figure 7.5 after detector simulation, respectively.

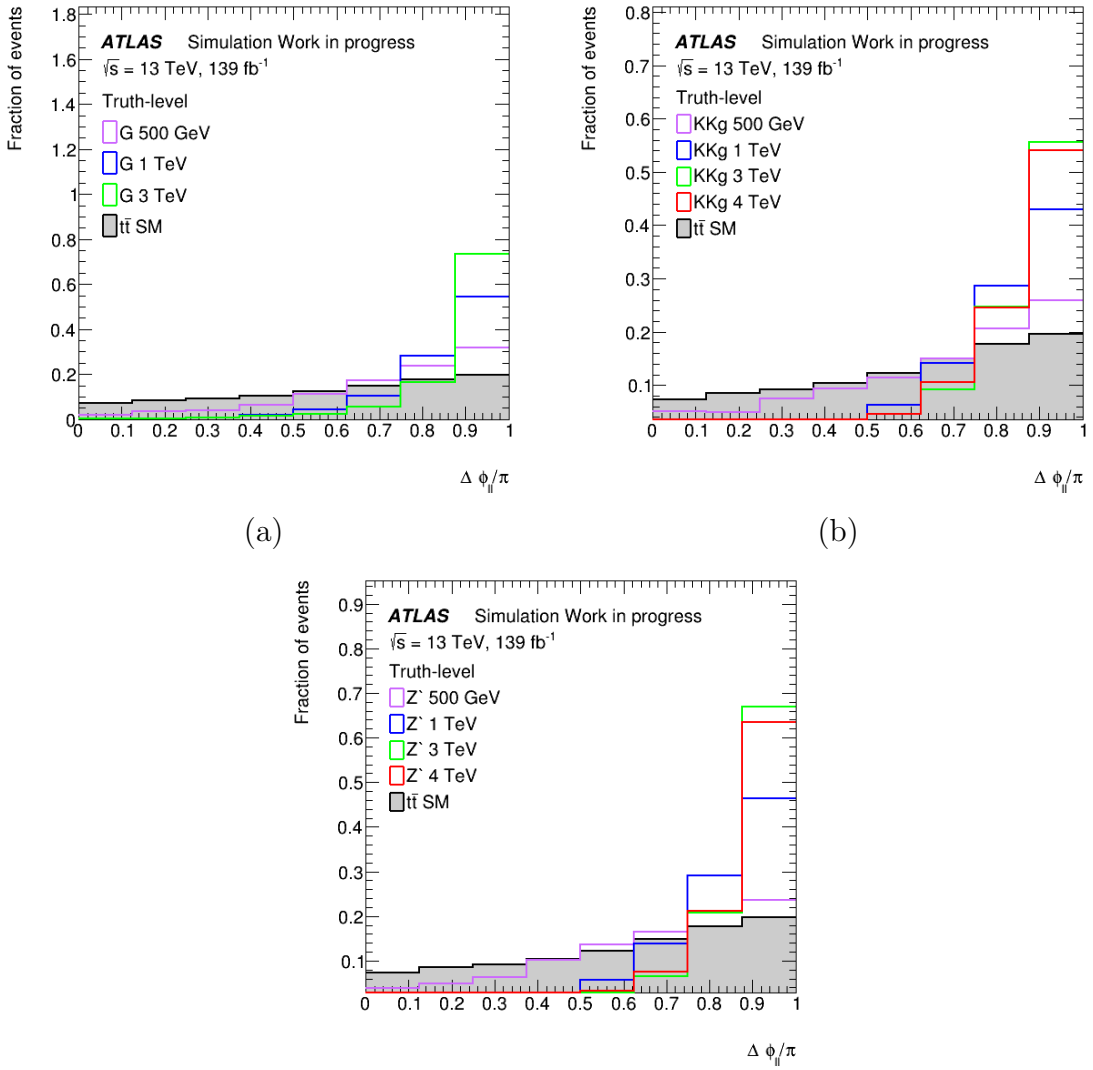

FIGURE 7.3: $\Delta\phi_{l^+l^-}$ distributions at truth-level for (a) G, (b) KK_g, and (c) Z' with different mass hypotheses (colours) compared with the SM $t\bar{t}$ decays in the dilepton channel (grey).

To investigate the effect of the production of massive excitations of gluons (KK_g) or gravitons (G), respectively, as well as the production of new heavy gauge bosons (Z') on the spin correlation of top-antitop quark pairs, a new variable has been studied at truth-level, referred to as $\cos(\theta^*_{l^+})\cos(\theta^*_{l^-})$. This variable can be extracted in the so-called helicity frame by boosting the leptons, and the top quarks into the top-antitop centre-of-mass (CM), as shown in Figure 7.6. Then, each lepton is boosted into the rest frame of its parent top-quark to measure $\theta^*_{l^+}(\theta^*_{l^-})$, which is the angle between the e^+ or μ^+ in the rest frame of the top (antitop) quark and the top (antitop) quark direction flight in the top-antitop pair CM frame.

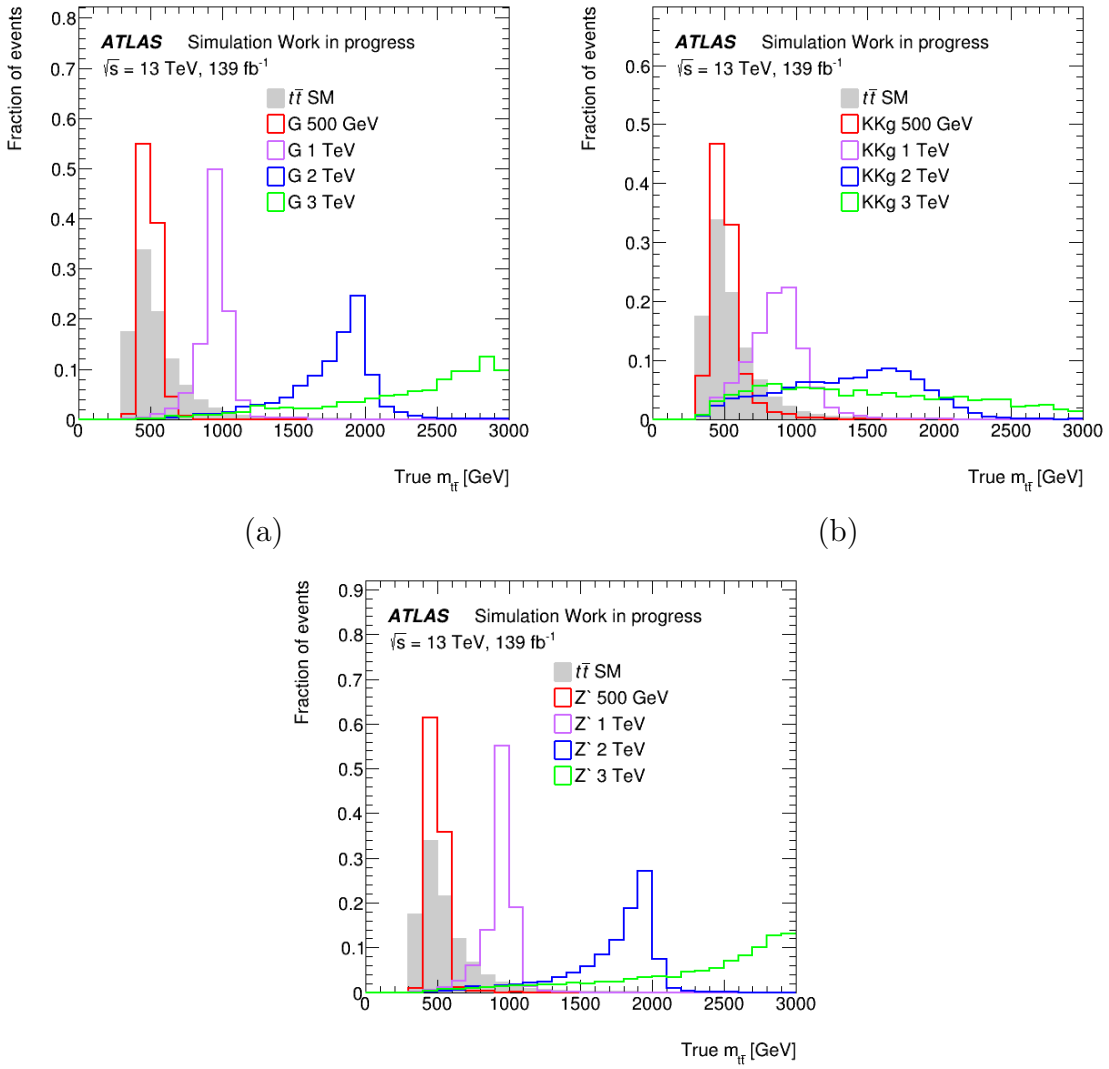

FIGURE 7.4: $m_{t\bar{t}}$ distributions at truth-level for (a) G, (b) KK_g, and (c) Z' with different mass hypotheses (colours) versus the SM $t\bar{t}$ decays in dilepton channel (grey) for events with ≥ 2 b-tag.

Figure 7.7 shows the $\cos(\theta^*_{l^+})\cos(\theta^*_{l^-})$ distributions in the helicity frame with and without the spin correlation assumption in the CMS experiment. Figure 7.8 instead shows the expected $\cos(\theta^*_{l^+})\cos(\theta^*_{l^-})$ distributions at truth-level in the helicity frame for the studied signals, which are presented in table 7.1, compared with the one from the SM $t\bar{t}$.

In Figure 7.3 and Figure 7.5, one can see that the $\Delta\phi_{l^+l^-}$ distribution shows a comparable sensitivity to the production of new physics compared to m_{llbb} distribution, in particular, in the low mass region. Then by taking a combination of the two variables, $\Delta\phi_{l^+l^-}$ and m_{llbb}, the sensitivity to BSM signals is improved since the two quantities are not fully

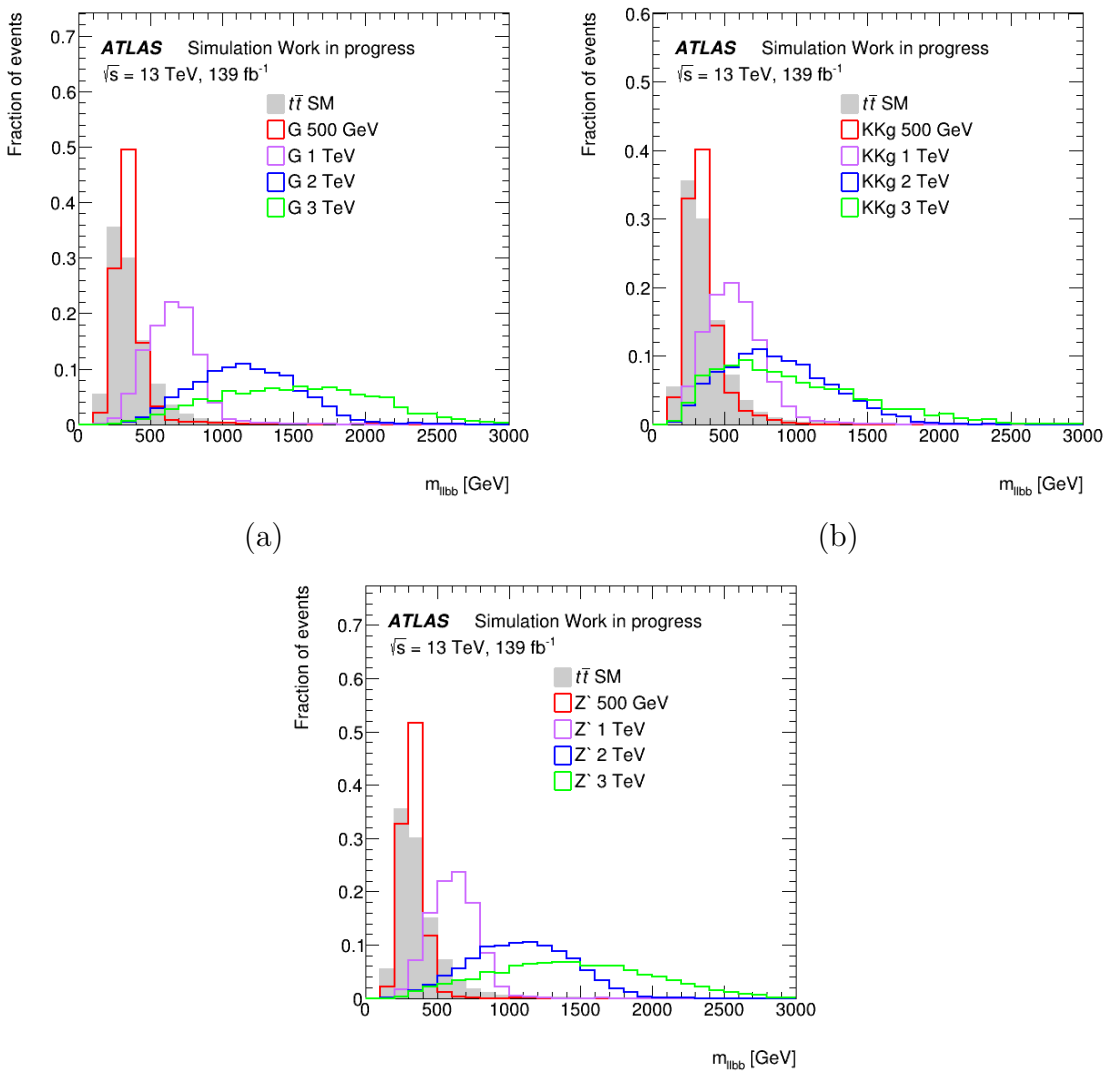

FIGURE 7.5: m_{llbb} distributions for (a) G, (b) KK_g, and (c) Z' with different mass hypotheses (colours) versus the SM $t\bar{t}$ decays in the dilepton channel (grey) for events with ≥ 2 b-tag.

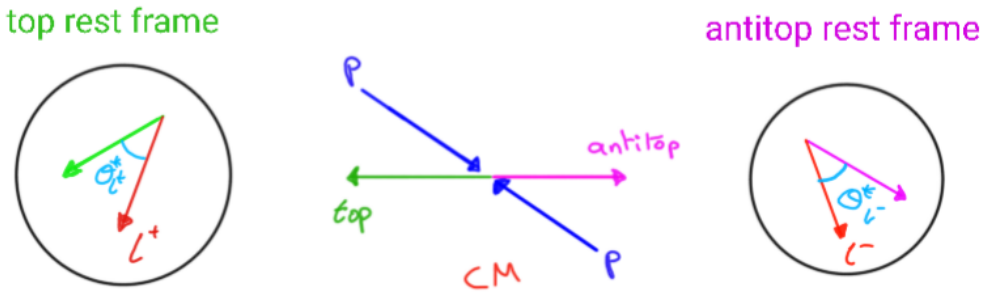

FIGURE 7.6: Sketch of the helicity frame where the top quarks are boosted to the top-antitop CM, and then the $\theta^*_{l^\pm}$ of the boosted leptons are measured in the rest frame of the top quarks.

Theoretical (Theor.) cross-section (σ) in [pb]					
Topcolor model (TC2)		Randall-Sundrum model			
Z' Mass [TeV]	Theor. [pb]	KK_g Mass [TeV]	Theor. [pb]	G Mass [TeV]	Theor. [pb]
0.5	52.162	0.5	240.86	0.4	7.19
0.75	13.913	1	20.176	0.5	5.84
1	4.808	1.5	3.790	0.75	1.18
2	0.223	2	1.052	1	0.289
3	0.0216	2.5	0.37339	2	0.00498
4	0.00276	3	0.15607	3	0.000248
5	0.00043	3.5	0.074283		
		4	0.039494		
		4.5	0.022862		

TABLE 7.1: Summary of the studied signals [40, 41].

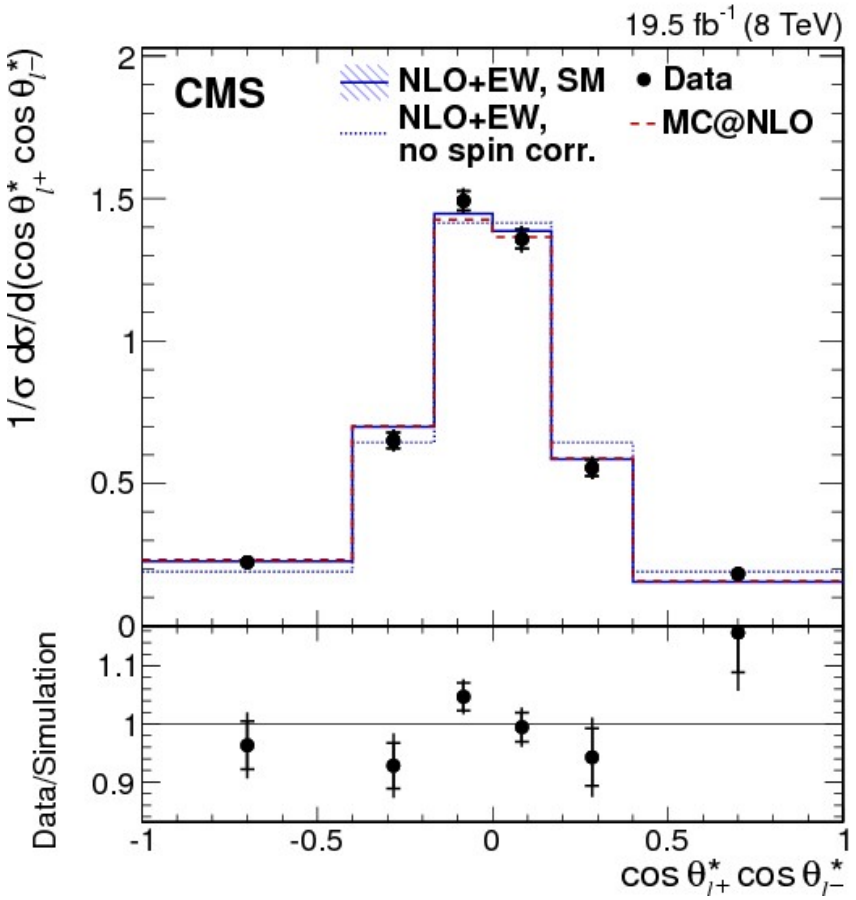

FIGURE 7.7: $\cos(\theta^*_{l^+})\cos(\theta^*_{l^-})$ distribution in the helicity frame. Data (points); parton-level predictions from MC@NLO(red dashed histograms); and the SM predictions at NLO+EW with and without (no spin corre) spin correlations (solid blue line) and (blue dotted line) respectively [35, 36].

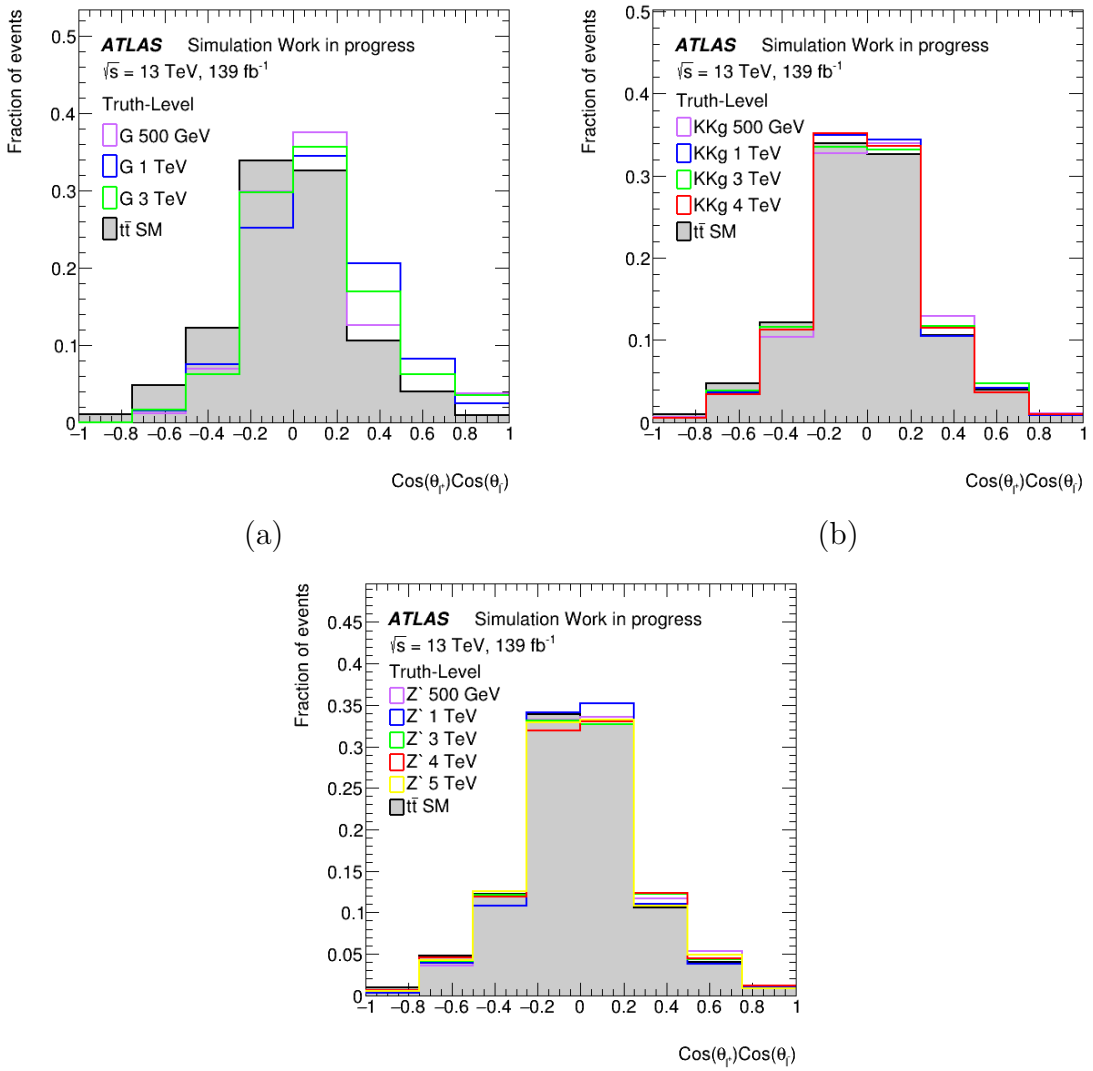

FIGURE 7.8: $\cos(\theta^*_{l^+})\cos(\theta^*_{l^-})$ distribution in the helicity frame for (a) G, (b) KK_g, and (c) Z' with different mass hypotheses (colours) versus the SM $t\bar{t}$ decays in dilepton channel (grey) for events ≥ 2 b-tagged jets.

correlated. Therefore, the expected limits for each model (TC2 and Randall-Sundrom) are derived by scanning $\Delta\phi_{l^+l^-}$ as a function of m_{llbb}. Technically, $\Delta\phi_{l^+l^-}$ is fitted simultaneously in ten bins of m_{llbb}, effectively defining ten orthogonal signal regions. The size of each of these bins is chosen based on samples statistics in each of them as well as on the sensitivity of $\Delta\phi_{l^+l^-}$ to each studied signal. The physics objects used to build the m_{llbb} and $\Delta\phi_{l^+l^-}$ variables are presented in the following section (Section 7.2) and defined in Chapter 4. The applied event selections on these objects are derived to maximise the signal sensitivity and to reduce the background contributions, especially when comparing with the truth-level distributions.

7.2 Physics Objects and Event Selection

7.2.1 Physics Objects

The physics objects considered in this analysis are jets, including the b-tagging jets and the missing transverse energy as well as charged leptons (electron and muon). In contrast, the leptonically-decaying channel $\tau(\tau \rightarrow e\upsilon_e\upsilon_\tau \; or \; \tau \rightarrow \mu\upsilon_\mu\upsilon_\tau \;)$ contribute in a similar way as the other charged leptons, while no attempt to explicitly reconstruct hadronic τ decays is made.

Jet candidates are reconstructed using the anti-kT algorithm with $\Delta R = 0.4$, and they have to pass the JetVertexTagger (JVT) selection, see Section 4.3 for more details. After energy calibration, jets in the active region $|\eta| < 2.5$ of the ATLAS detector and with $p_T > 25$ GeV are considered here. To identify jets initiated from b-quarks (Section 4.3), a multivariate technique (see Section 4.3) based on MV2c10 algorithm with working point referred to as MV2c10_77, which corresponds to an efficiency of tagging b-jets (ϵ_b) of 77%, is used.

Electron and muon candidates considered here are reconstructed and identified based on the methods described in Sections 4.1 and 4.2, respectively. Electron candidates are required to have $p_T > 25$ GeV and to satisfy the Tight (TighLH) identification criteria. Also, they have to be in the active detector region with $|\eta| < 2.5$ while those in the so-called LAr crack region with $1.37 < |\eta| < 1.52$ are rejected to reduce the non-prompt and fake contributions. On the other hand, muon candidates are reconstructed based on the combined approach (see Section 4.2) and must have $p_T > 25$ GeV and $|\eta| < 2.5$. Also, they are required to satisfy the Medium identification criteria.

The $t\bar{t}$ pairs produced from the decay of heavy resonances are predicted to have a high p_T. Therefore, electrons and muons arising from heavy resonances decaying to $t\bar{t}$ might be produced particularly close to jets, especially high-p_T ones. As a result, to retain a high selection efficiency for such electrons and muons, special isolation requirements and overlap removal are applied. In the case of electrons, no explicit cut is applied on any of the commonly used isolation variables (see Section 4.1). Instead, in the case of muons,

the isolation requirement is based only on track information and found to be very efficient at high pT is used (referred to as textbf*FixedCutTightTrackOnly* working point).

The energy deposits in the calorimeter are used to reconstruct both electrons and jets. Therefore, the overlaps between these physics objects can occur because, in some cases, the electron energy deposits in the calorimeter might be used to reconstruct the jet. To prevent this, the angular difference ($\Delta R = \sqrt{(\Delta\eta)^2 + (\Delta\phi)^2}$, see equation 3.4) between the closest jet and electron is calculated. To have an efficient selection when the electron is produced close to a jet (might be b-tagged jet) at high p_T (boosted regime), the Electron-in-Jet-subtraction overlap removal is used. In this method, the electron four-momentum is subtracted from the reconstructed jet with an ΔR smaller than 0.4 with respect to an electron. Then, if the jet p_T is higher than a certain threshold, the jet is retained, and the ΔR between it and the subtracted electron is recalculated. If ΔR is less than 0.2 ($\Delta R < 0.2$), an electron is removed, and its four-momentum is re-added to the jet one. Otherwise, both electron and jet are retained in the event for further analysis. In the case of muons, the overlap removal applied is similar to the electron one. However, muons are removed if they are within a p_T-dependent ΔR with respect to jets, instead of using a fixed ΔR since the ΔR tend to be zero for high-p_T muon. This ensures that high-p_T muons from high-p_T (hence collimated) top quarks are kept and not classified as secondary muons from heavy-flavour hadron decays.

For both, the electron and the muon candidates are required to pass the recommended standard cuts on the impact parameters. The scale factors to correct the identification efficiency differences between data and the MC samples are applied for both electrons and muons. In contrast, the isolation factor is derived only for muon since there is no isolation requirement on the electron candidates. A summary of the object requirements in this analysis is presented in table 7.2.

7.2.2 Event Selection

In this analysis, events are required to pass a set of selections to increase the sensitivity of the search for BSM particles and to reduce different background contributions. Events

	Electrons	Muons	Jets	b-jets
p_T(GeV)	> 25	> 25	> 25	> 25
$\|\eta\|$	< 1.37 or $1.52 - 2.47$	< 2.5	< 2.5	< 2.5
ID quality	TightLH	medium	Cleaning+JVT	MV2c10 77%
Isolation	None	FixedCutTightTrackOnly		
Track Vertex:				
$-\|d_0/\sigma_{d_0}\|$	< 5	< 3		
$-\|z_0 sin(\theta)\|$mm	< 0.5	< 0.5		

TABLE 7.2: Summary of the requirements applied to various physics objects.

are required to pass the same single-lepton trigger selections as that defined in table 6.2 and used in the four-top-quark analysis presented in Chapter 6.

Events are then retained if they have exactly two leptons and at least two b-tagged jets. Moreover, a cut on the E_T^{miss} is applied, requiring it to be larger than 45 GeV and the invariant mass of any same lepton flavour (M_{ll}) is required to be larger than 15 GeV and

outside the mass range of Z-boson ($80 - 100$ GeV). Table 7.3 summarises all the applied selections in this analysis:

	Requirement
Trigger	Single-lepton triggers
Leptons	OS dilepton
Jets	≥ 2
b-jets	≥ 2
Other	$E_T^{miss} > 45$ GeV $\quad m_{ll} > 15$ GeV
	$\lvert m_{ll} - 90 \rvert > 10$ GeV

TABLE 7.3: Summary of the event preselection requirements.

The selection requirements on M_{ll} are introduced in order to reduce the Drell-Yan and Z+jets contributions, in the ee and $\mu\mu$ channels only. Figure 7.9 shows the expected M_{ll} distributions in the decay channels ee, $\mu\mu$ and $e\mu$ without applying the M_{ll} cut to be outside the mass window of the SM Z-boson.

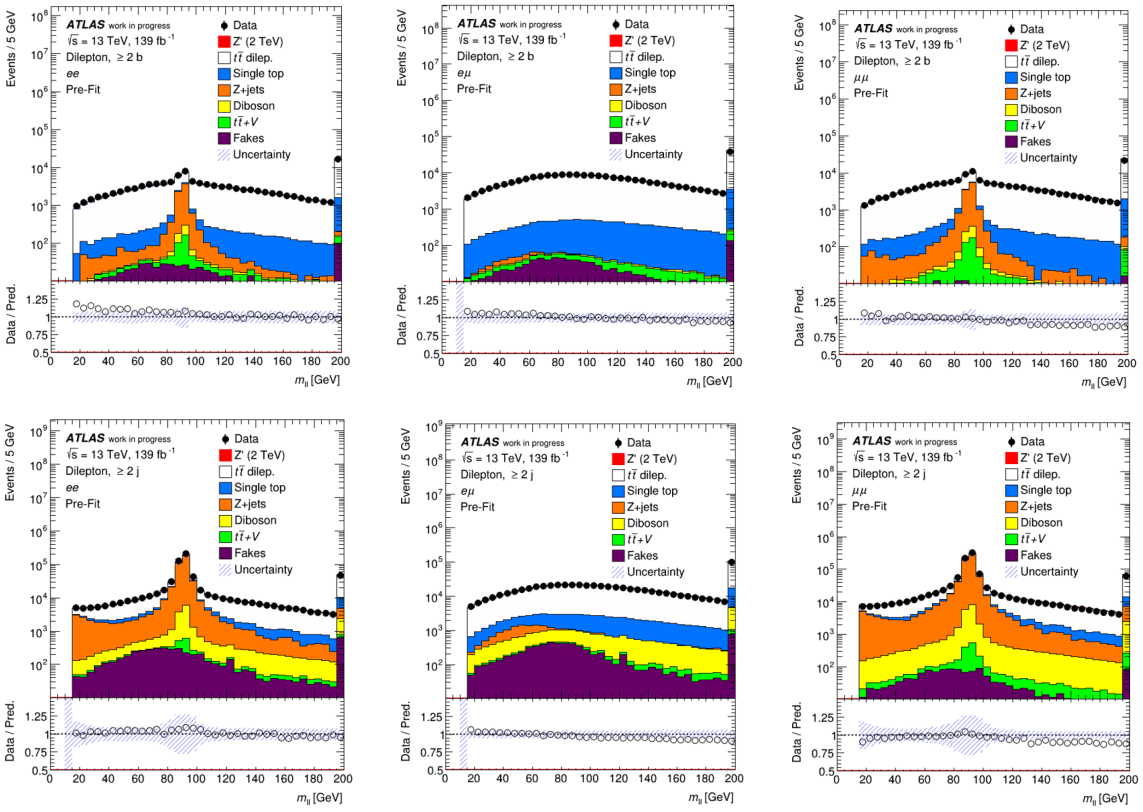

FIGURE 7.9: M_{ll} distribution in the decay channels ee, $e\mu$ and $\mu\mu$ requiring ≥ 2 b-tag (top) and ≥ 2 jet, respectively, and including the statistical and systematic uncertainties.

The requirement to have at least two b-tagged jets is obtained from the comparison between the m_{llbb} with the invariant mass of the top-antitop quark pair ($m_{t\bar{t}}$) at parton-level with requiring $1 \geq$ b-tag and $2 \geq$ b-tag respectively, as shown in Figure 7.10. On Figure 7.10(a) is shown the correlation between the m_{llbb} and $m_{t\bar{t}}$ for events with at least one b-tagged jets where the jet with highest p_T is used to reconstruct m_{llbb} (see Appendix D for other relations). From this plot, there is a non-negligible contribution from events with large m_{llbb} in the low mass region compared to $m_{t\bar{t}}$. However, with the requirement to have at least two b-tagged jets, the number of events with high m_{llbb} in the low mass region is reduced and becomes correlated with $m_{t\bar{t}}$ distribution, see Figure 7.10(b).

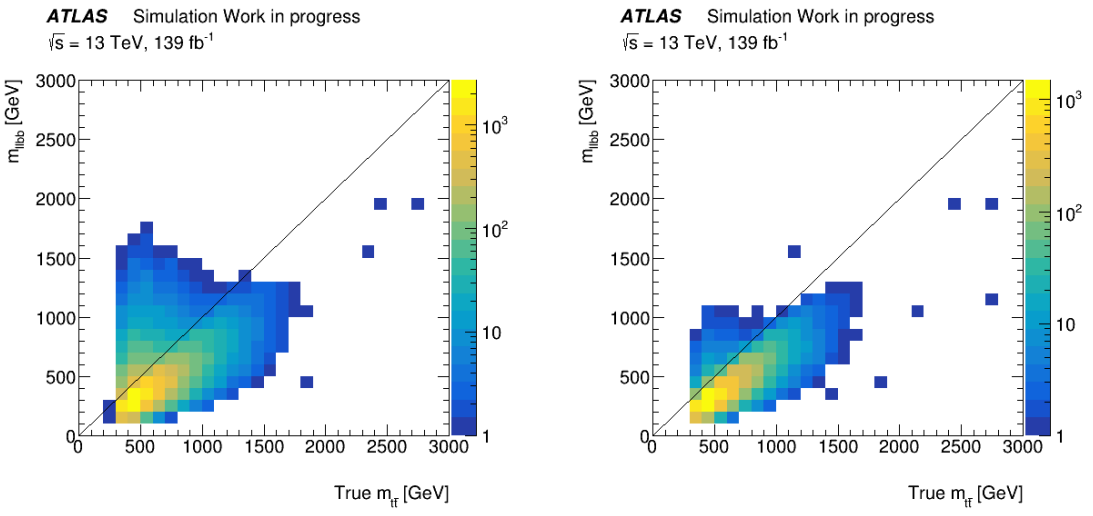

FIGURE 7.10: Correlation between m_{llbb} (Reco–level) and m_{tt} (Parton–level) requiring at least one (left) and two (right) b-tagged jets.

7.3 Signal and Background Simulation

Monte Carlo (MC) simulated samples are used to estimate both the BSM signals and the SM background. The main BSM signal samples were generated and showered using PYTHIA8 and NNPDF23LO PDF set with A14 [149] tune for both Z' and Kaluza-Klein gluon (KK_g) signal samples. Furthermore, the Randall-Sundrum graviton (G) was simulated using MADGRAHPH5_AMC@NLO generator and events were interfaced with PYTHIA8 and A14 tune for showering. The dominated $t\bar{t}$+jets events were estimated using the POWHEGBOX [150–153] v2 generator at NLO with NNPDF3.0NLO PDF set [154]

and the hdamp parameter, which is a model parameter that controls the matrix-element and the parton shower matching in POWHEG and regulates the high p_T radiation, is set to 1.5 mTop [155, 156]. Showering was performed using PYTHIA8.230 with NNPDF23LO PDF set and A14 tune. To assess the uncertainties on the choice of the matrix-element, as well as the parton shower and hadronisation modelling, samples were generated using MADGRAHPH5_AMC@NLO +PYTHIA8 and POWHEGBOX+HERWIG7.04, respectively.

Single-top in association with W-boson (tW) was modelled using POWHEGBOX [150, 151, 157] v2 generator at NLO in QCD in the five flavour scheme with the NNPDF2.0NLO PDF set [154]. To handle the interference with the $t\bar{t}$ production [155, 158], the diagram scheme removal was performed. The production of the single-top in t and s channels were modelled using the POWHEGBOX [150–153, 159] v2 generator at NLO in QCD in four and five flavour schemes with NNPDF3.0NLOnf4 and NNPDF23LO PDF sets, respectively. Showering were performed in all single-top events using PYTHIA8.230 [126] with A14 tune [149] and NNPDF23LO PDF set.

The $t\bar{t}V$ production was generated using the MADGRAPTH5_AMC@NLO [125] v2.3.3 generator at NLO with the PDF set NNPDF3.0NLO. The events were interfaced with PYTHIA8.210 [126] using the A14 tune and the NNPDF2.3LO PDF set. On the other hand, the $t\bar{t}H$ production was generated using the POWHEGBOX [150–153] generator at NLO with the PDF set NNPDF3.0NLO while showering was performed using PYTHIA8.230 with the A14 tune and the NNPDF2.3LO PDF set. In the case of rare top-quark processes, such as the productions of tZq and tWZ, MADGRAPTH5_AMC@NLO [125] v2.3.3 was used to generate the samples at NLO with the NNPDF3.0NLO PDF set. The showering is performed for tZq and tWZ events by using PYTHIA8.230 and PYTHIA8.212 [126], respectively, as well as using the A14 tune and the NNPDF2.3LO PDF set in both samples.

The diboson samples in the dilepton decay channel were simulated using the SHERPA [160] v2.2 generator. In this setup, several matrix elements are matched and merged with the SHERPA parton shower based on Catani-Seymour [161, 162] dipole using the MEPS@NLO prescription [163–166]. The QCD virtual correction at NLO accuracy for the matrix elements is provided using the OPENLOOPS library [167, 168].

Massive-vector-boson production plus QCD jets (V+jets, with $V = W$ or Z) was modelled using SHERPA [160] v2.2 generator. In this setup, several matrix elements are matched and merged with the SHERPA parton shower based on Catani-Seymour dipole [161, 162] using the MEPS@NLO prescription[163–166]. The QCD virtual correction at NLO accuracy for the matrix elements is provided using the OPENLOOPS library [167, 168].

7.3.1 Correction to the momentum of the Top quark throughout theoretical predictions

Theoretical prediction, both for the total $t\bar{t}$ cross-section and the main differential distributions for this process, have been computed with high accuracy at the LHC, in particular, with calculations that included the electro-weak (EW) corrections on top of next-to-next-to-leading-order (NNLO-QCD) predictions, see Ref[169].

The top quark transverse momentum (Top_{p_T}) distribution from these calculations, is predicted to be softer than those performed using NLO at QCD only. Also, it is even softer than other MC predictions that were generated at NLO and interfaced to various Parton showers (PS), like those used in this analysis. The scale and PDF uncertainties on the calculated Top_{p_T} spectrum are smaller than those derived from the comparison of different MC generators and PS for the same Top_{p_T} variable. On the other hand, the difference between this calculated Top_{p_T} spectrum and those from the various MC generators and PS settings is larger than the spread of these alternative MC predictions. Therefore, the so-called Top_{p_T} reweighting has been derived for each MC sample by producing histograms for each top-quark p_T distribution at parton-level using all generated events without applying any event selection. The resulting histogram is normalised to unity and then compared to the normalised top, and anti-top quarks average transverse momentum ($p_{T,avg}$) histogram which is obtained from the theoretical calculation at NNLO QCD + NLO EW in the $t\bar{t}$ differential cross-section calculation, see Ref[169].

In Figure 7.11, the derived Top_{p_T} reweighting scale factor as a function of the top transverse momentum is shown. The Top_{p_T} reweighting is derived from the ratio between the two histograms and used as systematic uncertainty on the expected limits. It is used as

a nominal correction for the $t\bar{t}$ background contribution when comparing data with the simulation in the various presented control plots.

Figure 7.12 shows the p_T distribution for leading lepton and jet in ee channel before and after applying the reweighting scale factor. From these plots, we can see that the MC prediction for these variables is improved and well modelled the data once the reweighting scale factor is applied.

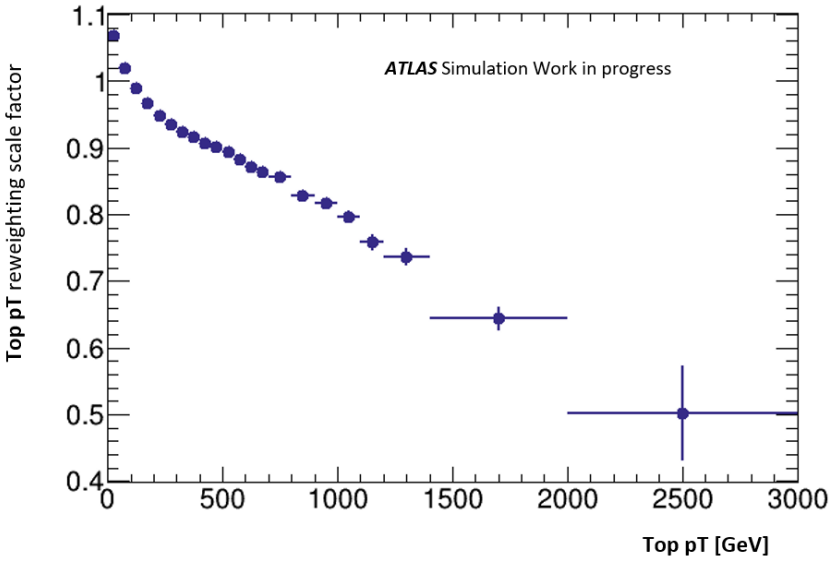

FIGURE 7.11: Top$_{p_T}$ reweighting scale factor as a function of the top transverse momentum.

7.4 Control regions and non-top backgound corrections

To study several background effects and to extract other information which might affect the Data and MC agreement in the regions enriched by the dominated background, two control regions are defined. The first one, referred to as CRz, is defined to study the data and MC agreement in the control region enriched by Z+jets in the ee and $\mu\mu$ decay channels. The second control region referred to as CRf, which is enriched with $t\bar{t}$+jets and W+jets events, is used to estimate the fake or non-prompt lepton background.

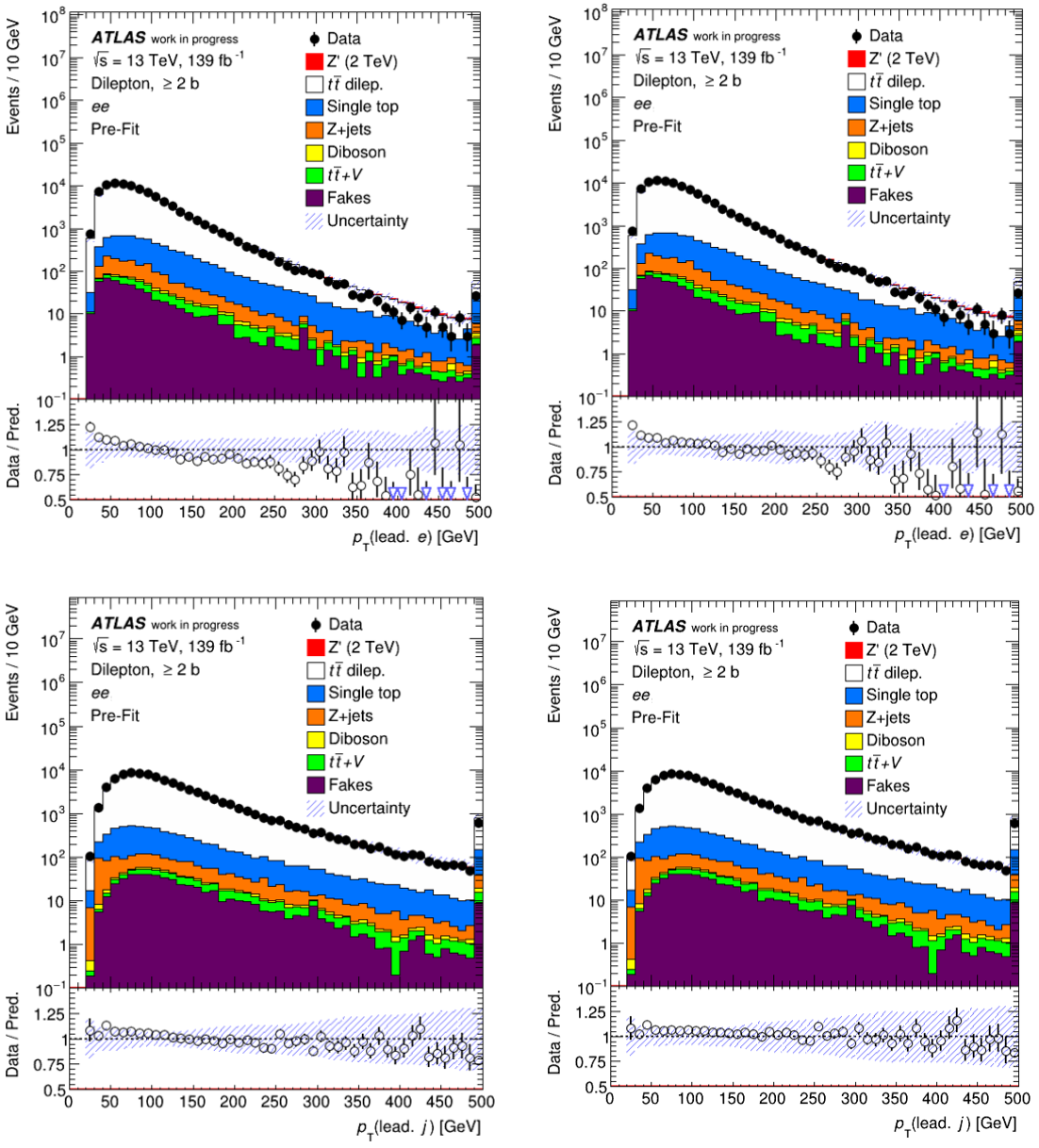

FIGURE 7.12: p_T of leading electron and jet in the ee channel with $\geq$ 2 b-tagged jet without (right) and with (left) applying the Top_{p_T} reweighting scale factor and including the statistical and systematic uncertainties.

7.4.1 Z+jets background

The CRz region is obtained by selecting events in ee and $\mu\mu$ final states with at least two jets and to be in the Z-boson mass window, $80 < M_{ll} < 100$ GeV. Despite the good Data and MC agreement for the M_{ll} distributions in ee and $\mu\mu$ channels, as shown in Figure 7.9, there is a slight disagreement between data and MC predictions for some variables such as the leading p_T of the electrons and the jets in ee channel and, in particular, the p_T of the dilepton system. This suggests a mismodelling of the Z-boson p_T spectrum by the MC simulation, which could be corrected by using the pure data available in this CR. Therefore, a scale factor ($Z_{SF,p_{T_{ll}}}$) is derived from the Data and MC ratio (Data/MC) of the $p_{T_{ll}}$ distribution in CRz region and implemented as a systematic uncertainty on the expected limits of the cross-section×branching-ratio.

The p_T distributions for the leading lepton and jet as well as the $p_{T_{ll}}$ distribution in the CRz region before and after applying the derived scale factor are shown in Figure 7.13 and Figure 7.14, respectively. From these figures, one can see that the Data and MC agreement is improved, and the ratio is now well within the uncertainties band (which includes both statistical and systematic uncertainties).

7.4.2 Fake and non-prompt lepton backgrounds

The $t\bar{t}$+jets events are selected based on the identification of one or two charged isolated lepton originating from the W-boson decays. These leptons are referred to as real-prompt leptons. However, electrons or muons produced from semileptonic decays of b- and c-quarks, or electrons from photon conversions or misidentified jets, may pass the lepton identification and isolation requirements and end up being identified as real prompt leptons. These leptons are referred to as fake or non-prompt leptons, mainly coming from the W+jets, and $t\bar{t}$ decays in the single-lepton channel (it is infrequent to have two fake or non-prompt leptons event). In this analysis, a so-called CRf region, enriched in events with one prompt and one fake or non-prompt lepton, is obtained by inverting the selection on the dilepton charges from opposite-sign to same-sign. The leading jet p_T

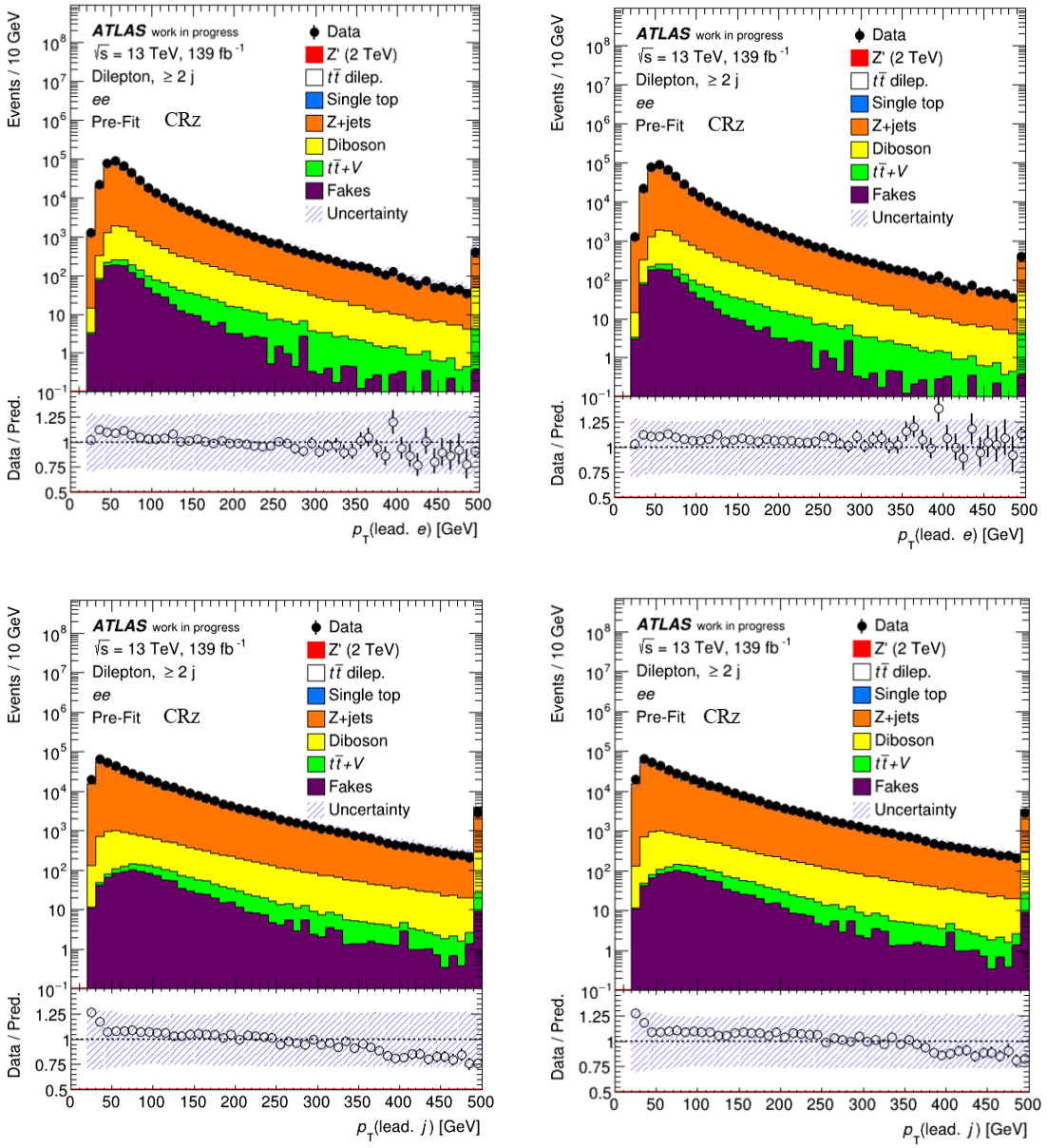

FIGURE 7.13: p_T of leadind electron and jet in ee channel and the dilepton system without (right) and with (left) the $Z_{SF,p_{T_{ll}}}$ reweighting scale factor for events with at least two jets and including the statistical and systematic uncertainties.

distribution in the CRf without applying the Z-boson mass window cut for events in the regions ≥ 2 jet and ≥ 2 b-tag, respectively, are shown in Figure 7.15.

From these figures, it can be noted how significant contributions are coming from $t\bar{t}$+jets, Z+jets, diboson events are obtained with two real prompt leptons. This is due to the non-negligible misidentification of electron charge, which is defined as the probability for an electron to have a wrong reconstructed electric charge and happens only in ee and $e\mu$ decay channels. To ensure that the MC simulations model correctly the charge-misidentification

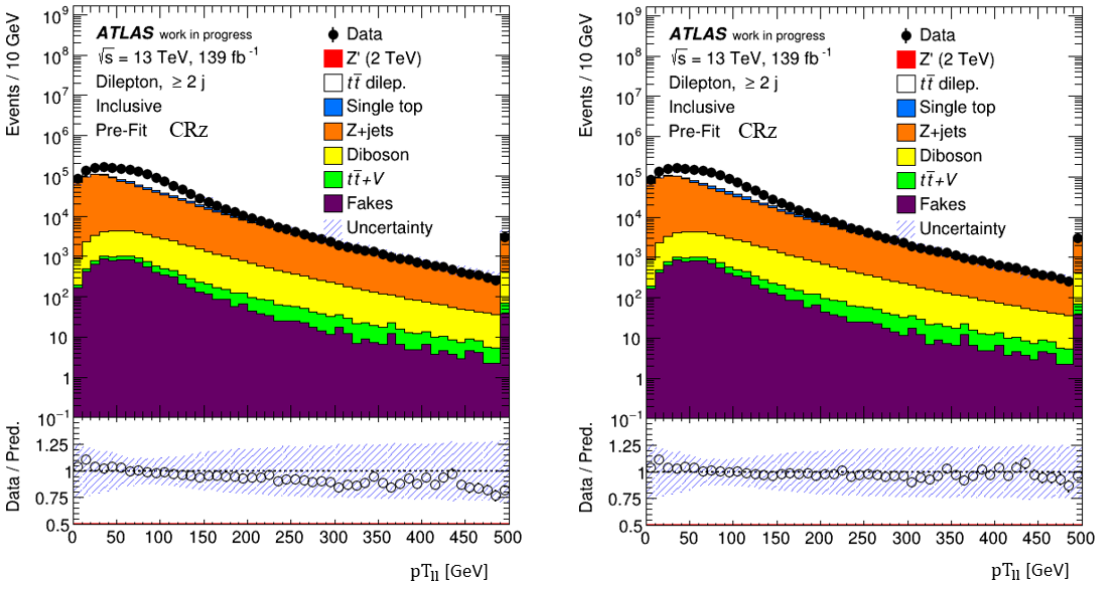

FIGURE 7.14: Dilepton system $p_{T_{ll}}$ without (left) and with (right) the $\mathrm{Z}_{SF,\mathrm{pT_{ll}}}$ reweighting scale factor for events with at least two jets and including the statistical and systematic uncertainties.

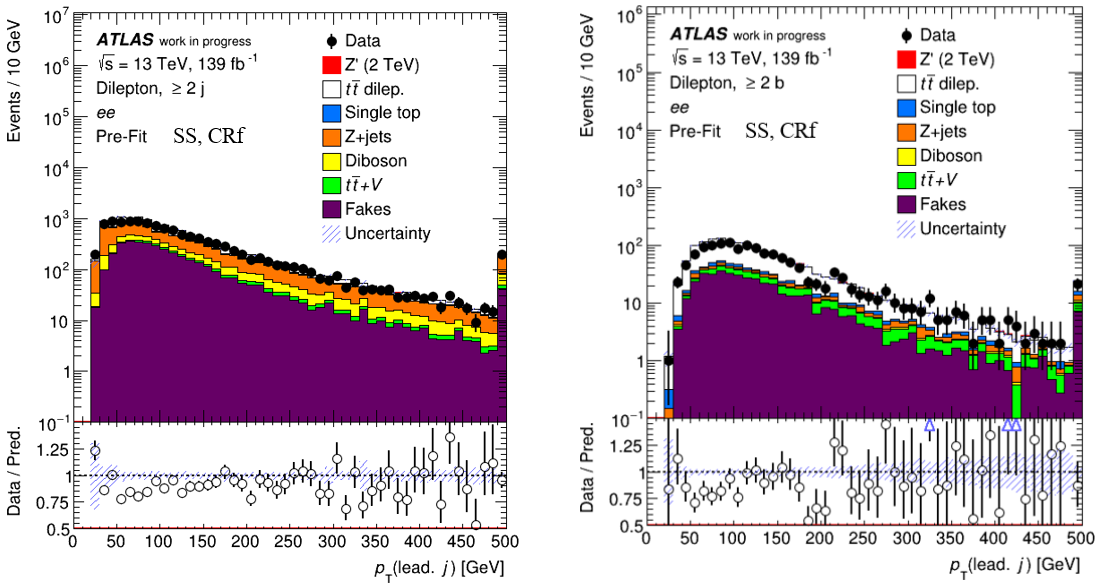

FIGURE 7.15: Leading jet p_T in the CRf for events with same-sign SS lepton, and at least two jets (left) and two b-tagged jets (right), respectively, including only the statistical uncertainty.

rate, data is compared with simulation for events with dielectron invariant mass $85 < M_{ee} < 95$ GeV for events and in the region ≥ 2 jet and ≥ 2 b-tag, respectively, as shown in Figure 7.16.

Table 7.4 presents the expected number from data and MC samples events in the CRf region and with applying different selections on the number of b-tagged jets. From this table, one can see that the fake or non-prompt electron rate and the electron charge misidentification probability are well modelled in the MC samples and in agreement with data based on the number of selected b-tagged jets. The main contribution in the region ≥ 2 jet comes from Z+jets while in the region ≥ 2 b-tag, it comes from the Z+jets and $t\bar{t}$+jets. Finally, neither of the systematic uncertainties or scale factor is applied based on the CRf test. Since the Data and MC agreement is good, and the fake-background uncertainty is already including the systematic uncertainty at 30% variations (see Section 7.5).

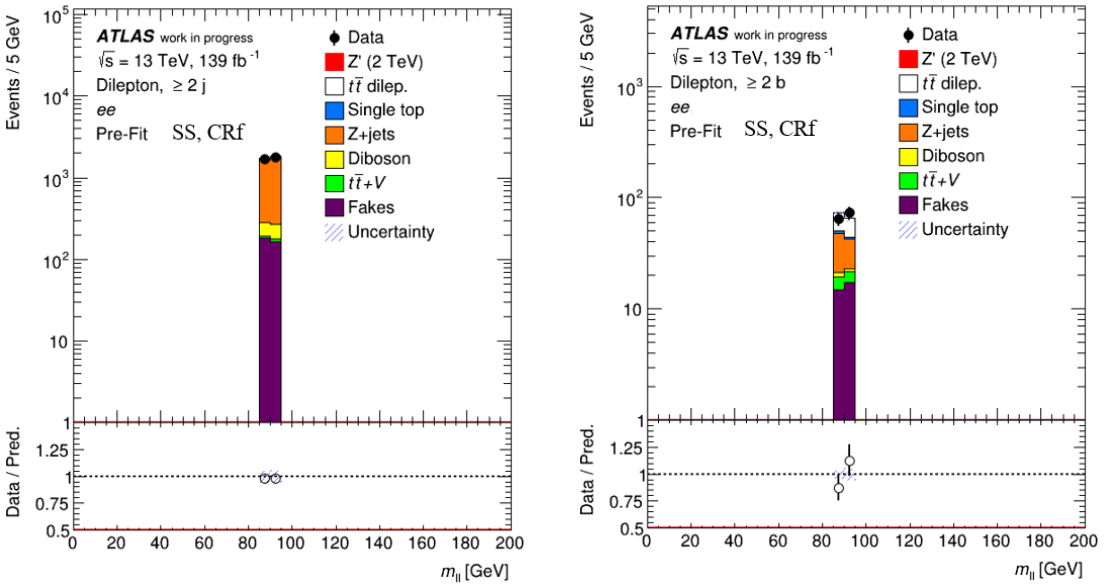

FIGURE 7.16: Dielectron invariant mass in the CRf and the Z-boson mass window for events with same-sign SS lepton and at least two jets (left) and b-tagged jets (right) and including only the statistical uncertainty.

	≥ 2 jet	≥ 1 b-tag	≥ 2 b-tag
$t\bar{t}$	155	125	45
Single top	10	9	3
Z+jets	2831	393	46
Diboson	183	27	3
$t\bar{t}V$	25	730	9
Fakes	730	347	32
total MC	3552	791	138
Data	3468	730	137

TABLE 7.4: Number of events in the Z-mass window for different jets selection in the decay channel *ee*.

7.5 Systematic uncertainties

In this analysis, several sources of systematic uncertainties are affecting the expected limits on the cross-sections×branching-ratio for different BSM signals. These uncertainties are separated into two categories and illustrated in details in the following sections. The first category includes the experimental systematics uncertainties, which are related to the detector response for different physics objects. The second one includes theoretical uncertainties, which are mainly related to the modelling of the background events. Table 7.5 summarises all the considered systematic uncertainties, their types, which indicate if they affect the normalisation only or both the shape and the normalisation, and the number of components to parametrise the uncertainty.

7.5.1 Experimental uncertainties

The experimental uncertainties, which are coming from detector response, particle identifications, etc., might be affecting the expected limits on the cross-sections×branching-ratio in the dilepton final state. They are as follows:

Luminosity: The uncertainty in the integrated luminosity corresponding to the full Run 2 dataset and obtained from the LUCID-2 detector for the baseline luminosity measurements [170], is set to 2.1%. The calibration of the luminosity scale is derived using the x-y beam-separation scan following the methodology presented in Ref[171].

Pile-up reweighting: The uncertainty on the reweighting procedure to correct the pile-up distributions predicted by MC simulation to those in data ones is derived based on the disagreement between data and MC pile-up distributions [172].

Lepton identification, reconstruction, isolation and trigger: The uncertainties on the scale factors to correct the differences between data and MC for electrons and muons reconstruction, identification, isolation and trigger performances are obtained using the tag-and-probe method [18, 21, 91, 173].

Lepton momentum scale and resolution: The uncertainties on the momentum scale and resolution are derived using the methods introduced in Ref[18, 21] to reconstruct events in $Z \to l^+l^-$, $J/\psi \to ll$ and $W \to e\nu_e$ samples [21, 173].

Jet Vertex Tagger: The uncertainty associated with the JVT is evaluated using the JetVertexTagger-Tool by varying the JVT cut up and down. It is, also included the uncertainty on the pile-up jets estimation after pile-up suppression and the systematic uncertainty assessed by generating the $Z \to \mu\mu$ and $t\bar{t}$ events using different MC generators [174].

Jet Energy Scale: The JES uncertainty in data is obtained using the MC-based corrections and in situ techniques, as described in Ref[95, 104]. Here, the JES uncertainty set contains 22 independent systematic variations with different jet p_T and η dependencies and including their up and down variation [175].

Jet Energy Resolution: The JER uncertainty is determined using a similar strategy to the JES scale systematic uncertainties and obtained using the JERSmearingTool as a function of the jet p_T and η. Therefore, seven nuisance parameters take into account various effects evaluated from the difference between the JES for data and MC simulation [101, 175].

Heavy flavour tagging: The b-tagging calibration uncertainties for b-jets, c- and light-jets are determined separately. Nine, four and four independent systematic variations are assigned to tagging efficiencies for b-, c- and light-jets, respectively. Two additional variations are assigned to the high-p_T extrapolation for b- and c-jets efficiencies, respectively, [105, 107–109].

Missing Transverse energy scale and resolution: Several sources of uncertainties are combined into three independent systematic variations for the total uncertainty on MET scale and resolution [110].

7.5.2 Background modelling

The uncertainties related to the main background, which is the SM $t\bar{t}$ production, are grouped into three main uncertainties and presented in the following. These uncertainties affect the $\Delta\phi_{l^+l^-}$ and $\Delta\eta_{l^+l^-}$, which will be indroduced in the following Section 7.7, between the real prompt leptons coming from $t\bar{t}$ decays in the chain of the BSM signals with different mass hypotheses, see Section 7.1. Also, they affect the m_{llbb} variable, which is reconstructed from the real prompt leptons and the b-tagged jets.

$t\bar{t}$ matrix element uncertainty, parton shower and the hadronisation modelling: To estimate the so-called ME-PS matching uncertainty, which is related to the choice of the NLO matrix element (ME) generator, the nominal SM $t\bar{t}$ sample (genereted using PowhegBox +Pythia8 see Section 7.3) is compared with an alternative sample generated using Madgraph5+ aMC@NLO interfaced with Pythia8. Similarly, the uncertainty arising from the parton shower (PS) and hadronisation model is evaluated by comparing with the nominal one with another alternative sample generated using PowhegBox and interfaced with Herwig7.

Radiation modelling: To obtain the uncertainty arising from the initial- (ISR) and final-state radiations (FST), respectively, alternative samples with different factorisation and renormalisation scales are generated using PowhegBox and interfaced with Pythia8 for showering. In the case of ISR variations, four uncorrelated variations are considered: factorisation and renormalisation scales in the hard scattering are independently varied up and down by a factor of two, the α_S parameter controlling the ISR in the parton shower was varied according to the A14 tune Var3c variation, see Ref[176]. Finally the nominal configuration was compared with a sample where the h_{dame} parameter, which controls the p_T of the first additional emission beyond the Born configuration, was increased from 1.5 to 3 times the top-quark mass. On the other hand, to obtain the

FSR uncertainty, the renormalisation scale is varied by a factor of two or half to reduce or enhance the FSR radiation in the parton shower, respectively [176].

Other background uncertainties: In this analysis, to take into account the theoretical cross-section and the acceptance uncertainties, normalisation uncertainties of 30% or 50%, depending on the process, are assigned to take into account both effects, but in an uncorrelated way between different processes.

Systematic uncertainty	Type	Number of Components
Experimental uncertainties		
Luminosity	N	1
Pile-up reweighting	SN	1
Electron trigger, reco, ID and isolation	SN	4
Electron energy scale and resolution	SN	2
Muon trigger, reco, ID and isolation	SN	8
Muon energy scale and resolution	SN	5
Jet vertex tagger (JVT)	SN	1
Jet energy scale (JES)	SN	22
Jet energy resolution (JER)	SN	7
Missing transverse energy scale and resolution	SN	3
b-tagging efficiency	SN	9
c-tagging efficiency	SN	4
light-tagging efficiency	SN	4
high-p_T extrapolation for b- and c-jets	SN	2
Background modelling		
$t\bar{t}$ matrix element and parton shower (ME-PS)	SN	1
$t\bar{t}$ parton shower (PS) and hadronisation	SN	1
Radiation modelling (ISR)	SN	4
Radiation modelling (FSR)	SN	1
Top_{p_T} reweighting	SN	1
Z+jets $p_{T_{ll}}$ reweighting	SN	1
Z+jets normalisation	N	1
W+jets normalisation	N	1
Fakes normalization	N	1
$t\bar{t}V$ normalization	N	1
Diboson normalisation	N	1
Single top normalisation	N	1

TABLE 7.5: Summary of the considered systematic uncertainties. The systematic uncertainties of type "N" mean that they are affected as normalization-only in all processes and channels, while those with "SN" type they are taken on both shape and normalization. Some of the systematic uncertainties are split into several components for more accurate treatment.

7.6 Statistical interpretation

The goal of many experiments in High Energy Physics is to search for new physics predicted by the SM or BSM models and to set the upper limits on the prediction of one or more parameters of interest, e.g. production cross-section or particle mass predicted by these hypotheses, in the absence of significant excess about the background expectations. In this analysis, The expected limit on the $t\bar{t}$ resonances cross-section×branching-ratio is set with 95% Confidence Level (CL) using the CLs method, see Ref[124, 177, 178]. The procedure for setting the expected limit is built based on a binned likelihood [124], which is constructed as a product of Poisson probability terms overall bins considered for each BSM signal and defined as,

$$L = \prod_i Poiss(n_i; \mu(\theta_1 ... \theta_m)) \tag{7.3}$$

where μ is the signal-strength parameter, which is a multiplicative factor to the theoretical cross-section, and θ is a set of nuisance parameters which encode the effect of several systematic uncertainties on both signal and background expectations. The nuisance parameters can be implemented as Gaussian, log-normal or Poisson constraints in the Likelihood, see Ref[124]. The BSM models with different mass assumptions (signal hypotheses) are tested based on the so-called profile likelihood ratio (test statistic) q_μ, which is defined as follows,

$$q_\mu = -2ln(\frac{L(\mu,\hat{\hat{\theta}})}{L(\hat{\mu},\hat{\theta})}) \tag{7.4}$$

where $\hat{\hat{\theta}}$ correspond to the values that maximise the $L(\mu, \hat{\hat{\theta}})$ for a specific value of μ (conditional maximum-Likelihood), and $\hat{\mu}$ and $\hat{\theta}$ are the values of parameters that maximize the $L(\hat{\mu}, \hat{\theta})$ (unconditional maximum-Likelihood) with constraint $0 \leq \hat{\mu} \leq \mu$. The test statistic q_μ is implemented in RootFit package [179, 180] and used with CLs method to set the upper limit on signal cross-section production×branching-ratio where CLs is computed based on the asymptotic approximation, see Ref[181].

7.7 Results and Conclusion

In this section, a preliminary study is presented for the search for $t\bar{t}$ resonances in the dilepton channel using the full ATLAS run-2 proton-proton collision data. Moreover, the importance of including angular observables sensitive to the top-quark pair spin correlation is assessed. A signal region is defined using events which are passing the selections, see table 7.3, in order to extract the expected limits on the cross-section×branching-ratio for the studied BSM signals. In this region, three observables are used to set the expected limits on the cross-section×branching-ratio for each BSM signal and to show which observable might increases the sensitivity to the presence of BSM signals. These observables are m_{llbb}, $\Delta\phi_{ll}$ and $\Delta\eta_{ll}$, where the $\Delta\eta_{ll}$ is the η difference between the two leptons produced from the W-boson decay in the chain of $t\bar{t}$. For each of the two options $\Delta\phi_{ll}$ and $\Delta\eta_{ll}$, the variable is scanned in ten bins of m_{llbb}, i.e. ten of the $\Delta\phi_{ll}$ or $\Delta\eta_{ll}$ distributions, each filled with events in a certain m_{llbb} bin (e.g. $300 < m_{llbb} < 400$ GeV) are built and simultaneously used for the statistical analysis.

The inclusive distributions for m_{llbb}, $\Delta\phi_{ll}$ and $\Delta\eta_{ll}$ are shown in Figure 7.17. On the other hand, Figure 7.18 and Figure 7.19 show the expected distributions for $\Delta\phi_{ll}$ and $\Delta\eta_{ll}$, respectively, in each bin of m_{llbb}. To keep analysis blind, no real data is shown for all the up-coming figures as well as for the fits and limit extractions.

The expected limits on the cross-sections×branching-ratio in the dilepton decay channel extracted using the defined observables in the signal region, including the statistical uncertainty only is shown in Figure 7.20. On the other hand, Figure 7.21 shows the expected limits extracted from the three observables, including both statistical and systematic uncertainties for all studied BSM signal (see table 7.1). The obtained expected exclusion limits are found to be worse, but of the same order of magnitude, of those obtained in different $t\bar{t}$ decay channels (see Refs[40, 41]), hence suggesting sensible gain from the combination of all these channels.

Tables 7.6, 7.7 and 7.8 summarise the expected limits on the cross-sections×branching-ratio with 95% CL upper limits in the studied channel using the defined observables (the $\Delta\phi_{ll}$ and $\Delta\eta_{ll}$, which are scanned in ten bins of m_{llbb}, and the inclusive m_{llbb}) in the signal

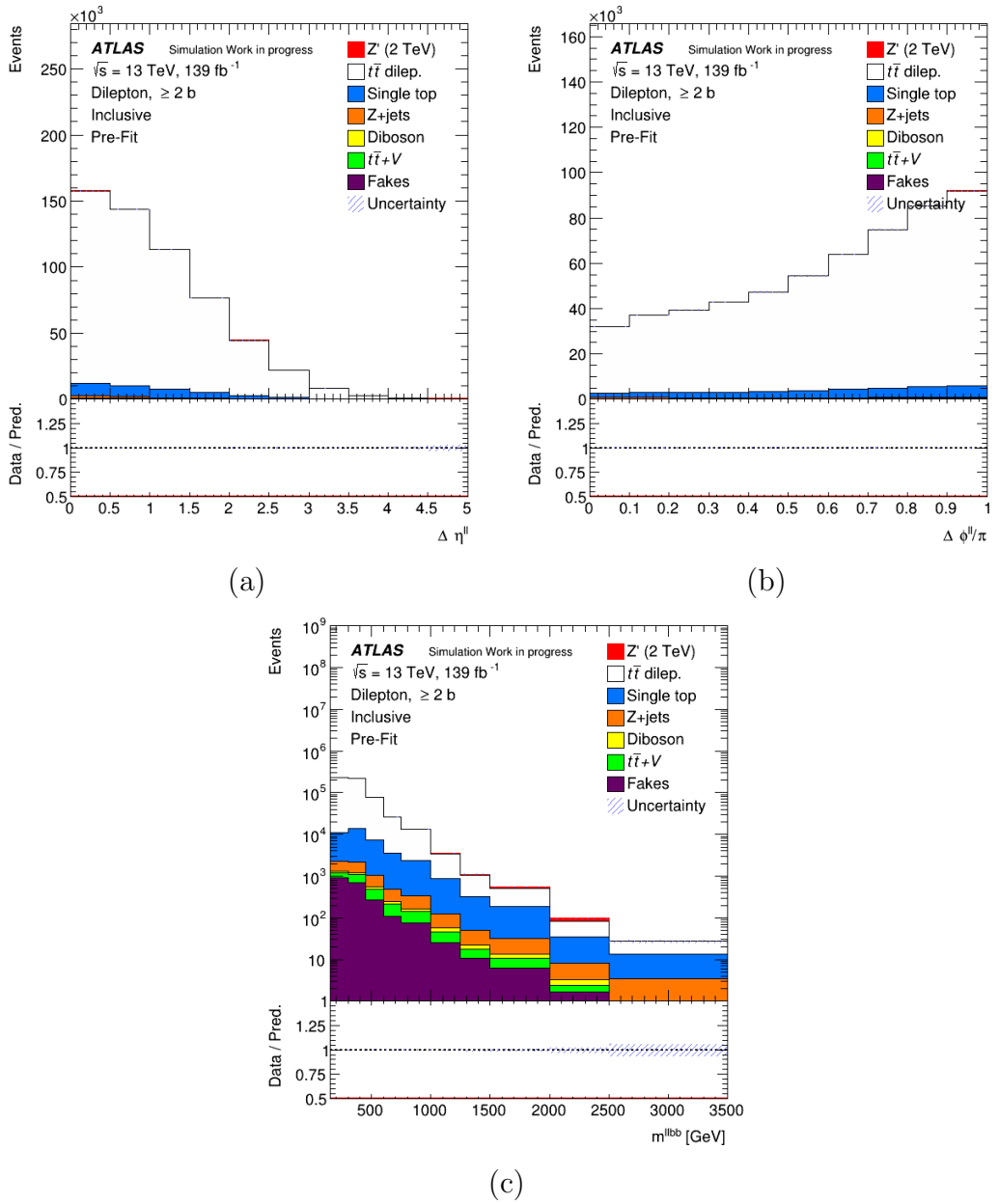

FIGURE 7.17: Inclusive distributions for (a) $\Delta\eta_{ll}$, (b) $\Delta\phi_{ll}$ and (c) m_{llbb}, respectively.

region as a function of the hypothetical particle mass for Z' signal (see Appendix D for KK_g and G signals).

From Figure 7.20 and Figure 7.21 (see tables 7.6, 7.7 and 7.8), one can see that the expected limits on the cross-sections×branching-ratio for the studied BSM signals obtained from the scanning of $\Delta\phi_{ll}$ in ten bins of m_{llbb} are slightly better, in particular for massive BSM particles in the TeV range, compared to those extracted from m_{llbb} alone and from $\Delta\eta_{ll}$ scanned in ten bins of m_{llbb}. Therefore, new expected limits are set using the $\Delta\phi_{ll}$ scanning in the ten bins of m_{llbb} on to the theoretical prediction of the cross-sections in

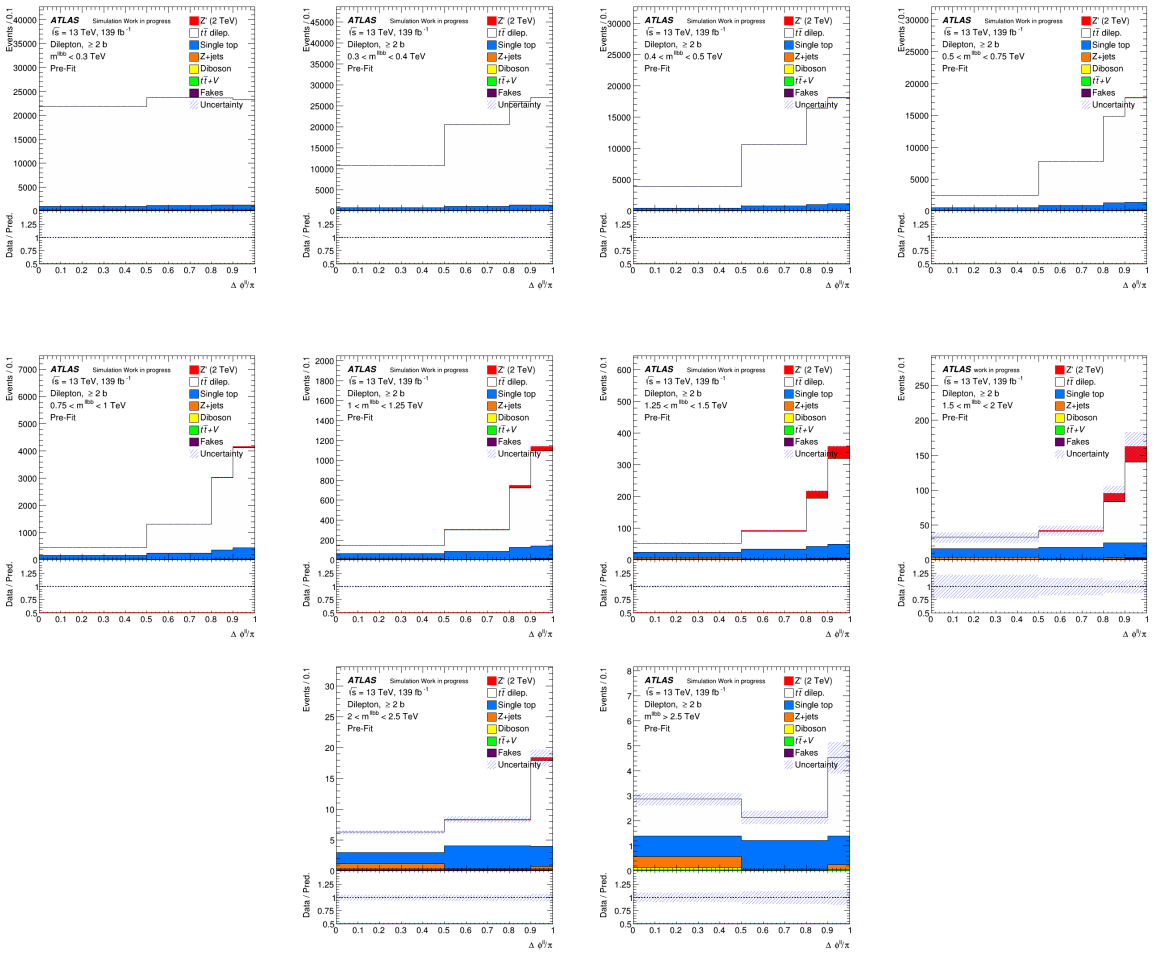

FIGURE 7.18: $\Delta\phi_{ll}$ distributions for each bin of m_{llbb}.

	Expected $\sigma(pp\to Z')\times BR(Z'\to t\bar{t})$			Scanned $\Delta\phi_{ll}$	
		Statistical only		Statistical + Systematics	
Z' Mass [TeV]	Theor. [pb]	Exp. [pb]	$\pm1\sigma$	Exp. [pb]	$\pm1\sigma$
.5	52.162	2.128	[2.961, 1.534]	14.075	[19.502, 10.142]
.75	13.913	1.	[1.392, 0.721]	2.771	[3.855, 1.996]
1.	4.808	0.538	[0.749, 0.388]	1.543	[2.147, 1.112]
2.	0.2239	0.1126	[0.1574, 0.0812]	0.1526	[0.2129, 0.1099]
3.	0.0217	0.0603	[0.0850, 0.0434]	0.0739	[0.1041, 0.0532]
4.	0.00275	0.0528	[0.0755, 0.0381]	0.0624	[0.0898, 0.0449]
5.	0.00043	0.0657	[0.0947, 0.0474]	0.0768	[0.1124, 0.0553]

TABLE 7.6: Expected limits (Exp.), using the scanned $\Delta\phi_{ll}$ in ten m_{llbb} bins, on the cross-sections×branching-ratio ($\sigma(pp\to Z')\times BR(Z'\to t\bar{t})$) with a CL of 95% on the Z' boson, from the Topcolor (TC2) model, decaying to a top-quark pair. The expected limits are quoted both without and with systematics uncertainties taken into account. Also, the $\pm1\sigma$ uncertainty on the expected limits is shown.

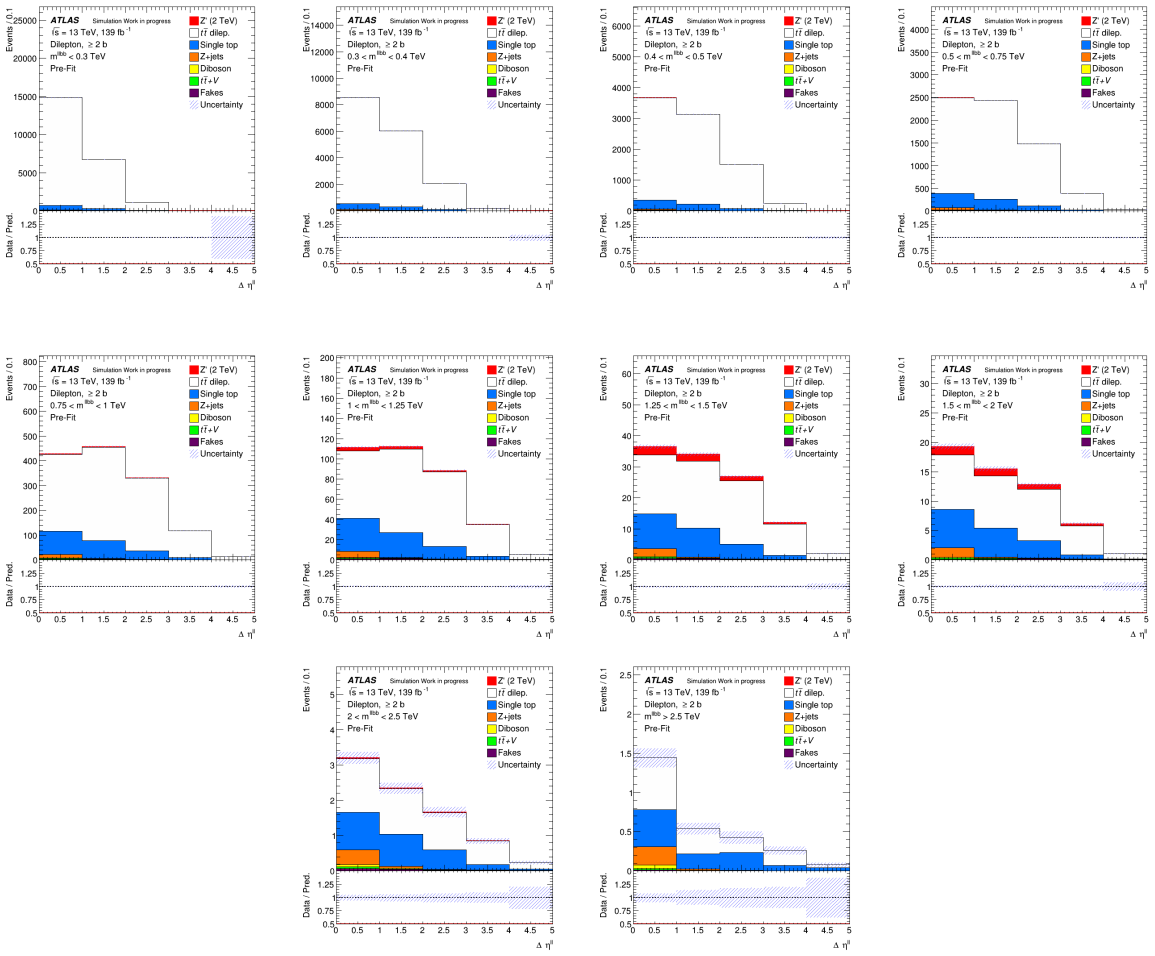

FIGURE 7.19: $\Delta\eta_{ll}$ distribution for each bin of m_{llbb}.

	Expected $\sigma(pp\to Z')\times BR(Z'\to t\bar{t})$			Scanned $\Delta\eta_{ll}$	
		Statistical only		Statistical + Systematics	
Z' Mass [TeV]	Theor. [pb]	Exp. [pb]	$\pm1\sigma$	Exp. [pb]	$\pm1\sigma$
.5	52.162	2.251	[3.132, 1.622]	10.412	[14.374, 7.502]
.75	13.913	0.992	[1.380, 0.715]	3.216	[4.463, 2.317]
1.	4.808	0.533	[0.743, 0.384]	1.551	[2.16, 1.118]
2.	0.2239	0.1389	[0.1937, 0.1]	0.2662	[0.37, 0.1918]
3.	0.0217	0.0839	[0.1177, 0.0605]	0.1149	[0.161, 0.08277]
4.	0.00275	0.0756	[0.107, 0.0545]	0.0941	[0.1337, 0.0678]
5.	0.00043	0.09159	[0.1304, 0.066]	0.1142	[0.1640, 0.0823]

TABLE 7.7: Expected limits (Exp.), using the scanned $\Delta\eta_{ll}$ in ten m_{llbb} bins, on the cross-sections×branching-ratio ($\sigma(pp\to Z')\times BR(Z'\to t\bar{t})$) with a CL of 95% on the Z' boson, from the Topcolor (TC2) model, decaying to a top-quark pair. The expected limits are quoted both without and with systematics uncertainties taken into account. Also, the $\pm1\sigma$ uncertainty on the expected limits is shown.

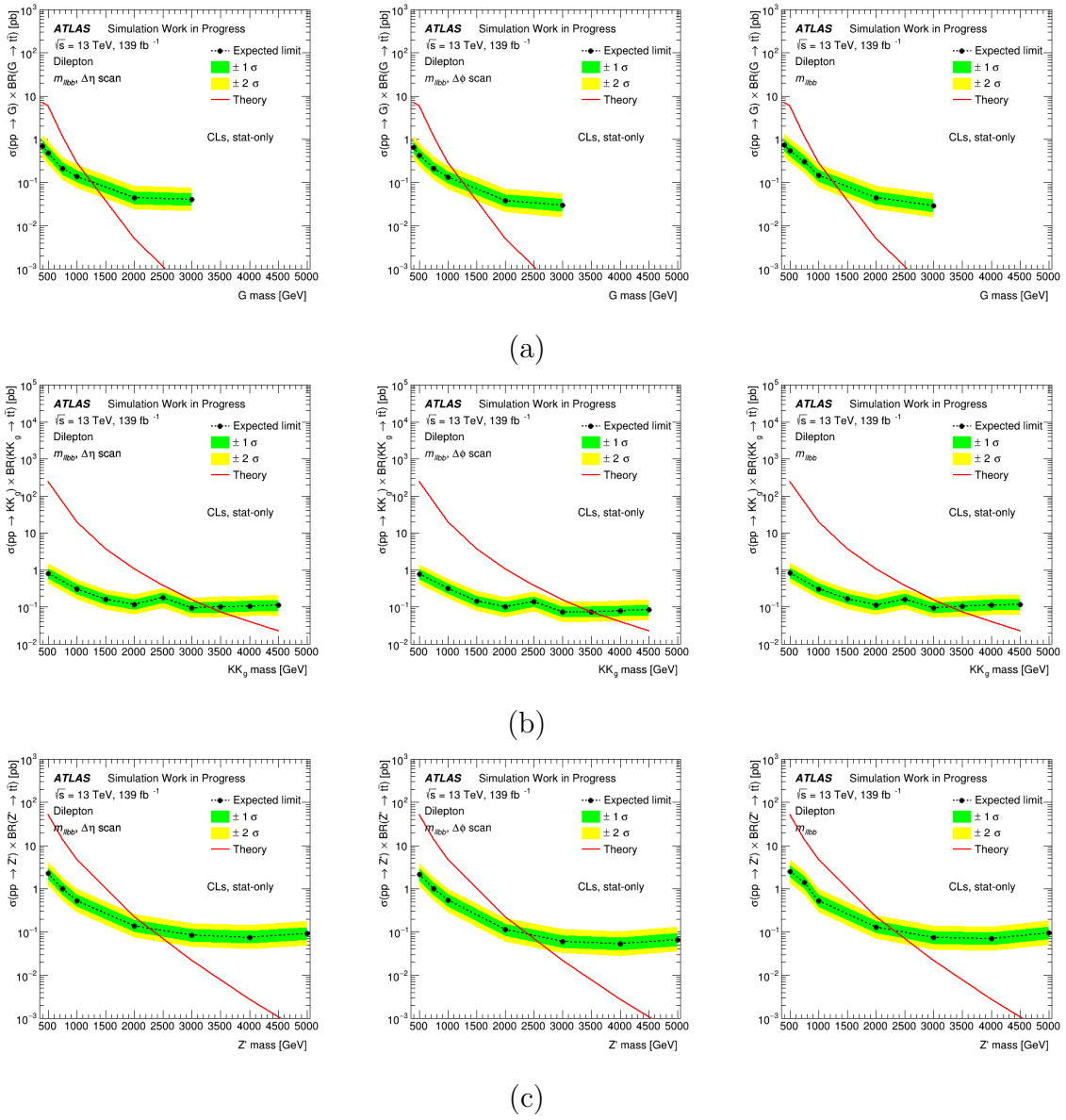

FIGURE 7.20: Expected limits on the cross-sections×branching-ratio of (a) G (b) KK_g and (c) Z' in the dilepton final state including stat-only.

the dilepton channels for the TC2 (Z') and the Randall-Sundrum (KK_g and G) models, respectively. The new expected limits on the cross-section×btranching-ratios for masses less than, 2 TeV, 3.5 TeV and 1 TeV, for the BSM particles Z', KK_g and G, respectively, are higher than the theoretical predictions. On the other hand, for higher masses, expected limits on the cross-sections×branching-ratios are two times higher the theoretical predictions.

A background-only fit is performed to the Asimov dataset, to investigate the fitted model responses before the unblinding process as well as the expected constraints on the nuisance

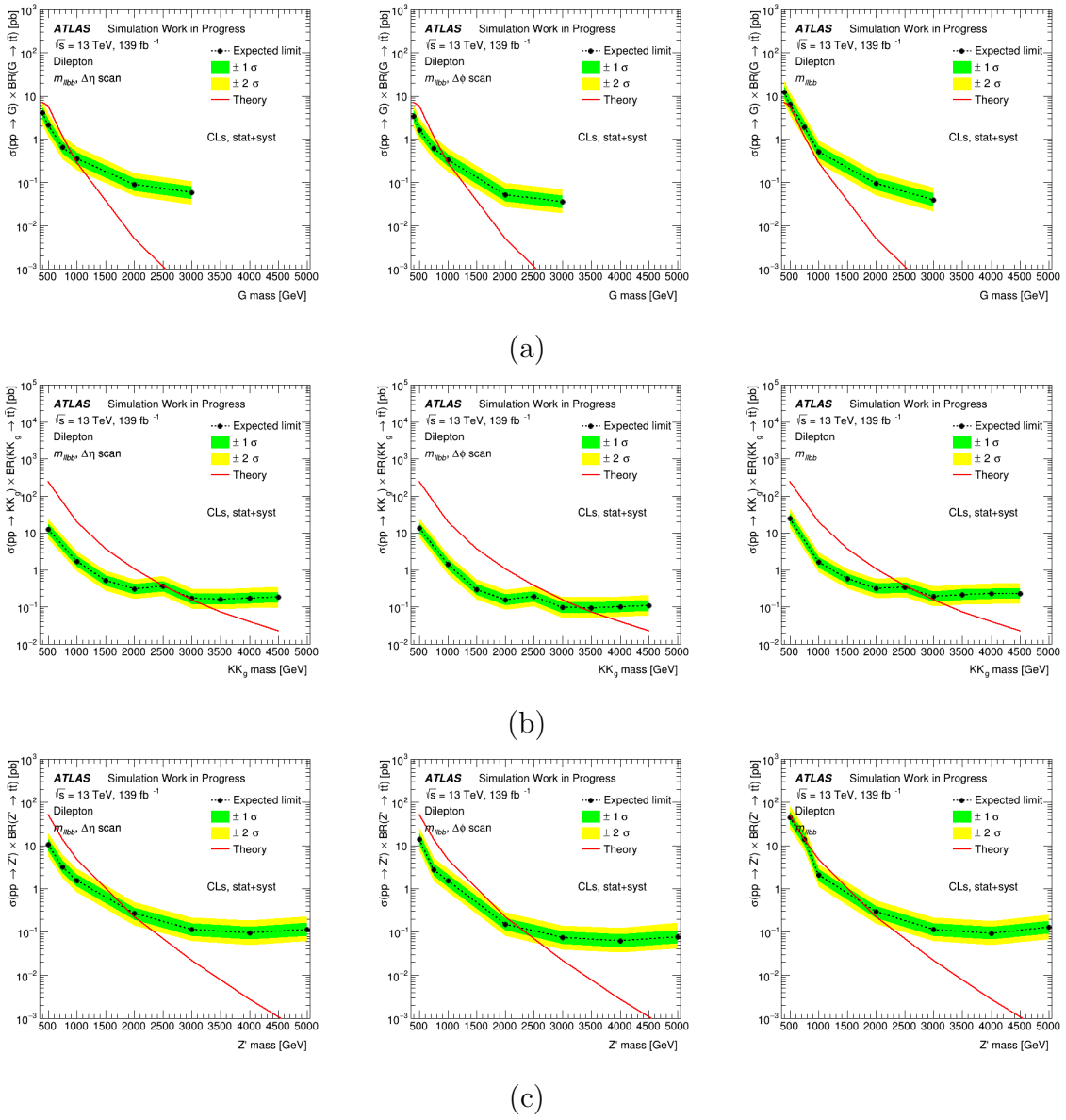

FIGURE 7.21: Expected limits on the cross-sections×branching-ratio of (a) G (b) KK_g and (c) Z' in the dilepton final state including stat+syst uncertainties.

parameters. Figure 7.22 shows the constraints on the nuisance parameters, which are included in the instrumental and modelling systematic uncertainties, after applying the pruning procedure as well as the correlation matrix between all the nuisance parameters.

Despite the systematic uncertainty model is still incomplete, all the main sources of uncertainty were included and their impact evaluated. Figure 7.23 shows the ranking plots (see Ref[33] for more details about ranking plots) of nuisance parameters extracted from the fitting of the three observables for the Z' particle with a mass equal to 2 TeV. From these plots, where the nuisance parameters appearing on the top are those associated

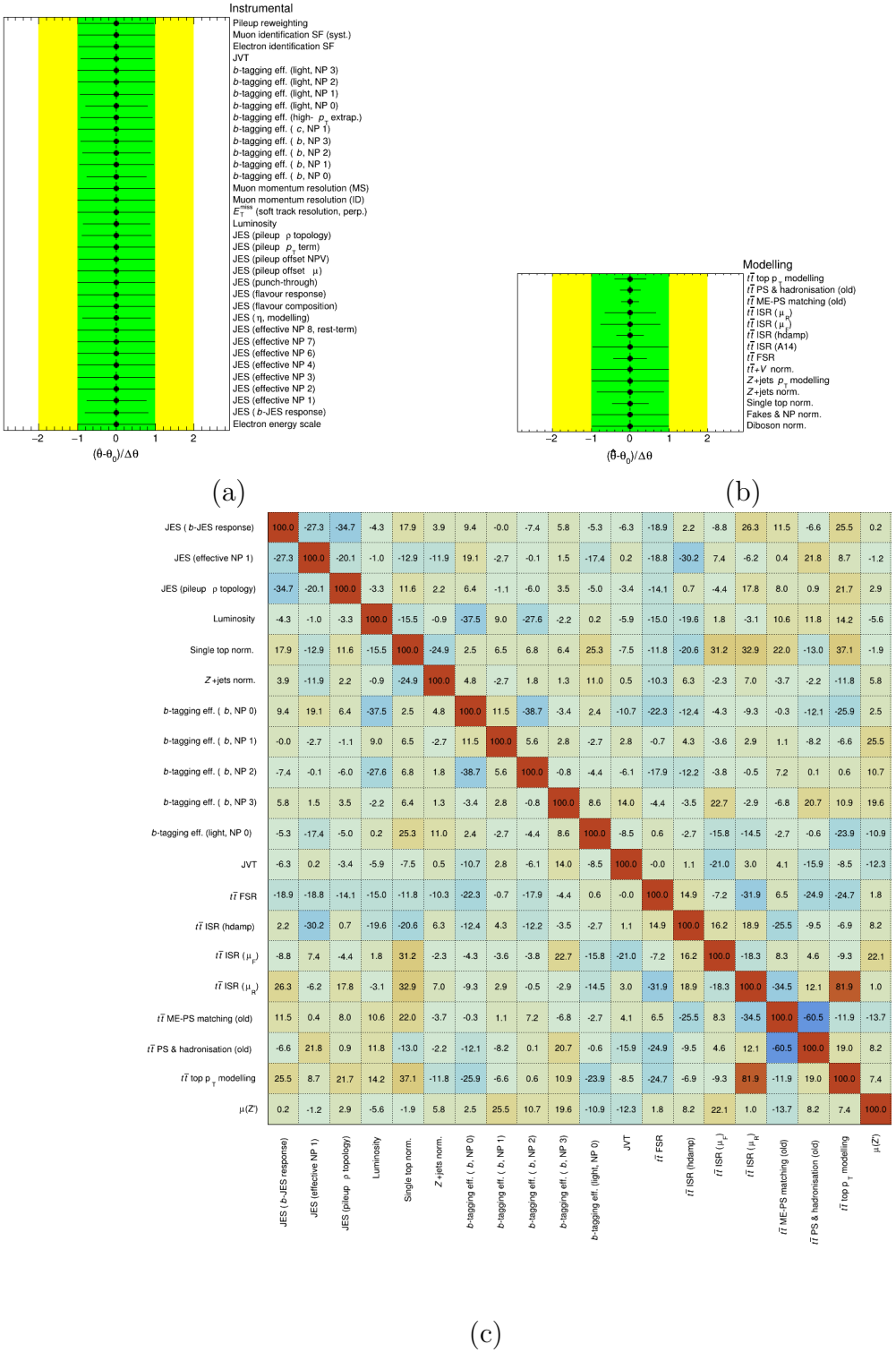

FIGURE 7.22: Constraints on the instrumental (a) and the modelling (b) nuisance parameters, respectively. Below (c) is the correlation matrix between all the nuisance parameters. The green and yellow areas represent the $\pm 1\sigma$ and $\pm 2\sigma$, respectively, on the pre-fit systematic uncertainty.

Expected $\sigma(pp \to Z') \times BR(Z' \to t\bar{t})$		Inclusive m_{llbb}			
		Statistical only		Statistical + Systematics	
Z' Mass [TeV]	Theor. [pb]	Exp. [pb]	$\pm 1\sigma$	Exp. [pb]	$\pm 1\sigma$
.5	52.162	2.534	[3.524, 1.826]	44.358	[60.967, 31.962]
.75	13.913	1.392	[1.936, 1.003]	13.843	[19.439, 9.974]
1.	4.808	0.53	[0.737, 0.382]	2.058	[2.838, 1.483]
2.	0.2239	0.13	[0.1815, 0.0937]	0.2923	[0.4049, 0.2106]
3.	0.0217	0.0737	[0.104, 0.0532]	0.1138	[0.16, 0.082]
4.	0.00275	0.0691	[0.0978, 0.0498]	0.0930	[0.1321, 0.0670]
5.	0.00043	0.0943	[0.1334, 0.0679]	0.128	[0.1819, 0.0922]

TABLE 7.8: Expected limits (Exp.), using the inclusive m_{llbb}, on the cross-sections×branching-ratio ($\sigma(pp \to Z') \times BR(Z' \to t\bar{t})$) with a CL of 95% on the Z' boson, from the Topcolor (TC2) model, decaying to a top-quark pair. The expected limits are quoted both without and with systematics uncertainties taken into account. Also, the $\pm 1\sigma$ uncertainty on the expected limits is shown.

with the systematic uncertainties with the highest impact on the fitted signal strength, different lists of systematic uncertainties are seen. For example, using the scanned $\Delta\phi_{ll}$ variable, the main uncertainty is coming from the b-tagging efficiency, see Figure 7.23(b), while, the main ones are the Single-top normalisation and $t\bar{t}$ ME+PS for the scanned $\Delta\eta_{ll}$, see Figure 7.23(a), and the inclusive m_{llbb} variables, see Figure 7.23(c). Other ranking plots are presented for the studied model with different masses from the scanned $\Delta\phi_{ll}$, see Appendix D.

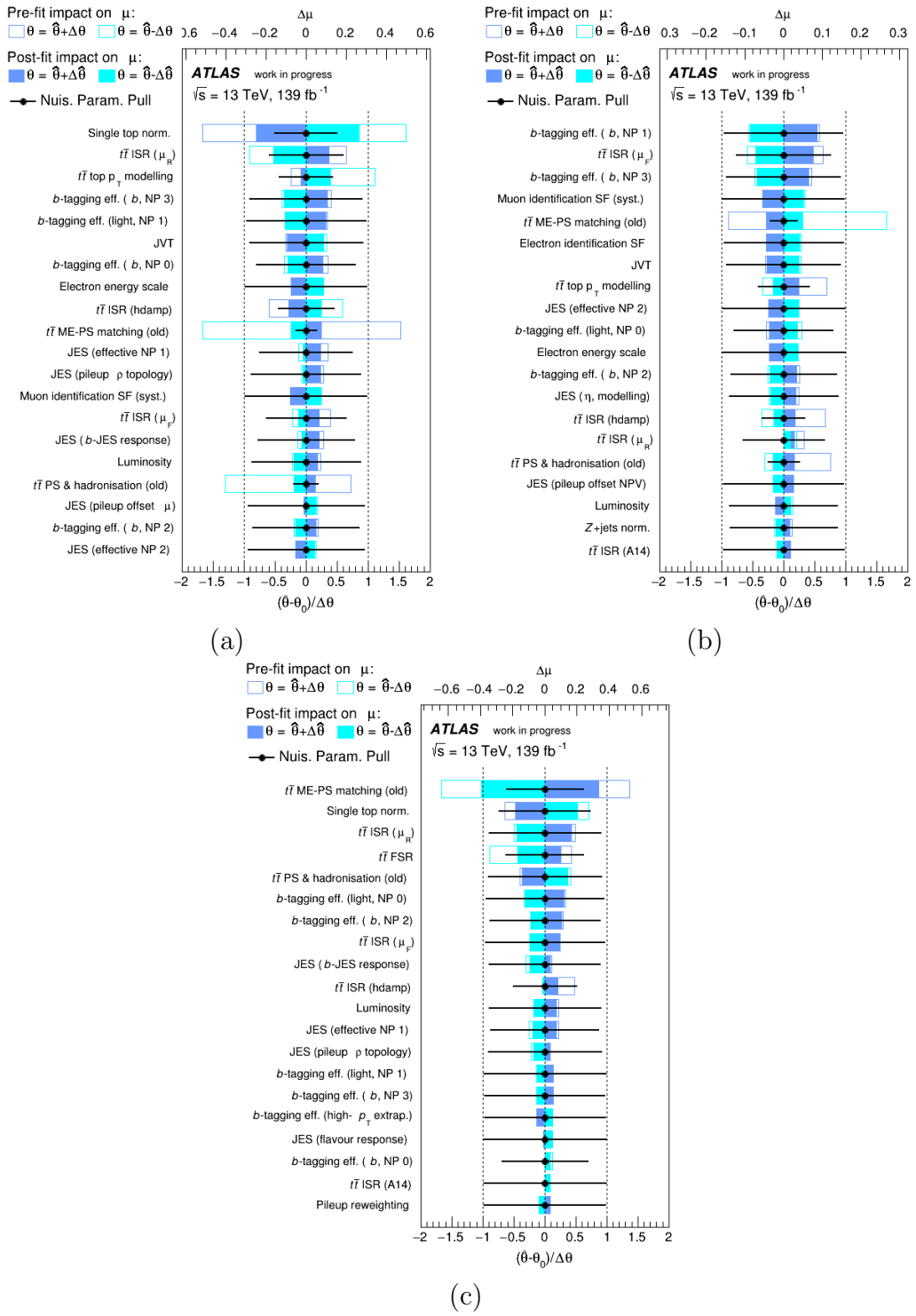

FIGURE 7.23: The ranking plot of the nuisance parameters in the signal regions depending on their impact on the expected signal strength μ for the observables (a) $\Delta\eta_{ll}$, (b) $\Delta\phi_{ll}$, and (c) m_{llbb}. The fit is performed under the signal-plus-background (SPLUSB) hypothesis with the benchmark TC2, Z', model with a mass = 2 TeV as a signal. Only the top 20 nuisance parameters (NP) are shown while those corresponding to the statistical uncertainties of the MC samples are not included here. The impact of each NP ($\Delta\mu$) is computed by measuring the difference between two fitted μ: the one corresponds to the nominal best-fit and the other obtained from the fit when fixing the considered NP (all other NP's are free to float) to its best-fit value, $\hat{\theta}$, shifted by its pre- ($\pm\Delta\theta$) and post-fit ($\pm\Delta\hat{\theta}$) uncertainties, respectively. The empty dark-blue/cyan rectangles correspond to the pre-fit impact on μ while the solid ones correspond to the post-fit impact on μ (both are referring the top horizontal scale). The black points (referring to the bottom horizontal scale) show the deviation of each of the fitted NP ($\hat{\theta}$) with respect to their nominal values (θ_0), in units of the pre-fit standard deviation $\pm\Delta\theta$.

Chapter 8

Conclusions

This thesis was developed in the field of top-quark physics at the Large Hadron Collider. The presented work made use of 139 fb^{-1} of data collected by the ATLAS experiment in the period 2015-2018, looking for possible deviations from the expected results predicted by the Standard Model.

My study mainly focusses on the production of multi-top-quark and the existence of possible resonances in the top pair, as two possible ways to identify New Physics beyond the Standard Model.

Throughout the analyses preparation, a detector performance study has also been exploited in the thesis. In essence, the study has been focused on ATLAS Inner Detector Performance Evaluation, a crucial tool for the identification and reconstruction of top-quark processes, due to the possibility that it offers to reconstruct secondary vertices characterising jets produced in the fragmentation of b-quarks coming from top-quark decays.

A new method has been presented to determine the relative efficiency of reconstructing pion tracks at low p_T in data and Monte Carlo (MC) in the ATLAS inner detector. This is crucial to extract the detector efficiency to reconstruct the charged pion at low transverse momentum and to have a cross-check on the MC estimations and performance. Also, it is play a central role to tag long-lived particles and to reconstruct their SV inside jets. The number of reconstructed events in both MC and data is determined by

fitting the $\Delta M = D^{*-}_{Mass} - D^{0}_{Mass}$ distributions using the sum of the modified Gaussian function, which is describing the signal, and a threshold function to fit the combinatorial background.

Initially, R, which is the ratio of BR($D^0 \to K^- 2\pi^+\pi^-$) relative to BR($D^0 \to K^-\pi^+$)), is evaluated using MC samples to check the validity of the defined selections and to test this method. The expected R-value using only the simulated events is equal to 1 while the measured one from this method is $R = 1.059^{-0.017}_{+0.023} \cong 1.06 \pm 0.03$, where the included uncertainty is only statistical. From this value, one can conclude that the tool and the applied selections are well defined.

Then, the relative efficiency $\epsilon(Data)/\epsilon(MC))$ for reconstructing pion tracks at low transverse momentum $p_T > 500$ MeV in data and MC is measured, and it is equal to $\epsilon(Data)/\epsilon(MC) = 0.99 \pm 0.13(stat)$. From this result, we can conclude that the ID efficiency of reconstructing the pion track is equal to the predicted one from MC simulation. Additionally, the pion tracks at low p_T are well modelled in the MC samples and in agreement with data.

As a second original contribution presented in this dissertation, a χ^2–based method is introduced to solve the final- state combinatorics in four-top-quark events partially and to help distinguish this process from background processes. This method is first studied in the single-lepton (1L) channel, in the signal region characterised by ≥ 10 jet and ≥ 4 b-tagged jets, using the fully-matched events where all the reconstructed physics objects (jets and charged leptons) are matched to those at parton- and truth-level.

On these fully-matched events (~ 700 events) in the 1L decay channel, the efficiency of the reconstruction of the two hadronic top quarks through the χ^2 method is estimated to be 32%. As a second step, the χ^2 method is applied and studied to reconstruct two hadronically decaying top-quarks (without requiring any matching process) in both the 1L and opposite-sign dilepton (OS) highest sensitive signal regions, SR1L and SROS.

A set of χ^2 output variables (i.e. the kinematics of the reconstructed top quarks and W-bosons, of jet combinations with χ^2_{min} value) have been produced using $t\bar{t}t\bar{t}$ signal events, and compared to those from the predicted background events.

These χ^2 output variables are used as inputs for a boosted decision tree (BDT) algorithm to discriminant the signal ($t\bar{t}t\bar{t}$) events from the total expected background estimated via MC simulation in the defined signal regions of 1L and OS dilepton decay channels, respectively. The expected separation between the signal and total background in 1L and OS dilepton channels using set1 (set2) variables are 9.4% (18.4%) and 16.6%(21.4%), respectively.

Finally, a preliminary study to a search for $t\bar{t}$ resonances in the dilepton channel is presented, highlighting the importance of including angular observables sensitive to the top- quark pair spin correlation. A signal region is defined using events, which passed the defined selections. The expected limits on the cross-section×branching-ratio of a new physics decaying to $t\bar{t}$ pair are set in the context of Topcolour Model (TC2) and Randall-Sundrum (RS) Models.

Three combinations of observables, including a partial reconstruction of the $t\bar{t}$ invariant mass and two simple spin-correlation sensitive variables, have been studied as signal discriminant variables. In particular, for massive BSM particles in the TeV, the $\Delta\phi_{l^+l^-}$, which is defined as the azimuthal opening angle between the two charged leptons (electron or muon), shows considerable sensitivity to the presence of new physics. As a result, the best-expected limits are obtained from the scanning of $\Delta\phi_{l^+l^-}$ in ten bins (The size of these bins is chosen based on the sample statistics) of m_{llbb}, where m_{llbb} is defined as the partial invariant mass of the top-antitop quark. These limits are obtained using the test statistic q_μ, which is implemented in RootFit, and used with CLs method.

Using this observable, one can conclude that, the expected limits on the cross section×branching-ratio for masses less than, 2 TeV, 3.5 TeV and 1 TeV, for the BSM particles Z', KK_g and G, respectively, are higher than the theoretical predictions. On the other hand, for higher masses, the expected limits on the cross-sections×branching-ratios are two times higher than the theoretical predictions. Therefore, for the three considered new physics models with masses below 2 TeV, 3.5 TeV and 1 TeV are expected to be excluded at 95% CL for a hypothetical heavy resonance decaying to $t\bar{t}$ pairs. Moreover, even if this gives weaker limits than those reachable in other $t\bar{t}$ decay channels, this $t\bar{t}$ dilepton decay channel may have a significant contribution if combined with them the others.

Appendix A

Quadratic equation

In several analyses, we need to obtain the Pz component for the neutrino from the missing energy to build the four-momentum component of the neutrino vector and to reconstruct, e.g. the top quark, W boson, new massive particles masses. One of these methods is to solve the quadratic equation to obtain the momentum component in the z-axis, Pz. The quadratic equation can be derived as follows,

$$m = 0(SM), \;\; E_T = p_T, \quad p_x = E_T \cos(\phi), \quad p_y = E_T \sin(\phi) \tag{A.1}$$

To find the p_z of the neutrino, the invariant mass for W-boson is reconstructed in details below,

$$m_w^2 = (P^\nu + P^l)^2 + m_\nu^2 + m_l^2 + 2E^\nu E^l - \vec{P^\nu}.\vec{P^l} \tag{A.2}$$

where $P^\nu(P^l)$ is the neutrino (lepton) four-momenta and m_l is lepton mass. Also, $\vec{P^\nu}.\vec{P^l}$ is the dot product between the 3-momenta (p_x, p_y, p_z) vectors of neutrino and lepton, which is defined as,

$$\vec{P^\nu}.\vec{P^l} = p_x^\nu p_x^l + p_y^\nu p_y^l + p_z^\nu p_z^l \tag{A.3}$$

$$m_w^2 - m_l^2 + 2(p_x^\nu p_x^l + p_y^\nu p_y^l) = 2|P^\nu|E^l - 2p_z^\nu p_z^l \tag{A.4}$$

For simplicity lets define $\alpha = m_w^2 - m_l^2 + 2(p_x^\nu p_x^l + p_y^\nu p_y^l)$. Then,

$$(\tfrac{\alpha}{2})^2 = (|P\nu E^l - p_z^\nu p_z^l)^2 \tag{A.5}$$

$$\frac{\alpha^2}{4} = [(p_x^\nu)^2 + (p_y^\nu)^2](E^l)^2 + (p_z^\nu)^2(E^l)^2 + (p_z^\nu)^2(p_z^l)^2 - 2|P^\nu|E^l p_z^\nu p_z^l \tag{A.6}$$

substitute $|P^\nu|E^l = \frac{\alpha}{2} + p_z^\nu p_z^l$,

$$\frac{\alpha^2}{4} = [(p_x^\nu)^2 + (p_y^\nu)^2](E^l)^2 + (p_z^\nu)^2(E^l)^2 + (p_z^\nu)^2(p_z^l)^2 - 2|P^\nu|E^l p_z^\nu p_z^l \tag{A.7}$$

$$(p_z^\nu)^2[(p_z^l)^2 - (E^l)^2] + \alpha p_z^\nu p_z^l + \frac{\alpha^2}{4} - [(p_x^\nu)^2 + (p_y^\nu)^2](E^l)^2 = 0 \tag{A.8}$$

$$x \to p_z^\nu, \;\; a = (p_z^l)^2 - (E^l)^2, \quad b = \alpha p_z^l, \quad c = \frac{\alpha^2}{4} - [(p_x^\nu)^2 + (p_y^\nu)^2](E^l)^2 \tag{A.9}$$

Finally, equation A.8 is in the form of the quadratic equation,

$$ax^2 + bx + c = 0 \tag{A.10}$$

and with the following solutions:

$$p_z^\nu = \frac{-b \pm \sqrt{(b^2 - 4ac)}}{2a} \tag{A.11}$$

Appendix B

Pion Track Efficiency

Figure B.1(a,b) shows the $\cos(\theta^*)$ and L_{xy} distributions at truth-level. From Figure B.1(a), it can be noted that the $\cos(\theta^*)$ distribution is uniformed over the full range $(-1, 1)$, this is because of the D^0 is a spin-zero particle. Therefore, from the conservation of angular momentum, the produced K^- meson in the reference frame of the D^0 does not have a specific orientation. On the other hand, the L_{xy} distribution shows that the D^0 meson flies away from the PV before it decays. As a result, the expected position of the SV from the D^0 decay to be outside the PV resolution, as shown in Figure B.2. Furthermore, the expected position of the D^{*+} decay vertex in Cartesian coordinates (x, y, z) at truth-level is shown in Figure B.2.

The transverse momentum, p_T, distributions for the D^{*+} and D^0 in the three decay channels ($D^0 \rightarrow K^-2\pi^+\pi^-$, $D^0 \rightarrow K^-\pi^+\rho^0$; $\rho^0 \rightarrow \pi^-\pi^+$ and $D^0 \rightarrow \bar{K}^{*0}\rho^0$) are shown in Figure B.3. Moreover, in Figure B.4, the kinematic distributions for the K^- and π^- mesons produced in the three studied channels are shown. From these figures, one can conclude (as expected) that the p_T, in particular for K^- and π^- mesons, has comparable distributions of those produced in the studied ($D^0 \rightarrow K^-2\pi^+\pi^-$) channel.

Figure B.5 shows the ΔM distributions for the $K\pi$ and $K3\pi$ channels using the simulated events, which are generated at $\sqrt{s} = 13$ TeV in 2018 and passed the defined selection in Section 5.3.3. From this figure, one can see the effect of applying the trigger selections on the studied channels (four-body and two-body decay channels). In the case of four-body

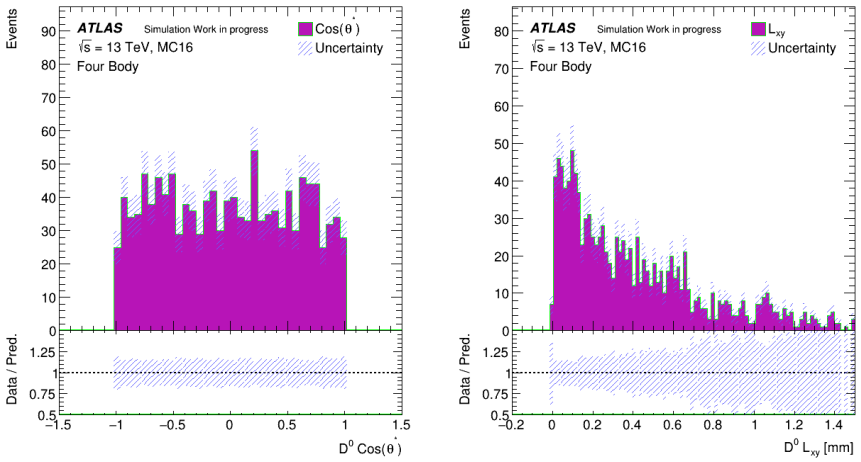

(a) (b)

FIGURE B.1: (a) $\cos(\theta^*)$ distribution between the Kaon in $K3\pi$ channel and D^0 in the reference frame of D^0. (b) the transverse decay length L_{xy} for D^0 (Uncertainty here is stat only).

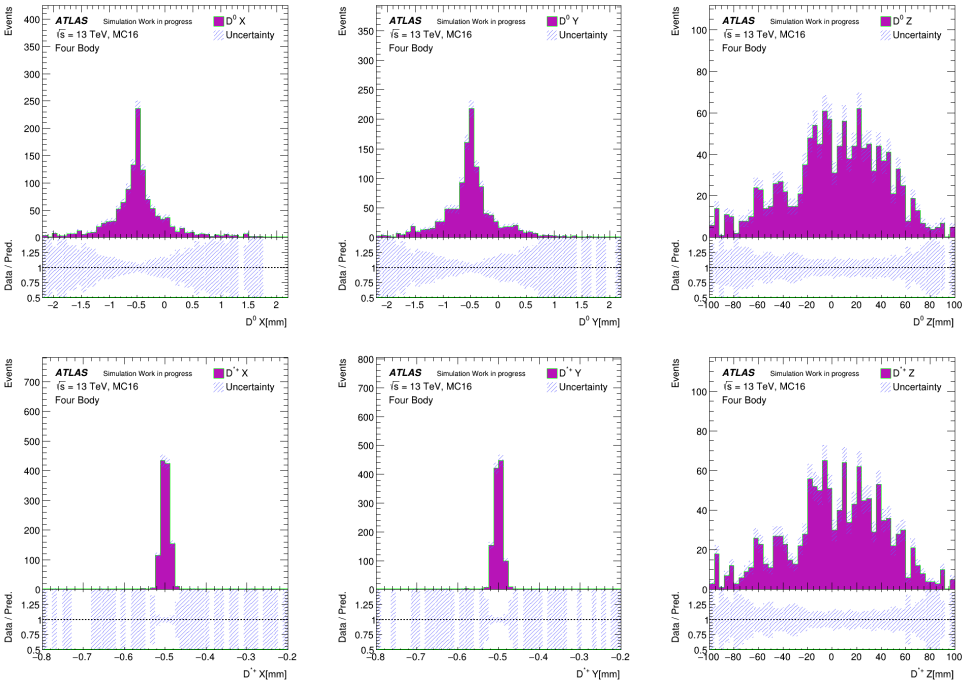

FIGURE B.2: Decay vertex position (SV) for D^0 in $K3\pi$ channel (top), and the decay position for D^{*+} at truth-level for simulated events (Uncertainty here is stat only).

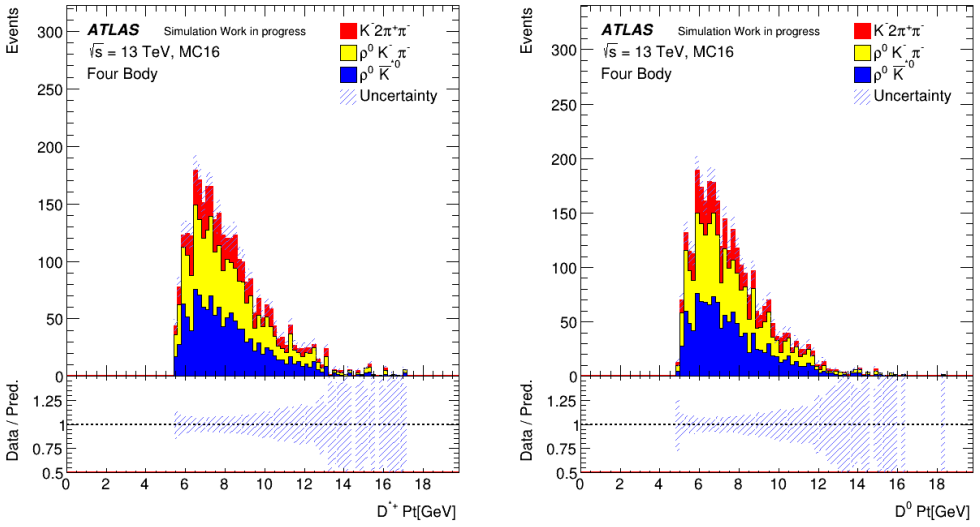

(a) (b)

FIGURE B.3: The transverse momentum distributions for D^{*+}(left) and D^0 (right) reconstructed from different decay channels, where (red) is for $D^0 \rightarrow K^-2\pi^+\pi^-$ (yellow) for $D^0 \rightarrow K^-\pi^+\rho^0$; $\rho^0 \rightarrow \pi^-\pi^+$ and (blue) for $D^0 \rightarrow \bar{K}^{*0}\rho^0$;$\bar{K}^{*0} \rightarrow K^-\pi^+$ and $\rho^0 \rightarrow \pi^-\pi^+$ (Uncertainty here is stat only).

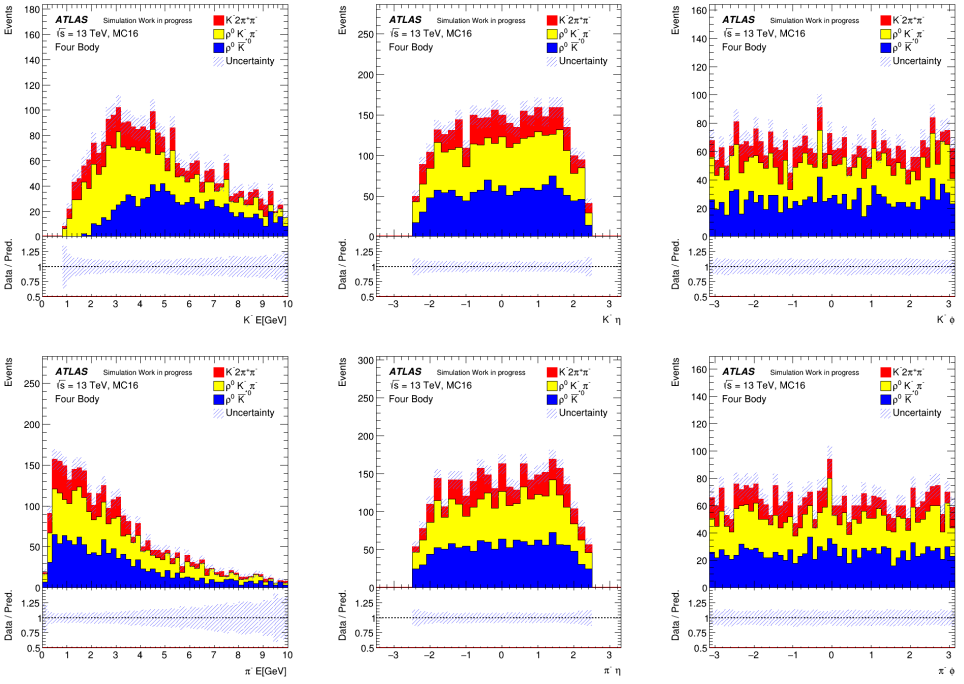

FIGURE B.4: The kinematic distributions for K^-(top) and π^- (bottom) produced in different decay channels, where (red) is for $D^0 \rightarrow K^-2\pi^+\pi^-$ (yellow) for $D^0 \rightarrow K^-\pi^+\rho^0$; $\rho^0 \rightarrow \pi^-\pi^+$ and (blue) for $D^0 \rightarrow \bar{K}^{*0}\rho^0$;$\bar{K}^{*0} \rightarrow K^-\pi^+$ and $\rho^0 \rightarrow \pi^-\pi^+$ (Uncertainty here is stat only).

decay channel, the number of events pass these selections is very small compared to the two-body one.

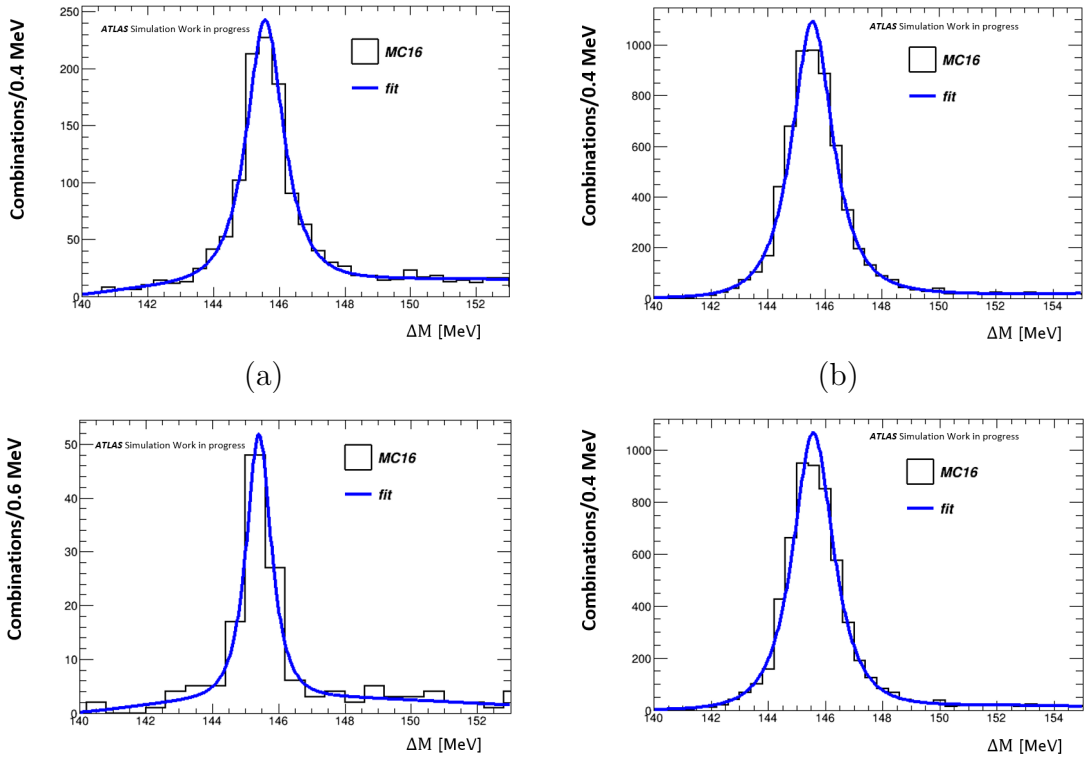

FIGURE B.5: Mass difference distributions, $\Delta M = D^{*+}_{Mass} - D^{0}_{Mass}$, for the reconstructed MC events in the decay channels $K3\pi$ (a,c) and $K\pi$ (b,d), without (top) and with (bottom) requiring the trigger selections (Uncertainty here is stat only).

Figure B.6 shows the ΔM distributions for $K\pi$ and $K3\pi$ channels using data collected by the ATLAS experiment at $\sqrt{s} = 13$ TeV in 2018 without requiring the trigger selections.

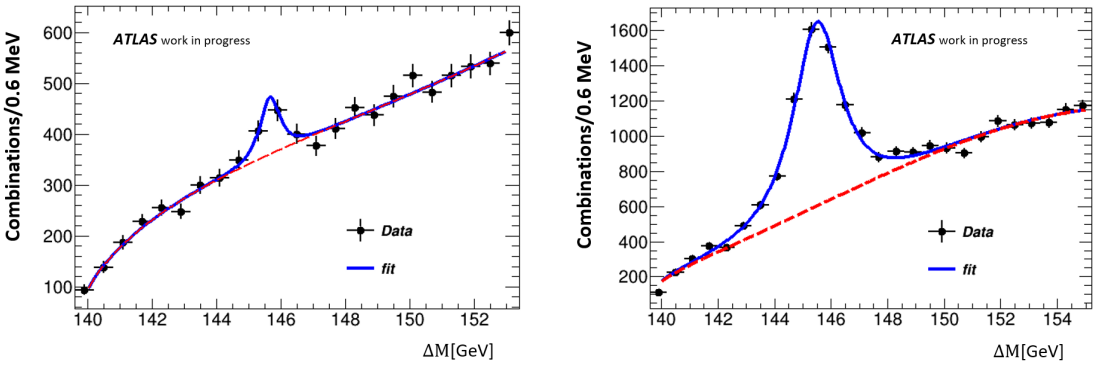

FIGURE B.6: Mass difference distributions, $\Delta M = D^{*+}_{Mass} - D^{0}_{Mass}$, for the reconstructed data events (using only the half number of the data sample) in the decay channels $K3\pi$ (right) and $K\pi$ (left) without requiring the trigger selections. The data is represented by points with error bars (stat). The solid blue line is the resulting fit from the sum of $Gauss^{Mode}$ and f^{T}. The dashed red line is representing the expected wrong charge combination.

Appendix C

$t\bar{t}t\bar{t}$ reconstruction based on χ^2–method in 1L and OS dilepton channels

The four-top-quark ($t\bar{t}t\bar{t}$) process is characterized by several final states depending on the W-boson decays. For example, the branching ratio (BR) of the single-lepton (1L) final state, which is the dominated one, is $\sim 42\%$. At the same time, the BR of the opposite-sign (OS) dilepton is $\sim 14\%$ (see the introduction of Chapter 6 for other BRs). Therefore, to reconstruct the four-top-quark system entirely, e.g. in the 1L channel, using the χ^2–method (the one presented in Section 6.1.1) or other methods, one should investigate if it has non-negligible contributions coming from other decay channels.

In this analysis, the $t\bar{t}t\bar{t}$ events in the 1L final state and with ≥ 10 jet and ≥ 4 b-tag are retained to study the other channels contributions in the 1L. This has been done by investigating the truth information of the 1L events and finding the fractions of the events that are not coming from the 1L at truth-level (it means, to find the number of events that are coming from other channels at the truth-level and counted as the 1L events at the Reco-level). Figure C.1 shows the contributions from other decay channels and counted in the 1L decay channel in the signal region ≥ 10 jet and ≥ 4 b-jet.

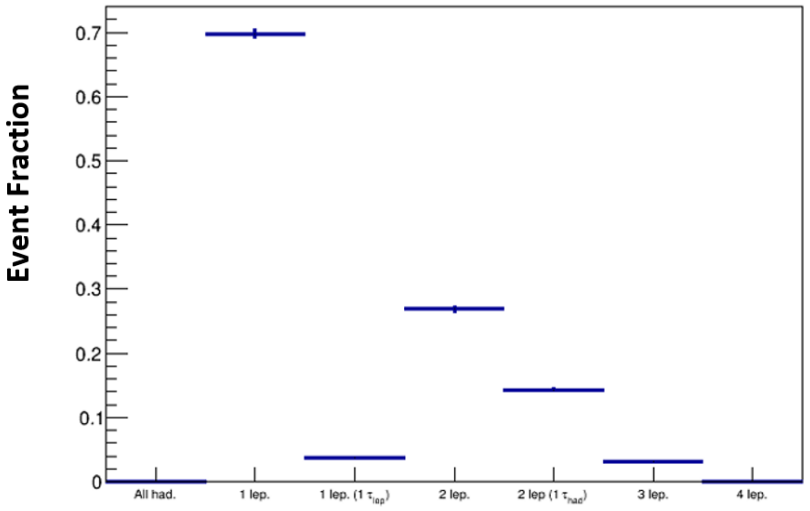

FIGURE C.1: Schematic graph shows the contribution from other decay channels in the 1L final state.

From Figure C.1, it can be noted that 70% of the considered 1L events are truly 1L. In contrast, $\sim$ 30% of the dilepton (lepton at truth level is included electron, muon and tau while at Reco-level it means either electron or muon) events are considered in the 1L final state. This means that $\sim$ 30% of the 1L events in the signal-region $\geq$ 10 jet and $\geq$ 4 b-jet are coming from the dilepton (OS or SS) final state. However, out of the $\sim$ 30% dilepton events are coming from the ditau decay whereas one of them decays hadronically, and the other decays leptonically. As a result, $\sim$ 15% from the ditau final state will end in the 1L channel. In contrast, there is $\sim$ 15% of the dilepton events will end in the 1L channel, due to one of the electron or muon is soft enough and does not pass the needed object requirements presented in table 6.1.

Finally, the contributions from other channels, e.g. 3L and 4L final states, are less than 4%. At the same time, the contribution from the fully-hadronic decay channel is zero. Therefore, this is an indirect indication that there is no non-prompt or fake lepton (electron or muon) coming from the misidentified jet as a lepton. To conclude, based on the truth study in the 1L decay channel and due to the non-negligible contributions that are coming from other decay channels, in particular from the dilepton channel, the χ^2–method is used to reconstruct only two hadronically-decaying top-quark.

Appendix D

Search for $t\bar{t}$ resonances in the dilepton channel

The invariant mass of $t\bar{t}$ can be reconstructed experimentally by using the neutrino weighting (NW) method (see Ref[133, 134]) and it is referred to as $t\bar{t}^{NW}$. However, one can see from Figure D.1 that there are a high fraction of signal events are failed to be reconstructed for the massive particles of the order of TeV, after using the neutrino weighting (NW) method. This means that the invariant mass of the $t\bar{t}$ system is set to the zero. For example, the Z' with a mass = 3 TeV, there are $\sim 22\%$ of the events with an invariant mass equal to zero after using the NW method to reconstruct the $t\bar{t}$ in the dilepton channel. Based on that, one should use other variables that might be sensitive to the presence of the new physics like the ones represented and used in Chapter 7, e.g. $\Delta\phi_{l^+l^-}$.

Figure D.2 shows the correlation between the $m_{T,t\bar{t}}$ (see equation D.1) for events with at least one and two b-tagged jets, respectively, to $m_{t\bar{t}}$, which is the truth (Parton-level) distribution of the invariant mass of the $t\bar{t}$.

$$m^2_{T,t\bar{t}} = (E^{l^+} + E^{l^-} + E^{b_1} + E^{b_2} + E_T^{miss})^2 - (\vec{p^{l^+}} + \vec{p^{l^-}} + \vec{p^{b_1}} + \vec{p^{b_2}} + \vec{p_T^{miss}})^2 \tag{D.1}$$

From this figure, it can be seen that the $m_{T,t\bar{t}}$ in the high mass region ($m_{T,t\bar{t}} > 1000$ GeV) follows the same distribution of $m_{t\bar{t}}$, which means that $m_{T,t\bar{t}}$ is large as the $m_{t\bar{t}}$ in

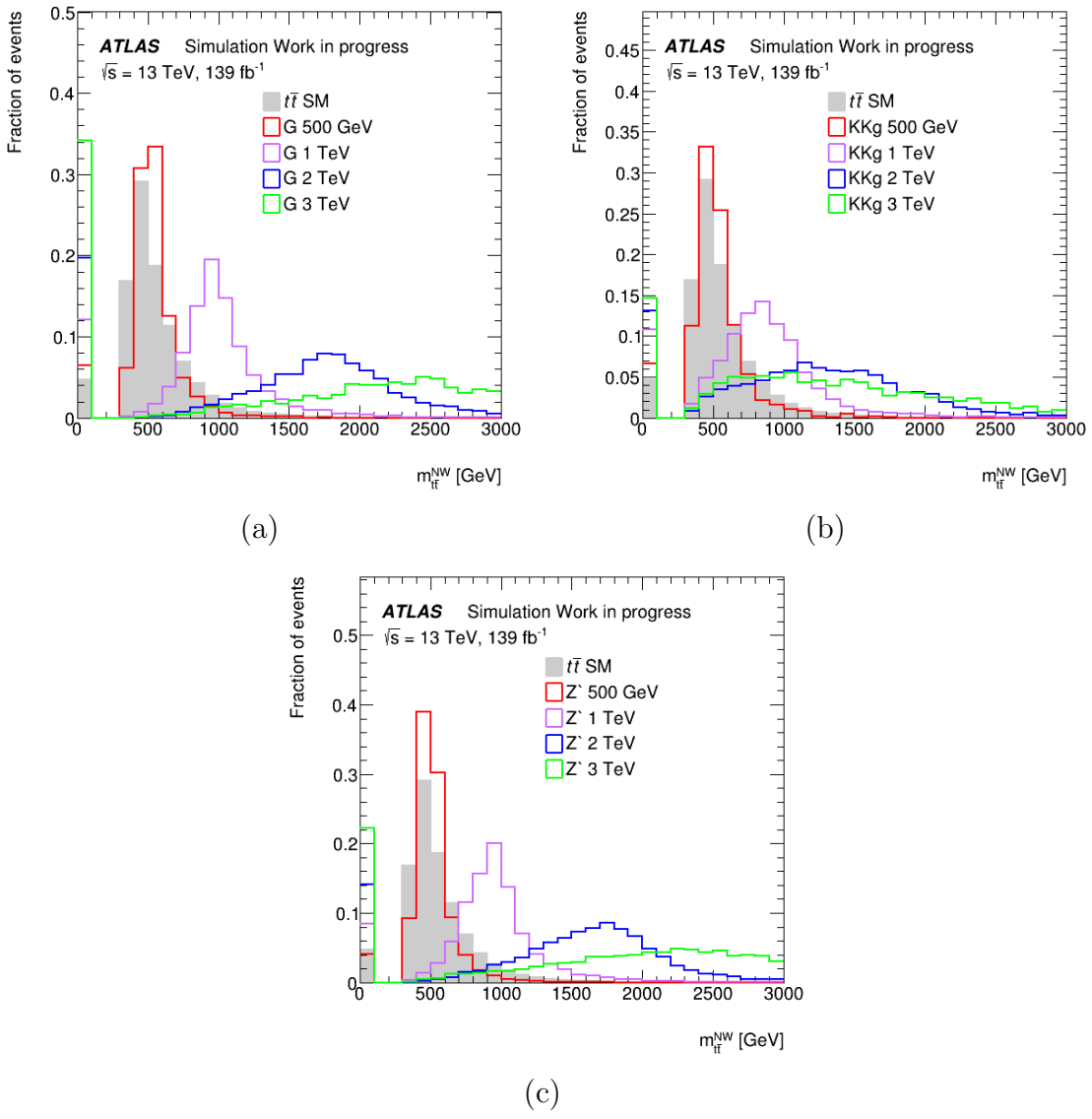

FIGURE D.1: $t\bar{t}^{NW}$ distributions at Reco-level for (a) G, (b) KK_g, and (c) Z' with different mass hypotheses (colours) versus the SM $t\bar{t}$ decays in dilepton channel (grey) for events ≥ 2 b-tagged jets.

the high mass region. In contrast, in the low mass region, as shown in Figure D.2(a), the $m_{T,t\bar{t}}$ has large transverse mass values compared to the $m_{t\bar{t}}$. For example, the $m_{T,t\bar{t}}$ in the low mass region is equal to $\sim$ 2500 GeV while the expected $m_{t\bar{t}}$ is $\sim$ 500 GeV. This is because of the $m_{T,t\bar{t}}$ is reconstructed using the jet (can be c- or light-jets) with highest p_T for the events with at least one b-tagged jet.

On the other hand, for events with at least two b-tagged jets, $m_{T,t\bar{t}}$ follows the same $m_{t\bar{t}}$ mass distribution in the low and high mass regions. Based on that, the number of b-tagged jets is required to be equal or larger than two b-tagged jets ($\geq$ 2b-tag) in this

analysis.

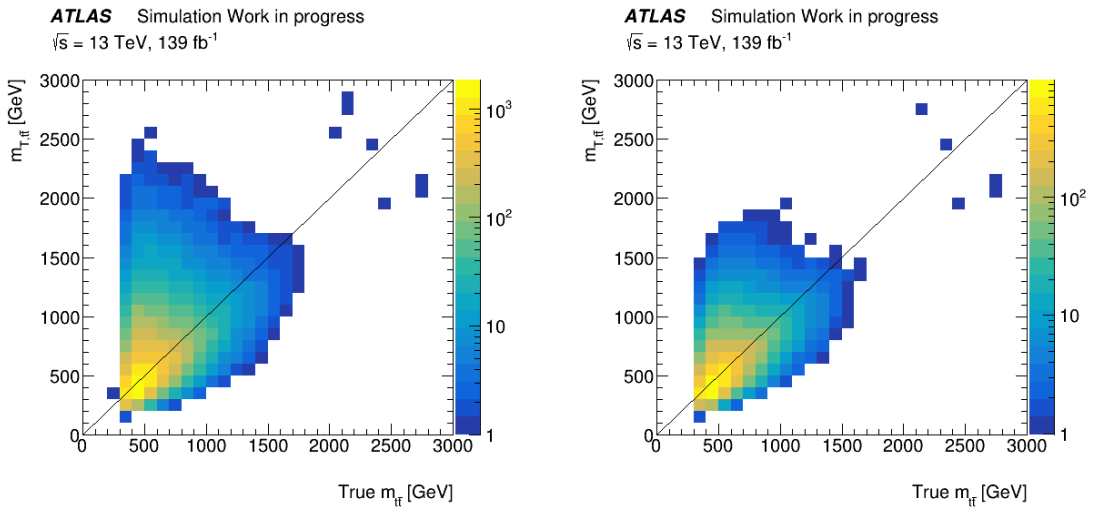

(a) (b)

FIGURE D.2: Correlation between the $m_{T,t\bar{t}}$ (Reco–level) and m_{tt} (Parton–level) with at least one (a) and two (b) b-tagged jets.

The ranking plot (see Ref[33]) is used to show the impact of different systematic uncertainties on the variable of interest, e.g. the fitted signal strength ($\mu = \sigma_{(SM,BSM...etc)}/\sigma_{Exp}$). The following figures (D.3, D.4 and D.5) present the ranking plots of nuisance parameters extracted from the fitting of the scanned $\Delta\phi_{ll}$ variable for different mass hypotheses predicted by the Topcolor Assisted Technicolor (TC2) and Randall-Sundrum (RS) models. From these plots, one can see that the impacts of the systematic uncertainties are changed from one mass hypothesis to another. However, the main effects still coming from the different $t\bar{t}$ modelling parameters, e.g. the $t\bar{t}$ final-stat radiations (FSR).

Tables D.1, D.2 and D.3 summarise the expected limits on the cross-sections×branching-ratio with 95% CL upper limits in the dilepton decay channel using the defined observables (the $\Delta\phi_{ll}$ and $\Delta\eta_{ll}$, which are scanned in ten bins of m_{llbb}, and the inclusive m_{llbb}) in the signal region as a function of the hypothetical particle mass of Kaluza-Klein gluon (KK_g) excitations. At the same time, Tables D.4, D.5 and D.6 are summarised the expected limits on the cross-sections×branching-ratio with 95% CL upper limits of those for the Kaluza-Klein graviton (G) excitations as a function of the particle mass in the signal region of the dilepton channel.

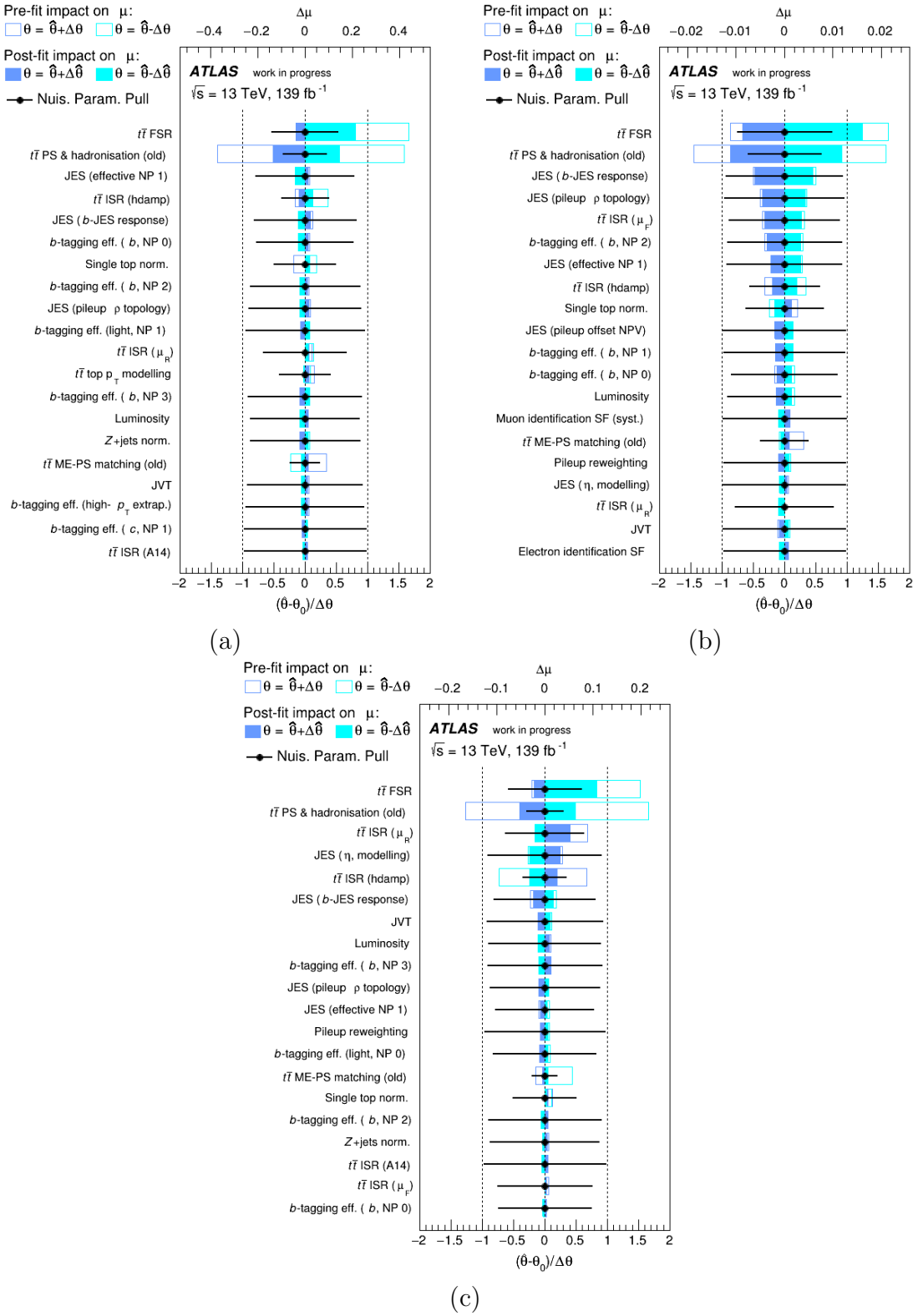

FIGURE D.3: Ranking plot for the nuisance parameters extracted from fitting of the scanned $\Delta\phi_{ll}$ for (a) $G = 400$ GeV, (b) $KK_g = 500$ GeV and (c) $Z' = 500$ GeV, respectively.

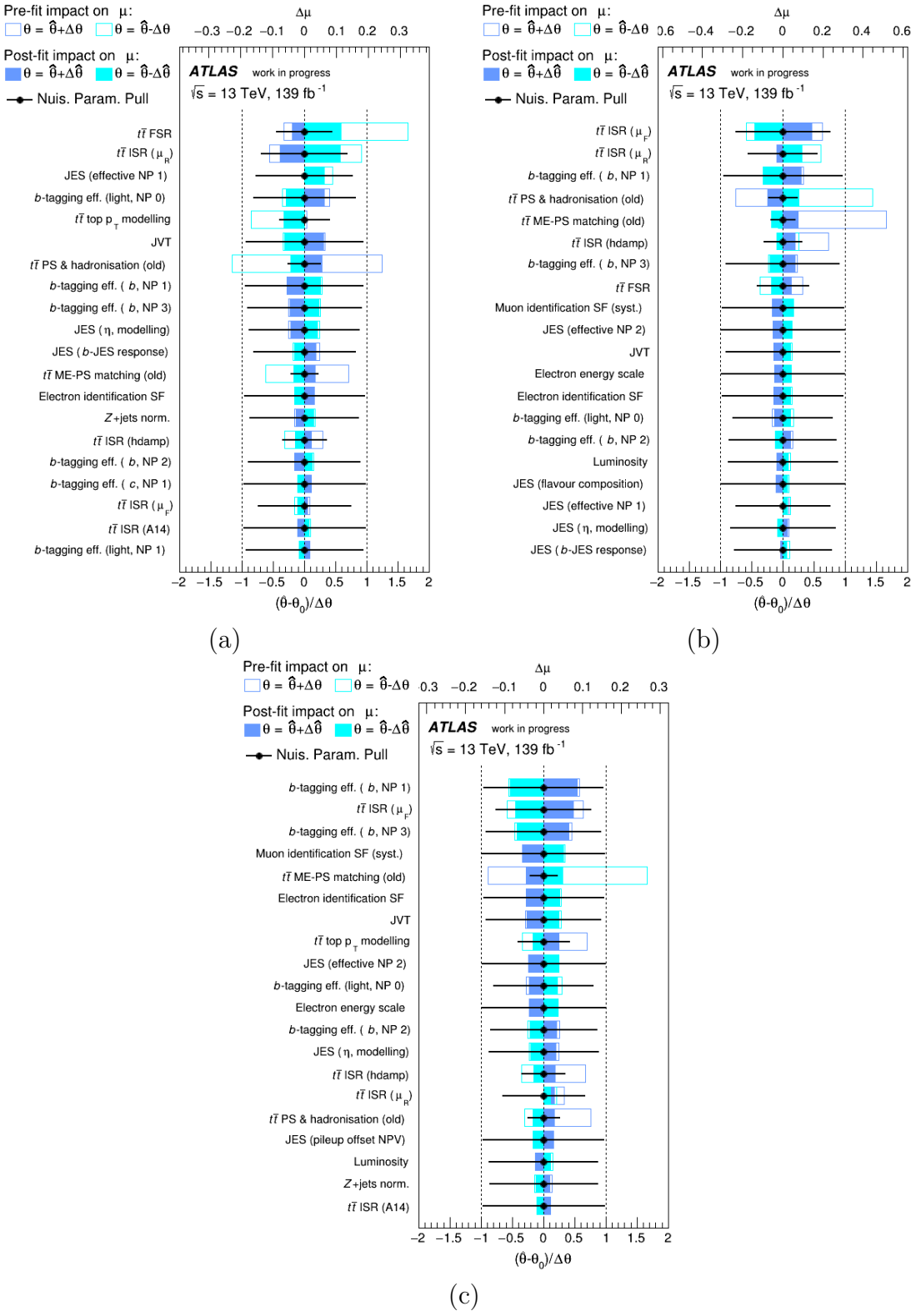

FIGURE D.4: Ranking plot for the nuisance parameters extracted from fitting of the scanned $\Delta\phi_{ll}$ for (a) $G = 750$ GeV, (b) $KK_g = 3500$ GeV and (c) $Z' = 2000$ GeV, respectively.

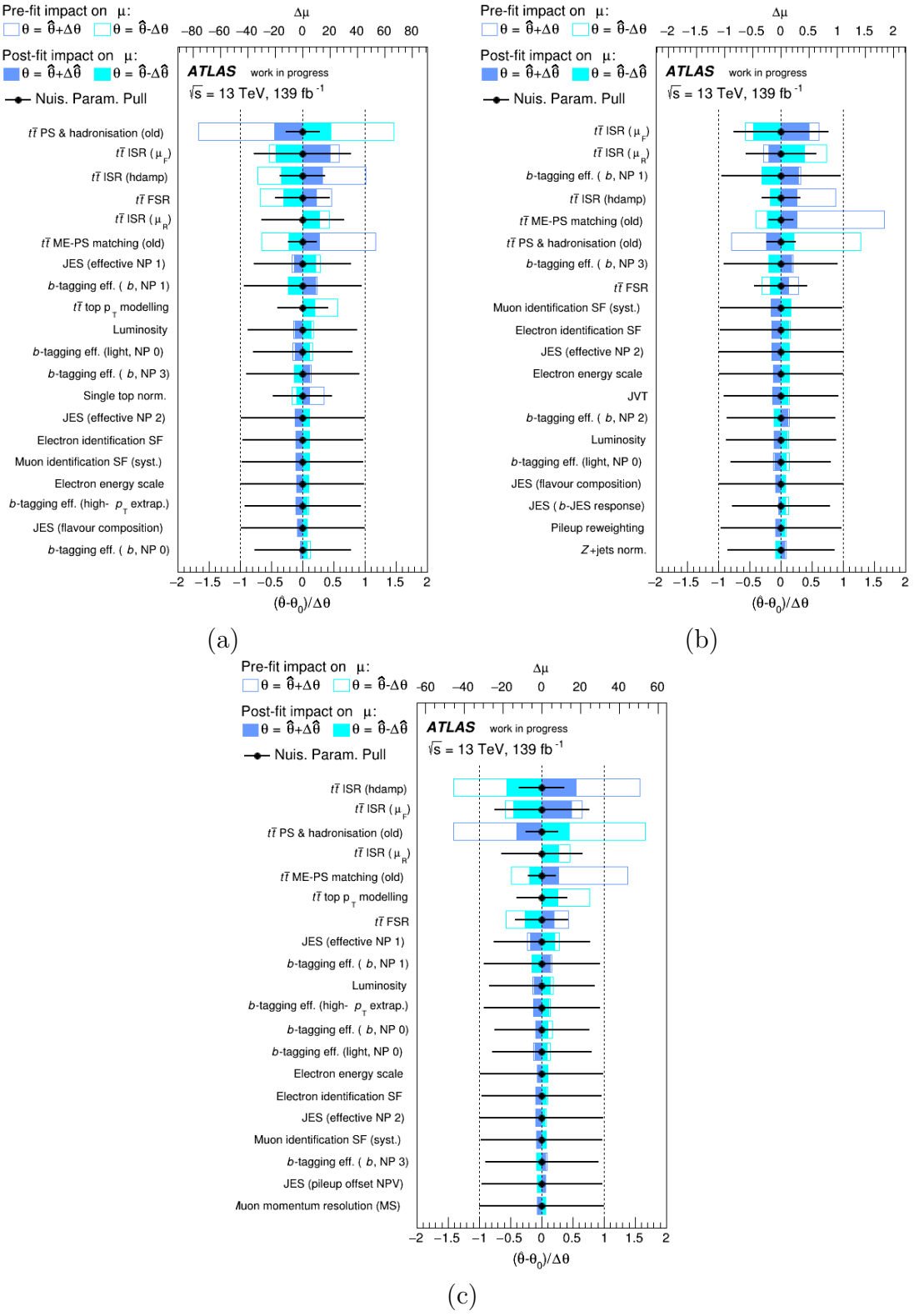

FIGURE D.5: Ranking plot for the nuisance parameters extracted from fitting of the scanned $\Delta\phi_{ll}$ for (a) $G = 3000$ GeV, (b) $KK_g = 4500$ GeV and (c) $Z' = 5000$ GeV, respectively.

Expected $\sigma(pp \to KK_g) \times BR(KK_g \to t\bar{t})$				Scanned $\Delta\phi_{ll}$	
		Statistical only		Statistical + Systematics	
KK_g Mass [TeV]	Theor. [pb]	Exp. [pb]	$\pm 1\sigma$	Exp. [pb]	$\pm 1\sigma$
.5	240.86	0.7705	[1.072, 0.555]	13.536	[18.759, 9.754]
1.	20.18	0.3177	[0.442, 0.229]	1.418	[1.97, 1.022]
1.5	3.79	0.1454	[0.203, 0.105]	0.2993	[0.418, 0.216]
2.	1.052	0.1	[0.1395, 0.0721]	0.1578	[0.220, 0.114]
2.5	0.3734	0.14	[0.1958, 0.101]	0.1926	[0.2693, 0.1388]
3.	0.1561	0.0730	[0.1024, 0.0526]	0.0964	[0.1352, 0.0695]
3.5	0.0743	0.0738	[0.1038, 0.0532]	0.0955	[0.1343, 0.0688]
4.	0.0394	0.0785	[0.1107, 0.0566]	0.1013	[0.143, 0.0730]
4.5	0.0229	0.0835	[0.118, 0.0602]	0.1089	[0.1543, 0.0785]

TABLE D.1: The expected limits (Exp.), using the scanned $\Delta\phi_{ll}$ in ten m_{llbb} bins, on the cross-sections×branching-ratio ($\sigma(pp \to KK_g) \times BR(KK_g \to t\bar{t})$) with a CL of 95% on the KK_g excitations, from the Randall-Sundrum model, decaying to a top-quark pair. The expected limits are quoted both without and with systematics uncertainties taken into account. Also, the $\pm 1\sigma$ uncertainty on the expected limits is shown.

Expected $\sigma(pp \to KK_g) \times BR(KK_g \to t\bar{t})$				Scanned $\Delta\eta_{ll}$	
		Statistical only		Statistical + Systematics	
KK_g Mass [TeV]	Theor. [pb]	Exp. [pb]	$\pm 1\sigma$	Exp. [pb]	$\pm 1\sigma$
.5	240.86	0.807	[1.123, 0.583]	12.741	[17.694, 9.181]
1.	20.18	0.305	[0.424, 0.22]	1.718	[2.391, 1.238]
1.5	3.79	0.1604	[0.223, 0.116]	0.520	[0.7185, 0.3747]
2.	1.052	0.118	[0.164, 0.0848]	0.3094	[0.4286, 0.223]
2.5	0.3734	0.178	[0.248, 0.128]	0.3694	[0.514, 0.2662]
3.	0.1561	0.0953	[0.133, 0.0686]	0.1705	[0.2381, 0.1229]
3.5	0.0743	0.1003	[0.140, 0.0723]	0.16304	[0.2285, 0.1175]
4.	0.0394	0.1069	[0.15, 0.0771]	0.1742	[0.2448, 0.1255]
4.5	0.0229	0.1115	[0.1564, 0.0803]	0.1842	[0.2605, 0.1327]

TABLE D.2: The expected limits (Exp.), using the scanned $\Delta\eta_{ll}$ in ten m_{llbb} bins, on the cross-sections×branching-ratio ($\sigma(pp \to KK_g) \times BR(KK_g \to t\bar{t})$) with a CL of 95% on the KK_g excitations, from the Randall-Sundrum model, decaying to a top-quark pair. The expected limits are quoted both without and with systematics uncertainties taken into account. Also, the $\pm 1\sigma$ uncertainty on the expected limits is shown.

Expected $\sigma(pp \to G) \times BR(KK_g \to t\bar{t})$		Inclusive m_{llbb}			
		Statistical only		Statistical + Systematics	
KK_g Mass [TeV]	Theor. [pb]	Exp. [pb]	$\pm 1\sigma$	Exp. [pb]	$\pm 1\sigma$
.5	240.86	0.838	[1.165, 0.6037]	24.632	[34.128, 17.748]
1.	20.18	0.3111	[0.433, 0.224]	1.619	[2.24, 1.166]
1.5	3.79	0.166	[0.2315, 0.12]	0.593	[0.8085, 0.4272]
2.	1.052	0.1134	[0.1582, 0.0817]	0.3207	[0.4431, 0.2311]
2.5	0.3734	0.1629	[0.2276, 0.1174]	0.3439	[0.479, 0.2478]
3.	0.1561	0.0948	[0.1326, 0.0683]	0.193	[0.2695, 0.1391]
3.5	0.0743	0.105	[0.1469, 0.0756]	0.2165	[0.3022, 0.156]
4.	0.0394	0.1147	[0.1606, 0.0827]	0.2281	[0.3187, 0.1644]
4.5	0.0229	0.1174	[0.1645, 0.0845]	0.2314	[0.3239, 0.1668]

TABLE D.3: The expected limits (Exp.), using the scanned $\Delta\phi_{ll}$ in ten m_{llbb} bins, on the cross-sections×branching-ratio ($\sigma(pp \to KK_g) \times BR(KK_g \to t\bar{t})$) with a CL of 95% on the KK_g excitations, from the Randall-Sundrum model, decaying to a top-quark pair. The expected limits are quoted both without and with systematics uncertainties taken into account. Also, the $\pm 1\sigma$ uncertainty on the expected limits is shown.

Expected $\sigma(pp \to G) \times BR(G \to t\bar{t})$		Scanned $\Delta\phi_{ll}$			
		Statistical only		Statistical + Systematics	
G Mass [TeV]	Theor. [pb]	Exp. [pb]	$\pm 1\sigma$	Exp. [pb]	$\pm 1\sigma$
.4	7.19	0.6461	[0.899, 0.4655]	3.387	[4.702, 2.441]
.5	5.84	0.4294	[0.5973, 0.3094]	1.653	[2.302, 1.192]
.75	1.18	0.212	[0.295, 0.1528]	0.622	[0.8622, 0.4482]
1.	0.289	0.1314	[0.1827, 0.0946]	0.3282	[0.4578, 0.2365]
2.	0.00498	0.03843	[0.0537, 0.0277]	0.05132	[0.0716, 0.037]
3.	0.000248	0.02938	[0.0415, 0.0212]	0.03587	[0.0507, 0.0258]

TABLE D.4: The expected limits (Exp.), using the scanned $\Delta\phi_{ll}$ in ten m_{llbb} bins, on the cross-sections×branching-ratio ($\sigma(pp \to G) \times BR(G \to t\bar{t})$) with a CL of 95% on the G excitations, from the Randall-Sundrum model, decaying to a top-quark pair. The expected limits are quoted both without and with systematics uncertainties taken into account. Also, the $\pm 1\sigma$ uncertainty on the expected limits is shown.

Expected $\sigma(pp \to G) \times BR(G \to t\bar{t})$		Scanned $\Delta\eta_{ll}$			
		Statistical only		Statistical + Systematics	
G Mass [TeV]	Theor. [pb]	Exp. [pb]	$\pm 1\sigma$	Exp. [pb]	$\pm 1\sigma$
.4	7.19	0.6937	[0.965, 0.5]	4.058	[5.537, 2.924]
.5	5.84	0.4879	[0.6786, 0.3515]	2.128	[2.931, 1.533]
.75	1.18	0.2107	[0.2931, 0.1518]	0.6473	[0.9, 0.4664]
1.	0.289	0.1392	[0.1937, 0.1003]	0.3577	[0.4984, 0.2577]
2.	0.00498	0.0442	[0.0616, 0.0318]	0.09	[0.125, 0.0648]
3.	0.000248	0.0404	[0.0567, 0.0291]	0.0576	[0.0805, 0.0415]

TABLE D.5: The expected limits (Exp.), using the scanned $\Delta\eta_{ll}$ in ten m_{llbb} bins, on the cross-sections×branching-ratio ($\sigma(pp \to G) \times BR(G \to t\bar{t})$) with a CL of 95% on the G excitations, from the Randall-Sundrum model, decaying to a top-quark pair. The expected limits are quoted both without and with systematics uncertainties taken into account. Also, the $\pm 1\sigma$ uncertainty on the expected limits is shown.

Expected $\sigma(pp \to G) \times BR(G \to t\bar{t})$		Inclusive m_{llbb}			
		Statistical only		Statistical + Systematics	
G Mass [TeV]	Theor. [pb]	Exp. [pb]	$\pm 1\sigma$	Exp. [pb]	$\pm 1\sigma$
.4	7.19	0.7351	[1.022, 0.53]	12.384	[17.13, 8.923]
.5	5.84	0.5486	[0.763, 0.3953]	6.5	[9.04, 4.68]
.75	1.18	0.3055	[0.425, 0.220]	1.93	[2.69, 1.4]
1.	0.289	0.1444	[0.201, 0.104]	0.512	[0.706, 0.37]
2.	0.00498	0.0444	[0.062, 0.032]	0.0944	[0.131, 0.068]
3.	0.000248	0.0288	[0.0407, 0.0207]	0.0393	[0.0559, 0.0283]

TABLE D.6: The expected limits (Exp.), using the inclusive m_{llbb}, on the cross-sections×branching-ratio ($\sigma(pp \to G) \times BR(G \to t\bar{t})$) with a CL of 95% on the G excitations, from the Randall-Sundrum model, decaying to a top-quark pair. The expected limits are quoted both without and with systematics uncertainties taken into account. Also, the $\pm 1\sigma$ uncertainty on the expected limits is shown.

Bibliography

[1] CDF collaboration. Observation of top quark production in $p\bar{p}$ collisions. *In:Phys.Rev.Lett.74, arXiv:hep-ex/9503002 [hep-ex]*, pages 2626–2631, 1995. doi: 10.1103/PhysRevLett.74.2626.

[2] D0 collaboration. Observation of the top quark. *In:Phys.Rev.Lett.74, arXiv:hep-ex/9503003 [hep-ex]*, pages 2632–2637, 1995. doi: 10.1103/PhysRevLett.74.2632.

[3] ATLAS Collaboration. Search for new high-mass resonances in the dilepton final state using proton–proton collisions at $\sqrt{s}$ = 13TeV with the ATLAS detector. *ATLAS-CONF-2016-045*, 2016. URL http://cds.cern.ch/record/2206127/files/ATLAS-CONF-2016-045.pdf.

[4] C.T.Hill R.M.Harris and S.J.Parke. Cross-section for Topcolor Z' decaying to top-antitop. *arXiv:9911288 [hep-ph]*.

[5] C.T.Hill. Topcolor assisted technicolor. *Phys.Lett.B345(1995)483489, arXiv:9411426 [hep-ph]*.

[6] B. Lillie, L. Randall and Lian-Tao Wang. The Bulk RS KK-gluon at the LHC. *ANL-HEP-PR-07-4, arXiv:hep-ph/0701166v1*, (2007).

[7] L. O·Raifeartaigh and N. Straumann. Early History of Gauge Theories and Kaluza-Klein Theories, with a Glance at Recent Developments. *arXiv:hep-ph/9810524v2*, 1999.

[8] L. Randall and R. Sundrum. A large mass hierarchy from a small extra dimension. *Phys.Rev.Lett.83, arXiv:9905221 [hep-ph]*, pages 3370–3373, 1999.

[9] L. Randall and R. Sundrum. An Alternative to Compactification. *arXiv:9906064 [hep-th]*, 1999.

[10] M. Thomson. *Modern Particle Physics*. 2013. ISBN 9781107034266.

[11] Summary plots from the ATLAS Top physics group. 2015. URL https://atlas.web.cern.ch/Atlas/GROUPS/PHYSICS/CombinedSummaryPlots/TOP/.

[12] The CERN accelerator complex. *OPEN-PHO-ACCEL-2013-056*, 2013. URL https://cds.cern.ch/record/1621894.

[13] ATLAS Collaboration. ATLAS data quality operations and performance for 2015-2018 data-taking. *arXiv:1911.04632v1 [physics.ins-det]*, 2019.

[14] ATLAS Collaboration. The ATLAS Experiment at the CERN Large Hadron Collider. *In: JINST 3*, 2008. doi: 10.1088/1748-0221/3/08/S08003.

[15] Potamianos and Karolos. The upgraded Pixel detector and the commissioning of the Inner Detecto tracking of the ATLAS experiment for Run-2 at the Large Hadron Collider. *arXiv:1608.07850*, 2015.

[16] M. Backhaus. The upgraded Pixel Detector of the ATLAS Experiment for Run 2 at the Large Hadron Collider. *Nuclear Instruments and Methods in Physics Research A*, 2016.

[17] D. O. Damazio. ATLAS LAr Calorimeter: Construction, Integration and Commissioning. *J. Phys.*, 2008. doi: 10.1088/1742-6596/110/9/092007.

[18] ATLAS Collaboration. Electron reconstruction and identification in the ATLAS experiment using the 2015 and 2016 LHC protonproton collision data at $\sqrt{s}$ =13 TeV. *Eur. Phys. J. C 79 (2019) 639, arXiv:1902.04655v2 [physics.ins-det]*, 2019. doi: 10.1140/epjc/s10052-019-7140-6.

[19] ATLAS Collaboration. Performance of electron and photon triggers in ATLAS during LHC Run 2. *Eur. Phys. J. C80 (2020) 47*, 2020.

[20] A. C. Henrichs. *Precision measurements of the top quark pair production cross-section in the single lepton channel with the ATLAS experiment*. PhD thesis, 2012.

[21] ATLAS Collaboration. Muon reconstruction performance of the ATLAS detector in proton–proton collision data at $\sqrt{s}$ =13 TeV. *Eur.Phys.J.C76(2016)292, arXiv:1603.05598v2 [hep-ex]*, 2016. doi: 10.1140/epjc/s10052-016-4120-y.

[22] B. Isildak. *Measurement of the differential dijet production cross section in proton–proton collisions at* $\sqrt{s} = 7\,TeV$. PhD thesis, 2011. URL http://inspirehep.net/record/1251416/files/arXiv:1308.6064.pdf.

[23] ATLAS Collaboration. Monte Carlo Calibration and Combination of In–situ Measurements of Jet Energy Scale. 2015. URL https://cds.cern.ch/record/2044941.

[24] ATLAS collaboration. Tagging and suppression of pileup jets. *Eur. Phys. J. C76 (2016) 581*, 2016.

[25] ATLAS Collaboration. Performance of b–Jet Identification in the ATLAS Experiment. *arXiv:1512.01094v2 [hep-ex]*, 2016.

[26] M. Limper. *Track and Vertex Reconstruction in the ATLAS Inner Detector*. PhD thesis, 2009. URL http://inspirehep.net/record/834028/files/CERN-THESIS-2009-061.pdf.

[27] Di Petrillo and K. Folan. *Search for long-lived, massive particle in events with a displaced vertex and displaced muon using* $\sqrt{s} = 13\,TeV$ *p–p collisions with the ATLAS detector*. PhD thesis, 2019. URL https://cds.cern.ch/record/2677474.

[28] ATLAS Collaboration. Early Inner Detector Tracking Performance in the 2015 Data at $\sqrt{s} = 13$ TeV. *ATL-PHYS-PUB-2015-051*, 2015.

[29] ATLAS Collaboration. Inner detector tracking public results. 2019. URL https://atlas.web.cern.ch/Atlas/GROUPS/PHYSICS/PLOTS/IDTR-2017-007/.

[30] G. C. Branco et al. Theory and phenomenology of two-Higgs-doublet models. *Phys. Rept. 516 (2012) 1, arXiv:1106.0034 [hep-ph]*.

[31] ATLAS Collaboration. ATLAS Collaboration, Search for new phenomena in events with same-charge leptons and b-jets in pp collisions at $\sqrt{s}$ = 13 TeV with the ATLAS detector. *arXiv:1807.11883v3 [hep-ex]*, . doi: 10.1007/JHEP12(2018)039.

[32] H. Georgi, L. Kaplan, D. Morin and A. Schenk. Effects of top quark compositeness. *Phys. Rev. D 51 (7 1995) 3888.*

[33] ATLAS Collaboration. Search for four-top-quark production in the single-lepton and opposite-sign dilepton final states in p p collisions at $\sqrt{s}$ = 13 TeV with the ATLAS detector. *arXiv:1811.02305v1 [hep-ex]*, .

[34] J. Linacre el al. Spin correlations in top physics at ATLAS and CMS in Run 2. *ATLAS-CONF-2016-045, arXiv:1905.08634v1 [hep-ex]*, 2016. URL http://cds.cern.ch/record/2675997/files/1905.08634.pdf?version=1.

[35] CMS Collaboration. Measurements of $t\bar{t}$ spin correlations and top quark polarization using dilepton final states in pp collisions at *sqrts* = 8 TeV. *Phys.Rev.D93,052007(2016), arXiv:1601.01107 [hep-ex]*, 2016.

[36] CMS Collaboration. Measurement of the top quark polarization and $t\bar{t}$ spin correlations using dilepton final states in proton–proton collisions at $\sqrt{s}$ = 13 TeV. *Phys.Rev.D100,072002*, 2019.

[37] M. Tanabashi et al. Particle Data Group. *Phys.Rev.D 98,030001*, 2018. URL http://pdg.lbl.gov/.

[38] B. Salvachua. Overview of proton runs during run 2. *9th LHC Operations Evian Workshop*, 2019. URL https://indico.cern.ch/event/751857/contributions/3259373/attachments/1783143/2910577/belen-Evian2019.pdf.

[39] ATLAS Collaboration. Study of the material of the ATLAS inner detector for Run 2 of the LHC. *arXiv:1707.02826 [hep-ex]*, 2017. doi: 10.1088/1748-0221/12/12/P12009.

[40] ATLAS Collaboration. Search for heavy particles decaying into a top-quarkpair in the fully hadronic final state in p–p collisions at $\sqrt{s}$ = 13 TeV with the ATLAS detector. *Phys. Rev. D 99 (2019) 092004, arXiv:1902.10077v2 [hep-ex]*, . doi: 10.1103/PhysRevD.99.092004.

[41] ATLAS Collaboration. Search for heavy particles decaying into top-quarkpairs using lepton-plus-jets events in proton–proton collisions at $\sqrt{s}$ = 13 TeV with the

ATLAS detector. *Eur.Phys.J.C78(2018)565, arXiv:1804.10823v2 [hep-ex]*, . doi: 10.1140/epjc/s10052-018-5995-6.

[42] F. Halzen and A. D. Martin. *Quarks and Leptons: An Introductory Course in Modern Particle Physics*. 1984. ISBN 9780471887416.

[43] S. L. Glashow. Partial Symmetries of Weak Interactions. *In: Nucl. Phys. 22*, pages 579–588, 1961. doi: 10.1016/0029-5582(61)90469-2.

[44] S. Weinberg. A Model of Leptons. *In: Phys. Rev. Lett. 19*, pages 1264–1266, 21 Nov 1967. doi: 10.1103/PhysRevLett.19.1264. URL https://link.aps.org/doi/10.1103/PhysRevLett.19.1264.

[45] A. Salam. Weak and Electromagnetic Interactions. *In: Conf. Proc. C680519 (1968)*, pages 367–377, 1968. doi: 10.1103/PhysRevLett.19.1264. URL https://link.aps.org/doi/10.1103/PhysRevLett.19.1264.

[46] M. Y. Han and Y. Nambu. Three Triplet Model with Double SU(3) Symmetry. *In: Phys. Rev. 139*, pages B1006–B1010, 1965. doi: 10.1103/PhysRev.139.B1006.

[47] H. Fritzsch, M. Gell-Mann and H. Leutwyler. Advantages of the Color Octet Gluon Picture. *In: Phys. Lett. 47B*, pages 365–368, 1973. doi: 10.1016/0370-2693(73)90625-4.

[48] O. W. Greenberg. Spin and Unitary Spin Independence in a Paraquark Model of Baryons and Mesons. *In: Phys. Rev. Lett. 13*, pages 598–602, 1964. doi: 10.1103/PhysRevLett.13.598.

[49] S. Descotes-Genon and P. Koppenburg. The CKM Parameters. *arxiv:1702.08834v4 [hep-ex]*, 2017. URL https://arxiv.org/pdf/1702.08834.pdf.

[50] N. Cabibbo. Unitary Symmetry and Leptonic Decays. *In: Phys. Rev. Lett. 10*, (531–533), 1963. doi: 10.1103/PhysRevLett.10.531. URL https://link.aps.org/doi/10.1103/PhysRevLett.10.531.

[51] M. Kobayashi and T. Maskawa. CP Violation in the Renormalizable Theory of Weak Interaction. *In: Prog. Theor. Phys. 49*, (652–657), 1973. doi: 10.1143/PTP.49.652.

[52] P. Higgs. Broken Symmetries, Massless Particles and Gauge Fields. *Physics Letters, 12*, (132–133), 1964. doi: 10.1016/0031-9163(64)91136-9.

[53] P. Higgs. Broken Symmetries and the Masses of Gauge Bosons. *Phys. Rev. Lett, 13*, (508–509), 1964. doi: 10.1103/PhysRevLett.13.508.

[54] G. S. Guralnik et al. Global Conservation Laws and Massless Particles. *Phys. Rev. Lett, 13*, (585), 1964. doi: 10.1103/PhysRevLett.13.585.

[55] F. Englert and R. Brout. Broken Symmetry and the Mass of Gauge Vector Mesons. *Phys. Rev. Lett, 13*, (321–322), 1964. doi: 10.1103/PhysRevLett.13.321.

[56] ATLAS Collaboration. Observation of a new particle in the search for the Standard Model Higgs boson with the ATLAS detector at the LHC. *In: Phys. Lett, B 716, arXiv: 1207.7214 [hep-ex]*, (1), 2012. doi: 10.1016/j.physletb.2012.08.020.

[57] CMS Collaboration. Observation of a new boson at a mass of 125 GeV with the CMS experiment at the LHC. *In: Phys. Lett, B 716, arXiv:1207.7235 [hep-ex]*, (30), 2012. doi: 10.1016/j.physletb.2012.08.021.

[58] ATLAS and CMS Collaborations. Combined Measurement of the Higgs Boson Mass in pp Collisions at $\sqrt{s}$ =7 and 8 TeV with the ATLAS and CMS Experiments. *In:Phys.Rev.Lett.114, arXiv:1503.07589 [hep-ex]*, (191830), 2012. doi: 10.1103/PhysRevLett.114.191803.

[59] H.D. Politzer. Reliable Perturbative Results for Strong Interactions. *Phys.Rev.Lett 30*, pages 1346–1349, 1973.

[60] D.J. Gross and F. Wilczek. Ultraviolet Behavior of Non-Abelian Gauge Theories. *Phys.Rev.Lett 30*, pages 1343–1346, 1973.

[61] D.J. Gross and F. Wilczek. Asymptotically Free Gauge Theories. *Phys.Rev.D 8*, pages 3633–3652, 1973.

[62] W. Wagner. Top quark physics in hadron collisions. *In:Rept.Prog.Phys.68, arXiv:hep-ph/0507207 [hep-ph]*, pages 2409–2494, 2005. doi: 10.1088/0034-4885/68/10/R03.

[63] A. Quadt. Top quark physics at hadron colliders. *In:Eur.Phys.J.C48*, pages 835–1000, 2006. doi: 10.1140/epjc/s2006-02631-6.

[64] D. Wicke. Properties of the Top Quark. *In:Eur.Phys.J.C71, arXiv:1005.2460 [hep-ex]*, page 1627, 2011. doi: 10.1140/epjc/s10052-011-1627-0.

[65] F.P. Schilling. Top Quark Physics at the LHC: A Review of the First Two Years. *In:Int.J.Mod.Phys.A27, arXiv:1206.4484 [hep-ex]*, 2012. doi: 10.1142/S0217751X12300165.

[66] A. Giammanco and R. Schwienhorst. Single top-quark production at the Tevatron and the LHC. *arXiv:1710.10699 [hep-ex]*, 2017.

[67] H.L. Lai et al. New parton distributions for collider physics. *In: Phys. Rev. D82, arXiv:1007.2241 [hep-ph]*, 2011. doi: 10.1103/PhysRevD.82.074024.

[68] ATLAS - CMS recommended predictions for top-quark-pair cross sections using the Top++v2.0 program. 2015. URL https://twiki.cern.ch/twiki/bin/view/LHCPhysics/TtbarNNLO.

[69] ATLAS Collaboration. Measurement of the $t\bar{t}$ production cross-section using $e\mu$ events with b-tagged jets in pp collisions at $\sqrt{s} = 13$ TeV with the ATLAS detector. *In:Phys.Lett.B761, arXiv:1606.02699 [hep-ex]*, 2016. doi: 10.1016/j.physletb.2016.08.019.

[70] CMS Collaboration. Measurement of the $t\bar{t}$ production cross-section using events in $e\mu$ final state in pp collisions at $\sqrt{s} = 13$ TeV. *In:Eur.Phys.J.C77, arXiv:1611.04040 [hep-ex]*, 2017. doi: 10.1140/epjc/s10052-017-4718-8.

[71] ATLAS Collaboration. Measurement of the $t\bar{t}$ production cross-section using $e\mu$ events with b-tagged jets in pp collisions at $\sqrt{s}$ 7 and 8 TeV with the ATLAS detector. *In:Eur.Phys.J.C74, arXiv:1406.5375 [hep-ex]*, 2014. doi: 10.1140/epjc/s10052-016-4501-2.

[72] Measurement of the $t\bar{t}$ production cross-section using events in $e\mu$ channel in proton–proton collisions at $\sqrt{s}$ =7 and 8 TeV, author=CMS Collaboration. *In: JHEP 08, arXiv:1603.02303 [hep-ex]*, 2016. doi: doi:10.1007/JHEP08(2016)029.

[73] R.M.Harris and S.Jain. Cross-sections for leptophobic Topcolor Z' decaying to top-antitop. *Eur.Phys.JC72(2012)2072, arXiv:1112.4928 [hep-ph].*

[74] G.Altarelli, B.Mele and M.Ruiz-Altaba. Searching for new heavy vector bosons in pp colliders. *Z.Phys.C-Particles and Fields 45,109-121 (1989)*, 1989.

[75] G. Altarelli, B.Mele and M.Ruiz-Altaba. Searching for new heavy vector bosons in pp colliders. *CERN-TH.5323/89*, 1989.

[76] M. Aoki and N. Oshimo. A Supersymmetric Model with an Extra U(1) Gauge Symmetry. *OCHA-PP-137, arXiv:hep-ph/9907481v1*, 1989.

[77] T. G. Rizzo. Z' Phenomenology and the LHC. *arXiv:hep-ph/0610104v1*, 2006.

[78] CDF Collaboration. Search for $Z' \to e^+e^-$ Using Dielectron Mass and Angular Distribution. *arXiv:hep-ex/0602045v1*, 2006.

[79] B.A. Dobrescu and S. Willocq. Z'-Boson Searches. *Chin.Phys.C,40,100001*, 2006.

[80] U. Baur and L.H. Orr. Searching for $t\bar{t}$ Resonances at the Large Hadron Collider. *UB-HET-08-01, arXiv:0803.1160v1 [hep-ph]*, 2008.

[81] L. Evans and P. Bryant. LHC Machine. *In:Journal of Instrumentation 3.08*, 2008. URL http://stacks.iop.org/1748-0221/3/i=08/a=S08001.

[82] CMS Collaboration. The CMS experiment at the CERN LHC. *In: JINST 3*, 2008. doi: 10.1088/1748-0221/3/08/S08004.

[83] LHCb Collaboration. The LHCb Detector at the LHC. *In: Journal of Instrumentation 3.08*, 2008. URL http://stacks.iop.org/1748-0221/3/i=08/a=S08005.

[84] ALICE Collaboration. The ALICE experiment at the CERN LHC. *In: Journal of Instrumentation 3.08*, 2008. URL http://stacks.iop.org/1748-0221/3/i=08/a=S08002.

[85] MoEDAL Collaboration. Technical Design Report of the MoEDAL Experiment. *Technical report CERN-LHCC-2009-006. MoEDAL-TDR-001. CERN*, 2009. URL http://cds.cern.ch/record/1181486.

[86] The LHCf Collaboration. The LHCf detector at the CERN Large Hadron Collider. *In: Journal of Instrumentation 3.08*, 2008. URL http://stacks.iop.org/1748-0221/3/i=08/a=S08006.

[87] TOTEM Collaboration. The TOTEM Experiment at the CERN Large Hadron Collider. *In: Journal of Instrumentation 3.08*, 2008. URL http://stacks.iop.org/1748-0221/3/i=08/a=S08007.

[88] ATLAS Collaboration. Performance of the ATLAS Trigger System in 2010. *In:Eur.Phys.J.C72, arXiv:1110.1530 [hep-ex]*, 2012. doi: 10.1140/epjc/s10052-011-1849-1.

[89] ATLAS Collaboration. Performance of the ATLAS Trigger System in 2015. *Eur.Phys.J.C77, arXiv:1611.09661v2 [hep-ex]*, 2015. doi: 10.1140/epjc/s10052-017-4852-3.

[90] ATLAS Collaboration. Trigger public results. 2019. URL https://twiki.cern.ch/twiki/bin/view/AtlasPublic/TriggerPublicResults.

[91] ATLAS Collaboration. Electron efficiency measurements with the ATLAS detector using the 2015 LHC proton–proton collision data. *ATLAS-CONF-2016-024*, pages 9–10, 2016.

[92] ATLAS Collaboration. Electron and photon performance measurements with the ATLAS detector using the 2015–2017 LHC protonproton collision data. *JINST 14 (2019) P12006, arXiv:1908.00005v2 [hep-ex]*, 2019. doi: 10.1088/1748-0221/14/12/P12006.

[93] ATLAS Collaboration. Electron efficiency measurements with the ATLAS detector using 2012 LHC protonproton collision data. *Eur.Phys.J.C(2017)77, arXiv:1612.01456v2 [hep-ex]*, 2015. doi: 10.1140/epjc/s10052-017-4756-2.

[94] ATLAS Collaboration. Measurement of the muon reconstruction performance of the ATLAS detector using 2011 and 2012 LHC proton–proton collision data. *In:Eur.Phys.J.C74(2014), arXiv:1407.3935 [hep-ex]*, 2014. doi: 10.1140/epjc/s10052-014-3130-x.

[95] T. Plehn. *Lectures on LHC Physics*, chapter LHC Phenomenology. 2015. ISBN 978-3-319-05941-9. doi: 10.1007/978-3-319-05942-6.

[96] K. Rabbertz. *Jet Physics at the LHC*, chapter Jet Measurement. 2017. ISBN 9783319421131 (Print), 9783319421155 (eBook). doi: 10.1007/978-3-319-42115-5.

[97] M. Cacciari, G. P. Salam and G. Soyez. The Anti-k(t) jet clustering algorithm. *In: JHEP 04 (2008), arXiv:0802.1189 [hep-ph]*, 2008. doi: 10.1088/1126-6708/2008/04/063.

[98] ATLAS Collaboration. Topological cell clustering in the ATLAS calorimeters and its performance in LHC Run 1. *In:Eur.Phys.J.C77(2017), arXiv:1603.02934 [hep-ex]*, 2017. doi: 10.1140/epjc/s10052-017-5004-5.

[99] T. Barillari et al. Local Hadronic Calibration. Technical report. *ATL-COM-LARG-2008-006, the report-number ATL-LARGPUB-2009-001-2 has been assigned. Geneva: CERN, June 2008*, 2008. URL https://cds.cern.ch/record/1112035.

[100] ATLAS Collaboration. Jet energy measurement with the ATLAS detector in proton–proton collisions at $\sqrt{s} = 7$TeV. *In:Eur.Phys.J.C73(2013), arXiv:1112.6426 [hep-ex]*, 2013. doi: 10.1140/epjc/s10052-013-2304-2.

[101] ATLAS Collaboration. Jet energy scale measurements and their systematic uncertainties in protonproton collisions at $\sqrt{s} = 13$ TeV with the ATLAS detector. *Phys. Rev. D., arXiv:1703.09665v2 [hep-ex]*, 2017.

[102] ATLAS Collaboration. Pile-up subtraction and suppression for jets in ATLAS. *ATLAS-CONF-2013-083*, 2013.

[103] ATLAS Collaboration. Jet global sequential corrections with the ATLAS detector in proton–proton collisions at $\sqrt{s} = 8$ TeV. *ATLAS-CONF-2015-002*, 2015.

[104] ATLAS Collaboration. In–situ measurements of the ATLAS large-radiusjet response in $\sqrt{s} = 13$TeV p–p collisions. *ATLAS-CONF-2017-063*, 2017.

[105] ATLAS Collaboration. ATLAS b–jet identification performance and efficiency measurement with $t\bar{t}$ events in p–p collisions at $\sqrt{s} = 13$TeV. *Eur.Phys.J.C 79 (2019) 970, arXiv:1907.05120v2 [hep-ex]*, 2019. doi: 10.1140/epjc/s10052-019-7450-8.

[106] ATLAS Collaboration. ATLAS b–jet identification performance and efficiency measurement with $t\bar{t}$ events in p–p collisions at $\sqrt{s} = 13$TeV. *Eur.Phys.J.C 79 (2019) 970*, springer. URL https://link.springer.com/content/pdf/10.1140/epjc/s10052-019-7450-8.pdf.

[107] ATLAS Collaboration. Calibration of the ATLAS b–tagging algorithm in $t\bar{t}$ semileptonic events. *ATLAS-CONF-2018-045*, 2018.

[108] ATLAS Collaboration. Calibration of light–flavour b–jet mistagging rates using ATLAS proton–proton collision data at $\sqrt{s} = 13$TeV. *ATLAS-CONF-2018-006*, 2018.

[109] ATLAS Collaboration. Measurement of b–tagging efficiency of c–jets in $t\bar{t}$ events using a likelihood approach with the ATLAS detector. *ATLAS-CONF-2018-001*, 2018.

[110] ATLAS Collaboration. Performance of missing transverse momentum reconstruction with the ATLAS detector using protonproton collisions at $\sqrt{2} = 13$ TeV. *Eur.Phys.J.C78(2018)903, arXiv:1802.08168v2 [hep-ex]*, 2018. doi: 10.1140/epjc/s10052-018-6288-9.

[111] ATLAS Collaboration. Performance of algorithms that reconstruct missing transverse momentum in $\sqrt{2} = 8$ TeV proton–proton collisions in the ATLAS detector. *Eur.Phys.J.C77(2017), arXiv:1609.09324 [hep-ex]*, 2017. doi: 10.1140/epjc/s10052-017-4780-2.

[112] T. Cornelissen et al. Concepts, Design and Implementation of the ATLAS New Tracking (NEWT). *ATL-COM-SOFT-2007-002. Geneva: CERN, Mar. 2007*, 2007. URL https://cds.cern.ch/record/1020106.

[113] ATLAS Collaboration. Performance of the ATLAS track reconstruction algorithms in dense environments in LHC Run 2. *Eur. Phys. J. C 77 (2017) 673, arXiv:1704.07983v2 [hep-ex]*, 2017. doi: 10.1140/epjc/s10052-017-5225-7.

[114] R. Fruhwirth. Application of Kalman filtering to track and vertex fitting. *In: Nucl.Instrum.Meth.A262(1987)*, 1987. doi: doi:10.1016/0168-9002(87)90887-4.

[115] ATLAS Collaboration. Track Reconstruction Performance of the ATLAS Inner Detector at $\sqrt{s} = 13$TeV. *ATL-PHYS-PUB-2015-018*, 2015.

[116] S Boutle et al. Primary vertex reconstruction at the ATLAS experiment. *ATL-SOFT-PROC-2017-051*, 2017.

[117] ATLAS Collaboration. Reconstruction of primary vertices at the ATLAS experiment in Run 1 protonproton collisions at the LHC. *Eur. Phys. J. C 77 (2017) 332, arXiv:1611.10235v2 [physics.ins-det]*, 2017. doi: 10.1140/epjc/s10052-017-4887-5.

[118] CMS Collaboration. Measurement of Tracking Efficiency. *CMS PAS TRK-10-0021*, 2010.

[119] ATLAS Collaboration. Measurement of $D^{\pm}$, $D^{\pm}$ and $D_s^{\pm}$ meson production cross sections in pp collisions at $\sqrt{s} = 7$TeV with the ATLAS detector. *Nucl. Phys. B, arXiv:1512.02913v2 [hep-ex]*, 2015.

[120] G. Cacciapaglia, A. Deandrea and J. Llodra-Perez. A dark matter candidate from Lorentz invariance in 6D. *JHEP 03 (2010) 083, arXiv:0907.4993 [hep-ph].*

[121] R. Frederix, D. Pagani, and M. Zaro. Large NLO corrections in $t\bar{t}W^{\pm}$ and $t\bar{t}t\bar{t}$ hadroproduction from supposedly subleading EW contributions. *arXiv:1711.02116v2 [hep-ph]*, pages 23–24, 2018.

[122] CMS Collaboration. Search for standard model production of four top quarks in proton–proton collisions at $\sqrt{s} = 13$ TeV. *Phys.Lett.B772(2017,336358,arXiv:1702.06164*, .

[123] CMS Collaboration. Search for standard model production of four top quarks with same-sign and multilepton final states in proton–proton collisions at $\sqrt{s} = 13$ TeV. *Eur.Phys.J.C78(2018), arXiv:1710.106144*, .

[124] L. Lista. statistical methods for Data Analysis in particle physics. *Springer*, 2016. doi: 10.1007/978-3-319-20176-4.

[125] J. Alwall et al. The automated computation of tree-level and next-to-leading order differential cross sections, and their matching to parton shower simulations. *JHEP 1407 (2014) 079, arXiv:1405.0301 [hep-ph]*, 2014.

[126] T. Sjstrand et al. An Introduction to PYTHIA 8.2. *Comput. Phys. Commun. 191 (2015) 159, arXiv:1410.3012 [hep-ph]*, 2015.

[127] NeuroBayes. URL https://twiki.cern.ch/twiki/bin/view/Main/NeuroBayes.

[128] ATLAS Collaboration. Measurements of top-quark pair differential cross-sections in the hadronic channel in p p collisions at $\sqrt{s} = 13$ TeV using the ATLAS detector. *ANA-TOPQ-2018-18*, .

[129] M. Erdmann B. Fischer and M. Rieger. Jet-Parton Assignment in $t\bar{t}H$ Events using Deep Learning. *arXiv:1706.01117v2 [hep-ex]*.

[130] F. Pedregosa et al. Scikit-learn: Machine Learning in Python. *JMLR 12 (2011) 2825*, 2011.

[131] G. James, D. Witten, T. Hastie and R. Tibshirani. *An Introduction to Statistical Learning with Applications in R*. 2017. ISBN 978-1-4614-7137-0. doi: 10.1007/978-1-4614-7138-7.

[132] A. Hoecker, P. Speckmayer et al. TMVA 4Toolkit for Multivariate Data Analysis with ROOT Users Guide. *arXiv:physics/0703039 [Data Analysis, Statistics and Probability]*, 2017. URL https://root.cern.ch/download/doc/tmva/TMVAUsersGuide.pdf.

[133] DØ Collaboration. Measurement of the Top Quark Mass Using Dilepton Events. *Phys.Rev.Lett.80:2063-2068,1998, arXiv:hep-ex/9706014*, 1998.

[134] ATLAS Collaboration. Measurements of top-quark pair spin correlations in the $e\mu$ channel at $\sqrt{s} = 13$TeV using pp collisions in the ATLAS detector. *arXiv:1903.07570v1 [hep-ex]*, 2019.

[135] ATLAS Collaboration. Observation of spin correlation in $t\bar{t}$ events from pp collisions at $\sqrt{s} = 7$TeV using the ATLAS detector. *Phys.Rev.Lett.108(2012)212001, arXiv:1203.4081 [hep-ex]*, 2012.

[136] ATLAS Collaboration. Measurements of spin correlation in topantitop quark events from proton–proton collisions at $\sqrt{s} = 7$TeV using the ATLAS detector. *Phys. Rev. D 90 (2014) 112016, arXiv:1407.4314 [hep-ex]*, 2014.

[137] ATLAS Collaboration. Measurement of the correlation between the polar angles of leptons from top quark decays in the helicity basis at $\sqrt{s} = 7$TeV using the ATLAS detector. *Phys. Rev. D 93(2016) 012002, arXiv:1510.07478 [hep-ex]*, 2016.

[138] CMS Collaboration. Measurements of $t\bar{t}$ spin correlations and top-quark polarization using dilepton final states in pp collisions at $\sqrt{s} = 7$TeV. *Phys. Rev. Lett. 112 (2014) 182001, arXiv:1311.3924 [hep-ex]*, 2014.

[139] ATLAS Collaboration. Measurements of top quark spin observables in $t\bar{t}$ events using dilepton final states in $\sqrt{s} = 8$ pp collisions with the ATLAS detector. *Phys.Rev.Lett.114(2015)142001, arXiv:1412.4742 [hep-ex]*, 2015.

[140] ATLAS Collaboration. Measurement of Spin Correlation in TopAntitop Quark Events and Search for Top Squark Pair Production in pp Collisions at $\sqrt{s} = 8$TeV Using the ATLAS Detector. *JHEP 03 (2017) 113, arXiv:1612.07004 [hep-ex]*, 2017.

[141] CMS Collaboration. Measurement of spin correlations in $t\bar{t}$ production using the matrix element method in the muon+jets final state in pp collisions at p $\sqrt{s} = 8$TeV. *Phys. Lett. B 758 (2016) 321, arXiv:1511.06170 [hep-ex]*, 2016.

[142] CMS Collaboration. Measurements of $t\bar{t}$ spin correlations and top quark polarization using dilepton final states in pp collisions at $\sqrt{s} = 8$TeV. *Phys.Rev.D93(2016)052007, arXiv:1601.01107 [hep-ex]*, 2016.

[143] CMS Collaboration. Measurement of the top quark polarization and $t\bar{t}$ spin correlations using dilepton final states in proton–proton collisions at $\sqrt{s} = 13$ TeV. *arXiv:1907.03729v2 [hep-ex]*, 2019. doi: 10.1103/PhysRevD.100.072002.

[144] DØ Collaboration. Measurement of Spin Correlation in $t\bar{t}$ Production Using a Matrix Element Approach. *Phys.Rev.Lett.107(2011)032001, arXiv:1104.5194 [hep-ex]*, 2011.

[145] DØ Collaboration. Measurement of Spin Correlation in $t\bar{t}$ Production Using Dilepton Final States. *Phys.Lett.B702(2011)16, arXiv:1103.1871 [hep-ex]*, 2011.

[146] DØ Collaboration. Evidence for Spin Correlation in $t\bar{t}$ Production. *Phys.Rev.Lett.108(2012)032004, arXiv:1110.4194 [hep-ex]*, 2012.

[147] DØ Collaboration. Measurement of spin correlation between top and antitop quarks produced in $p\bar{p}$ collisions at $\sqrt{s} = 1.96$TeV. *Phys.Lett.B757(2016)199, arXiv:1512.08818 [hep-ex]*, 2016.

[148] CDF Collaboration. Measurement of $t\bar{t}$ Spin Correlation in $p\bar{p}$ Collisions Using the CDF II Detector at the Tevatron. *Phys.Rev.D83(2011)031104, arXiv:1012.3093 [hep-ex]*, 2011.

[149] ATLAS Collaboration. ATLAS Pythia 8 tunes to 7 TeV data. . URL https://cds.cern.ch/record/1966419.

[150] S. Frixione, P. Nason and G. Ridolfi. A Positive-weight next-to-leading-order Monte Carlo for heavy flavour hadroproduction. *JHEP 09 (2007) 126, arXiv:0707.3088 [hep-ph]*, 2007.

[151] P. Nason. A New method for combining NLO QCD with shower Monte Carlo algorithms. *JHEP 0411 (2004) 040, arXiv:hep-ph/0409146*, 2004.

[152] S. Frixione, P. Nason and C. Oleari. Matching NLO QCD computations with Parton Shower simulations: the POWHEG method. *JHEP 11 (2007) 070,arXiv:0709.2092 [hep-ph]*, 2007.

[153] S. Alioli, P. Nason, C. Oleari and E. Re. A general framework for implementing NLO calculations in shower Monte Carlo programs: the POWHEG BOX. *JHEP 1006 (2010) 043, arXiv:1002.2581 [hep-ph]*, 2010.

[154] NNPDF Collaboration, R.D. Ball et al. Parton distributions for the LHC Run II. *JHEP 04 (2015) 040, arXiv:1410.8849 [hep-ph]*, 2015.

[155] ATLAS Collaboration. Studies on top-quark Monte Carlo modelling for Top2016. . URL https://cds.cern.ch/record/2216168.

[156] ATLAS Collaboration. Comparison of Monte Carlo generator predictions to ATLAS measurements of top pair production at 7 TeV. *ATL-PHYS-PUB-2015-002*, . URL https://cds.cern.ch/record/1981319/files/ATL-PHYS-PUB-2015-002.pdf.

[157] E. Re. Single-top Wt-channel production matched with parton showers using the POWHEG method. *Eur. Phys. J. C 71 (2011) 1547, arXiv:1009.2450 [hep-ph]*, 2011.

[158] S. Frixione, E. Laenen, P. Motylinski, B. R. Webber and C. D. White. Single-top hadroproduction in association with a W boson. *JHEP 0807 (2008) 029, arXiv:0805.3067 [hep-ph]*, 2008.

[159] E. Re R. Frederix and P. Torrielli. Single-top t-channel hadroproduction in the four-flavour scheme with POWHEG and aMC@NLO. *JHEP 09 (2012) 130, arXiv:1207.5391 [hep-ph]*, 2012.

[160] T. Gleisberg et al. Event generation with SHERPA 1.1. *JHEP 02 (2009) 007, arXiv:0811.4622 [hep-ph]*, 2009.

[161] T. Gleisberg and S. Hoeche. Comix, a new matrix element generator. *JHEP 12 (2008) 039, arXiv:0808.3674 [hep-ph]*, 2008.

[162] S. Schumann and F.Krauss. Parton shower algorithmbased onCatani-Seymour dipole factorisation. *JHEP 03 (2008) 038, arXiv:0709.1027 [hep-ph]*, 2008.

[163] S. Hoeche, F. Krauss, M. Schonherr and F. Siegert. A critical appraisal of NLO+PS matching methods. *JHEP 09 (2012) 049, arXiv:1111.1220 [hep-ph]*, 2012.

[164] S. Hoeche, F. Krauss, M. Schonherr and F. Siegert. QCD matrix elements + parton showers: The NLO case. *JHEP 04 (2013) 027, arXiv:1207.5030 [hep-ph]*, 2013.

[165] S. Catani, F. Krauss, R. Kuhn and B. R. Webber. QCD matrix elements + parton showers. *JHEP 11 (2001) 063, arXiv:hep-ph/0109231 [hep-ph]*, 2001.

[166] S. Hoeche, F. Krauss, S. Schumann and F. Siegert. QCD matrix elements and truncated showers. *JHEP 05 (2009) 053, arXiv:0903.1219 [hep-ph]*, 2009.

[167] F. Cascioli, P. Maierhofer and S. Pozzorini. Scattering Amplitudes with Open Loops. *Phys. Rev. Lett. 108 (2012) 111601, arXiv:1111.5206 [hep-ph]*, 2012.

[168] A. Denner, S. Dittmaier and L. Hofer. Collier: a fortran-based Complex One-Loop LIbrary in Extended Regularizations. *Comput. Phys. Commun. 212 (2017) 220, arXiv:1604.06792 [hep-ph]*, 2017.

[169] M. Czakon et al. Top-pair production at the LHC through NNLO QCD and NLO EW. *arXiv:1705.04105v2 [hep-ph]*, 2017.

[170] ATLAS Collaboration. Luminosity Determination in pp Collisions at $\sqrt{s} = 13$TeV using the ATLAS Detector at the LHC. *ATLAS-CONF-2019-021*, 2019. URL https://cdsweb.cern.ch/record/2677054.

[171] G. Avoni et al. The new LUCID-2 detector for luminosity measurement and monitoring in ATLAS. *JINST 13 (2018) P07017*, 2018.

[172] ATLAS Collaboration. Luminosity Determination in pp Collisions at $\sqrt{s} =$ 8TeV using the ATLAS Detector at the LHC. *Eur. Phys. J. C 76 (2016) 653, arXiv:1608.03953 [hep-ex]*, 2016.

[173] ATLAS Collaboration. Electron and photon energy calibration with the ATLAS detector using LHC Run 1 data. *Eur. Phys. J. C 74 (2014) 3071, arXiv:1407.5063 [hep-ex]*, 2014.

[174] ATLAS Collaboration. Tagging and suppression of pileup jets with the ATLAS detector. *ATLASCONF-2014-018, 2014*, 2014. URL https://cds.cern.ch/record/1700870.

[175] ATLAS Collaboration. Jet Calibration and Systematic Uncertainties for Jets Reconstructed in the ATLAS Detector at $\sqrt{s} = 13$ TeV. *ATL-PHYS-PUB-2015-015*, 2015. URL https://cds.cern.ch/record/2037613.

[176] ATLAS Collaboration. Simulation of top-quark productionfor the ATLAS experiment at $\sqrt{s} =$ 13TeV. *ATL-PHYS-PUB-2016-004*, 2016. URL https://cds.cern.ch/record/2120417/files/ATL-PHYS-PUB-2016-004.pdf.

[177] T. Junk. Confidence level computation for combining searches with small statistics. *Nucl. Inst. Meth. A 434 (1999) 435, arXiv:9902006 [hep-ex]*, 1999.

[178] A. L. Read. Presentation of search results: The CLs technique. *J. Phys. G 28 (2002) 2693.*, 2002.

[179] W. Verkerke and D. P. Kirkby. The RooFit toolkit for data modeling. *arXiv:physics/0306116 [physics.data-an]*, .

[180] W. Verkerke and D. Kirkby. RooFit Users Manual. . URL http://roofit.sourceforge.net/.

[181] G. Cowan, K. Cranmer, E. Gross, and O. Vitells. Asymptotic formulae for likelihood-based tests of new physics. *Eur. Phys. J. C 71 (2011) 1554, arXiv:1007.1727v3 [physics.data-an]*, 2011.